Electron transport in low-dimensional systems: optoelectronic device simulations

Sergio Illera Robles

ADVERTIMENT. La consulta d'aquesta tesi queda condicionada a l'acceptació de les següents condicions d'ús: La difusió d'aquesta tesi per mitjà del servei TDX (**www.tdx.cat**) i a través del Dipòsit Digital de la UB (**diposit.ub.edu**) ha estat autoritzada pels titulars dels drets de propietat intel·lectual únicament per a usos privats emmarcats en activitats d'investigació i docència. No s'autoritza la seva reproducció amb finalitats de lucre ni la seva difusió i posada a disposició des d'un lloc aliè al servei TDX ni al Dipòsit Digital de la UB. No s'autoritza la presentació del seu contingut en una finestra o marc aliè a TDX o al Dipòsit Digital de la UB (framing). Aquesta reserva de drets afecta tant al resum de presentació de la tesi com als seus continguts. En la utilització o cita de parts de la tesi és obligat indicar el nom de la persona autora.

ADVERTENCIA. La consulta de esta tesis queda condicionada a la aceptación de las siguientes condiciones de uso: La difusión de esta tesis por medio del servicio TDR (**www.tdx.cat**) y a través del Repositorio Digital de la UB (**diposit.ub.edu**) ha sido autorizada por los titulares de los derechos de propiedad intelectual únicamente para usos privados enmarcados en actividades de investigación y docencia. No se autoriza su reproducción con finalidades de lucro ni su difusión y puesta a disposición desde un sitio ajeno al servicio TDR o al Repositorio Digital de la UB. No se autoriza la presentación de su contenido en una ventana o marco ajeno a TDR o al Repositorio Digital de la UB (framing). Esta reserva de derechos afecta tanto al resumen de presentación de la tesis como a sus contenidos. En la utilización o cita de partes de la tesis es obligado indicar el nombre de la persona autora.

WARNING. On having consulted this thesis you're accepting the following use conditions: Spreading this thesis by the TDX (**www.tdx.cat**) service and by the UB Digital Repository (**diposit.ub.edu**) has been authorized by the titular of the intellectual property rights only for private uses placed in investigation and teaching activities. Reproduction with lucrative aims is not authorized nor its spreading and availability from a site foreign to the TDX service or to the UB Digital Repository. Introducing its content in a window or frame foreign to the TDX service or to the UB Digital Repository is not authorized (framing). Those rights affect to the presentation summary of the thesis as well as to its contents. In the using or citation of parts of the thesis it's obliged to indicate the name of the author.

Electron transport in low-dimensional systems: optoelectronic device simulations

Sergio Illera Robles

Departament d'Electrònica, Facultat de Física
Institut de Nanociència i Nanotecnologia IN^{2}UB
Universitat de Barcelona

Directores: Dr. Albert Cirera Hernández
Dr. Joan Daniel Prades García

Thesis submitted for the degree of *Philosophiæ Doctor (PhD) in Nanosciences*
Tesis presentada para optar al titulo de Doctor en Nanociencias
por la Universitat de Barcelona

Barcelona, March 2015

A mi familia.

Abstract

The main topic of this thesis is the theoretical and computational investigation of the optoelectronic properties of large arrays of semiconductor quantum dots embedded in an insulator matrix. For that purpose, an electronic transport model has been formulated and implemented in a code for numerical simulations.

The relevance of this research is given by the possibility to simulate from basic design parameters, such as the device geometry and basic material constants, the electrical response of quantum dot based devices which are promising candidates to enhance and further downscaling the actual electronics.

Quantum dot properties have not analogous in the standard bulk semiconductor theory. Their electrical and optical properties are dominated by the quantum effects arising from the quantum confinement. This fact creates discrete energy level spectra and makes the electrical response of this kind of system different to the bulk case.

The developed electrical transport methodology is based on rate equations within the Transfer Hamiltonian approach in the ballistic regime. A set of non-coherent rate equations can be written for a random distribution of interacting quantum dots embedded in a dielectric media and the interaction among the quantum dots and between the quantum dots and the electrodes are introduced by transition rates and capacitive couplings. The effects of the local potential are computed within the self-consistent field regime.
The electrical transport model has been developed and expressed in a matrix form in order to make it extendable to larger systems. Transport through several quantum dot configurations has been studied in order to validate the model. Despite its simplicity, well-known effects are satisfactorily reproduced and explained. The results qualitatively agree with more complex theoretical approaches

While the description of the theoretical framework is kept as general as possible, a realistic modelization of: the capacitive couplings, the transmission coefficients, the electron/hole tunneling currents and the density of states of each quantum dot have been taken into account. Creating a new simulation tool that can foster the development of quantum dot based nanosystems aiding in their design.
To illustrate the kind of unique insight that these numerical simulations can provide,

two specific prototypical devices, an arbitrary array and a transistor device based on quantum dots, have been simulated.
To conclude, the previous developed transport model has been completed including illumination effects being able to study an design optoelectronic devices.

Acknowledgments

First of all, I would like to acknowledge my supervisors Albert and Dani, for their guidance, long discussion times and valuable comments and suggestions.
I also thank to Albert Cornet for all the received monetary founds.

Kristian, to give me the possibility to stay in the DTU.

All the colleges of the office: Oriol, Luis, Olga, Cristian, Aïda, Nuria, Xavi, Giovanni, Elena, Jordi, Yonder, Joan Manel, Julià ...

My friends from the Physics degree: Ferran, Hector, Juan, Miguel, Montse, Pol, Victor..for have been there and keep seeing during these years.

This work would have not been possible without the financial support of the FI program of the Catalan Government.

Contents

Contents **vii**

Symbols **xi**

Acronyms **xiii**

1 Introduction **1**
1.1 The quantum confinement: QDs properties . . . 3
1.2 Electronic transport in the nanoscale . . . 4
1.3 From theory to applications . . . 6
1.4 Objectives of the PhD Thesis . . . 8
1.5 Outline . . . 9
Bibliography . . . 11

2 Model fundamentals **17**
2.1 System decomposition . . . 18
2.1.1 Electron transport in the nanoscale: The Landauer-Büttiker approach . . . 21
2.1.2 Expression for the electric current: the Transfer Hamiltonian approach . . . 22
2.1.3 The Non-equilibrium Distribution Functions . . . 25
2.1.4 Charge effects . . . 26
2.1.4.1 Single electron charging effect: the Coulomb blockade regime . . . 27
2.1.4.2 Self-consistent field regime . . . 30
2.1.4.3 Comparison between the Coulomb blockade and the self-consistent field regimes . . . 31
2.2 Examples with simple cases . . . 33
2.2.1 Single QD: energy level position and transmission coefficients . . . 34
2.2.2 Two QDs in serial configuration: the role of the capacitive couplings 36
2.2.3 Two QDs in parallel configuration: double current paths . . . 39
2.3 Model validation: comparison with NEGFF . . . 41
2.3.1 NEGFF: the Non-Equilibrium Green's Function Formalism . . . 41
2.3.2 Comparison . . . 45
2.3.2.1 One single QD . . . 46

2.3.2.2 Two QDs 47
2.3.2.3 Serial case 47
2.3.2.4 Parallel case 48
2.3.2.5 Other two QDs configurations 49
2.3.2.6 Three QDs 51
2.3.2.7 Large QDs arrangements 52
2.3.3 Conclusions of the comparison with NEGFF 54
2.4 Conclusions 54
2.5 Annexes 56
2.5.1 The Hamiltonian in a second quantization: transmission coefficients 56
2.5.1.1 One single QD 57
2.5.1.2 Two QDs in series 57
2.5.1.3 Two QDs antiresonance configuration 58
Bibliography 59

3 Model implementation 65
3.1 The Density of States 65
3.1.1 Discrete energy spectrum 67
3.1.2 From discrete energy states to the continuum DOS 69
3.2 Electron & Holes 69
3.2.1 Transport tunneling processes 71
3.3 Transmission coefficients 71
3.3.1 The transfer matrix approach 72
3.3.2 Wentzel Kramers Brillouin approximation 74
3.3.2.1 Direct tunneling 76
3.3.2.2 Fowler-Nordheim tunneling 77
3.3.3 Transfer matrix vs. WKB approximation: a comparison 78
3.4 Capacitive couplings 79
3.4.1 Image charge method 79
3.4.2 QD-lead coupling 81
3.4.3 QD-QD coupling 82
3.5 Putting all together: final equations 82
3.6 Code implementation: the SimQD simulator 84
3.6.1 Input parameters 85
3.6.2 Self-consistent field process 85
3.6.2.1 Computational strategies: Anderson mixing 86
3.6.2.2 From equations to code: oriented matrix language 87
3.6.3 Code outputs 88
3.6.4 Computational performance 89
3.7 Conclusions 90
Bibliography 92

4 Study of the electronic transport in Silicon QDs 95
4.1 From DOS to current: preliminary discussion 95
4.2 Running the simulations 96
4.2.1 Device description 96
4.2.2 Material parameters 97

4.2.3 Example with the Effective Mass Approximation DOS 98
4.2.4 Example with Density Functional Theory inputs 99
4.3 One single Si/SiO_2 QD 101
4.3.1 Accumulated charge trends 103
4.4 Multilayered structures 104
4.5 Electronic devices based on QD 106
4.5.1 Transistor structure: the single electron transistor 107
4.5.2 Device simulation 108
4.5.3 QD array transistor 111
4.5.4 Double gate transistor 112
4.6 Carrier transport mechanisms in Si/SiO_2 structures 115
4.6.1 Si/SiO_2 transport mechanisms 115
4.6.1.1 Poole-Frenkel emission 115
4.6.1.2 Schottky emission 116
4.6.1.3 Tunneling processes 116
4.6.1.4 Trap assisted tunneling 117
4.6.2 Beyond the QD model 117
4.6.2.1 Tunneling through the total oxide 118
4.6.2.2 Defect inclusion 119
4.6.3 Transport simulations: experimental validation 120
4.6.3.1 SiO_2 layer: pure defects conduction 121
4.6.3.2 SiO_2 layer: defect and direct tunneling 123
4.6.3.3 Si QD/SiO_2 structure 125
4.6.3.4 Superlatice Si QD/SiO_2 structures 126
4.7 Conclusions 127
Bibliography 129

5 Interaction with Light **137**
5.1 Modifying the rate equations: the light terms 138
5.1.1 Toy examples: the role of each coefficient 140
5.2 Complete energy level spectrum 143
5.2.1 Single particle properties 143
5.2.2 Pair states 145
5.3 Derivation of the optical properties 146
5.3.1 Intraband transitions 148
5.3.2 Interband transitions 149
5.3.3 Absorption coefficient 149
5.4 Optical device simulations 151
5.4.1 Si/SiO_2 QDs: simulations 152
5.4.1.1 Si QDs: optical properties 152
5.4.1.2 Single QD: the symmetry role 154
5.4.1.3 Parallel case 156
5.4.1.4 Serial configuration 157
5.4.2 Comparison with experiments: PbSe QDs 158
5.4.2.1 PbSe QDs: optical properties 159
5.4.2.2 Simulation vs. Experiments 161
5.5 Conclusions 163

5.6 Appendix . . . 165
5.6.1 DFT vs. EMA in Si/SiO_2 QDs . . . 165
Bibliography . . . 167

6 Conclusions **173**

A Scientific Curriculum **181**
A.1 List of Publications . . . 181
A.1.1 Journal Articles . . . 181
A.1.2 Oral Presentations . . . 182
A.1.3 Poster Presentations . . . 182
A.1.4 Stays in Foreign Centers . . . 183
A.1.5 Participation in Projects . . . 183
A.1.6 Specialization Courses . . . 183

B Resumen en Castellano **185**

List of Figures **191**

Symbols

a_B	Bulk exciton Bohr radius
C_{ij}	Capacitive coupling between the ith and j^{th} elements
$C_{tot,i}$	Total capacitive coupling of the ith QD
E_{gap}	Bulk band gap
E_{gap}^{QD}	QD band gap
E_f	Equilibrium Fermi Level
$f_{R/L}(E)$	Fermi functions of the leads
G	Conductance
I_{FN}	Direct current between the two leads
I_{ij}	Current from the ith to the jth element
I_{QD}	Current through the QD matrix
I_{Traps}	Current assisted by intermediate traps
I(V)	Current voltage curve
M	Number of conducting channels
$M(E)$	Number of propagating modes
$\|M\|^2$	Transfer Hamiltonian matrix element
m_{ox}^{e}	Effective electron mass in the oxide
m_{ox}^{ECB}	Effective mass for ECB tunneling process
m_{ox}^{EVB}	Effective mass for EVB tunneling process
m_{ox}^{h}	Effective hole mass in the oxide
m_{ox}^{HVB}	Effective mass for HVB tunneling process
N	Number of QDs
N_i	Electron number in the ith QD
n_i	Non-equilibrium distribution function of the ith QD
$-q$	Electron charge
R	QD radius
R_{jk}	Optical transition probability
$T_{ij}(E)$	Transmission coefficient
$T_n(E)$	Transmission probability of eigenchannel n
U_0/E_c	Charging energy
U_i	Local potential in the ith QD
U_i^L	i^{th} QD Laplace solution of the Poisson equation

V	External applied voltage
V_{ds}	Drain-source applied voltage
V_{gate}	Gate polarization
V_j	Voltage in the jth element
$\triangle N_i$	Electron variation in the ith QD

$\alpha(h\nu)$	Absorption coefficient
ϵ	QD energy level
ε_0	Vacuum permittivity
ε_r	Relative dielectric permittivity of the material
$\mu_{L/R}$	Electrochemical potentials of the leads
ρ_i^e	Electron DOS of the ith QD
ρ_i^h	Hole DOS of the ith QD
$\rho_{L/R}(E)$	Leads densities of states
ϕ_b^{ECB}	Electron confinement potential
ϕ_b^{HVB}	Electron confinement potential
Ω	QD volume

Acronyms

CB	Coulomb Blockade
CMOS	Complementary Metal-Oxide-Semiconductor structure
DEG	Dimensional Electron Gas
DFT	Density Functional Theory
DOS	Density of States
DT	Direct Tunneling
ECB	Electron tunneling from conduction band to conduction band
EMA	Effective Mass Approximation
EVB	Hole tunneling from valence band to conduction band
FN	Fowler-Nordheim
HOMO	Highest Occupied Molecular Orbital
HVB	Hole tunneling from valence to valence band
LUMO	Lowest Unoccupied Molecular Orbital
MIM	Metal-Insulator-Metal structure
MOS	Metal-Oxide-Semiconductor structure
NCRE	Non-Coherent Rate Equation
NDR	Negative Differential Resistance
NEGFF	Non-Equilibrium Green's Function Formalism
PECVD	Plasma-Enhanced Chemical-Vapor Deposition
PF	Poole-Frenkel
QD	Quantum Dot
SCF	Self-Consistent Field
SET	Single Electron Transistor
SL	Supperlattice
STM	Scanning Transmission Microscopy
TAT	Trap Assisted Tunneling
TB	Thigh Binding
TEM	Transmission Electron Microscopy
WKB	Wentzel Krammers Brillouin

Chapter 1

Introduction

The invention of the solid state transistor and the semiconductor integrated circuits started a rapid development towards faster and smaller electronic devices. Nowadays, our way of life can not be imaginable without the use of electronics and therefore, semiconductor materials. Further progress in the integrability of these devices to achieve new capabilities and their miniaturization has arrived to the nanometric scale. Although the precise control of atoms is still a challenge, the nanoscale reflects behaviors that are intrinsically associated to atomic properties only well described by the quantum mechanics. Thus, these devices are reaching the regime where the quantum mechanical description of the system is of major importance and the classical models can not describe it correctly. Additionally, many new possible applications are rapidly emerging from these small quantum systems.

Up to now, all the developed semiconductor technology has grounded on Silicon (Si) since it is an abundant material; its impurity concentration can be easily controlled; it exhibits a semiconductor behavior at higher temperatures than germanium; its native oxide is easily thermally grown and forms a better semiconductor/insulator interface than any other material. Furthermore, the non-toxicity and the economic value of this material have made the Si as the widest used material for electronic devices being the nucleus of the CMOS (Complementary Metal-Oxide-Semiconductor) transistor technology. Nevertheless, the complete development of the optoelectronic technology based on Si is strongly limited by the band structure of the material and its indirect band gap, limiting the efficiency of these devices.

The progress in the fabrication techniques has opened the possibility to create structures of size ranging from few to tens of nanometers, which consist on hundreds to thousands of atoms called quantum dots (QDs). In these structures, the electrons are confined in all three spatial dimensions being the ultimate goal in the semiconductor technology. In the last decades, there was a lot of interest in QDs since their electrical and optical properties differ from their bulk counterparts. Due to the strong electron confinement,

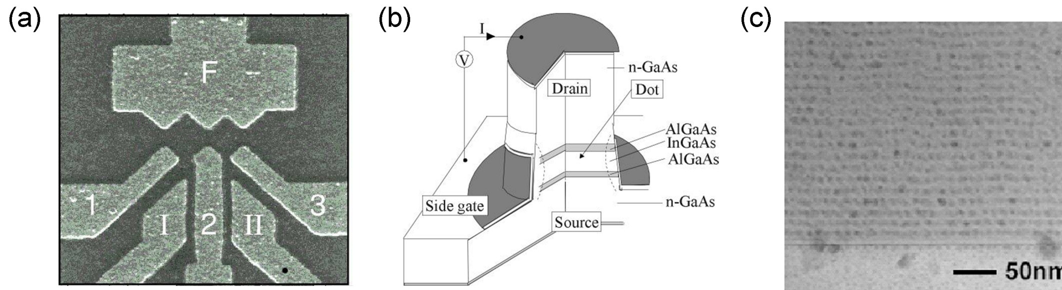

FIGURE 1.1: (a) Scanning electron microscopy (SEM) picture of a lateral quantum dot structure. Six metallic gates that create the confinement potentials are deposited on top of a GaAs/AlGaAs heterostructure. The picture has been extracted from Ref. [1]. (b) Scheme of a vertical QD structure [2]. (c) Transmission electron microscopy (TEM) image of large array of Si Qds in a SiO_2 matrix with low magnification, extracted from Ref. [3].

a single QD exhibits a discrete energy spectrum [4] and it is usually called an "artificial atom". This system constitutes an excellent candidate for the study of the electronic quantum transport on mesoscopic length scales. Two main systems based on QDs can be distinguished: *lateral* and *vertical* structures. *Lateral* QDs take advantage of the two dimensional electron gas (2DEG) formed at the interface of two different semiconductor materials (usually GaAs/AlGaAs [1]) whereas the confinement in the other directions is achieved by external gates that deplete the electron gas in the other two directions (Fig. 1.1(a)). Using this strategy, one and two QDs can be created.
Vertical QDs are formed by layered semiconducting heterostructures. The different band gap of the materials produce the confinement potential in the transport direction whereas the lateral confinement is provided by pillars that are etched out of the layered heterostructure [2] (see the scheme in Fig. 1.1(b)).

The previous described fabrication methods are based on sophisticated combination of growth techniques and lithographical/etching methods. However, there are also technologies available to obtain QDs via chemical methods. Their size and shape can be controlled by the duration, temperature and ligand molecules used in the synthesis [5]. Other growing technique is based on heteroepitaxial systems with different lattice constants. During the growth of a layer of one material on top of the other, the formation of nanoscale islands takes place [6, 7] if the thickness of the layer (so called wetting layer) is larger than a certain critical value. Ensembles of millions of more or less homogeneous QDs in a small volume can be obtained in these manners being the preferred fabrication methods to create large QDs arrays (Fig. 1.1(c)).

1.1 The quantum confinement: QDs properties

The MOS (metal-oxide-semiconductor) transistor is the archetype of a confined two-dimensional system [8]. Nevertheless, the possibility to enhance this confinement by embedding low-dimensional structures in an insulating matrix has opened new way for further downscaling. Compared to the standard bulk technology, the corresponding devices based on these structures have increased the structural and conceptual complexity. The study of devices based on quantum confinement began in 1969 when Esaki *et al.* suggested a multilayer structure consisting in different bilayers of ultra-thin semiconductors creating the so called resonant tunnel diode [9, 10].

Quantum confinement describes the variation of the electronic and optical properties respect to the bulk case when the sampled material is sufficiently small. The phenomena results from the spatial confinement of the electrons and holes. In such small systems, the electronic properties of the material differ from the bulk case since the wave functions of the carriers have extra boundary conditions.

Three different nanostructures emerge as a function of the number of the confined dimensions: 1D confinement structure is a quantum well, 2D confinement forms a quantum wire and 3D confinement is called quantum dot (QD). Concerning QDs, the main property is that the energy states are discrete and well separated. Thus, the density of states (DOS) is now represented by a sequence of delta functions. Moreover, from the quantum confinement the energy gap of the QD is strongly dependent on the QD size. For spherical QDs, the relation is usually written as [11, 12]

$$E_{gap}^{Qd} = E_{gap} + \frac{A}{R^d}, \tag{1.1}$$

where E_{gap} is the bulk band gap and A is a constant that involves several material parameters. The QD radius is R and d is usually fitted as $d \in [1, 2]$. This property makes the QDs valuable objects that can be exploited in order to build light absorbers or emitting devices (LEDs) for photovoltaic applications [13, 14, 15].

Concerning Si QDs, the first device that emits visible light was presented in 1990 [16]. The interest in Si nanostructures arises from the possibility to overcome the limitations of bulk Si which are: (1) small band gap for optical purposes and (2) it is an indirect band gap semiconductor. With the carrier confinement, the emission wavelength is tuned by the QD size and the radiative paths (in absence of extra phonons) are favored [17] increasing dramatically the photon emission efficiencies. Moreover, these systems show lower operation currents due to the strong reduction in layer thickness and increased quantum efficiency. Thus, the light emitting device can provide the same optical output power with a lower injected current.

1.2 Electronic transport in the nanoscale

The conventional description of the electronic motion is based on the drift-diffusion equations which means that the electron takes a random walk or it travels along the direction of the applied field for some length before getting scattered into some random direction. The electrical resistance of the materials is directly related to the scattering processes that suffer the carriers. However, the miniaturization of the electronic devices from μm to nm sizes has led to the limit of the classical theory. When the size of the device is shorter than the mean free path of the carriers, described as the length that the carriers can travel without suffer an scattering process, the transport changes from diffusive to ballistic regime.
According to Ohm's law (diffusive transport), the resistance R of a material with cross-sectional area A and length L is given by

$$R = \frac{V}{I} = \rho \frac{L}{A} \tag{1.2}$$

being ρ the material resistivity. When the device length is decreased, the resistance tends to zero. However, numerous experiments since the 1980's have shown that this is not the usual behavior at the nanoscale and the resistance of the material at this scale becomes independent of the length. In the case of ballistic transport, the resistance follows

$$R = \underbrace{\frac{h}{q^2}}_{25.9\,k\Omega} \frac{1}{M}, \tag{1.3}$$

where M is an integer described as the number of conducting channels. The factor $\frac{h}{q^2}$ is associated to the channel-contact interfaces [18]. The minimum of conductance for ballistic transport is $G \approx 38.6\,\mu$S.
The total resistance of a device that includes both transport regimes (diffusive and ballistic) can be written as

$$R = \frac{h}{q^2} \frac{1}{M} \left(1 + \frac{L}{\lambda}\right), \tag{1.4}$$

where λ and L are the mean free path and the device length, respectively. From this expression, the two limits are clearly visible for $L >> \lambda$, diffusive transport, and $L << \lambda$, for ballistic regime. We must note that in the case of $L = 0$, there still is a resistance associated to the contacts.

From the semiclassical semiconductor theory, the simulation and modeling of semiconductor devices are based on a set of partial-differential equations. These so-called semiconductor-device equations describe the static and dynamic behavior of carriers in semiconductors under the influence of external fields that cause deviations from the thermal equilibrium. The set of equations is known as drift-diffusion equations, it consists on the Poisson equation, the continuity equations and the current density equations for

electrons and holes, respectively. The drift-diffusion equations are macroscopic equations which describe the flow of charged particles using appropriate models for their macroscopic physical behavior. They are based on semiclassical approximations (parabolic bands, effective masses). However, when the devices become smaller, the quantum limit is achieved and some quantum mechanicals effects that do not have equivalent in macroscopic physics appear and dominate the final response of the system.

Concerning QDs, they possess discrete energy levels and quantum properties more similar to natural atoms or molecules than to infinite semiconductors due to the strong confinement in all three directions. This fact affects dramatically the electronic transport properties. Until now, the research has mostly concentrated on single QDs and many novel transport phenomena have been discovered, such as the staircase-like current-voltage I(V) characteristic [19], Coulomb blockade oscillation [20], negative differential capacitance [21] and the Kondo effect [22] which can not be explained with the semiclassical theory.

From experimental point of view, rapid progress in microfabrication technology has made possible coupling QDs system with aligned levels [23, 24, 25]. Although one single QD contacted to the leads has been obtained, creating a so called single electron transistor (SET) [26, 27], the research mainstream is focused on the properties of structures with many QDs to create non-volatile memories [28], light-emitting devices [29] or solar cells devices [30]. An experimental route, the superlattice approach (SL) [31], was developed to create Si QDs embedded in SiO_2 matrices. Where thin silicon rich oxide (SRO) and thin SiO_2 layers are deposited alternatively making feasible that the SiO_2 layers act as a diffusion barriers. In a later temperature annealing process, the QDs are formed in the SRO layer. Thus, the QD size can be controlled tuning the thickness of the Si layer. However, the large band offsets between Si and SiO_2 ($\approx$ 3.1 and 4.5 eV for conduction and valence band, respectively) focus the problem on the charge transport through the oxide matrix.

From a theoretical perspective, researchers have recently paid much attention to electron transport through several QDs, since multiple QDs provide more Feynman paths for the electron transmission [32]. The complexity of structural and physical mechanisms as well as the prominent role of dimensional and quantum effects characterizing the operation of these novel QDs devices preclude the use of standard macroscopic bulk semiconductor transport theory. If the transport description for an electronic device requires the inclusion of quantum mechanical properties of the carriers, the choice is between two models:

- *Dynamical models* based on equations of motion for the Non-Equilibrium Green's Functions formalism (NEGFF) or for quantum-phase-space distributions such as Wigner functions.

- *Kinetic models* that use time-independent representations of the quantum-mechanical states solving kinetic- or rate equations.

Concerning dynamical models, NEGFF has been used to study the different transport material properties, such as electron conductance [33, 34] or thermoelectric characteristics [35]. Generally, NEGFF is used in combination with Tight Binding (TB) approach or Density Functional Theory (DFT) in order to describe from first principles the electrical transport. However, the computational effort demanded by NEGFF computations for systems with a large number of atoms exceeds the capabilities of the current high-computing facilities being unfeasible to simulate realistic devices. Thus, several approximations have to be done like decreasing the system size; considering only one or two QDs; a simplified description of the energy level spectra of the QDs or assuming constant transitions rates [36, 37, 38, 39, 40]. Although some extra implementations have been included in NEGFF, like the potential due to the self-charge [41, 42], nobody has done a fully quantum transport study in an extended arbitrary array of QDs using this framework since this approach is usually unfeasible to implement for large systems being large QD arrays a computational challenge.
The kinetic models are usually used due to their simplifications and the possibility to explain the electron transport from an intuitive point of view [43]. However, for large QD arrays, the number of possible states of the system increases dramatically being also impossible to solve it.
On the other hand, the single computations of transport in an extended QD array have been done by Carreras *et al.* [44], which use a semiempirical tunneling current model. However, their model is based on semiclassical current expressions and can not reproduce the intrinsic properties of the QDs.

Therefore, we can see that there exists a mismatch among the theoretical tools that allow to simulate in detail devices based on QDs and the current experimental ones. Although no substantial new physics can be inferred from QD matrices, they are the cheapest systems obtained by the experimentalists and thus, the preferred structure for the new devices based on QDs.
For this reason, the possibility to develop a transport methodology that includes: the intrinsic properties of the QDs (discrete energy levels), the nature of the carrier transport (tunneling processes) and the effects of the accumulated charge in the QDs (Coulomb blockade or self-charge effects) for describing large QDs arrays can be a valuable tool if it only depends on basic material constants and the device geometry.

1.3 From theory to applications

Currently, cell efficiencies of large scale production silicon solar cells are around 17% and will be increased to the 20% in the future [45]. To increase further this efficiency,

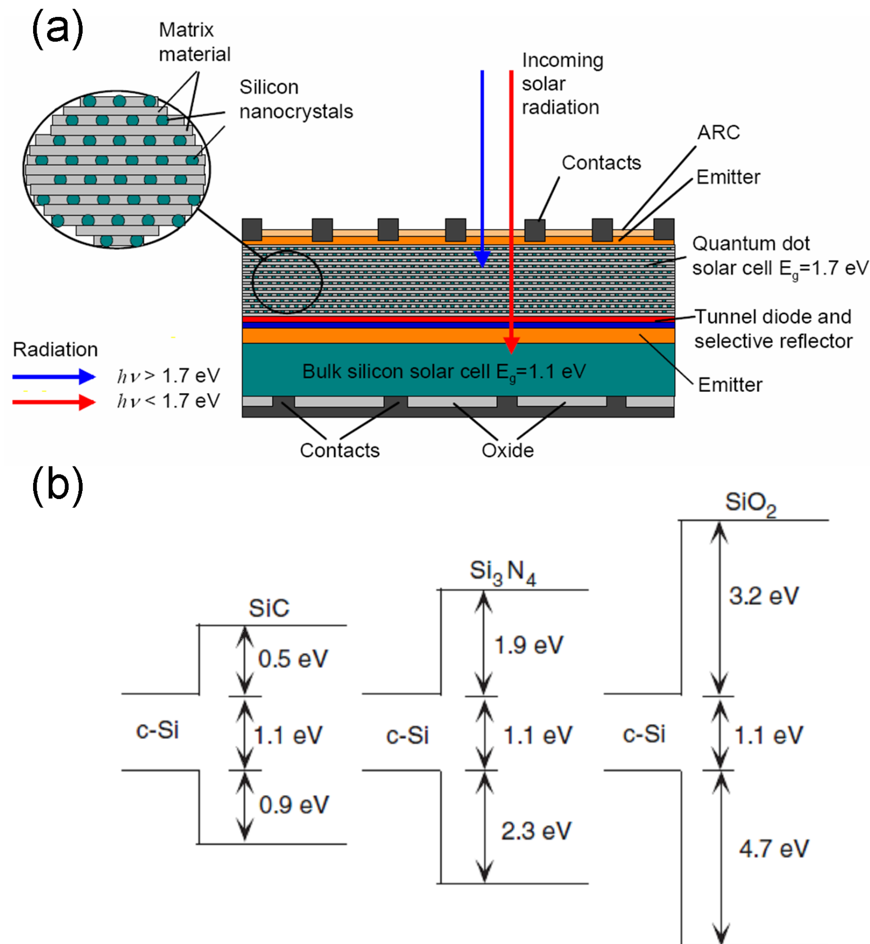

FIGURE 1.2: (a) Scheme of the Si-based tandem solar cell. (b) Bulk energy band alignments between crystalline silicon and its carbide, nitride and oxide.

tandem cells are proposed based on Si QDs multilayer embedded in a dielectric matrix allowing the band gap tuning by controlling the nanocrystal size and density. By these means, it is possible to optimize the band gap of the cell. This property can be used to solve the fundamental problem existing with silicon photovoltaic technology allowing to increase the photo-response of the device in a wide range of the solar spectrum. Silicon multi-junction solar cells have the potential to reach efficiencies above $30\% - 40\%$ in the near future [46, 47]. Moreover, Si QDs have low production costs.

In order to overcome the Shockley-Queisser limit [48, 49], i.e. the maximum theoretical efficiency of optoelectronic devices, the spatial confinement in the QDs provides a size dependent energy gap that in combination with bulk material overcome the efficiency limit. Tandem solar cells [3, 50] are stacks of individual cells with different energy thresholds each absorbing a different photon energy of the solar spectrum, usually connected together in series. The NASCEnt European project (FP7-NMP-245977) aims to develop new nanomaterials with new production technologies based on QDs materials for the enhancement of tandem solar cells efficiencies. To achieve this objective, the

understanding and correct description of the electrical transport as well as the optical interactions in these new materials are needed in order to overcome the efficiency limits of conventional solar cell concepts.

Fig. 1.2(a) shows the scheme of the proposed tandem solar cell of the NASCEnt project. To fabricate the Si QD matrix, several experimental techniques can be used but the multilayer approach, as proposed by Zacharias [31, 51], shows an accurate control of the QD size by stoichiometric diffusion barriers. However, the main problem in the QD matrix is the extraction of the photogenerated carriers [52] through the embedding matrix. Thus, in order to obtain high efficiencies not only carriers have to be created, besides, these carriers have to be extracted from the QDs before they recombine again imposing sufficient carrier mobility and hence, a reasonable conductivity. Therefore, the electrical transport properties of these matrices have to be also studied.

It is noted that the quantum confinement imposes localization of the carrier wave functions but, the carrier transport takes place through the insulator matrix by tunneling processes. Therefore, overlapping of the wave functions is necessary which requires close spacing between the QDs and/or low barrier height. Concerning Si QDs, engineers have embedded them in different insulating matrices: SiO_2, Si_3N_4 and SiC matrices tuning the transport properties. In Fig. 1.2(b), the different band alignment between the bulk Si and the matrices are shown.

In conclusion, the optoelectronic device response can be decomposed in two different parts: (i) a pure electrical carrier transport and (ii) the inclusion of the light interaction via the carrier generation. However, these two parts are directly correlated since the carriers have to be efficiently extracted from the QDs before recombining. Thus, although the QD band gap will govern the light absorption threshold, the final electrical response will be dependent on the carrier tunneling processes which are strongly dependent on the insulator material and also on the geometrical arrangement of the QDs. Here is where this thesis provides a valuable tool not only to understand the electronic processes, but also to design and simulate these optoelectronic devices.

1.4 Objectives of the PhD Thesis

A realistic theoretical estimate of the specific device performance is highly desirable in order to be able to asses the potentials and capabilities of the various novel devices concepts based on nanostructures. Within this context, theoretical simulations of such devices must be performed not only to understand but also to predict experimental behaviors. Moreover, from a physical point of view, one can learn a lot from these simulations if they are independent of high-level experimental parameters (as tunneling rates, defective interfaces...) and are based solely on low-level concrete ones (geometrical data, barrier height...). Despite the tremendous progress in the computational power

and the possibility to use supercomputer facilities, a complete theoretical description in large nanostructures based on first principles/atomistic description is still far to be achieved. This impractical computational time, forced us to write a compact model with some assumptions and relaxing the expectation of accuracy when treating with few-electron devices operating through quantum features.

The aim of this Thesis is to **cover the gap between the theoretical electronic transport studies and the built experimental optoelectronic devices** based on large QDs arrays. To achieve this purpose, two boundary conditions emerge: (i) the here proposed model has to reproduce the well-known theoretical behaviors and (ii) it also has to agree with the experimental data.

Here, a **compact electronic transport model** is developed in order to describe these nanostructures. It is based on rate equations, which have been previously used to model lasers or light-emitting diodes often offering a satisfactory description of the charge transport. Moreover, they present a more transparent vision of the electron transport. Thus, this model is easier to thinker with, in order to deal with more complicated nanostructures based on QDs. The here presented model was used to explain the ballistic electronic transport through a random distribution of interacting QDs embedded in a dielectric media taking in mind the simulation of realistic devices. The method underlying the model depends only on fundamental material parameters and the system geometry and it is based on the Transfer Hamiltonian approach. A set of non-coherent rate equations can be written and the interaction among the QDs and between the QDs and the electrodes is introduced by transition rates and capacitive couplings. The effects of the local potential are computed within the self-consistent field regime.

First of all, the electronic transport model was used to explain and highlight the main parameters that govern the response of the QDs under an external applied voltage. Once the transport model was validated, the light carrier generation/recombination was also included. This work was focused on Si QDs embedded in SiO_2 matrix however, it can be used to describe other materials changing the material parameters. The two unique features of this work are: (i) the model is based on just a few basic material parameters and on the device geometry and, (ii) it is simple enough to tackle problems involving a large number of QDs, which is the case of real devices. Besides, the complete framework has been implemented in a MATLAB© code creating a new theoretical tool, the SimQD simulator, that can foster the development of new QD-based nanodevices by aiding in their design.

1.5 Outline

As in any "theoretical" methodology, first of all the basic equations that conforms the model are presented and in a second stage, they are developed to include extra effects or

the parameters that initially were considered as constant are further developed. Within this form, a bottom-up strategy is followed (from simplest or basic cases to more complex ones). This strategy also allowed us to study in detail each sequence of this building up process.
Following this process, this PhD Thesis is organized as:

- In Chapter 2, the fundamental theory of the here developed electronic transport methodology is presented. In a second section, the main results for simplest cases allow us to highlight the parameters that will govern the electrical response of the system. To conclude this chapter, a direct comparison between our transport model and the well-known methodology based on NEGFF is also presented.

- In Chapter 3, the fundamental parameters that govern the electrical response (transmission coefficients, density of states and capacitive couplings) are described in a realistic form. Moreover, the computational strategies followed to the implementation of this transport methodology in a compact simulator tool to deal with large and arbitrary array of QD are also presented.

- In Chapter 4, the simulator tool is used to study the electrical response of QDs arrays. Furthermore, the single gate as well as a double gate transistor structures based on QDs are also presented and studied. To conclude, experimental measurements are well reproduced.

- In Chapter 5, the light interaction with the QDs is included creating an optoelectronic simulator. Again, the theory used to describe the optical transition rates is presented as well as the code implementation. Prior to simulate a realistic device, several examples are studied. To conclude this chapter, the simulation of a realistic device is presented and compared to experimental measurements.

- Finally, in Chapter 6, the main conclusions of the Thesis as well as the future work with possible ideas to extend this model are presented.

Bibliography

[1] S. De Franceschi, S. Sasaki, J. M. Elzerman, W. G. van der Wiel, S. Tarucha, and L. P. Kouwenhoven. Electron cotunneling in a semiconductor quantum dot. *Phys. Rev. Lett.*, 86:878–881, Jan 2001.

[2] S. Tarucha, D. G. Austing, T. Honda, R. J. van der Hage, and L. P. Kouwenhoven. Shell filling and spin effects in a few electron quantum dot. *Phys. Rev. Lett.*, 77:3613–3616, Oct 1996.

[3] Gavin Conibeer, Martin Green, Eun-Chel Cho, Dirk König, Young-Hyun Cho, Thipwan Fangsuwannarak, Giuseppe Scardera, Edwin Pink, Yidan Huang, Tom Puzzer, Shujuan Huang, Dengyuan Song, Chris Flynn, Sangwook Park, Xiaojing Hao, and Daniel Mansfield. Silicon quantum dot nanostructures for tandem photovoltaic cells. *Thin Solid Films*, 516(20):6748 – 6756, 2008. Proceedings on Advanced Materials and Concepts for Photovoltaics {EMRS} 2007 Conference, Strasbourg, France.

[4] S. Bandyopadhyay and H. S. Nalwa. *Quantum Dots and Nanowires.* American Scientific Publishers (ASP), 2003.

[5] A. P. Alivisatos. Semiconductor clusters, nanocrystals, and quantum dots. *Science*, 271(5251):933–937, 1996.

[6] M. Grundmann D. Bimberg and N.N. Ledentsov. *Quantum Dot Heterostructures.* (John Wiley Sons Ltd, 1999.

[7] J. Stangl, V. Holý, and G. Bauer. Structural properties of self-organized semiconductor nanostructures. *Rev. Mod. Phys.*, 76:725–783, Sep 2004.

[8] Tsuneya Ando, Alan B. Fowler, and Frank Stern. Electronic properties of two-dimensional systems. *Rev. Mod. Phys.*, 54:437–672, Apr 1982.

[9] L. Esaki and R. Tsu. Research and development superlattice and negative differential conductivity in semiconductors,. *IBM J. Res. Dev.*, 14(61), 1970.

[10] T. C. L. G. Sollner, W. D. Goodhue, P. E. Tannenwald, C. D. Parker, and D. D. Peck. Resonant tunneling through quantum wells at frequencies up to 2.5 THz. *Applied Physics Letters*, 43(6), 1983.

[11] J. P. Proot, C. Delerue, and G. Allan. Electronic structure and optical properties of silicon crystallites: Application to porous silicon. *Applied Physics Letters*, 61(16):1948–1950, 1992.

[12] L. E. Brus. Electron–electron and electronhole interactions in small semiconductor crystallites: The size dependence of the lowest excited electronic state. *The Journal of Chemical Physics*, 80(9), 1984.

[13] Thomas Kirchartz, Kaori Seino, Jan-Martin Wagner, Uwe Rau, and Friedhelm Bechstedt. Efficiency limits of Si/SiO_2 quantum well solar cells from first-principles calculations. *Journal of Applied Physics*, 105(10):104511, 2009.

[14] Gavin Conibeer, Martin Green, Richard Corkish, Young Cho, Eun-Chel Cho, Chu-Wei Jiang, Thipwan Fangsuwannarak, Edwin Pink, Yidan Huang, Tom Puzzer, Thorsten Trupke, Bryce Richards, Avi Shalav, and Kuo lung Lin. Silicon nanostructures for third generation photovoltaic solar cells. *Thin Solid Films*, 511–512(0):654 – 662, 2006.

[15] Eun-Chel Cho, Sangwook Park, Xiaojing Hao, Dengyuan Song, Gavin Conibeer, Sang-Cheol Park, and Martin A Green. Silicon quantum dot/crystalline silicon solar cells. *Nanotechnology*, 19(24):245201, 2008.

[16] L. T. Canham. Silicon quantum wire array fabrication by electrochemical and chemical dissolution of wafers. *Applied Physics Letters*, 57(10), 1990.

[17] Lorenzo Pavesi. Routes toward silicon-based lasers. *Materials Today*, 8(1):18 – 25, 2005.

[18] Supriyo Datta. *Electronic Transport in Mesoscopic Systems*. Cambridge University Press, 1995.

[19] J. B. Barner and S. T. Ruggiero. Observation of the incremental charging of Ag particles by single electrons. *Phys. Rev. Lett.*, 59:807–810, Aug 1987.

[20] J. Weis, R. J. Haug, K. v. Klitzing, and K. Ploog. Competing channels in single-electron tunneling through a quantum dot. *Phys. Rev. Lett.*, 71:4019–4022, Dec 1993.

[21] S. D. Wang, Z. Z. Sun, N. Cue, H. Q. Xu, and X. R. Wang. Negative differential capacitance of quantum dots. *Phys. Rev. B*, 65:125307, Mar 2002.

[22] W. G. van der Wiel, S. De Franceschi, T. Fujisawa, J. M. Elzerman, S. Tarucha, and L. P. Kouwenhoven. The kondo effect in the unitary limit. *Science*, 289(5487):2105–2108, 2000.

[23] R.J. Haug, J.M. Hong, and K.Y. Lee. Electron transport through one quantum dot and through a string of quantum dots. *Surface Science*, 263(1â“3):415 – 418, 1992.

[24] N. C. van der Vaart, S. F. Godijn, Y. V. Nazarov, C. J. P. M. Harmans, J. E. Mooij, L. W. Molenkamp, and C. T. Foxon. Resonant tunneling through two discrete energy states. *Phys. Rev. Lett.*, 74:4702–4705, Jun 1995.

[25] F. R. Waugh, M. J. Berry, D. J. Mar, R. M. Westervelt, K. L. Campman, and A. C. Gossard. Single-electron charging in double and triple quantum dots with tunable coupling. *Phys. Rev. Lett.*, 75:705–708, Jul 1995.

[26] M. A. Kastner. The single-electron transistor. *Rev. Mod. Phys.*, 64:849–858, Jul 1992.

[27] B. H. Choi, S. W. Hwang, I. G. Kim, H. C. Shin, Yong Kim, and E. K. Kim. Fabrication and room-temperature characterization of a silicon self-assembled quantum-dot transistor. *Applied Physics Letters*, 73(21):3129–3131, 1998.

[28] H.I. Hanafi, S. Tiwari, and I. Khan. Fast and long retention-time nano-crystal memory. *Electron Devices, IEEE Transactions on*, 43(9):1553 –1558, sep 1996.

[29] O. Jambois, Josep Carreras, A. Pérez-Rodríguez, B. Garrido, C. Bonafos, S. Schamm, and G. Ben Assayag. Field effect white and tunable electroluminescence from ion beam synthesized Si- and C-rich SiO_2 layers. *Applied Physics Letters*, 91(21):211105, 2007.

[30] A.J Nozik. Quantum dot solar cells. *Physica E: Low-dimensional Systems and Nanostructures*, 14(1-2):115 – 120, 2002.

[31] M. Zacharias, J. Heitmann, R. Scholz, U. Kahler, M. Schmidt, and J. Bläsing. Size-controlled highly luminescent silicon nanocrystals: A SiO/SiO_2 superlattice approach. *Applied Physics Letters*, 80(4), 2002.

[32] Weijiang Gong, Yisong Zheng, Yu Liu, and Tianquan Lü. A feynman path analysis of the fano effect in electronic transport through a parallel double quantum dot structure. *Physica E: Low-dimensional Systems and Nanostructures*, 40(3):618 – 626, 2008.

[33] U. Aeberhard. Theory and simulation of quantum photovoltaic devices based on the non-equilibrium green's function formalism. *Journal of Computational Electronics*, 10(4):394–413, 2011.

[34] Min Wang and Chang Ming Li. Negative differential resistance in oxidized zigzag graphene nanoribbons. *Phys. Chem. Chem. Phys.*, 13:1413–1418, 2011.

[35] Yuhong Huang, Zongquan Zhang, Fei Ma, Paul K. Chu, Cuiping Dong, and Xiumei Wei. First-principles calculation of the band structure, electronic states, and optical properties of Cr-doped ZnS double-wall nanotubes. *Computational Materials Science*, 101(0):1 – 7, 2015.

[36] Kamal K. Saha, Branislav K. Nikolić, Vincent Meunier, Wenchang Lu, and J. Bernholc. Quantum-interference-controlled three-terminal molecular transistors based on a single ring-shaped molecule connected to graphene nanoribbon electrodes. *Phys. Rev. Lett.*, 105:236803, Dec 2010.

[37] Kamal K. Saha, Wenchang Lu, J. Bernholc, and Vincent Meunier. First-principles methodology for quantum transport in multiterminal junctions. *The Journal of Chemical Physics*, 131(16):–, 2009.

[38] U. Aeberhard. Effective microscopic theory of quantum dot superlattice solar cells. *Optical and Quantum Electronics*, 44(3-5):133–140, 2012.

[39] E. Taranko, M. Wiertel, and R. Taranko. Transient electron transport properties of multiple quantum dots systems. *Journal of Applied Physics*, 111(2):–, 2012.

[40] Yu Han, Weijiang Gong, Haina Wu, and Guozhu Wei. Decoupling and antiresonance in electronic transport through a quantum dot chain embodied in an aharonov–bohm interferometer. *Physica B: Condensed Matter*, 404(14–15):2001 – 2007, 2009.

[41] A. Levy Yeyati, A. Martin-Rodero, and F. Flores. Electron correlation resonances in the transport through a single quantum level. *Phys. Rev. Lett.*, 71:2991–2994, Nov 1993.

[42] Yigal Meir and Ned S. Wingreen. Landauer formula for the current through an interacting electron region. *Phys. Rev. Lett.*, 68:2512–2515, Apr 1992.

[43] Carsten Timm. Tunneling through molecules and quantum dots: Master-equation approaches. *Phys. Rev. B*, 77:195416, May 2008.

[44] Josep Carreras, O Jambois, S Lombardo, and B Garrido. Quantum dot networks in dielectric media: from compact modeling of transport to the origin of field effect luminescence. *Nanotechnology*, 20(15):155201, 2009.

[45] R.M. Swanson. *DOE Solar Program Review Meeting*, 48, 2004.

[46] F. Meillaud, A. Shah, C. Droz, E. Vallat-Sauvain, and C. Miazza. Efficiency limits for single-junction and tandem solar cells. *Solar Energy Materials and Solar Cells*, 90(18–19):2952 – 2959, 2006.

[47] R. T. Ross and A. J. Nozik. Efficiency of hot-carrier solar energy converters. *Journal of Applied Physics*, 53:3813–3818, May 1982.

[48] William Shockley and Hans J. Queisser. Detailed balance limit of efficiency of pn junction solar cells. *Journal of Applied Physics*, 32(3), 1961.

[49] C. H. Henry. Limiting efficiencies of ideal single and multiple energy gap terrestrial solar cells. *Journal of Applied Physics*, 51(8), 1980.

[50] Ivan Perez-Wurfl, Xiaojing Hao, Angus Gentle, Dong-Ho Kim, Gavin Conibeer, and Martin. A. Green. Si nanocrystal p-i-n diodes fabricated on quartz substrates for third generation solar cell applications. *Applied Physics Letters*, 95(15):–, 2009.

[51] Lixin Yi, Roland Scholz, and Margit Zacharias. Size and density control of Si-nanocrystals realized by SiO_x/SiO_2 superlattice. *Journal of Luminescence*, 122–123(0):750 – 752, 2007. Luminescence and Optical Spectroscopy of Condensed Matter Proceedings of the 2005 International Conference on Luminescence and

Optical Spectroscopy of Condensed Matter 2005 International Conference on Luminescence and Optical Spectroscopy of Condensed Matter.

[52] Jan Linnros. Optoelectronics: Nanocrystals brighten transistors. *Nature Materials*, 4:117–119, 2005.

Chapter 2

Model fundamentals

Confined structures have been available to the experimentalist for a very long time, the MOS transistor is the archetype of a confined two-dimensional system [1]. Nevertheless, the possibility to enhance this confinement by embedding low-dimensional structures in an insulating matrix has renewed the interest. These structures (quantum dots, wires or layers) can be used in single-electron device [2], new memory concepts [3] and photon or electroluminescent devices [4].

Concerning quantum dots (QDs), they are particularly attractive because they possess discrete energy levels and quantum properties similar to natural atoms or molecules. From a fundamental point of view, research has been mostly concentrated on single QDs. These simple systems have been studied using many-body approaches, including Non-Equilibrium Green's Function Formalism (NEGFF) [2, 5]. From a practical point of view, many novel phenomena have been discovered, such as the staircaselike current-voltage I(V) characteristic [6], Coulomb blockade oscillation [7], negative differential capacitance [8], and the Kondo effect in QDs [9].

Researchers have recently paid much attention to electron transport through several QDs since multiple QD provides more Feynman paths for the electron transmission [10]. Furthermore, due to the current fabrication processes, all these structures are created in a multi layer structure. Thus, the final structure intrinsically is a superlattice of insulator-semiconductor bilayers. In this configuration, transport occurs in series, from one layer to the next one [11]. In the case of QDs, this makes the serial transport between QDs the most relevant case of study.

In this chapter, we present the basis of the electron transport methodology that we are going to use and expand in the rest of this thesis in order to simulate systems based on QD arrays. Here, we are interested in the electrical response of the system under an external applied bias voltage. First of all, the description of the electrical transport focus our attention on the importance of the tunneling junctions. From the decomposition

of these junctions, the two equations that govern the system which are similar to the Kirchhoff's laws are found. Expression for the tunneling currents is also presented within the Transfer Hamiltonian approach and the non-equilibrium distribution functions for each QD are obtained. Concerning the potential in each QD, it is evaluated in the self-consistent field regime. The interactions among the QDs, and between the QDs and the electrodes are introduced by transition rates and capacitive couplings. Electron transport and charge densities inside the QDs depend on the tunnel transparency of the barriers limiting each dot.

Once the basis of the electron transport are presented, three main QDs configurations are studied in detail to elucidate the main parameters that govern the system response. Finally, a direct comparison with a pure quantum approach as the NEGFF is presented. This chapter gives analytical expressions to the current for several QDs arrangements, and it is used to elucidate the main features of the electrical transport in these systems. Once the basis are presented, in next chapters, some parameters will be described in detail.

2.1 System decomposition

The system under study is composed by several QDs embedded in a dielectric matrix placed between two leads (or electrodes). In the equilibrium state, all the system is described by a common energy Fermi level and the Fermi Dirac equilibrium distribution function. When an external voltage is applied, one lead acts as an electron reservoir and injects electrons to the QD array. The electrons cross through different pathways among the QDs (as we will see later) and arrive to the other lead creating a net current. When the steady state is reached, the occupations in the QDs are not well described by the equilibrium distribution functions and these new non-equilibrium QD distribution functions are, a priori, unknown. Therefore, the accumulated charge in each QD in this new steady state can differ from the accumulated charge in the equilibrium state.

We are going to study the electronic transport in such systems assuming ballistic regime, this means that we are not going to include scattering processes that involve energy loss of the carriers. Therefore, carriers start in one lead at a given energy, they cross through the QDs and the oxide matrix and arrive to the other lead with the same energy. Then, a basic question emerges: how does the electron cross the oxide?

In order to answer this question, in Fig. 2.1(a) we present a 1D energy band scheme of the system. Here, it is clearly visible the kind of structure that the electrons have to deal with: they have to cross the oxide matrix by tunneling processes from one QD to the other QDs. Since the tunneling processes are strongly dependent on the tunneling distance, we are going to neglect direct tunneling between the leads. Thus, an electron starts in one electrode and assisted by tunneling processes between the different QDs, it

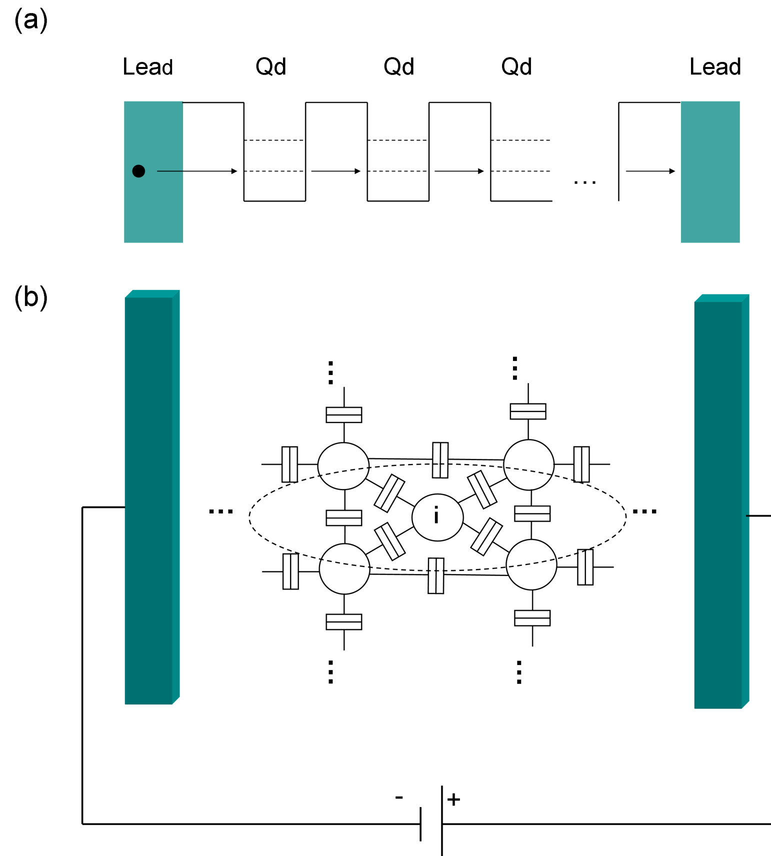

FIGURE 2.1: (a) 1D Energy band scheme of the structure of the system. The QDs are described as wells in the band structure of the oxide matrix. Since we are only considering ballistic transport, the electron crosses through the potential barriers by tunneling events. (b) Equivalent electrical scheme of a QD array embedded in an insulator matrix. The QDs (circles) are connected between them and the leads (color blocks) by tunneling junctions. The tunneling junctions can be described as a capacitor in parallel with a current path.

crosses to the other lead. We are going to assume that each tunneling process is independent from the other. From this basic assumption, the electrons do not have "memory" of the previous tunneling processes. Therefore, the tunneling events are independent and each electron can be treated independently neglecting the coherence between them. According to this, the electron transport occurs as following: (i) some external perturbation drives the leads out of the equilibrium state and one of them injects an electron; (ii) the electron tunnels from the lead to a QD; (iii) the electron in this QD crosses to other QD (or lead) according to some probability; (iv) the process is repeated until the electron arrives to the other lead; (v) the transport process is repeated again for other electrons. This transport scheme is known as sequential tunneling and it basically assumes that the electron is treated as a particle that resides in a particular QD instead of a coherent wave that is delocalized over different QDs [12].

The basic parameter that contains all the information necessary to describe the electrical

response of the system under external voltage polarization is the non-equilibrium distribution functions of each QD. These functions contain information about the occupancy of the QD energy levels. The net current that crosses the structure and the accumulated charge in the QD array can be inferred from them.

Following this strategy and taking into account that the electron transport is dominated by the tunneling processes among the different parts of the system, the first step is the description of the tunneling junctions in order to be able to write the dynamical equations that finally govern the system response. The tunneling junctions are usually modeled as a capacitance and a resistance placed in a parallel configuration. The resistance includes the electron tunneling probability through the potential barrier whereas the capacitance represents the electrostatic potential coupling between both elements of the junction. The equivalent electrical scheme of the system for a random QD arrangement is shown in Fig. 2.1(b), where we have included the tunneling junctions between the QDs.

From an electrical point of view, when an external bias voltage is applied to the electrodes a net current appears. The current crosses through the different pathways created by the QD arrangement being the total current decomposed in partial currents. We have to note that these partial currents (i.e current between two QDs or current among a QD and lead) will depend on the difference voltage of these two elements. These partial currents will also depend on the transmission coefficients of the potential barriers (reflected as the resistance of the tunneling junctions). Therefore, we can describe the electrical response as a function of the different partial currents among the different elements that form the system and their voltages.

In the steady state, the charge conservation for this system is analogous to the electronic Kirchhoff's current law (i.e. the total current that crosses the system is conserved). Thus, using the decomposition of the tunneling junctions in partial currents from the ith QD to the jth element (either QD or lead) we can write

$$0 = \sum_j I_{ij} \qquad i \in N, \tag{2.1}$$

where N is the number of QDs and the summation takes into account all the linked elements to this QD. On the other hand, it is necessary a second equation that describes the voltage in each QD, quite similar as the Kirchhoff's voltage law. These two coupling equations will govern the electrical response of the system.

Now, we are going to describe in deep the two basic equations that govern the electron transport in our approach. As we will see, both equations are linked by the non-equilibrium distribution function. First of all, we are going to present in detail the analytical expressions for the tunneling currents through a junction in order to solve Eq. 2.1 for each QD. Then, the non-equilibrium distribution functions can be obtained.

In a second part, the Poisson equation is used to obtain the QD voltage. Moreover, the influence of the QD accumulated charge in the final electrical response is also discussed.

2.1.1 Electron transport in the nanoscale: The Landauer-Büttiker approach

Sticking to the level of quantum mechanics, the electron transport is simply treated in absence of phase breaking scattering processes, being referred as quantum-ballistic transport or ballistic transport. The ballistic transport assumption strongly depends on the device dimensions that should not exceed the coherence length of the charge carriers or in other words, in the ballistic transport regime the device dimensions are much smaller than the carriers mean free path [13, 14, 15]. However, ignoring this prerequisite, the ballistic transport approach is still used to study the performance limit of an ideal device [14].

We will sketch briefly the Landauer-Büttiker approach [16, 17, 18] and explain the results for the current in a non-equilibrium situation assuming ballistic transport. Within this formalism, a two terminal device is decomposed in three main regions: two leads (or electrodes) and a central region. The current flowing through the device is related to the probability of a charge carrier injected from one lead to be transmitted through the central region to the other lead. The leads are treated as two electron reservoirs which are in thermal equilibrium. Thus, they can be described by Fermi functions f_L and f_R for left an right leads, respectively. We assume that the scattering matrix which contains information about the transmission and reflection properties of the central region is already known from previous quantum mechanical calculations. Applying the Landauer-Büttiker formalism, the average current can be written as

$$I = \frac{q}{\pi\hbar} \sum_n \int dE M(E) T_n(E) \left[f_L(E) - f_R(E) \right], \tag{2.2}$$

where the Fermi functions are described by the corresponding electrochemical potential μ_L and μ_R. $T_n(E)$ are the eigenvalues of the transmission matrix reflecting the transmission probability of eigenchannel n and $M(E)$ is the number of propagating modes in the channel. This result illustrates that there is only net current from lead to lead when the electrochemical potentials of the leads are different, $\mu_L \neq \mu_R$, therefore $f_L(E) \neq f_R(E)$. This difference is created by the external voltage, $\mu_L - \mu_R = qV$. For the system under study (depicted in Fig. 2.1(b)), the central region is all the insulator matrix in which the QDs are embedded. Thus, the transmission probabilities and the eigenchannels are the solutions of the whole QD matrix.

From a direct comparison between this methodology and the system decomposition that we have used, the main difference appears in the quantum calculation of the transmission probabilities. From pure quantum calculations, when the transmission through a system

like the one depicted in Fig. 2.1(a) is evaluated, the total transmission coefficient takes into account the transmission through each individual barriers but it also includes the reflections in the intermediate barriers. Since we have assumed that each tunneling event is independent from the previous ones, we loose these "intermediate" reflections. As we will show later, in a direct comparison between the here proposed transport model and a pure quantum transport calculations based on NEGFF, our model can not reproduce the coherent effects related to the calculation of the transmission coefficient of the whole system.

2.1.2 Expression for the electric current: the Transfer Hamiltonian approach

There are several ways to describe the tunnel effect in quantum mechanics. The first approach is the exact solution of the total Hamiltonian of the system obtaining the eigenstates and eigenfunctions and then, calculate the transmission coefficient via the probability current conservation. However, this approach is limited by a practical reason: only a few number of Hamiltonians can be solved exactly. Thus, several approximations are needed.

The Transfer Hamiltonian approach was introduced by Bardeen [19] based on the time dependent perturbation theory. Later, it was developed by Harrison [20] and formulated in a most familiar second quantization form by Cohen *et al.* [21]. This approach has been widely used in many tunneling transport studies [21, 22, 23, 24] through potential barriers since the perturbative treatment of the tunneling events simplifies the calculation of the transmission coefficient. Although there are many effects that can be included in the tunneling currents such as: the coupling with phonons [25], displacement and oscillations of the junction structure [26, 27], fluctuations of charges [28, 29] and temperature effects [30, 31]. Here, we are going to consider a pure tunneling process neglecting these extra sophistication and assuming only ballistic transport as said before.

Bardeen viewed the tunneling current as the net effect of many independent scattering events that transfer electrons across the tunneling barrier. Since the eigenvalues and eigenfunctions of a general Hamiltonian can not be usually obtained, the main idea is to decompose the total system (see Fig. 2.2(a)) as the sum of three subsystems. From a mathematical point of view, the total Hamiltonian H is written as: left H_L, right H_R and the tunneling H_T parts as follows

$$H = H_L + H_R + H_T. \tag{2.3}$$

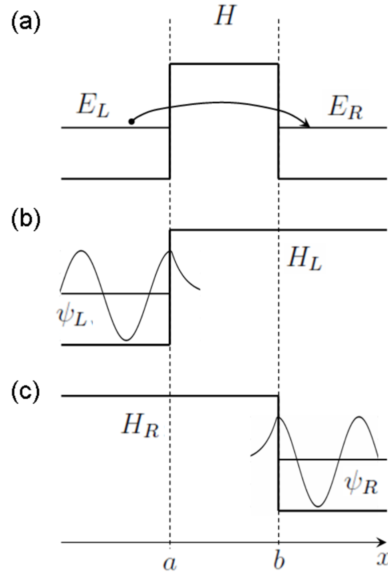

FIGURE 2.2: (a) Band energy scheme of the tunnel junction. The electron tunnels from an eigenstate E_L on the left side of the barrier to the eigenstate E_R on the right side. (b-c) The decomposition of the total Hamitonian H into two subsystems: H_L and H_R. The wave function ψ_L and ψ_R are also presented showing the exponential decay in the barrier region.

Following the decomposition proposed in Fig. 2.2(b-c), we can write

$$H_L \psi_L = E_L \psi_L$$
$$H_R \psi_R = E_R \psi_R,$$

where we have assumed that the eigenenergies ($E_{L/R}$) and the eigenfunctions ($\psi_{L/R}$) of these parts can be obtained exactly. Considering tunneling from a left eigenstate E_L into a right eigenstate E_R using the time-dependent perturbation theory, the Schrödinger equation $i\hbar\frac{\partial}{\partial t}|\psi\rangle = H|\psi\rangle$ has to be solved imposing that the particle is in a left eigenstate at $t = 0$. If the tunneling is weak, we can anticipate that $\psi(t)$ will be close to $\psi_L e^{-itE_L/\hbar}$, when t is small enough. So, we can write

$$\psi(t) = \underbrace{\psi_L e^{-itE_L/\hbar}}_{\substack{\text{at } t=0\text{, the electron} \\ \text{is in an eigenstate of } H_L}} + \underbrace{\sum_R a_R(t)\psi_R}_{\substack{\text{due to the tunneling effect,} \\ \text{there is some probability that} \\ \text{the electron will be in each } H_R \\ \text{eigenstates later } (t>0)}}, \quad (2.4)$$

where the sum is over all the right eigenstates. We use $a_R(0) = 0$ as initial condition and $|a_R(t)| << 1$ which implies a small tunneling probability. The projection of the

wave function into the right eigenstates can be written as

$$\langle\psi_R|\psi(t)\rangle = a_R(t) + \langle\psi_R|\psi_L\rangle e^{-itE_L/\hbar}. \tag{2.5}$$

Assuming that E_L and E_R eigenstates are nearly orthogonal $\langle\psi_R|\psi_L\rangle \approx 0$, the transmission coefficient is defined as $P_{L\to R} \equiv |\langle\psi_R|\psi(t)\rangle|^2 \approx |a_R(t)|^2$ where we have neglected the second term due to the nearly orthogonality of the eigenstates. The transmission coefficient reads as

$$|a_R(t)|^2 = \frac{2\pi}{\hbar} t |\langle\psi_L|H_T|\psi_R\rangle|^2 \delta(E_L - E_R). \tag{2.6}$$

We must note that this final expression looks like the Fermi's Golden rule for transitions between two eigenstates assisted by a perturbation described by H_T. The matrix element reads as

$$M = \langle\psi_L|H_T|\psi_R\rangle = \frac{\hbar^2}{2m} \int \left[\psi_L \vec{\nabla}\psi_R - \psi_R \vec{\nabla}\psi_L\right] d\vec{S}. \tag{2.7}$$

It can be demonstrated that the matrix element is symmetric, i. e. $P_{L\to R} = P_{R\to L}$. Doing the sum over all the initial and final states, the final expression for the tunneling probability assuming continuous states in both sides of the barrier is written as

$$P_{L\to R} = \frac{2\pi}{\hbar} t |M|^2 \delta(E_L - E_R) \rho_R(E_R) \rho_L(E_L) dE_L dE_R, \tag{2.8}$$

where $\rho_{L/R}$ are the density of states in the L/R sides, respectively.
Up to now, we have an expression for the tunneling probability. However, in order to obtain a tunnel current, we have to define the tunneling frequency rate which will give us the number of particles that tunnel in the t and $t + dt$ time step. We must include the occupancy of the initial and final states since we are treating with electrons. Thus, we can write the tunneling frequency as

$$\Gamma_{L\to R} = \int_{-\infty}^{+\infty} \int_{-\infty}^{+\infty} \frac{2\pi}{\hbar} |M|^2 \rho_L(E_L) \rho_R(E_R) \delta(E_R - E_L) \times f_L(E_L) \times [1 - f_R(E_R)]\, dE_L dE_R, \tag{2.9}$$

where $f_{L/R}$ are the distribution functions that describes the occupancy of the energy levels in each side of the barrier. The last factor $f_L(E_L) \times [1 - f_R(E_R)]$ takes into account that the initial state is fill and the final state is empty. Then, the net current that crosses a tunnel junction can be written as

$$I = q\left[\Gamma_{L\to R} - \Gamma_{R\to L}\right] = \frac{4\pi q}{\hbar} \int_{-\infty}^{+\infty} |M|^2 \rho_L(E) \rho_R(E) \left[f_L(E) - f_R(E)\right] dE, \tag{2.10}$$

where the symmetry in both directions of the element matrix $|M|^2$ has been considered [17]. Moreover, we have included a factor 2 to take into account the spin degeneracy. We have written explicitly the obtained expression for the tunnel current in order to compare it to the previously presented Landauer-Büttiker expression (Eq. 2.2). From a direct comparison with Eq. 2.2, the transmission matrix is $M(E)T_n(E) = 4\pi^2|M|^2\rho_L\rho_R$.

Hereafter, we are going to define the matrix element as the transmission coefficient $|M|^2 = T(E)$ of a single energy channel that includes the "opacity" of the barrier whereas the number of conductive modes are given by the multiplication of both density of states.

It is interesting to show how, a tunnel resistance can be inferred from Eq. 2.10. Assuming that $f_{L/R}$ are the Fermi functions, at low temperatures they restrict the energy integration to the energy range $E \in [\mu_L, \mu_R]$. If the matrix element and the density of states are constant in the energy range and taking into account that $\mu_L - \mu_R = qV$, we can write

$$I = \frac{V}{R_t} \text{ where } R_t = \frac{\hbar}{4\pi q^2 \rho_L \rho_R |M|^2}. \tag{2.11}$$

R_t is the tunnel resistance and it can be defined as a constant if the current voltage curve I(V) follows a linear trend. However, these approximations are too restrictive and the tunneling transmission coefficient is strongly dependent on the energy as we will show in next chapters.

2.1.3 The Non-equilibrium Distribution Functions

Since the tunneling current through a single tunneling junction is well described by Eq. 2.10, we go back to the system under study. We assume that the leads can be treated as perfect electron reservoirs and they are described by the equilibrium Fermi Dirac distribution function but taking into account the applied bias voltage that modifies the electrochemical potentials as $\mu_L - \mu_R = qV$. Where μ_L and μ_R are the electrochemical potentials of the leads and V is the applied bias voltage. Hereafter, we will use the subscripts L and R to refer to the left and right leads, respectively. The QD time charge evolution can be written as a rate equation as a function of the sum of the different partial currents. Using Eq. 2.10 to describe the tunnel currents, we can write

$$\begin{aligned} q\frac{dN_i}{dt} = \frac{4\pi q}{\hbar} \Bigg\{ \int T_{Li}\rho_L\rho_i(f_L - n_i)dE + \int T_{Ri}\rho_R\rho_i(f_R - n_i)dE \\ + \sum_{j \neq i}^{(N-1)} \int T_{ji}\rho_j\rho_i(n_j - n_i)dE \Bigg\} \quad \forall i = 1 \dots N. \end{aligned} \tag{2.12}$$

Where we have written explicitly all the current terms: the leads current contributions (first and second term) and the neighbor QDs contributions (the last term). ρ_i and $\rho_{L/R}$ are the density of states (DOS) of the ith QD and the leads, whereas T_{ij} is the transmission probability. N_i and n_i are the electron number and the non-equilibrium distribution function of the ith QD, respectively. Eq. (2.12) can be rewritten for the steady state and n_i can be obtained as a solution of this set of equations (one equation

per QD)

$$\begin{pmatrix} -T_{L1}\rho_L - T_{R1}\rho_R - \sum_{j\neq 1}^{(N-1)} T_{1j}\rho_j & \dots & T_{1N}\rho_N \\ \vdots & \ddots & \vdots \\ T_{1N}\rho_1 & \dots & -T_{LN}\rho_L - T_{RN}\rho_R - \sum_{j\neq N}^{(N-1)} T_{Nj}\rho_j \end{pmatrix} \begin{pmatrix} n_1 \\ \vdots \\ n_N \end{pmatrix} = \begin{pmatrix} -T_{L1}\rho_L f_L - T_{R1}\rho_R f_R \\ \vdots \\ -T_{LN}\rho_L f_L - T_{RN}\rho_R f_R \end{pmatrix} \quad (2.13)$$

From this system of non-coherent rate equations (NCRE), the function that describes the occupancy of the QD energy levels under external polarization can be inferred. The total number of electrons N_i inside the ith QD can be easily obtained as the sum of all the occupied energy levels

$$N_i = 2\int \rho_i(E) n_i(E) dE, \quad (2.14)$$

where we have included the spin degeneracy factor. From these equations, we can see that the occupancy of the energy levels of the QDs is strongly dependent on the transmission coefficients of the different conduction channels.

2.1.4 Charge effects

Physicists often focus their attention on the low-bias conductance regime (the "linear regime") in which the current can be written as [32]

$$I = \left[\frac{2q^2}{h}\int M(E)T(E)\left(-\frac{\partial f_0}{\partial E}dE\right)\right]V, \quad (2.15)$$

where we have used $f_L - f_R = \left(-\frac{\partial f_0}{\partial E}\right) qV$, being f_0 the equilibrium Fermi Dirac distribution and V the applied voltage. The response in this regime is determined solely by the properties of the energy levels around the equilibrium electrochemical potential μ. However, from the point of view of the design of new electrical devices, this regime is not enough and the full current-voltage characteristics are necessary. Then, one has to take into account the potential created in the device (not only the difference potential among the leads) as a response of the applied external voltage. We must note that this potential modifies the energy levels and therefore, it affects to the final response of the system. Basically, we can obtain a exact solution of this problem solving simultaneously the Schrödinger equation and the Poisson equation [33, 34, 35] since the the transmission function includes potential dependence. When the device is connected to the contacts, there is some charge transferred into or out of the device, which creates a potential U. The Schrödinger-Poisson solvers iterate the Poisson equation, which gives the potential U for a given electron density n relative to that required for local charge neutrality. However, the electron density is related to the wave functions and the Hamiltonian of

the system includes the potential U. It is interesting to note that this approach is quite similar to the Density Functional Theory (DFT). However, the last one includes extra terms in the potential in order to reflect the exchange-correlation effects [36].

Now, we are going to describe in detail the two main regimes observed in the nanoscale: the Coulomb blockade (CB) and the self-consistent field (SCF) regimes. In the CB regime, the electron-electron interaction is included explicitly and the charge is assumed as an integer. Whereas, in the SCF regime the potential is simple given by the Poisson equation (Hartree potential) and it neglects the exchange-correlation term using a mean-field treatment.

2.1.4.1 Single electron charging effect: the Coulomb blockade regime

The Coulomb blockade (CB) or single-electron charging effect, which allows for the precise control of small numbers of electrons, provides an alternative operating principle for nanometre-scale devices. Single electron devices differ from conventional devices in the sense that the electronic transport is governed by quantum mechanics. These devices consist of an "island", a region containing localized electrons, isolated by tunnel junctions with barriers that allow the electron tunneling.

The evolution of a consistent theory for single-electron tunneling goes back to the early 1950s. It was first suggested by Gorter as an explanation for the observation of anomalous increase of the resistance of thin granular metallic films with a reduction in temperature [37, 38]. More than 30 years later, Fulton and Dolan [39] observed CB effects in a microfabricated metallic sample and initiated a huge number of experimental and theoretical studies. Nowadays, there are many text books and reviews [40, 41, 42, 43] on single electron systems, both in metals and in semiconductor QDs, that explain the orthodox CB theory as a function of the capacitive coupling of the tunneling junctions and the accumulated charge in the QD. Besides, the theory has been extended to explain the conductance oscillations of the single electron transistor (SET) [12, 44].

An entirely classical model for electron-electron interaction is based on the electrostatic capacitive charging energy. The interaction arises from the fact that for every additional charge dq, which is transported to a conductor, extra work has to be done against the field generated by the already present charges residing on the conductor. Charging a QD with capacitance C with an electron of charge $-q$ requires and extra energy

$$E_c = \frac{q^2}{2C}. \tag{2.16}$$

This energy suppresses electron transfer unless extra energy is given to the electron by either thermal excitations $T = \frac{E_c}{k_B}$ or by an externally applied voltage $V_T = \frac{E_c}{q} = \frac{q}{2C}$. For this electron transport suppression, a new term was coined: CB tunneling. The temperature effects were firstly reported by Gorter. Independently from Gorter, this

effect was observed and explained by Neugebauer and Webb [45]. Yet another effect, Coulomb exclusion became known in the late 1960s through the work of Giaever and Zeller [46] and Lambe and Jaklevic [47]. If the applied voltage V is less than the threshold voltage V_T, the system is in the Coulomb blockade state and the current is blocked. When the voltage V exceeds V_T, an electron tunnels through the barrier into the QD. However, due to the Coulomb repulsion, it can not be followed by another electron unless the external applied voltage V is increased even further by $\triangle V = \frac{q}{2C}$. Thus, the charge in the QD as well as the current follow a staircase-like function with the applied voltage, commonly known as the Coulomb staircase.

The first quantitative theory for two barrier systems was given by Kulik and Shekhter in 1975 [48] using a master equation to calculate the system states probabilities and their time evolution. An state is defined as a function of the number of accumulated electrons inside each QD. This approach conforms the basis of the so called orthodox theory of single-electron tunneling. This theory was generalized in the pioneering papers of Meir *et al.* [2], Averin *et al.* [44] and Beenakker [12] with the inclusion of effects of both charge and energy conservation in semiconductor structures

The formulation of the classical or the orthodox CB theory assumes:

- Electron is localized in the QDs. In a classical picture this assumption is clear, an electron is either on a QD or not. The electron localization is implicitly assumed in a classical treatment. However, a more precise quantum mechanical analysis describes the number of electrons N localized in a QD in terms of an average value, $\langle N \rangle$ which is not necessarily an integer. The condition that the charge has to be an integer value can be summarized as $|N - \langle N \rangle|^2 << 1$. Clearly, if the tunnel barriers are not present or are insufficiently opaque, one can not speak of charging or localizing electrons on a QD, because nothing will constrain an electron to be confined within a certain volume.

- The orthodox theory focuses on the charging of metallic QDs assuming a continuous density of states. However, the theory was extended to include semiconductor QDs by Van der Wiel *et al.* [49].

- A qualitative argument is to consider the Heisenberg energy uncertainty of an electron $\triangle E \triangle t > \frac{h}{4\pi}$. The charging energy associated with a single electron is E_c and the characteristic time for charge fluctuations is related to the time constant for charging a capacitance C through a tunnel resistor R_T, $\triangle t \approx R_T C$. Therefore, we obtain a condition for the tunnel resistance $R_T > \frac{h}{2\pi e^2} = 25813\,\Omega$. This condition implies that the tunnel transmission has to be lesser than one.

- The thermal kinetic energy of the electron must be less than the Coulomb repulsion energy $E_c > k_B T$. Doing some numbers, an estimation of the capacitive value can be obtained. At room temperature $k_B T \approx 0.025$ eV, the capacity is in the order

of $C \approx \frac{e^2}{2k_BT} << 1aF$ where 1 aF=10^{-18} F. Assuming spherical QD, the capacity is $C = 4\pi\varepsilon_r\varepsilon_0 R$ and the QD size is estimated as $R \approx 5$ nm for $\varepsilon_r = 10$.

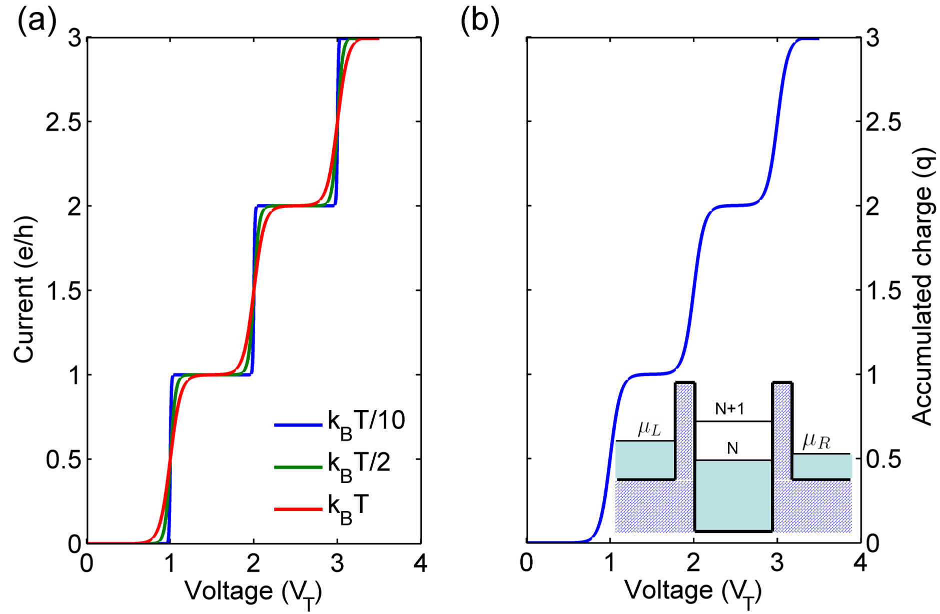

FIGURE 2.3: (a) I(V) curves of a single metallic QD in the Coulomb blockade regime for different temperature ranges. The current step-like behavior is recovered when the external bias voltage increases in multiples values of V_T. (b) Electron number in the QD as a function of the applied bias voltage. The accumulated charge also increases in discrete steps. In the inset, the energy band scheme, the Fermi levels of the leads (μ_L and μ_R) as well as the QD states with N and $N+1$ electrons are shown. The energy separation among the $N+1$ and N states is E_c.

The main transport features as a function of external polarization V for a single QD in the Coulomb blockade regime can be explained as:

- $V < V_T$ The electron does not have enough energy to overcome the repulsion effect inside the QD. Therefore, it is blocked in the lead being zero the total current that crosses the system. Besides, the value of V_T can be tuned as a function of the QD radius.

- $V_T < |V| < 2V_T$ One electron crosses from the left lead to the QD increasing the energy of the QD and avoiding the possibility of a second one coming from the left electrode. Then, the electron crosses to the right lead emptying the QD and the process is repeated for another electron. Thus, this single electron transport creates a net current. Furthermore, no more electrons can crosses simultaneously through the structure until the energy of the incoming electrons are grater than $2V_T$ being constant the current in this voltage range.

- $2V_T < |V| < 3V_T$ Two electrons have enough energy to cross simultaneously the system. Therefore, the current value is the double as in the previous case. This

description is repeated for larger voltages, allowing the simultaneous tunneling of three, four,... and so on electrons.

The current and the accumulated charge in a metallic QD are shown in Fig. 2.3(a-b), respectively. The current and charge increase by steps instead of a continuous form. In the inset of Fig. 2.3(b) we show the energy band scheme of the system, the Fermi levels of the leads (μ_L and μ_R) and the position of the last filled energy level of the QD as a function of its occupancy. The energy separation between the state with N and $N+1$ electrons is E_c and it is reflected in the current and the accumulated charge curves.

Up to now, we have focused on the CB in metallic QDs, however, it has also been observed in semiconductor QDs. From a theoretical point of view, the explanation is analogous to metallic ones, but due to the strong confinement regime, the internal electronic structure of the QD is discrete, i.e. the energy levels in the QD form a discrete spectra. Therefore, when the charge increases in discrete form the separation between the energy states with N and $N+1$ electron is $Ec+\triangle E$, where E_c is the energy repulsion as in the metallic QD and $\triangle E$ takes into account the energy separation between two consecutive discrete energy levels of the QD. Thus, the step-like behavior in the current and the accumulated charge is not periodic with V_T as in the previous case.

2.1.4.2 Self-consistent field regime

In the self-consistent field regime (SCF), the electron-electron problem is approximated directly by the solution of the Poisson equation. The Poisson equation reads as follows

$$\vec{\nabla}\cdot(\varepsilon_r\vec{\nabla}V) = -\frac{q\triangle N}{\varepsilon_0\Omega}, \tag{2.17}$$

where ε_r is the relative permitivity, Ω is the QD volume and $\triangle N$ is the increment of the electrons in the QD respect to the original number. If we treat each QD as a single point, ignoring any spatial variation of the potential inside it, the potential solution can be expressed in terms of the different capacitive couplings of the tunneling junctions [50, 51] and the boundary conditions described by the external voltage applied in the leads. The general solution for the local potential energy $U_i = -qV_i$ in the ith QD is

$$U_i = \sum_{j\neq i}\frac{C_{ij}}{C_{tot,i}}(-qV_j) + \frac{q^2}{C_{tot,i}}\triangle N_i, \tag{2.18}$$

where the subscript j runs over all elements of the system, C_{ij} is the capacitive coupling between the different components and $C_{tot,i} = \sum_{j,j\neq i} C_{ij}$ is the total capacitive coupling of the i^{th}QD. The first term is usually called the Laplace solution and reflects the potential created by the different elements (V_j) surrounding the QD. Therefore, in this term, the influence of the voltage applied to the leads is included. When a voltage

difference is applied between the two leads, the common electrochemical potential is splitted and the potential in the intermediate QDs will lie within the applied potential on the leads.

The second term reflects the possibility that the QD increases its charge. The charge energy constant $U_{0i} = q^2/C_{tot,i}$ is the potential increase as a consequence of the injection of one electron into the QD and $\triangle N_i$ is the change in the number of electrons, calculated respect to the number of electrons N_0 initially in the i^{th}QD. We have to note that U_{0i} plays the same role as the charging energy in the CB regime.

The effects of the local potential on each QD U_i, which will modify the QD charge and the currents, should be taken into account in the QD DOS $\rho_i(E) \rightarrow \rho_i(E - U_i)$, that is the local potential in each QD shifts the energy levels. Thus, the external applied voltage affects to the QDs energy levels shifting their positions. Therefore, the electron transport will take place through different conductive channels modifying the QD distribution function. Thus, the local potential depends on the increasing charge density but at the same time the charge depends on the DOS that it is modified by the local potential. These considerations impose a self-consistent solution of Eq. (2.14) and Eq. (2.18). Within this form, the effect of the charge and the external applied voltage are included in the transport approach.

2.1.4.3 Comparison between the Coulomb blockade and the self-consistent field regimes

We have explained two different ways to introduce the charge effects in the calculation of the local potential of the QD. As it is expected, in nanoscale systems the effects of the charge interaction plays an important role in the final response of the device. Here, we are going to compare the two previous explained regimes. The range of validity of each regime can be summarized as:

- Self-consistent field regime: if k_BT and/or $T_{ij}\rho_i\rho_j/\hbar$ is comparable to U_0.
- Coulomb blockade regime: if U_0 is well in excess of both k_BT and $T_{ij}\rho_i\rho_j/\hbar$. The orthodox theory based on the multi-electron master equation has to be used.

Thus, for strong localized electrons in the QD (low transmission coefficients) and low temperatures, the pure quantum nature of the system is recovered reflecting that the charge increases by integer values and the electron-electron repulsion effect dominates the response of the system. However, for larger temperature values or greater transmission coefficients, the effect of the electron-electron interaction decreases and the SCF approximation can be used. Moreover, we have to take into account that the charging energy (E_c or U_0) decreases when the QD radius increases.

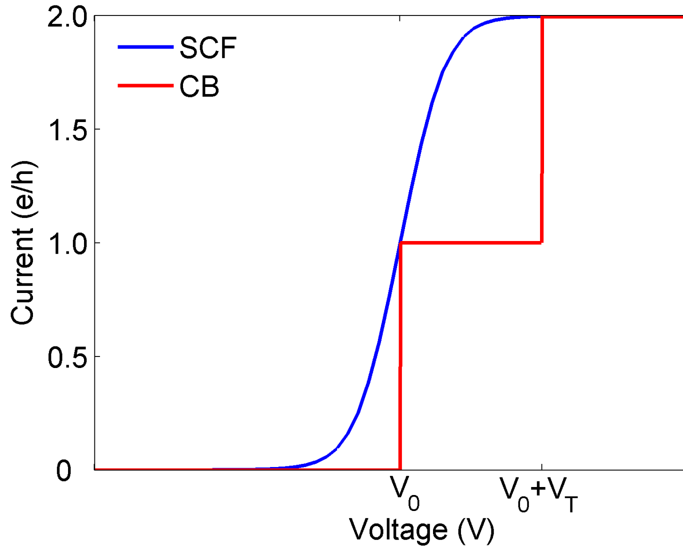

FIGURE 2.4: Obtained I(V) curves for single semiconductor QD with a spin degenerated energy level for the two studied regimes: the self-consistent field (SCF) and the Coulomb blockade (CB).

Fig. 2.4 shows the obtained I(V) curve for a single semiconductor QD with one energy level (spin degenerated) in the two studied regimes: the CB and the SCF. For the CB, two current steps are obtained whereas for the SCF only one step is recovered. We focus on the V_0 voltage point, the energy level enters in the conduction window and the current increases. For the CB case, the current is blocked as we have explained previously until the voltage reach the point $V_0 + V_T$ then, the current increases again. However, for the SCF case, the current increases monotonically from V_0 to V_0+V_T. We have to note that the total current at the $V_0 + V_T$ voltage point are common in both regimes reflecting that the final energy level position is the same in both cases. Thus, what's it wrong? The differences can be explained by:

- The charge is not quantified in the SCF regime.
- In the SCF regime, two energy levels with the same energy (degenerate) are always degenerate as long as they feel the same potential.

The second difference can be rewritten as the electron does not feel any potential due to itself. Suppose that the up-spin level gets filled first, causing the down-spin level to float up by E_c. But the up-spin level does not float up because it does not feel any self-interaction, recovering the two steps in the I(V) curve (CB regime). Whereas in the SCF, we are using a mean field treatment and both energy levels (spin up and down) are shifted by the same potential neglecting the splitting of the two energy levels.

From the point of view of the mathematical treatment, the CB is described using the master equation approach presented in detail in Ref. [52]. Different states are defined as

a function of the number of electrons accumulated in each QD and a set of rate equations is written for the state dynamics. When the number of QDs increases, the number of different states increases dramatically being impossible to use this approach for large systems. However, the SCF methodology can be easily implemented via rate equations in order to obtain the non-equilibrium distribution function of each QD using Eq. 2.13 and Eq. 2.18 as we have presented before.

2.2 Examples with simple cases

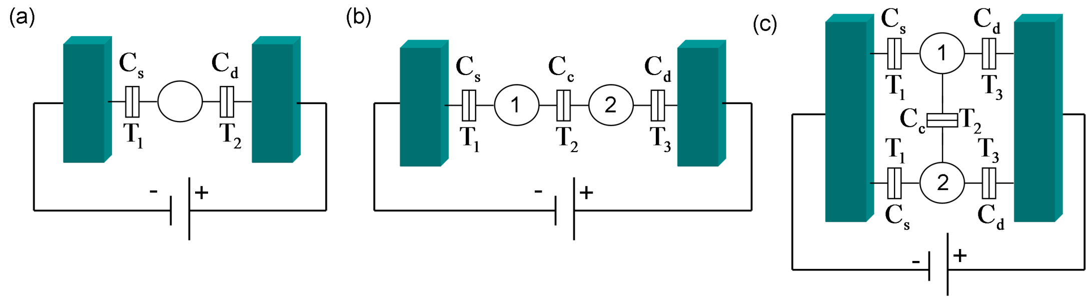

FIGURE 2.5: Equivalent electrical scheme of the three basic systems under study: (a) single QD, (b) two QDs in serial configuration and (c) two QDs in a parallel arrangement. We also show the notation used to describe the tunneling junctions, the capacities and the transmission probabilities.

Now, we are going to show in detail the applicability of the previous explained methodology: the rate equations in the SCF regime. In order to expose clearly all the physics behind the electron transport process and the main parameters that govern the final response of the system, we will focus on the simplest cases: one and two QDs described by a single energy level. The systems formed by two QDs include extra "sophistication" since we have to write two rate equations (one per QD) and they also include the current among both QDs. From the solution of the Poission equation, the Laplace term will also include the capacitive coupling between the QDs. Therefore, each QD will influence its neighbor. Two possible arrangements appear for a system composed by two QDs: a serial or parallel configurations. From hereon, we are going to define the serial case as the case in which each QD is only connected to one lead and its neighbor QD. The parallel configuration will be the case in which each QD is connected to both leads and also connected to the other QD.
The electrical scheme of the three systems under study are shown in Fig. 2.5(a) for the single, two QDs in (b) serial and (c) parallel configurations, respectively. We are going to assume constant transmission coefficients and the QDs are described by a single energy level (ϵ_0) placed above the equilibrium Fermi level. The value of the charging energy is $U_0 = 0.25eV$ to show clearly the effect of the accumulated charge in the electrical response and we assume $\mu_L = qV$ and $\mu_R = 0$ for the left and right leads, respectively.

2.2.1 Single QD: energy level position and transmission coefficients

The study of the electron transport through a single QD conforms the basis of the here presented model and it will give us the main features and the most important parameters that govern the final response. Thus, prior to study more complex systems, we are going to present in detail this system (see Fig. 2.5(a)). The rate equation that describes the non-equilibrium distribution function for the single QD reads as

$$q\frac{dn}{dt} = \frac{2\pi q}{\hbar}(T_1\rho_L f_L + T_2\rho_R f_R - n(T_1\rho_L + T_2\rho_R)), \tag{2.19}$$

being in the steady state

$$n = \frac{T_1\rho_L f_L + T_2\rho_R f_R}{T_1\rho_L + T_2\rho_R}. \tag{2.20}$$

The electron number stored in the QD can be easily obtained as $N = 2\int \rho\ n\ dE$ where ρ is the QD DOS. However, due to the discrete nature of the QD energy levels, the integration in the energy range is restricted to the value of the single QD energy level ϵ.

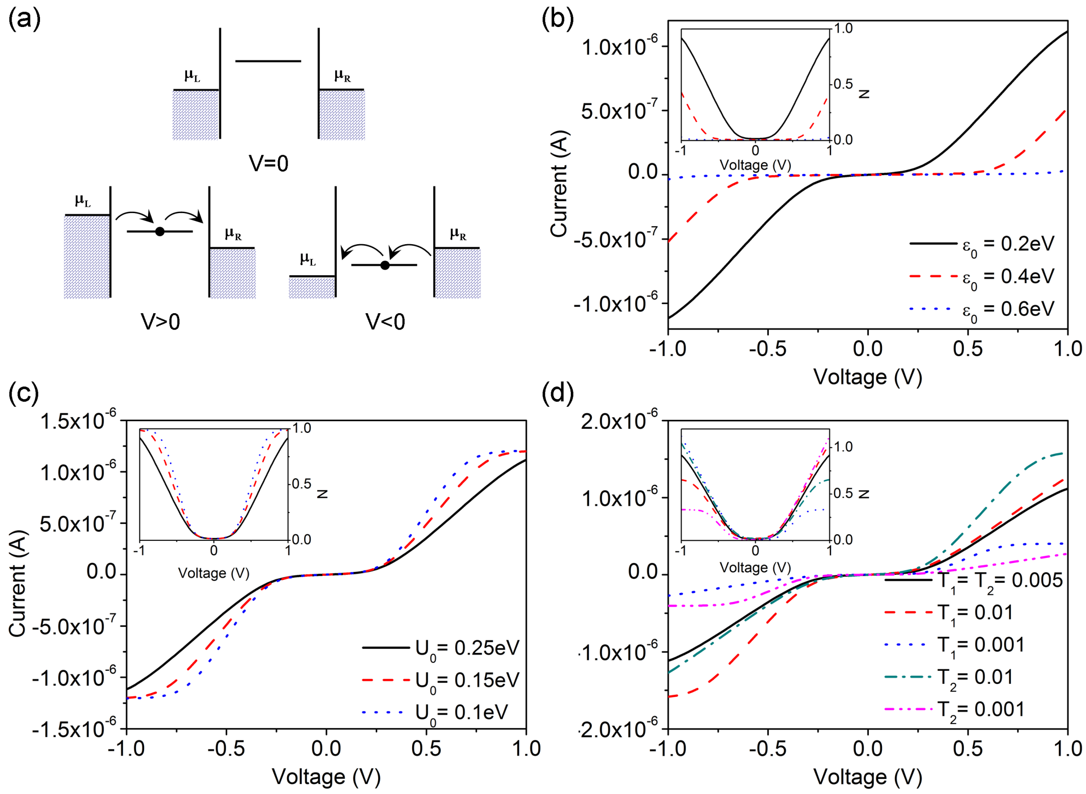

FIGURE 2.6: (a) Band scheme for the cases: $V = 0$ upper, $V > 0$ left and $V < 0$ right figures, respectively. (b) I(V) curves as a function of the QD energy level. (c) I(V) curves as a function of the charging energy and (d) varying the transmission coefficients of the leads. In the insets, the accumulated electrons in the QD (N) for each case is also shown. The used parameters were: $k_BT = 0.025eV$, $T_1 = T_2 = 0.005$, $U_0 = 0.25eV$, $C_d = C_s$, $\varepsilon_r\varepsilon_0 = 1$ and $\epsilon_0 = 0.2eV$. The varied parameters are shown in the legend of their respective figures.

Since the QD non-equilibrium distribution function is obtained, the current that crosses the system can also be evaluated. If we focus on the left contact, we can write

$$I = \frac{4\pi q}{\hbar}\int T_1\rho_L\rho(f_L - n)dE = \frac{4\pi q}{\hbar}\int \frac{T_1T_2\rho_L\rho\rho_R}{T_1\rho_L + T_2\rho_R}(f_L - f_R)dE, \tag{2.21}$$

where we have substituted the value of n for the expression presented in Eq. 2.20. We obtain the same expression for the current if we focus on the right contact. As in the evaluation of the charge, we can consider that the integration is restricted to the QD energy level. Thus, in order to obtain a net current the following condition has to be fulfilled: $f_L(\epsilon) \neq f_R(\epsilon)$. We have to recall that the Fermi functions depend on the electrochemical potentials of the leads, therefore, the transport conditions can be rewritten as

$$\begin{aligned} \mu_L \geq \epsilon \geq \mu_R \text{ for } I > 0 \\ \mu_L \leq \epsilon \leq \mu_R \text{ for } I < 0. \end{aligned} \tag{2.22}$$

Where, basically, the transport condition imposes that the energy level of the QD has to lie between the electrochemical potentials of the leads (see Fig. 2.6(a)). The sign of the current is related to the current convention that we have used assuming positive currents when the current enters the QD and negative when the current goes out from the QD.

On the other hand, we can see (Eq. 2.20) that the accumulated charge in the QD increases when the transport process occurs. Assuming the same transmission coefficient, the non-equilibrium distribution function will be $n \approx 1/2$. However, this value can be tuned changing the transmission coefficient respect to the leads.

In Fig. 2.6(b-c-d) several I(V) curves are shown as a function of the main parameters that govern the system. The transport conditions are summarized in Fig. 2.6(a) for both voltage polarizations. From Fig. 2.6(b), the current and the accumulated charge (see the inset) are presented for different QD energy levels. In order to explain this figure, we are going to write the voltage evolution of the energy level. Using the solution of the Poisson equation we can write

$$\epsilon(V) = \epsilon_0 + \frac{C_s}{C_s + C_d}qV + U_0\triangle N, \tag{2.23}$$

where V is the external applied bias voltage. C_s is the capacity coupling between the QD and the left lead while C_d is the coupling with the right lead. As we can see, if we assume $\mu_L = qV$ and $\mu_R = 0$ and taking into account the transport condition obtained previously, for positive voltages the electron transport will occur when $\mu_L \geq \epsilon \geq 0$. The minimum bias voltage or the threshold voltage that fulfills this condition is

$$V \geq \frac{1}{q}\frac{\epsilon_0 + U_0\triangle N}{1 - \frac{C_s}{C_s+C_d}}. \tag{2.24}$$

For the cases under study ($C_s = C_d$), it can be approximated as $V \approx (2\epsilon_0 + 2U_0 \triangle N)/q$. Therefore, as we can see, the position of the QD energy level respect to the equilibrium Fermi level is a crucial point that controls when the conduction channel is open. This behavior is clearly shown in Fig. 2.6(b) when the energy level increases. For the same reason, the QD starts to accumulate charge at higher applied voltages as we present in the inset.

In Fig. 2.6(c), the I(V) curves as a function of the value of the charging energy U_0 are presented. Here, we use a constant value for ϵ_0. However, as we have explained before, the threshold voltage depends on the value of U_0 (see Eq. 2.24). Then, for the smallest U_0, the transport condition is fulfilled for lowest external voltages. We can see how the current tends to saturate since the QD has only one conductive channel.

Finally, in Fig. 2.6(d), the current and the accumulated charge dependence with the transmission coefficients are also presented. The main results can be summarized as: the current increases when the transmission coefficients increases and the symmetry of the I(V) curve is broken when the QD is asymmetrically coupled to the leads. This result reflects the balance between the incoming charge from the lead and the facility that the QD can evacuate it to the other lead. Therefore, the QD occupation is governed by the strong lead coupling and the lead distribution function.

2.2.2 Two QDs in serial configuration: the role of the capacitive couplings

Now, we are going to study the serial case (the scheme of the system is shown in Fig. 2.5(b)). The rate equation for each QD can be written as

$$q\frac{dn_1}{dt} = \frac{2\pi q}{\hbar}(T_1\rho_L f_L + T_2\rho_2 n_2 - n_1(T_1\rho_L + T_2\rho_2)) \tag{2.25}$$

$$q\frac{dn_2}{dt} = \frac{2\pi q}{\hbar}(T_3\rho_R f_R + T_2\rho_1 n_1 - n_2(T_2\rho_1 + T_3\rho_R)). \tag{2.26}$$

Finally, the expression for the current is

$$I = \frac{4\pi q}{\hbar}\int \frac{T_1T_2T_3\rho_L\rho_1\rho_2\rho_R}{T_1T_2\rho_L\rho_1 + T_1T_3\rho_R\rho_L + T_2T_3\rho_2\rho_R}(f_L - f_R)dE. \tag{2.27}$$

As in the previous case, there is only a net current if the condition $f_L \neq f_R$ is fulfilled (i. e. $\mu_L \neq \mu_R$). The energy level of each QD must lie between the electrochemical potentials of the leads as we can see from Eq. 2.27. The current is governed by the term $\rho_L\rho_1\rho_2\rho_R$, this means that the electrons need available states in each part of the system in order to transport from left lead to the right lead trough the two QDs. Thus, a new transport condition is imposed: the electron transport only takes place when the position of the energy levels of the QDs are the same, i.e. energy level alignment. We can summarize the two transport conditions for a system of N QDs in a serial configuration

as

$$\mu_L > \epsilon_1 = \cdots = \epsilon_i = \cdots = \epsilon_N > \mu_R, \tag{2.28}$$

where ϵ_i is the energy of the ith QD. We must note that this condition is a direct consequence of the ballistic treatment of the electron transport. Besides, from the electrical point of view, the expression for the current can be interpreted as follows: the three barriers in the QD stack act as a series connection of resistors $R_{total} = \sum_i^N R_i$. Where R_i has been defined previously as the tunnel resistance of a junction.

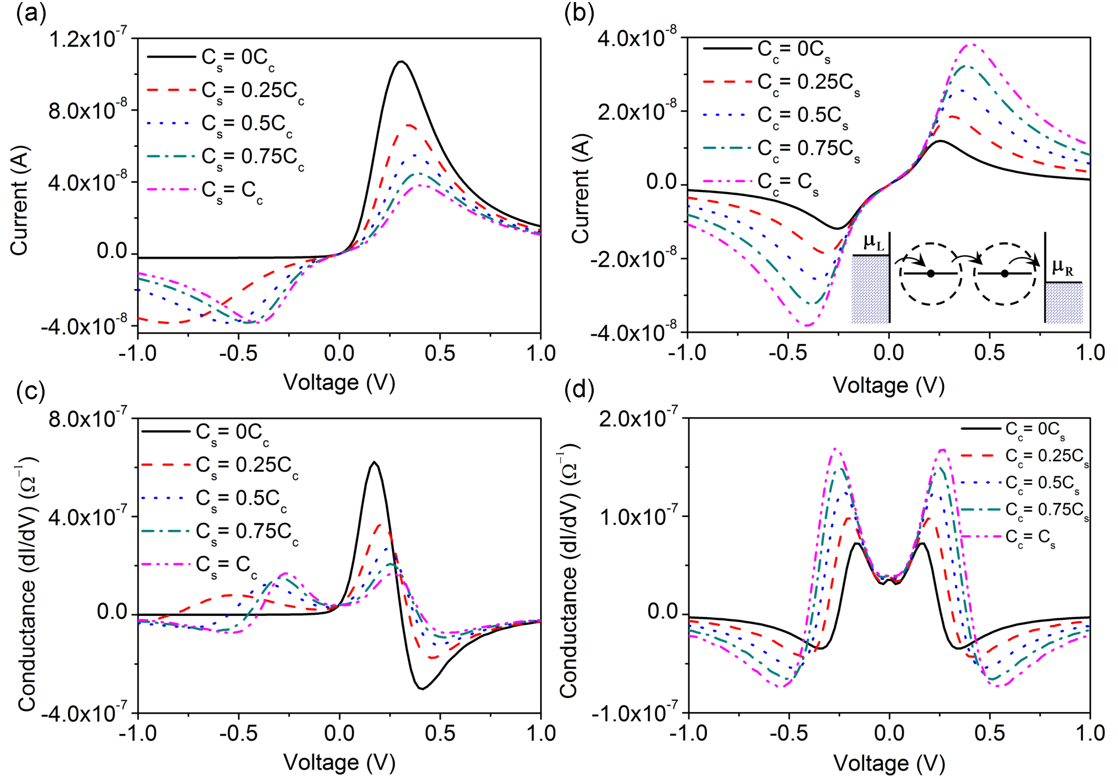

FIGURE 2.7: (a-b) I(V) curves and (c-d) conductance characteristics obtained for the serial arrangement depicted on Fig. 2.5(b) for different capacitive coupling. (a-c) As a function of the left lead QD capacity C_s, showing a rectifying effect when the system is weakly coupled with the left lead. (b-d) As a function of the inter-dot capacity C_c. In both cases, NDR is obtained since when the voltage increases the overlapping between the energy levels decreases and the current also decreases. The simulation parameters were: $\mu_L = qV$, $\mu_R = 0$, $T_1 = T_2 = T_3 = 0.005$, $k_\beta T = 0.025eV$, $U_0 = 0.25eV$, $\epsilon = 0.2eV$ and $\varepsilon_r\varepsilon_0 = 1$. C_d is fixed at the initial C_s value.

For simplicity, we have considered the same transmission probability in all the tunneling junctions $T_1 = T_2 = T_3$. In addition to this, we assume that the boths QDs are identical. Therefore, the energy level is the same in each QD with a value ϵ. As we have shown in the electrical scheme (Fig. 2.5(b)), we do not consider direct transmission between the leads. Using the general solution of the Poisson equation, the local potential in each QD

is written as

$$U_1 = \frac{C_s}{C_{tot,1}}(qV) + \frac{C_c}{C_{tot,1}}U_2 + U_0\triangle N_1 \tag{2.29}$$

$$U_2 = \frac{C_c}{C_{tot,2}}U_1 + U_0\triangle N_2 \tag{2.30}$$

where V is the applied bias voltage to left lead, whilst the right lead remains at zero (i.e. $\mu_L = qV$ and $\mu_R = 0$). C_s is the capacity coupling between the first QD with the left lead while C_d is the coupling between the second QD with the right lead. C_c is the capacity between QDs. So, we define the total capacitive coupling of each QD as $C_{tot,1} = C_s + C_c$ and $C_{tot,2} = C_d + C_c$ for the first and the second QD, respectively. Figs. 2.7(a-b) show the obtained I(V) curves varying the QD-lead and the QD-QD capacitive couplings with different C_s/C_c ratios, ranging from zero to one. Besides, the corresponding conductance defined as dV/dI is also depicted in Figs. 2.7(c-d) for the same cases as before. From the conductance plots, we can see clearly when the transport channels are opened or closed.

The I(V) curves are strongly dependent on C_s and C_c trough the Laplace solution of the system. The value of the capacity indicates how the system is coupled. When C_s tends to zero, the two QDs are electrically decoupled with the leads; this case implies a weakly coupled system. The other limit case is when the value of the capacity between QD (C_c) goes to zero which means that there is no electrical influence between QDs. The Poisson term follows the charge qN_i in each QD, therefore, it is always positive inducing a shift on the potential. In order to explain the I(V) curves, we can write the evolution of the energy level of each QD as a function of the applied bias voltage. Taking into account only the Laplace terms, they read as

$$\epsilon_1(V) = \epsilon + \frac{C_s}{C_{tot,1}}(qV) + \frac{C_c}{C_{tot,1}}U_2 \tag{2.31}$$

$$\epsilon_2(V) = \epsilon + \frac{C_c}{C_{tot,2}}U_1, \tag{2.32}$$

for the first an the second QD, respectively. U_1 and U_2 are the Laplace solutions of the potential in its respective QD. In order to analyze this set of recursive equations, we have used the relation $a + ar + ar^2 \ldots = a/(1-r)$ for a geometric series to write them as a function of the applied bias voltage. Finally, the energy level evolution can be written as

$$\epsilon_1 = \epsilon + \frac{C_s}{C_{tot,2} - C_c^2/C_{tot,1}}(qV) \tag{2.33}$$

$$\epsilon_2 = \epsilon + \frac{C_c C_s}{C_{tot,1}C_{tot,2} - C_c^2}(qV). \tag{2.34}$$

As we can see from the previous expressions, ϵ_1 increases faster than ϵ_2 when the voltage increases. Thus, the transport condition $\epsilon_1 = \epsilon_2$ can not be fulfilled in all the voltage region. Introducing a energy broadening in the QD energy level (we will explain in detail

this energy broadening in the next chapter) relaxes this restrictive condition and electron transport takes place as a result of the energy channel overlapping. When the voltage increases, the separation between ϵ_1 and ϵ_2 increases. Therefore, the energy overlapping decreases and the current trough the system also decreases. As a consequence, a negative differential resistance (NDR) appears due to the different QD electrostatic coupling [53]. NDR was previously observed in several experimental current measurements for QD stacks as it was reported in [54, 55, 56, 57]. Concerning the current peak, it is related to the maximum overlapping between the QD energy levels and its width is directly related to the energy broadening.

On the other hand, if the system is decoupled from the left lead ($C_s = 0$), the position of the energy levels become independent on the applied bias voltage. Therefore, electron transport only occurs in one polarization direction obtaining a rectifying effect in the current. The current would be constant once the energy levels lie in the conductive energy window. Nevertheless, in Fig. 2.7(a), we do not observe this behavior because the first QD increases its charge. Therefore, the charge term dominates the Poisson solution while the charge in the second QD is not the same as in the first QD creating different potentials in each QD, changing the energy level position. This case is a particular situation that Eq. 2.33 and Eq. 2.34 do not consider because they are first approximations. Furthermore, we must note that in this configuration we obtain the maximum current since the position of the two energy levels are practically identical until the charge modifies the local potential and the overlapping decreases.

2.2.3 Two QDs in parallel configuration: double current paths

Since the single and the serial cases have been studied, now we are going to focus on the third arrangement: the parallel configuration (see Fig. 2.5(c)). The rate equation can be written as

$$q\frac{dn_1}{dt} = \frac{2\pi q}{\hbar}(T_1\rho_L f_L + T_3\rho_R f_R + T_2\rho_2 n_2 - n_1(T_1\rho_L + T_3\rho_R + T_2\rho_2)) \tag{2.35}$$

$$q\frac{dn_2}{dt} = \frac{2\pi q}{\hbar}(T_1\rho_L f_L + T_3\rho_R f_R + T_2\rho_1 n_1 - n_2(T_1\rho_L + T_3\rho_R + T_2\rho_1)) \tag{2.36}$$

for each QD, respectively. Since both QDs are connected to the leads, the current expression has two terms (one per QD) and it reads as

$$I_i = \frac{4\pi q}{\hbar}\int \frac{T_1T_3(T_1\rho_L + T_3\rho_R + T_2(\rho_1+\rho_2))\rho_L\rho_R\rho_i}{(T_1\rho_L + T_3\rho_R)^2 + T_3T_2\rho_R(\rho_1+\rho_2) + T_1T_2\rho_L(\rho_1+\rho_2)}(f_L - f_R)dE, \tag{2.37}$$

where the subscript i runs for all the QDs being the total current $I_{tot} = \sum_i^N I_i$. Moreover, we can see from this equation that if the QDs are decoupled ($T_2 = 0$), we will recover the expression for the current as in the single QD arrangement (Eq. 2.21). Using the

general solution of the Poisson equation, the local potential in each QD is written as

$$U_1 = \frac{C_s}{C_{tot}}(qV) + \frac{C_c}{C_{tot}}U_2 + U_0\triangle N_1 \tag{2.38}$$

$$U_2 = \frac{C_s}{C_{tot}}(qV) + \frac{C_c}{C_{tot}}U_1 + U_0\triangle N_2. \tag{2.39}$$

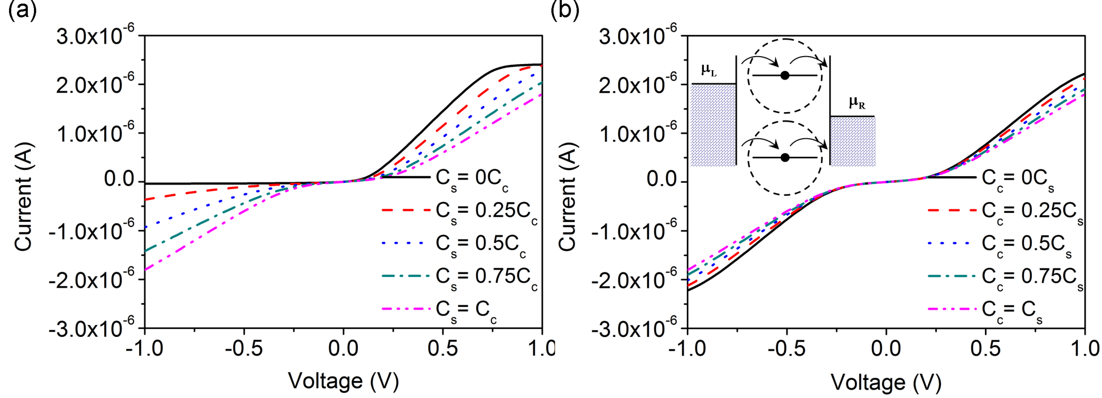

FIGURE 2.8: I(V) curves for two QDs in the parallel arrangement for different capacitive couplings: (a) as a function of the left lead QD capacity C_s and (b), as a function of the inter-dot capacity C_c. In the inset the band scheme of the two QDs are also shown. The simulation parameters were: $\mu_L = qV$, $\mu_R = 0$, $T_1 = T_2 = T_3 = 0.005$, $k_\beta T = 0.025eV$, $U_0 = 0.25eV$, $\epsilon = 0.2eV$ and $\varepsilon_r\varepsilon_0 = 1$. C_d is fixed at the initial C_s value.

As in the previous cases, the I(V) curves can be obtained as a function of the different capacitive couplings. We present the simulated I(V) curves as a function of the coupling to the left lead C_s in Fig. 2.8(a) and the coupling among the QDs C_c in Fig. 2.8(b), respectively. We have used the same parameters for all the capacitive couplings and transmission coefficients as in the previous cases. The two QDs are described by a single and identical energy level. As we have demonstrated previously, the I(V) curves are dominated by the evolution of the energy level of each QD as a function of the applied bias voltage. Thus, taking into account only the Laplace solution for each QD, we can write the energy level evolution as

$$\epsilon_1 = \epsilon + \frac{C_s}{C_s + C_d}(qV) \tag{2.40}$$

$$\epsilon_2 = \epsilon + \frac{C_s}{C_s + C_d}(qV), \tag{2.41}$$

where we have assumed that both QDs are symmetrically coupled to the leads ($C_s = C_d$). The summation of the geometric series $a + ar + ar^2 \ldots = a/(1-r)$ has also been used. An unexpected result is obtained from Eqs. 2.40 - 2.41, the voltage evolution of the energy level is independent from the capacitive coupling among the QDs.

In Fig. 2.8(a), a rectifying effect is obtained when the QDs are capacitive decoupled from the left lead $C_s = 0$. Using Eq. 2.40 and Eq. 2.41 and the transport condition $\mu_L > \epsilon_i >$

μ_R, we can see that this condition is only fulfilled for positive voltage polarization since $\mu_L = qV$, $\mu_R = 0$ and $\epsilon > 0$. Thus, the energy level only lies in the conductive window for positive voltages obtaining the rectifying effect. The effect gradually disappears when C_s increases and the current recovers the symmetric trend.

From Fig. 2.8(b), we observe that the I(V) curve is practically independent of the coupling among the QDs. This coupling can be treated as a small perturbation (it does not appear in Eq. 2.40 and Eq. 2.41) and it shifts to higher voltages the opening of the conduction channel. As we can see from Eqs. 2.38 - 2.39, it has different sign than the applied voltage thus, the local potential is slightly smaller than in the single case. Therefore, the external voltage needed to put the energy level in the conduction window increases.

2.3 Model validation: comparison with NEGFF

Since we have presented and studied the electron transport model based on the non-coherent rate equations (NCRE), now, we have to validate it. We are going to compare it to the Non-Equilibrium Green's Function Formalism (NEGFF). The NEGFF has been widely used to calculate current and charge densities in nanoscale conductors (e.g. molecular and semiconductor) under an external bias. This method is mainly used for ballistic conduction but may be extended to include inelastic scatterings. Thus, this is the preferred methodology when we are dealing with systems that need a pure quantum mechanical description.

For macroscopic systems, the transport properties are well described using the semi-classical Drude model whereas for micro- and nano- sizes the quantum effects become important and we need a quantum mechanical treatment. Our transport methodology, the non-coherent rate equations, lies in the frontier between these two approaches since it is based on continuity equations and also takes into account some quantum effects as the tunneling rates.

Now, we are going to describe briefly the NEGFF in order to obtain a new vision of a pure quantum mechanic treatment. In the second part, we will present a direct comparison between the NEGFF and the here presented transport model. This comparison includes different QDs arrangements being able to elucidate the major differences and common aspects between both approaches.

2.3.1 NEGFF: the Non-Equilibrium Green's Function Formalism

NEGFF is usually used to calculate current and charge densities in nanoscale under external bias. Several overviews of this methodology can be found in Ref. [58] for

molecular electronics and Ref. [59] for semiconductors devices, respectively. Since we only want to provide and intuitive overview and a general vision of this theory, we are going to explain the basics following Ref. [60]. However, complete tutorials of NEGFF can be found elsewhere [61, 62].

We start from the Schrödinger equation

$$H|n\rangle = E|n\rangle, \tag{2.42}$$

which is divided in three different subspaces: contact ($H_{1,2}, |\psi_{1,2}\rangle$) and device ($H_d, |\psi_d\rangle$) regions. We can write

$$\begin{pmatrix} H_1 & \tau_1 & 0 \\ \tau_1^\dagger & H_d & \tau_2^\dagger \\ 0 & \tau_2 & H_2 \end{pmatrix} \begin{pmatrix} |\psi_1\rangle \\ |\psi_d\rangle \\ |\psi_2\rangle \end{pmatrix} = E \begin{pmatrix} |\psi_1\rangle \\ |\psi_d\rangle \\ |\psi_2\rangle \end{pmatrix}, \tag{2.43}$$

where H_i and $|\psi_i\rangle$ are the Hamiltonian and the wave function in the ith subspace whereas $\tau_{1,2}$ describes the device and contacts interactions. We must note that we have assumed that each contact is independent to the other (no cross terms between them).

The Green's function is defined as

$$(E - H)G(E) = I \tag{2.44}$$

and it gives the system response to a constant perturbation $|v\rangle$ as

$$|\psi\rangle = -G(E)|v\rangle. \tag{2.45}$$

This scheme is used since it is easier to calculate the the Green's function than to solve the eigenvalue problem of the total Hamiltonian. From the previous definition and using Eq. 2.43, the wave function in the second contact ($|\psi_2\rangle$) reads as

$$\begin{aligned} H_2|\psi_2\rangle + \tau_2|\psi_d\rangle &= E|\psi_2\rangle \\ (E - H_2)|\psi_2\rangle &= \tau_2|\psi_d\rangle \\ |\psi_2\rangle &= g_2(E)\tau_2|\psi_d\rangle, \end{aligned} \tag{2.46}$$

where $(E - H_2)g_2 = I$ is the solution in the isolated second contact. Hereafter, we use the lowercase for the Green's functions of the isolated subsystems while the capital letter for the whole Green‘s function. It is important to note that we have two different solutions: the retarded and advanced solutions reflecting the outgoing and the incoming waves in the contacts (we will denote G for the retarded and $G^\dagger$ for the advanced one).

From the definition of the Green's function we obtain

$$\begin{pmatrix} E-H_1 & -\tau_1 & 0 \\ -\tau_1^\dagger & E-H_d & -\tau_2^\dagger \\ 0 & -\tau_2 & E-H_2 \end{pmatrix} \begin{pmatrix} G_1 & G_{1d} & G_{12} \\ G_{d1} & G_d & G_{d2} \\ G_{21} & G_{2d} & G_2 \end{pmatrix} = \begin{pmatrix} I & 0 & 0 \\ 0 & I & 0 \\ 0 & 0 & I \end{pmatrix}. \tag{2.47}$$

We can obtain G_d using $G_{1d} = g_1\tau_1 G_d$ and $G_{2d} = g_2\tau_2 G_d$. It is simple to find

$$G_d = (E - H_d - \Sigma_1 - \Sigma_2)^{-1}, \tag{2.48}$$

where $\Sigma_1 = \tau_1^\dagger g_1 \tau_1$ and $\Sigma_2 = \tau_2^\dagger g_2 \tau_2$ are the so called self-energies which contain the interaction of the contacts and the device.

Another important use of the Green's function is the spectral function A defined as

$$A \equiv i(G - G^\dagger), \tag{2.49}$$

which gives the density of states (DOS) and all solutions of the Schrödinger equation. We are not going to show in detail its derivation but, it can also be written as [60]

$$A = 2\pi \sum_k \delta(E - \epsilon_k)|k\rangle\langle k| \tag{2.50}$$

where $|k\rangle$ is all the eigenvectors of H with the corresponding eigenvalues ϵ_k.

It will be useful to have expressions for the device wave functions $|\psi_d\rangle$ and contact wave functions ($|\psi_{1,2}\rangle$). The device part is

$$|\psi_d\rangle = G_d \tau_1^\dagger |\psi_1\rangle \tag{2.51}$$

and using Eq. 2.46, the wave function of the second contact can be expressed as a function of the wave function in the first contact as

$$|\psi_2\rangle = g_2\tau_2|\psi_d\rangle = g_2\tau_2 G_d \tau_1^\dagger |\psi_1\rangle. \tag{2.52}$$

In the non equilibrium case, we are interested in two quantities: the current and the charge density matrix. The charge density matrix is defined as

$$n = \sum_k f(k,\mu)|\psi_k\rangle\langle\psi_k|, \tag{2.53}$$

where the sum runs over all states with the occupation number $f(E_k, \mu)$. The occupation number is determined by the reservoir filling of the incoming waves (i.e. injects electrons). We assume that it is well described by the Fermi Dirac distribution function with the corresponding Fermi level. The occupation of the device from the contact

labeled as one is written as

$$
\begin{aligned}
n_d = \int_{-\infty}^{\infty} dE \sum_k f(E,\mu_1)\delta(E-E_k)|\psi_d\rangle\langle\psi_d| \\
= \int_{-\infty}^{\infty} dE f(E,\mu_1) G_d \tau_1^\dagger \frac{a_1}{2\pi}\tau_1 G_d^\dagger
\end{aligned} \tag{2.54}
$$

where we have expanded $|\psi_d\rangle$ as a function of the incoming waves of the contact one. We have used $a_1/2\pi$, the spectral function of this contact. Introducing the quantity $\Gamma_1 = \tau_1^\dagger a_1 \tau_1 = i(\Sigma_1 - \Sigma_1^\dagger)$ and performing the summation for the second contact we can write:

$$
n = \frac{2}{2\pi}\int_{-\infty}^{\infty} dE \sum_i f(E,\mu_i) G_d \Gamma_i G_d^\dagger, \tag{2.55}
$$

where we have included a factor 2 to count for the spin an the sum runs over all the contacts.

Having different chemical potentials in the reservoirs filling the contacts gives rise to a current. We derive an expression for the current from the probability continuity equation. In the steady-state, the probability to find an electron in all the device ($\sum_i |\psi_i\|^2$ where the sum runs over all the subspaces) is conserved:

$$
0 = \frac{\partial \sum_i |\psi_i|^2}{\partial t} = \frac{i}{\hbar}\left(\left[\langle\psi_1|\tau_1|\psi_d\rangle - \langle\psi_d|\tau_1^\dagger|\psi_1\rangle\right] + \left[\langle\psi_2|\tau_2|\psi_d\rangle - \langle\psi_d|\tau_2^\dagger|\psi_2\rangle\right]\right). \tag{2.56}
$$

This equation takes into account the incoming probability fluxes from the leads to the central region and the outgoing ones being similar to the rate equations that we have used previously. Generalizing to an arbitrary contact j, the electric current (at one energy) can be inferred from the product of the probability current and the charge $(-q)$. Thus, for a single contact we can write

$$
i_j = -\frac{iq}{\hbar}\left(\langle\psi_j|\tau_j|\psi_d\rangle - \langle\psi_d|\tau_j^\dagger|\psi_j\rangle\right), \tag{2.57}
$$

where i_j is defined positive for current from contacts to device. To calculate the total current, we expand the wave functions into the contacts and device wave functions. We perform the summation over all the energy channels obtaining

$$
\begin{aligned}
I_{2\to 1} = 2\frac{q}{\hbar}\int_{-\infty}^{\infty} dE f(E,\mu_1)\sum_n \delta(E-E_n)\langle\psi_1|\tau_1 G_d^\dagger \Gamma_2 G_d \tau_1^\dagger|\psi_1\rangle \\
= \frac{2q}{\hbar}\int_{-\infty}^{\infty} dE f(E,\mu_1)\sum_{m,n}\delta(E-E_n)\langle\psi_1|\tau_1|m\rangle\langle m|G_d^\dagger\Gamma_2 G_d\tau_1^\dagger|\psi_1\rangle \\
= \frac{2q}{\hbar}\int_{-\infty}^{\infty} dE f(E,\mu_1)\sum_m \langle m|G_d^\dagger \Gamma_2 G_d \tau_1^\dagger \underbrace{\left(\sum_n \delta(E-E_n)|\psi_1\rangle\langle\psi_1|\right)}_{=\frac{a_1}{2\pi}}\tau_1|m\rangle \\
= \frac{q}{\pi\hbar}\int_{-\infty}^{\infty} dE f(E,\mu_1)\mathrm{Tr}(G_d^\dagger\Gamma_2 G_d \Gamma_1).
\end{aligned} \tag{2.58}
$$

for the current that crosses from contact two to the central region. To get the total current, the current through the other contact has to be subtracted obtaining the net current as

$$I = \frac{q}{\pi\hbar}\int_{-\infty}^{\infty} dE(f(E,\mu_1) - f(E,\mu_2))\mathrm{Tr}(G_d^{\dagger}\Gamma_2 G_d \Gamma_1) \tag{2.59}$$

which coincides with the Landauer formula for the current Eq. 2.2. Thus, from a pure quantum mechanical treatment of the system and decomposing the Hamiltonian in the contacts (leads or electrodes) and the device (the central region) parts, the current and the occupancy of the system can be calculated.

Once a pure quantum electron transport methodology has been explained, in the next section we are going to compare it with the here developed approach.

2.3.2 Comparison

In order to validate the model, we are going to compare it to the Sun *et al.* work [63]. In this paper, they studied the electron transport using NEGFF for different systems based on QDs in several configurations. The basic structure is basically the same that we studied previously: two electrodes (L lead and R lead regions) and a central region (C region). The central region will contain several QDs in different arrangements forming the system under study. The QDs are assumed to be weakly coupled to the leads. In the spirit of the NEGFF, the total Hamiltonian of the system can be written as

$$H = H_{L,R} + H_C + H_T, \tag{2.60}$$

where the different parts of the system are clearly visible: the Hamiltonians that describe the leads, left (L) and right (R), and the Hamiltonian of the central region (C). The H_T term includes the interaction between the QDs and the leads. Using the second quantization representation of the Hamiltonian, each part of the system reads as

$$\begin{aligned} H_{L,R} &= \sum_{k,\alpha\in(L,R),\sigma} \epsilon_{k,\alpha} c^{\dagger}_{k,\alpha,\sigma} c_{k,\alpha,\sigma}, \\ H_C &= \sum_{j=1,\sigma}^{N} \epsilon_j d^{\dagger}_{j,\sigma} d_{j,\sigma} + \sum_{i,j,\sigma} (t_{i,j} d^{\dagger}_{i,\sigma} d_{j,\sigma} + \mathrm{H.c.}), \\ H_T &= \sum_{k,\alpha\in(L,R),j,\sigma} (V_{k,\alpha,j} c^{\dagger}_{k,\alpha,} d_{j,\sigma} + \mathrm{H.c.}), \end{aligned} \tag{2.61}$$

where $c^{\dagger}_{k,\alpha,\sigma}, d^{\dagger}_{j,\sigma}(c_{k,\alpha,\sigma}, d_{j,\sigma})$ are the electron creation (annihilation) operators of the continuous states in the leads and the discrete state in the jth QD ($j = 1, 2, \ldots, N$), respectively. N is the number of QDs in the central region whereas $\alpha \in (L, R)$ denotes the left and right lead indexes. $\epsilon_{k,\alpha}$ and ϵ_j are the corresponding continuous energy spectrum in the leads and the discrete energy level in the jth QD, respectively. $t_{i,j}$ is the

interdot coupling coefficient between the ith and j^{th} QD, and $V_{k,\alpha,j}$ denotes the coupling strength between the jth QD and the two lead regions. The spin subscript σ in energy levels and couplings coefficients is omitted since no magnetic field is involved.

In the H_C part, we must note that only one energy level per QD has been assumed and the electron-electron interaction are not considered. The coupling coefficients $V_{k,\alpha,j}$, $t_{i,j}$ are simplified as constants with no energy dependence under the wide-band approximation [64]. In order to make the comparison, we have used the same value parameters for the QD energy levels and the transmission coefficients as Sun *et al.* The I(V) curves and the number of accumulated electrons in the ith QD, N_i, are presented. Analytical expressions for the current in the simplest cases and the evolution of the QD energy level as a function of the applied bias voltage are also shown. The expressions for the transmission coefficients derived from the NEGFF and the Hamiltonian described in Eq. 2.61 for each configuration are presented in the Annex I.

The electrochemical potentials in the two leads are set at $\mu_L = 0$ and $\mu_R = -qV$. We must note that we have changed the lead reference respect to the previous simulations. Within this form, we also demonstrate that the obtained results are independent of the energy reference. Electrons flow from the left lead to the right one for positive voltages. We do not consider direct transmission between the leads. For clarity, the DOS of the leads are considered to be constant over the whole energy range and we set a constant charge energy for all QDs: $U_0 = 0.25$ eV.

2.3.2.1 One single QD

We briefly review electron transport through one QD. Using the rate equations and only taking into account the lead contributions, the current can be written as

$$I = \frac{4\pi q}{\hbar} \int \frac{T_{R1} T_{L1} \rho_L \rho_1 \rho_R}{T_{L1}\rho_L + T_{R1}\rho_R} (f_L - f_R) dE. \tag{2.62}$$

Fig. 2.9(a) shows the numerical result for the current I(V). In the calculation we assumed symmetric coupling with respect to the right and left leads $T_{R1} = T_{L1} = 0.2$[1], respectively. The evolution of the energy level with the applied bias voltage is

$$\epsilon_1(V) = 1 - V/2 + U_0 \triangle N_1, \tag{2.63}$$

where the second and third terms are due to the electrostatic effect. As expected, the current increases with the bias when the energy of the QD moves across the left lead, which is $\mu_L = \epsilon_1(V) \rightarrow V \approx 2$. When V is high enough, the current saturates to a constant value, as $\epsilon_1(V)$ lies between the two electrochemical potentials of the leads. Fig. 2.9(b) shows the dependence of the electron number on the applied bias. Since the

[1]We use similar transmission values as Sun *et al.* in order to make possible the qualitative comparison between the models

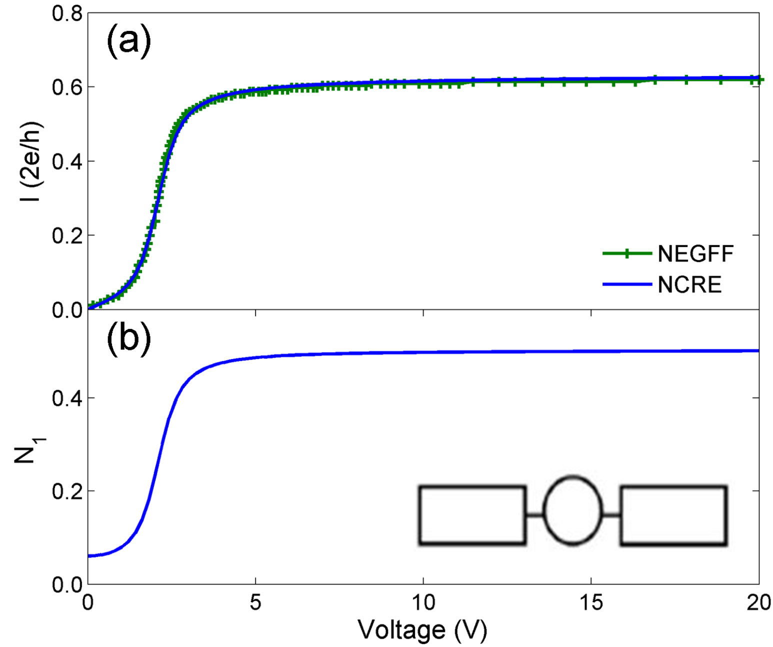

FIGURE 2.9: (a) The I(V) curve for one single QD obtained using the NCRE. We also show the NEGFF results for the same system. The NEGFF data have been taken from Sun *et al.* [63] (b) The electron number in the QD as a function of the applied bias voltage. The inset shows the connection geometry. The rectangles represent the two leads and the circle represents the QD.

two tunneling lead couplings are equal, when the energy enters in the conductive region the QD remains half charged.

2.3.2.2 Two QDs

We now study the case of two QDs. There are four different connection geometries between the QDs and the leads. In our calculations, we assume symmetric coupling with respect to the leads, $T_{R1} = T_{L1} = 0.2$, and the QD coupling $T_{12} = 0.2$. We use the same energy level as Sun *et al.* [63] in order to make possible the qualitative comparison between the two models.

2.3.2.3 Serial case

The first configuration of two QDs is the case that they are in series. The system is shown in the inset of Fig. 2.10(a). Each QD only interacts with one lead and the other QD. In this case, the expression for the current is

$$I = \frac{4\pi q}{\hbar} \int \frac{T_{L1}T_{12}T_{2R}\rho_L\rho_1\rho_2\rho_R}{T_{L1}T_{12}\rho_1\rho_L + T_{L1}T_{2R}\rho_R\rho_L + T_{12}T_{2R}\rho_2\rho_R}(f_L - f_R)dE \qquad (2.64)$$

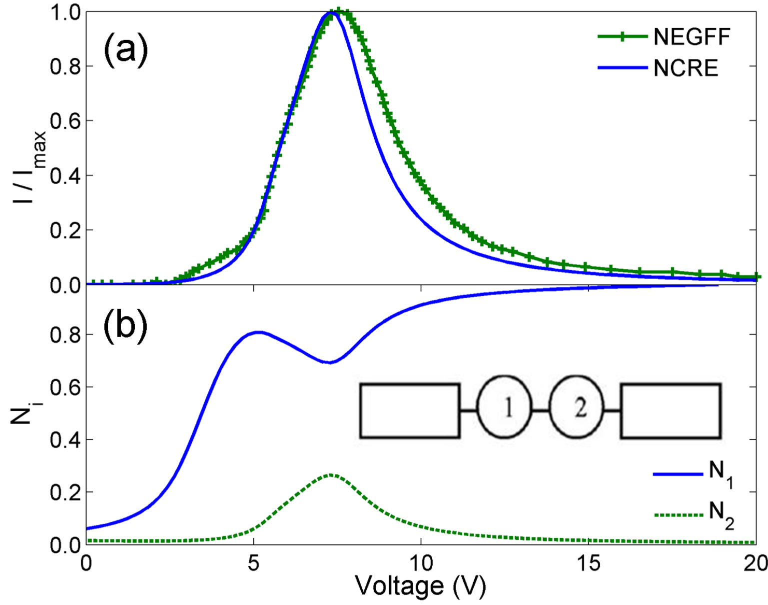

FIGURE 2.10: (a) The normalized I(V) curve for two QDs in a serial configuration obtained using NCRE. We also show the NEGFF results for the same system, the NEGFF data are taken from Sun *et al.* [63]. The inset also shows the connection geometry. (b) The electron number in the QDs as a function of the applied bias V.

and the evolution of the energy level of each QD with the applied bias voltage is

$$\epsilon_1(V) = 1 - qV_2/2 + U_0 \triangle N_1 \tag{2.65}$$

$$\epsilon_2(V) = 3.5 - qV/2 - qV_1/2 + U_0 \triangle N_2, \tag{2.66}$$

where we assumed that the QDs are only coupled to each other and to one lead. In order to have current flowing through the system, the energy levels must lie between the electrochemical potentials of the leads and overlapping of the QD energy levels is necessary as we have explained previously. When the energy levels are equal, $\epsilon_1 = \epsilon_2 \rightarrow V \approx 7.5$, this is a maximum overlapping between QD DOS, the system is in a resonance state being the current maximum. When the voltage increases further, the QD DOS overlapping decreases and NDR appears. In Fig. 2.10(b), we show the evolution of the electrons in each QD N_i as a function of the applied voltage V. Initially, N_1 increases since the channel between the first and second QD is closed. At the resonant condition, the channel between the QDs opens and some charge stored in the first QD flows to the second QD. At higher voltages the channel closes again and N_1 stores all the incoming charge, while N_2 loses its charge.

2.3.2.4 Parallel case

The second type of arrangement is the case of two QDs in parallel configuration. Both QDs are coupled to all elements of the system, the leads and the neighbor QD. In this

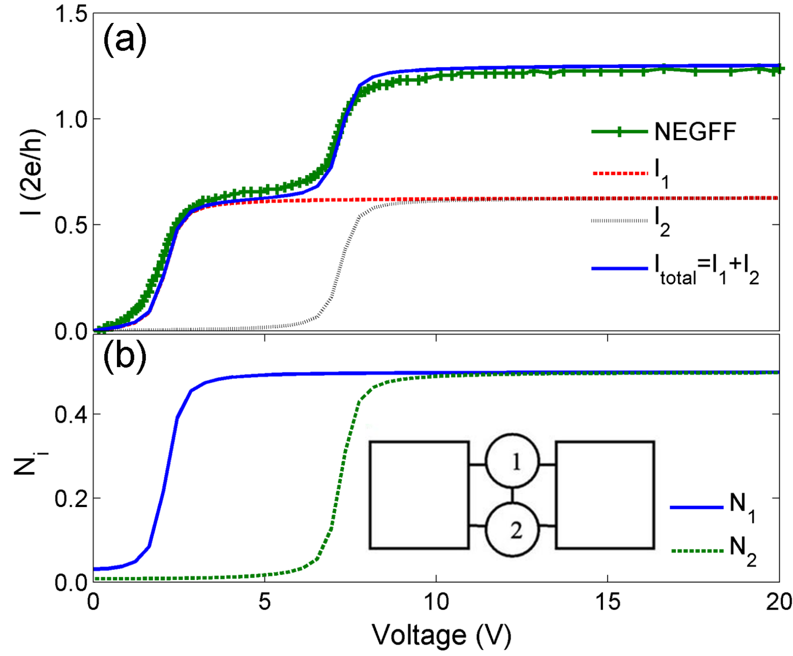

FIGURE 2.11: (a) The total and partial I(V) curves obtained using NCRE for a parallel configuration. The NEGFF results are taken from Sun *et al.* [63]. (b) The electron number in the QDs as a function of the applied bias V.

configuration the expressions for the current are

$$I_1 = \frac{4\pi q}{\hbar}\int \frac{T_{L1}T_{R1}(T_{L1}\rho_L + T_{1R}\rho_R + T_{12}(\rho_1+\rho_2))\rho_L\rho_R\rho_1}{D_2}(f_L - f_R)dE \tag{2.67}$$

$$I_2 = \frac{4\pi q}{\hbar}\int \frac{T_{L1}T_{R1}(T_{L1}\rho_L + T_{1R}\rho_R + T_{12}(\rho_1+\rho_2))\rho_L\rho_R\rho_2}{D_2}(f_L - f_R)dE, \tag{2.68}$$

where $D_2 = (T_{1R}\rho_L + T_{1L}\rho_R)^2 + T_{1L}T_{12}\rho_R(\rho_1+\rho_2) + T_{L1}T_{12}\rho_L(\rho_1+\rho_2)$. The position of the energy level of each QD is

$$\epsilon_1(V) = 1 - qV/3 - qV_2/3 + U_0\triangle N_1 \tag{2.69}$$

$$\epsilon_2(V) = 3.5 - qV/3 - qV_1/3 + U_0\triangle N_2. \tag{2.70}$$

We show the total and partial currents in Fig. 2.11(a). The I(V) curve shows two steps when the energy levels of the QDs are placed between the electrochemical potentials of the leads. This case is equivalent to a single QD with two energy levels (1eV and 3.5eV). Fig. 2.11(b) shows the electron number N_i $(i = 1, 2)$ with the applied bias voltage. The charge increases until it reach the saturation value similar as in the single QD case.

2.3.2.5 Other two QDs configurations

More possible QDs arrangements arise changing the couplings among the different parts of the system. In order to complete the transport study, we are going to simulate these

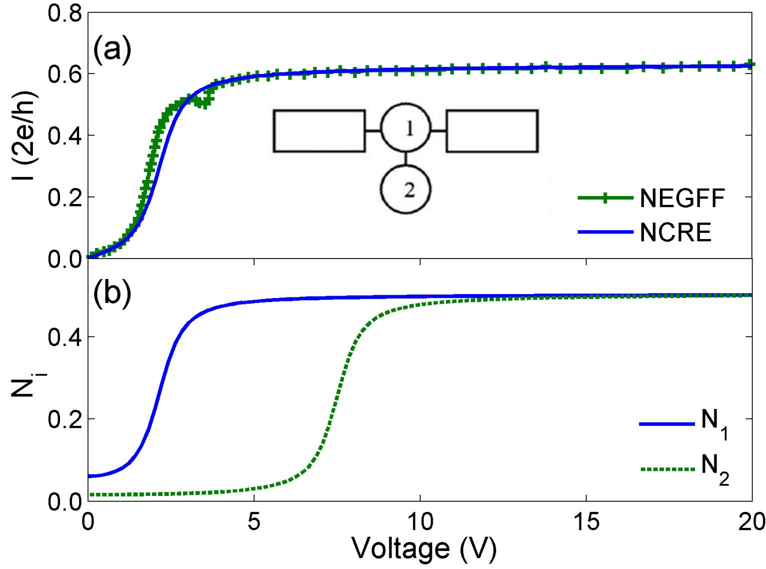

FIGURE 2.12: (a) The I(V) curve, for the configuration plotted in the inset, obtained using NCRE. We also show the NEGFF results for the same system, the NEGFF data are taken from Sun *et al.* [63]. (b) The electron number in the QDs as a function of the applied bias V.

system configurations based on two Qds.

We first examine the case in which one QD interacts with the two leads and it is also connected to the second QD, while the second QD is only connected to the first QD. The current is

$$I = \frac{4\pi q}{\hbar} \int \frac{T_{R1} T_{L1} \rho_L \rho_1 \rho_R}{T_{L1}\rho_L + T_{R1}\rho_R} (f_L - f_R) dE \tag{2.71}$$

and the position of the energy levels are

$$\epsilon_1(V) = 1 - qV/3 - qV_2/3 + U_0 \triangle N_1 \tag{2.72}$$

$$\epsilon_2(V) = 3.5 - qV_1 + U_0 \triangle N_2. \tag{2.73}$$

The obtained current expression Eq. 2.71 is the same as the one we have obtained for the single QD case. The non-equilibrium distribution function in the second QD is the same as in the first QD therefore the current between the QDs is zero. The results are presented in Fig. 2.12.

The second arrangement of QDs is shown in the inset of Fig. 2.13. The expressions for the partial currents are

$$I_1 = \frac{4\pi q}{\hbar} \int \frac{T_{1R}\rho_1\rho_R(T_{R2}\rho_R T_{L1}\rho_L + T_{12}\rho_1 T_{L1}\rho_L)}{D} (f_L - f_R) dE \tag{2.74}$$

$$I_2 = \frac{4\pi q}{\hbar} \int \frac{T_{2R}\rho_2\rho_R T_{12}\rho_1 T_{L1}\rho_L}{D} (f_L - f_R) dE, \tag{2.75}$$

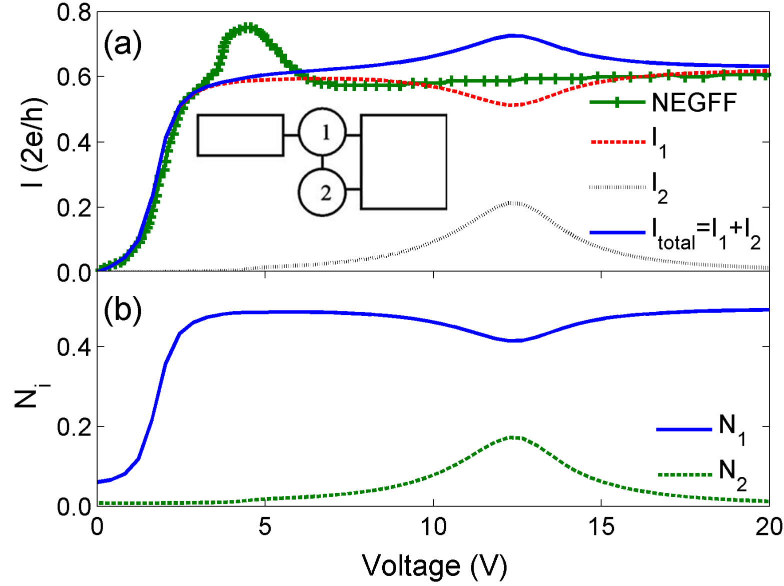

FIGURE 2.13: (a) The total and partial I(V) curves obtained using NCRE for the configuration showed in the inset. The NEGFF results are taken from Sun *et al.* [63]. (b) The electron number in the QDs as a function of the applied bias V.

where $D = T_{2R}\rho_R T_{L1}\rho_L + T_{R1}T_{R2}\rho_R^2 + T_{R2}\rho_R T_{12}\rho_2 + T_{12}\rho_1 T_{L1}\rho_L + T_{R1}\rho_R T_{12}\rho_1$ being the total current $I = I_1 + I_2$. The energy levels position is

$$\epsilon_1(V) = 1 - qV/3 - qV_2/3 + U_0\triangle N_1 \tag{2.76}$$

$$\epsilon_2(V) = 3.5 - qV_1/2 + U_0\triangle N_2. \tag{2.77}$$

In this case, we show the total and partial currents. The current through the first QD is similar to the single one QD configuration but the current through the second reminds the slope of a resonant state. This fact can be easily understood in the following way: if the channel between the two QDs is closed the current only flows through the first QD. When the QD1-QD2 channel is opened the QD2 also conducts. In the same case as before, when the voltage increases the overlapping decreases and the QD2 current decreases. Here, the main difference appears in the voltage position of the current peak associated to the second QD. This fact can be explained since we consider different capacitive coupling than Sun *et al.* For the energy level position of the second QD, they assume that it is fixed at $\epsilon_2 = 3.5eV$ whereas we have included the capacitive coupling to the neighbor QD.

2.3.2.6 Three QDs

The transport methodology developed previously can be easily extended into more complicated systems. Here, we present the results for some configurations based on three QDs. The I(V) curves and the accumulated charge are presented in Fig. 2.14(a-c-e) and Fig. 2.14(b-d-f), respectively. As we have shown before, the position of the energy levels

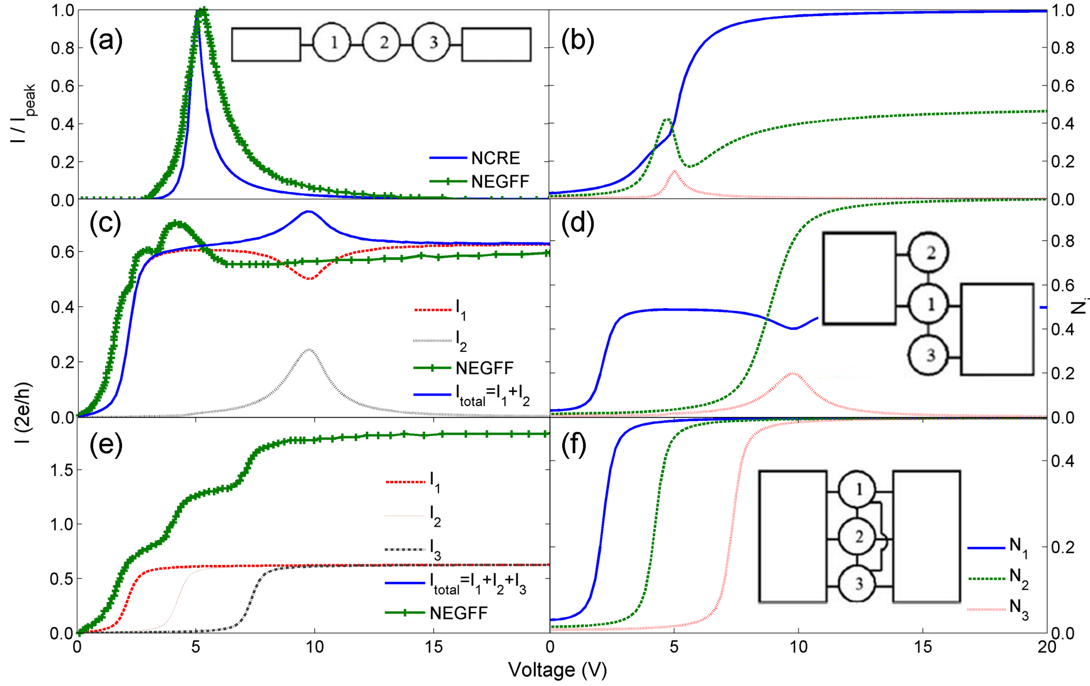

FIGURE 2.14: (a-c-e) I(V) curves and (b-d-f) accumulated electron number for three different QDs arrangement. The insets show the connection geometry. The NEGFF results are taken from Sun *et al.* [63].

plays an important role in the I(V) and N(V) curves. Using the solution of the Poisson equation, we can write the position of the each energy level as a function of the applied bias voltage in a general form as

$$\epsilon_1(V) = 1 - \sum_j \frac{C_{1j}}{C_{total1}} V_j + U_0 \triangle N_1 \quad (2.78)$$

$$\epsilon_2(V) = 2 - \sum_j \frac{C_{2j}}{C_{total2}} V_j + U_0 \triangle N_2 \quad (2.79)$$

$$\epsilon_3(V) = 3.5 - \sum_j \frac{C_{3j}}{C_{total3}} V_j + U_0 \triangle N_3, \quad (2.80)$$

where the subscript j runs over all connected elements of the system. The QD-lead coupling and the interdot coupling are set equal $T_{ij} = 0.2$. In the insets of Fig. 2.14, we show the scheme of the system under study.

2.3.2.7 Large QDs arrangements

To conclude, we present the results for larger systems which they are closer to the experimental devices. The systems are formed by 100 QDs placed in a parallel configuration, serial configuration and in an array geometry (10 × 10). The total I(V) curves and the geometries are presented in Fig. 2.15. The QD-lead coupling and the interdot coupling

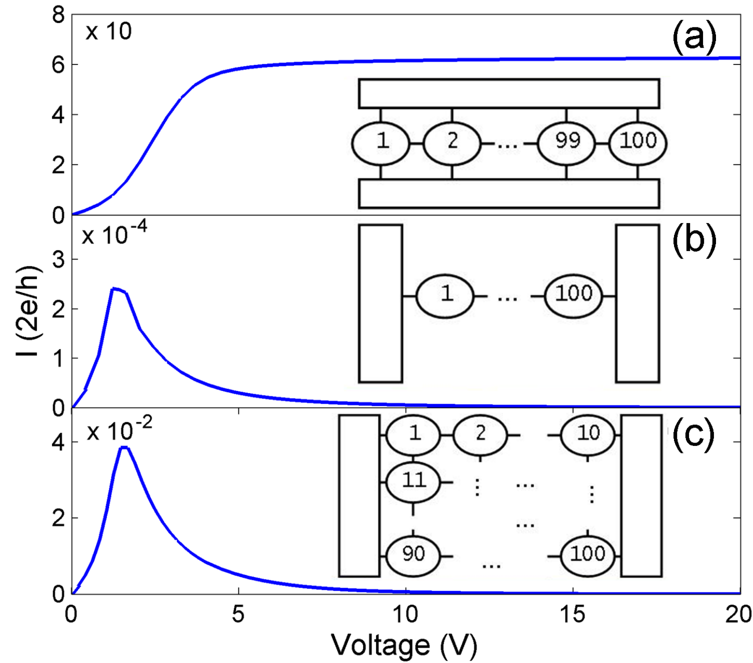

FIGURE 2.15: The I(V) curves for the largest systems: (a) 100 QDs in parallel configuration, (b) 100 QDs in serial configuration and (c) 100 QDs in an array disposition 10×10.

are set equal $T_{ij} = 0.2$. The capacitance between the linked elements are also equal. In order to represent an experimental system we considerer that the value of the energy level of each QD follows a normal distribution with mean value 1eV and deviation 0.2eV. This fact represents the usual distribution size that appears in the experiments [65]. The relationship between the QD radius and the energy level position is a well known effect and it is related to the quantum confinement of the electrons [66].

The I(V) curves show an interesting behavior. First, in the parallel case, Fig. 2.15(a), the I(V) curve shows a staircaselike behavior and saturates to a constant value at high bias. As we have seen before in the parallel configuration, each QD acts as an independent channel therefore the total current is the sum of all partial currents. As expected, the saturation current is 100 times the saturation current of a single QD.

For the serial configuration, Fig. 2.15(b), the current peak is recovered since the resonant state is necessary to have electron transport. The maximum value of the peak is hard to determine because it depends on the transmission coefficient, but it also depends of the overlapping between the DOS of the QDs.

Concerning the array configuration, Fig. 2.15(c), the I(V) curve is determined by a combination of the two previous cases. In order to have transport, the resonant state condition must be fulfilled. Therefore, a current peak appears but the total current is the sum of the partial currents of each row being grater than in the previous serial case.

2.3.3 Conclusions of the comparison with NEGFF

The conclusions of the comparison between the transport model proposed in this thesis an the NEGFF can be summarized as:

- The results presented in Figs. 2.9, 2.11, 2.10, 2.14(a) and 2.14(c) are in accordance between the two approaches. For the serial configuration (Fig. 2.10) the differences are due to the different values of the QD coupling, we also obtain a resonant peak when the energy levels of the QDs are placed in a resonant state. The resonant state is strongly dependent on the capacitive coupling of the QDs since the position of the energy level with the applied bias voltage depends on these capacitive couplings. In the parallel configuration Fig. 2.11, we obtain the same staircase shape but, in our case, we also take into account the energy charge terms. Thus, the current steps occur at higher voltages.
- The main difference appears in the case described in Fig. 2.12. For this configuration Sun *et al.* predicts an antiresonance effect [67]. We do not recover this effect because our model considers each QD as a separate quantum system. For this reason, our approach is known as a non-coherent model. The antiresonance is a pure quantum mechanical effect, it is related to scattering that suffers the electron by the new state (the second QD). For incident electron energies equal to the energy level of this scattering state, the propagation of the incident electron encounters the state and then, it is completely reflected back to the left. Thus, the transmission coefficient becomes zero and the incoming electron is trapped in the second QD.
- For the systems presented in Figs. 2.13 and 2.14(b) we obtain similar results. The position of the current peak is different because Sun *et al.* assume that the bias is uniformly applied throughout the whole system meanwhile we take into account all the electrostatic coupling between the different parts of the system.

2.4 Conclusions

In this chapter, we have presented the basis of the electron transport formalism to explain the electrical response of a QD array embedded in a dielectric matrix. This approach assumes that the whole system can be separated in small subsystem in order to describe the non-equilibrium properties. The electron transport between the two leads takes place as a consecutive tunneling events among the QDs assuming ballistic transport. This QD-QD and QD-lead couplings were described by tunnel junctions. These junctions can be described as a tunneling resistance that includes the quantum transmission coefficient and a capacitance in a parallel arrangement. Assuming that two

consecutive tunneling events are independent, the whole QD system was decomposed in different parts and the current conservation was applied to each QD.

Analytical expressions for the tunneling current among the different parts of the system were obtained within the Transfer Hamiltonian approach. It is based on the time dependent perturbation theory and the tunneling current can be expressed as the different electron occupancy in each side of the barrier. Moreover, in the current expressions, the transmission coefficient is also included.

From the system decomposition and the Transfer Hamiltonian approach, the non-equilibrium distribution function for each QD in the steady state was obtained, being possible to calculate the current that crosses the system and the accumulated charge in the QDs. Furthermore, we included the local potential of the QDs in the model. There are two main regimes in the nanoscale: the Coulomb Blockade (CB) and the Self-consistent field regime (SCF). Each one treat the charge effects in different ways, however, for its simplicity and the possibility to its application to larger systems, we chose the SCF regime. Despite these advantages, a direct comparison between both regimes were done.

The general solution of the SCF regime for a QD involves a Laplace term that takes into account the different capacity couplings of the elements and a charge term. Since the local potential shifts the energy level of the QDs, the accumulated charge in the QDs also changes and these considerations impose a simultaneous solution of the accumulated charge in the QDs (that depends on the non-equilibrium distribution function) and the solution of the Poission equation.

Once the basic model was explained, it was used to simulate three basic systems in order to obtain the main features that dominate the electrical response. From these simple systems, the transport conditions were highlighted being:

1. There is a net current flux only when the occupancy of the different elements given by the non-equilibrium distribution function are different.
2. The energy levels of the QDs have to lie between the electrochemical potentials of the leads.
3. The transport among two or more QDs takes places only when there is a resonant state. Thus, overlapping of the energy levels of the QDs is needed.

Besides, the basic current and charge trends were also observed: current steps reflecting the discrete nature of the energy levels in the QDs, resonant current peaks and NDR when the resonant state is opened and closed due to the different capacitive couplings. Furthermore, from the capacitive coupling studies that we done, the importance of the local potential inside each QD and how the capacitive coupling dominates the final I(V) curve were highlighted. Therefore, from these basic studies, the main parameters that

govern the final electrical response are: the transmission coefficients, the energy levels of the QDs and the capacitive couplings.

To conclude, we have compared the transport framework based on non-coherent rate equations in the SCF regime to a pure quantum transport approach, the NEGFF. Several configurations were studied obtaining very similar results in both cases. The success of this comparison shows that the here presented approach is a powerful and intuitive method for describing the electron transport. However, our transport approach can not reproduce the antiresonance effect since it is based on the system decomposition. Due to its simplicity, the model was extended to analyze arbitrary large arrays of QDs.

The here presented methodology are the fundamentals of the electronic transport formalism whereas, in the next chapters, the constant parameters used here are going to be realistically described.

2.5 Annexes

2.5.1 The Hamiltonian in a second quantization: transmission coefficients

Here, we are going to use the method of the equation of motion in order to obtain the NEGFF for the basic cases presented previously. It allows us to compute the transmission coefficient as well as the occupancy of the device region. From a physical point of view, the description of the Grenn's Functions are more intuitive if we speak in terms of incoming or outgoing wave functions than if we describe the system as a function of creator and annihilator operators. However, the operator description allows us to treat the mathematical problem in a easily way. Starting from the decomposition of the total Hamiltonian in the different parts that forms the system (we use the same notation defined previously) and using the equation of motion method [17, 63], we can write

$$(E-\epsilon_j)G^r_{j,i,\sigma} - \sum_{l=1}^{N} t_{j,l}G^r_{l,i,\sigma} - \sum_{l=1}^{N}\Sigma^r_{j,l,\sigma}G^r_{l,i,\sigma} = \delta_{ji}, \tag{2.81}$$

where we have defined the retarded self-energy function

$$\Sigma^r_{j,i,\sigma}(E) = \sum_{k,\alpha} V_{k,\alpha,j}V^*_{k,\alpha,i}/(E-\epsilon_{k,\alpha}). \tag{2.82}$$

The imaginary part can be approximated as $\Sigma^r \approx -i\Gamma/2$ where $\Gamma = \Gamma^L + \Gamma^R$ that takes into account the coupling among the central region and the leads. The usual definition of the retarded Green's function is used being

$$G^r_\sigma(E) = [E - H_C - \Sigma^r_\sigma(E)]^{-1}. \tag{2.83}$$

Finally, the transmission function is defined as

$$T(E) = Tr[\Sigma^L G^r \Sigma^R G^a], \tag{2.84}$$

where $G^a(E) = [G^r(E)]^\dagger$ is the advanced Green's function. Using these simple relations and taking into account the matrix form of the self-energies and the Green's functions, the transmission coefficients can be obtained.

2.5.1.1 One single QD

The coupling matrix and the GF matrix are one dimensional (numbers). Denoting $\Gamma^L_{11} = \Gamma_{L1}(\Gamma^R_{11} = \Gamma_{R1})$ for the left QD-lead and right QD-lead couplings, respectively. Being $\Gamma_1 = \Gamma_{L1} + \Gamma_{R1}$ the total lead coupling. The transmission coefficient can be written as

$$T(E) = \frac{\Gamma_{L1}\Gamma_{R1}}{(E-\epsilon_1)^2 + \Gamma_1^2/4}, \tag{2.85}$$

where ϵ_1 is the single energy level of the QD. If we recall the expression for the single QD, both expressions are quite similar. A product of the couplings is present and in the NEGF case, the broadening of the QD energy level (ϵ_1) appears "naturally".

2.5.1.2 Two QDs in series

In the case of two QDs in series, all the coupling matrices and GF matrices are two dimensional. H_C can be written as

$$H_C = \begin{pmatrix} \epsilon_1 & t_{12} \\ t_{12} & \epsilon_2 \end{pmatrix}, \tag{2.86}$$

where $\epsilon_{1(2)}$ are the energy levels of the QDs ant t_{12} is the coupling between them. From this Hamiltonian, the single energy level of each QD and their coupling are described. The coupling matrices to the leads are $\Gamma^L = \begin{pmatrix} \Gamma_{L1} & 0 \\ 0 & 0 \end{pmatrix}$ and $\Gamma^R = \begin{pmatrix} 0 & 0 \\ 0 & \Gamma_{R2} \end{pmatrix}$ where $\Gamma_{L1(R_2)}$ are the coupling constants. It is obvious that each lead is only coupled to one QD. The transmission coefficient is

$$T(E) = \Gamma_{L1}\Gamma_{R2}t_{12}^2/D_1, \tag{2.87}$$

where $D_1 = [(E-\epsilon_1)(E-\epsilon_2) - \Gamma_{L1}\Gamma_{R2}/4 - t_{12}^2]^2 + [\Gamma_{L1}(E-\epsilon_1) + \Gamma_{R2}(E-\epsilon_2)]^2/4$. Here, the energy level resonance condition in order to obtain the maximum current is clearly reflected in the first term of the D_1. For the resonant case, D_1 is minimum and the transmission has its maximum value obtaining the current peak. The NDR appears from the different electrostatic potential dependence of the QDs energy levels.

2.5.1.3 Two QDs antiresonance configuration

The coupling matrices of the first QD and the leads are $\Gamma^L = \begin{pmatrix} \Gamma_{L1} & 0 \\ 0 & 0 \end{pmatrix}$ and $\Gamma^R = \begin{pmatrix} \Gamma_{R1} & 0 \\ 0 & 0 \end{pmatrix}$. t_12 is the coupling among the QDs. We must note that the second QD is isolated to the leads and it is only coupled to the first QD. The transmission coefficient reads as

$$T(E) = \Gamma_{L1}\Gamma_{R1}(E - \epsilon_2)^2/D_2, \tag{2.88}$$

where $D_2 = [(E - \epsilon_1)(E - \epsilon_2) - t_{12}^2]^2 + [\Gamma_1(E - \epsilon_2)]^2/4$. In this case, the antiresonance effect is clearly visible when the energy is sweeping across the the energy of the level of the second QD. For $E = \epsilon_2$, $T(E) = 0$.

The last system in which an analytical expression can be found is the configuration described in Fig. 2.13. The coupling matrices are $\Gamma^L = \begin{pmatrix} \Gamma_{L1} & 0 \\ 0 & 0 \end{pmatrix}$ and $\Gamma^R = \begin{pmatrix} \Gamma_{R1} & \Gamma_{R12} \\ \Gamma_{R12} & \Gamma_{R2} \end{pmatrix}$ and the transmission coefficient is

$$\begin{aligned} T(E) = \{&\Gamma_{L1}\Gamma_{R1}[(E - \epsilon_2)^2 + \Gamma_{R12}^2/4] + \Gamma_{L1}\Gamma_{R2}(t_{12}^2 + \Gamma_{R12}^2/4) \\ &+2\Gamma_{L1}\Gamma_{R12}[t_{12}(E - \epsilon_2) - \Gamma_{R12}\Gamma_{R2}/4]\}/D_3. \end{aligned} \tag{2.89}$$

Where $D_3 = [(E - \epsilon_1)(E - \epsilon_2) - \Gamma_1\Gamma_{R2}/4 - t_{12}^2 + \Gamma_{R12}^2/4]^2 + [\Gamma_1(E - \epsilon_2)/2 + \Gamma_{R2}(E - \epsilon_1)/2 + t_{12}\Gamma_{R12}]^2$ $\Gamma_1 = \Gamma_{L1} + \Gamma_{R1}$.

Bibliography

[1] Tsuneya Ando, Alan B. Fowler, and Frank Stern. Electronic properties of two-dimensional systems. *Rev. Mod. Phys.*, 54:437–672, Apr 1982.

[2] Yigal Meir, Ned S. Wingreen, and Patrick A. Lee. Transport through a strongly interacting electron system: Theory of periodic conductance oscillations. *Phys. Rev. Lett.*, 66:3048–3051, Jun 1991.

[3] Sandip Tiwari, Farhan Rana, Kevin Chan, Leathen Shi, and Hussein Hanafi. Single charge and confinement effects in nano-crystal memories. *Applied Physics Letters*, 69(9):1232–1234, 1996.

[4] D. J. Lockwood. *Semiconductor and Semimetals, Light Emission in Silicon From Physics to Devices*. Academic Press, San Diego.

[5] A. Levy Yeyati, A. Martín Rodero, and F. Flores. Electron correlation resonances in the transport through a single quantum level. *Phys. Rev. Lett.*, 71:2991–2994, Nov 1993.

[6] J. B. Barner and S. T. Ruggiero. Observation of the incremental charging of Ag particles by single electrons. *Phys. Rev. Lett.*, 59:807–810, Aug 1987.

[7] J. Weis, R. J. Haug, K. v. Klitzing, and K. Ploog. Competing channels in single-electron tunneling through a quantum dot. *Phys. Rev. Lett.*, 71:4019–4022, Dec 1993.

[8] S. D. Wang, Z. Z. Sun, N. Cue, H. Q. Xu, and X. R. Wang. Negative differential capacitance of quantum dots. *Phys. Rev. B*, 65:125307, Mar 2002.

[9] W. G. van der Wiel, S. De Franceschi, T. Fujisawa, J. M. Elzerman, S. Tarucha, and L. P. Kouwenhoven. The kondo effect in the unitary limit. *Science*, 289(5487):2105–2108, 2000.

[10] Weijiang Gong, Yisong Zheng, Yu Liu, and Tianquan Lü. A feynman path analysis of the fano effect in electronic transport through a parallel double quantum dot structure. *Physica E: Low-dimensional Systems and Nanostructures*, 40(3):618 – 626, 2008.

[11] Marcello Rosini, Carlo Jacoboni, and Stefano Ossicini. Monte carlo simulation of electron transport in Si/SiO_2 superlattices: Vertical transport enhanced by a parallel field. *Phys. Rev. B*, 66:155332, Oct 2002.

[12] Beenakker, C. W. J. Theory of coulomb-blockade oscillations in the conductance of a quantum dot. *Phys. Rev. B*, 44:1646–1656, Jul 1991.

[13] Kees M. Schep, Paul J. Kelly, and Gerrit E. W. Bauer. Ballistic transport and electronic structure. *Phys. Rev. B*, 57:8907–8926, Apr 1998.

[14] M. Stephen Goodnick andJonathan Bird K. David Ferry. *Transport in Nanostructures*. Cambridge University press, 2009.

[15] V.S. Tsoi, M.D. Jaeger, B. Golding, M.V. Tsoi, and J. Bass. Transverse electron focusing, quantum electron kinetics, and the hall effect in Bi. *Physica B: Condensed Matter*, 218(1–4):22 – 25, 1996. Proceedings of the Second International Conference on Point-contact Spectroscopy.

[16] Ya.M. Blanter and M. Büttiker. Shot noise in mesoscopic conductors. *Physics Reports*, 336(1–2):1 – 166, 2000.

[17] Supriyo Datta. *Electronic Transport in Mesoscopic Systems*. Cambridge University Press, 1995.

[18] S Datta. A simple kinetic equation for steady-state quantum transport. *Journal of Physics: Condensed Matter*, 2(40):8023, 1990.

[19] J. Bardeen. Tunnelling from a many-particle point of view. *Phys. Rev. Lett.*, 6:57–59, Jan 1961.

[20] Walter A. Harrison. Tunneling from an independent-particle point of view. *Phys. Rev.*, 123:85–89, Jul 1961.

[21] M. H. Cohen, L. M. Falicov, and J. C. Phillips. Superconductive tunneling. *Phys. Rev. Lett.*, 8:316–318, Apr 1962.

[22] C. Julian Chen. Theory of scanning tunneling spectroscopy. *Journal of Vacuum Science Technology A*, 6(2), 1988.

[23] R. Clerc, A. Spinelli, G. Ghibaudo, and G. Pananakakis. Theory of direct tunneling current in metal-oxide-semiconductor structures. *Journal of Applied Physics*, 91(3):1400–1409, Feb 2002.

[24] Masaru Tsukada, Katsuyoshi Kobayashi, Nobuyuki Isshiki, and Hiroyuki Kageshima. First-principles theory of scanning tunneling microscopy. *Surface Science Reports*, 13(8):267 – 304, 1991.

[25] M. Berthe, A. Urbieta, L. Perdigão, B. Grandidier, D. Deresmes, C. Delerue, D. Stiévenard, R. Rurali, N. Lorente, L. Magaud, and P. Ordejón. Electron transport via local polarons at interface atoms. *Phys. Rev. Lett.*, 97:206801, Nov 2006.

[26] Andrew K. L. Lim Erik H. Anderson A. Paul Alivisatos Paul L. McEuen Hongkun Park, Jiwoong Park. Nanomechanical oscillations in a single-C_{60} transistor. *Nature*, 407, 2000.

[27] Kevin D. McCarthy, Nikolay Prokof'ev, and Mark T. Tuominen. Incoherent dynamics of vibrating single-molecule transistors. *Phys. Rev. B*, 67:245415, Jun 2003.

[28] M. G. Bawendi J. J. Macklin J. K. Trautman T. D. Harris L. E. Brus M. Nirmal, B. O. Dabbousi. Fluorescence intermittency in single cadmium selenide nanocrystals. *Nature*, 383, 1996.

[29] R. G. Neuhauser, K. T. Shimizu, W. K. Woo, S. A. Empedocles, and M. G. Bawendi. Correlation between fluorescence intermittency and spectral diffusion in single semiconductor quantum dots. *Phys. Rev. Lett.*, 85:3301–3304, Oct 2000.

[30] Peter Liljeroth, Karin Overgaag, Ana Urbieta, Bruno Grandidier, Stephen G. Hickey, and Daniël Vanmaekelbergh. Variable orbital coupling in a two-dimensional quantum-dot solid probed on a local scale. *Phys. Rev. Lett.*, 97:189901, Nov 2006.

[31] Mir Massoud Aghili Yajadda. Calculating electronic tunnel currents in networks of disordered irregularly shaped nanoparticles by mapping networks to arrays of parallel nonlinear resistors. *Journal of Applied Physics*, 116(15):–, 2014.

[32] Yu.A. Kruglyak. A generalized landauer-datta-lundstrom electron transport model. *Russian Journal of Physical Chemistry A*, 88(11):1826–1836, 2014.

[33] James Luscombe, Ann Bouchard, and Marshall Luban. Electron confinement in quantum nanostructures: Self-consistent poisson-schrödinger theory. *Phys. Rev. B*, 46:10262–10268, Oct 1992.

[34] IH. Tan, G. L. Snider, L. D. Chang, and E. L. Hu. A selfconsistent solution of schrödinger–poisson equations using a nonuniform mesh. *Journal of Applied Physics*, 68(8), 1990.

[35] Supriyo Datta. Nanoscale device modeling: the green's function method. *Superlattices and Microstructures*, 28(4):253 – 278, 2000.

[36] R. G. Parr and W. Yang. *Density Functional Theory of Atoms and Molecules.* Oxford University Press, 1989.

[37] C. J. Gorter. A possible explanation of the increase of the electrical resistance of thin metal films at low temperatures and small field strengths. *Physica*, 17:777–780, August 1951.

[38] R. Lambeir, A. Van Itterbeek, and G.J. Van Den Berg. Measurements on the electrical resistivity of thin iron films at. liquid helium temperatures. *Physica*, 16(11–12):907 – 914, 1950.

[39] T. A. Fulton and G. J. Dolan. Observation of single-electron charging effects in small tunnel junctions. *Phys. Rev. Lett.*, 59:109–112, Jul 1987.

[40] L. Jacak P. Hawrylak and A. Wojs. *Quantum dots.* Springer Verlag, Berlin, 1998.

[41] H. Grabert and M. H. Devoret. *Single Charge Tunneling.* Plenum Press, New York, 1992.

[42] K. Furuya S. Komiyama T. Ando, Y. Arakawa and H. Nakashima. *Mesoscopic Physics and Electronics*. Springer, 1998.

[43] P. L. McEuen S. Tarucha R. M. Westervelt L. P. Kouwenhoven, C. M. Marcus and N. S. Wingreen. *Nato ASI conference proceedings*. Kluwer, Dordrecht.

[44] A. N. Korotkov D. V. Averin and K. K. Likharev. Theory of single-electron charging of quantum wells and dots. *Phys. Rev. B*, 44:6199–6211, Sep 1991.

[45] C. A. Neugebauer and M. B. Webb. Electrical conduction mechanism in ultrathin, evaporated metal films. *Journal of Applied Physics*, 33(1), 1962.

[46] H. R. Zeller and Giaever I. Tunneling, zero-bias anomalies, and small superconductors. *Phys. Rev.*, 181:789–799, May 1969.

[47] Lambe John and Jaklevic R. C. Charge-quantization studies using a tunnel capacitor. *Phys. Rev. Lett.*, 22:1371–1375, Jun 1969.

[48] I. O. Kulik and R. I. Shekhter. Kinetic phenomena and charge discreteness effects in granulated media. *Soviet Journal of Experimental and Theoretical Physics*, 41:308, February 1975.

[49] W. van der Wiel, S. De Franceschi, J. Elzerman, T. Fujisawa, S. Tarucha, and L. Kouwenhoven. Electron transport through double quantum dots. *Rev. Mod. Phys.*, 75:1–22, Dec 2002.

[50] Anisur Rahman, Jing Guo, Supriyo Datta, and M.S. Lundstrom. Theory of ballistic nanotransistors. *Electron Devices, IEEE Transactions on*, 50(9):1853–1864, Sept 2003.

[51] Supriyo Datta. Electrical resistance: an atomistic view. *Nanotechnology*, 15(7):S433, 2004.

[52] C. W. J. Beenakker. Theory of coulomb-blockade oscillations in the conductance of a quantum dot. *Phys. Rev. B*, 44:1646–1656, Jul 1991.

[53] Garnett W. Bryant. Resonant tunneling through coupled, double-quantum-box nanostructures. *Phys. Rev. B*, 44:3064–3069, Aug 1991.

[54] M. Borgstrom, T. Bryllert, T. Sass, B. Gustafson, L.-E. Wernersson, W. Seifert, and L. Samuelson. High peak-to-valley ratios observed in InAs/InP resonant tunneling quantum dot stacks. *Applied Physics Letters*, 78(21), 2001.

[55] C. V. Reddy, V. Narayanamurti, J. H. Ryou, U. Chowdhury, and R. D. Dupuis. Observation of resonant tunneling through a quantized state in InP quantum dots in a double-barrier heterostructure. *Applied Physics Letters*, 77(8), 2000.

[56] Y. Ohno, K. Asaoka, S. Kishimoto, K. Maezawa, and T. Mizutani. Observation of resonant tunneling through single self-assembled InAs quantum dots using electrophotoluminescence spectroscopy. *Journal of Applied Physics*, 87(9), 2000.

[57] B. Aslan, H. C. Liu, J. A. Gupta, Z. R. Wasilewski, G. C. Aers, S. Raymond, and M. Buchanan. Observation of resonant tunneling through a self-assembled InAs quantum dot layer. *Applied Physics Letters*, 88(4):–, 2006.

[58] F. Zahid M. Paulsson and S. Datta. *Nanoscience, Engineering and Technology Handbook*. CRC Press, 2002.

[59] A. W. Ghosh P. S. Damle and S. Datta. *Molecular nanoelectronics*. 2002.

[60] M. Paulsson. Non Equilibrium Green's Functions for Dummies: Introduction to the One Particle NEGF equations. *eprint arXiv:cond-mat/0210519*, October 2002.

[61] A Prociuk, H Phillips, and B D Dunietz. Modeling transient aspects of coherence-driven electron transport. *Journal of Physics: Conference Series*, 220(1):012008, 2010.

[62] U. Aeberhard. Theory and simulation of quantum photovoltaic devices based on the non-equilibrium green's function formalism. *Journal of Computational Electronics*, 10(4):394–413, 2011.

[63] Z. Z. Sun, R. Q. Zhang, W. Fan, and X. R. Wang. Resonance and antiresonance effects in electronic transport through several-quantum-dot combinations. *Journal of Applied Physics*, 105(4):043706, 2009.

[64] Antti-Pekka Jauho, Ned S. Wingreen, and Yigal Meir. Time-dependent transport in interacting and noninteracting resonant-tunneling systems. *Phys. Rev. B*, 50:5528–5544, Aug 1994.

[65] M. Glover and A. Meldrum. Effect of "buffer layers" on the optical properties of silicon nanocrystal superlattices. *Optical Materials*, 27(5):977 – 982, 2005. Si-based Photonics: Towards True Monolithic Integration Proceedings of the European Materials Research Society — Symposium {A1} European Materials Research Society 2004 Spring Meeting.

[66] J. P. Proot, C. Delerue, and G. Allan. Electronic structure and optical properties of silicon crystallites: Application to porous silicon. *Applied Physics Letters*, 61(16):1948–1950, 1992.

[67] X. R. Wang, Yupeng Wang, and Z. Z. Sun. Antiresonance scattering at defect levels in the quantum conductance of a one-dimensional system. *Phys. Rev. B*, 65:193402, Apr 2002.

Chapter 3

Model implementation

In the previous chapter we have presented the electron transport methodology based on rate equations and the Transfer Hamiltonian Formalism in the self-consistent field regime. This formalism was used to study the electrical response of several quantum dot (QD) configurations and it was compared to Non-Equilibrium Green's Function Formalism (NEGFF) obtaining similar results. From these simulations, the main parameters that govern the final response of the system have been identified: the position of the energy levels, the transmission coefficients and the different capacitive couplings. Therefore, it is necessary a detailed and realistic description of these main parameters.

In order to be able to asses the potentials and capabilities of the various novel devices based on QDs, a realistic theoretical estimation of the specific device performance is thus highly desirable. Within this context, the simulations of such devices must be performed not only to understand but also to predict experimental behaviors. Moreover, from a physical point of view we can learn a lot from these simulations if they are independent on high level experimental parameters (as tunneling rates, defective interfaces...) and they are only based on low-level concrete ones (geometrical data, barrier height...).

In this chapter, first of all we present a formal derivation of the internal structure of the QDs based on effective mass approximation in order to obtain realistic densities of states (DOS). We also include the hole transport in the second part. In the third section, the transmission coefficients have been studied. Realistic capacitive couplings are evaluated in the fourth section. Finally, the code implementation is presented.

3.1 The Density of States

Quantum dots are nanostructures in which electrons and/or holes are confined into a small region [1]. The confinement is usually achieved by having a nanometer sized piece of low band gap semiconductor surrounded by a wider band gap material.

The wave function of the confined electrons and holes in the QD is the basic feature to determine its electrical and optical properties. These properties can be understood from the perspective of what happens when a cluster of atoms grows, or by considering what happens when the size of a bulk semiconductor is decreased. These perspectives are represented by top-down and bottom-up approaches, respectively.

- Top-down presents a convenient way to obtain qualitative results of the energetic structure of the QD. The main objective is showing how the electronic structure varies form energy bands to discrete energy levels when the system goes from bulk to QDs.
- Botom-up is focused on the study of the energetic structure of the QD as a function of a combination of the atomic orbitals that describes the surrounding electron of the nuclei that conforms the nanostructure.

In order to describe the electronic properties of the QD in an easy way, we use the top-down approach that gives an intuitive approximation of the nanostructure. Several models have been used to study and describe the internal electrical properties of the QDs using the top-down approach as the finite/infinite spherical potential well [2] and the $\mathbf{k} \cdot \mathbf{p}$ model [3, 4].

For its simplicity, we use the finite spherical potential well under the Effective Mass Approximation (EMA). In a following chapter, we will show how complex frameworks as the Density Functional Theory (DFT) can be included in order to describe accurately the electrical properties of the QDs. Here, we only want to describe the fundamental properties of the QDs (the discrete energy spectrum) and study how it affects to the electrical response of devices based on these nanostructures.

First of all, we write the assumptions that we have used to describe the QDs:

- The bulk effective masses are used to describe the electrons and holes. Although the Bloch theorem was derived only for large crystals and periodic potentials, it is commonly applied also to QDs which have crystalline order but dimensions corresponding to some tens of the lattice constant [5]. This is called the *Effective Mass Approximation* (EMA) [6].
- For multi-dot systems, we consider each *QD independent* from the other. Therefore, the electrical properties of each QD are independent of the surrounding QDs. This assumption is valid for weak tunnel coupling between the QDs, being the electrons localized on the individual QDs [7].
- For simplicity, we consider *spherical QDs*. However, different QD shapes (such as pyramid [8], lens [9] and disk [10]) are often reported and their energy levels are studied exploiting their symmetry.

- The electrical properties (the energy level spectra) are obtained in the *independent particle* framework. The discrete states arise as a solution of the Schrödinger equation assuming an effective finite potential barrier outside the QD. Since the system has spherical symmetry, we restrict the solution to the $l = 0$ case.

- The electron-electron interaction due to injected charge is included in the *self-consistent field* (SCF) treatment and in the *Poisson equation*.

- The electronic properties of the QDs are *independent of the applied electric field*. This requirement could appear dramatic for small systems in which, even the smallest excitation would modify the system geometry. This effect is generally smaller for larger (bulk) structures, in which the big number of atoms produces a much more stable environment, able to withstand the perturbations. The inclusion of the electric field only shifts the energy levels, as a solution of the Poisson equation.

3.1.1 Discrete energy spectrum

We are going to solve the single particle Schrödinger equation in order to obtain the internal electronic structure of the QD. We assume a finite spherical potential well in the EMA approximation and we only consider the $l = 0$ energy states.

The Hamiltonian that describes the QD can be written as

$$H = -\frac{\hbar^2}{2m_e}\nabla_e^2 - \frac{\hbar^2}{2m_h}\nabla_h^2 + V_e + V_h + E_g, \tag{3.1}$$

where V_e and V_h are the electron and hole finite confinement potentials. m_e and m_h are the electron and hole effective masses and E_g is the bulk band gap of the material. We must note that we have neglected the Coulomb interaction between electron and holes. The electron confinement potentials inside and outside for a given QD of radius R can be written as

$$V_e(r) = \begin{cases} 0 \text{ for } r < R \\ V_e \text{ for } R > r \end{cases} . \tag{3.2}$$

The hole confinement is also well described by the previous equation but using a different potential V_h. These potentials arise from the band offset between the material that forms the QD and the surrounding media. We have to include the discontinuity of the effective masses: we use different masses inside ($m_{e/h}$) and outside the QD ($m_{ox}^{e/h}$) for electrons and holes, respectively.

We present here the derivation of the wave function and the energy levels for the electron case. Concerning the hole case, the calculi are similar. The electron wave function for QDs can be represented as the product of the periodic Bloch function $u_\kappa(\mathbf{r})$ and an envelope function [11]. The envelope function ϕ_{env} describes the motion of particles in the confinement potential. This "envelope function approximation" is valid when the

QD diameter is much larger than the lattice constant of the crystal. The electron wave function can be written as

$$\psi_e = u_\kappa \cdot \phi_{env}. \tag{3.3}$$

The envelope function is the solution of the single particle Schrödinger equation.

Using the symmetry of the system, the electron Hamiltonian can be written in spherical coordinates as

$$\left\{ -\frac{\hbar^2}{2m_e}\left[\frac{\partial^2}{\partial^2 r} + \frac{2}{r}\frac{\partial}{\partial r}\right] + \frac{l(l+1)\hbar^2}{2m_e r^2} + V_e(r) \right\} R_l(r) = E_l R_l(r), \tag{3.4}$$

where the angular solution of the wave function is given by the spherical harmonics $Y_l^m(\theta, \phi)$. The radial solution is written for $l = 0$ case

$$R_0^{in}(r) = A\frac{sin(k_0 r)}{r} \text{ for } r < R \tag{3.5}$$

$$R_0^{out}(r) = B\frac{exp(-k'r)}{r} \text{ for } r > R \tag{3.6}$$

inside and outside the QD, respectively. Where $k_0 = \sqrt{\frac{2m_e E_0}{\hbar}}$, $k' = \sqrt{\frac{2m_{ox}^e(V_e - E_0)}{\hbar}}$ and we have used the different effective masses. The wave function must meet the continuity condition and the probability flow conservation in the boundary ($r = R$) [12]

$$R_0^{in}(R) = R_0^{out}(R) \tag{3.7}$$

$$\frac{1}{m_e}\frac{\partial R_0^{in}}{\partial r}|_{r=R} = \frac{1}{m_{ox}^e}\frac{\partial R_0^{out}}{\partial r}|_{r=R}. \tag{3.8}$$

Substituting Eq. 3.5 and Eq. 3.6 into Eqs. 3.7-3.8, we get

$$\cot x = -\sqrt{\frac{m_{ox}^e}{m_e}}\sqrt{\left(\frac{\sigma_0}{x}\right)^2 - 1}, \tag{3.9}$$

where $\sigma_0 = \sqrt{\frac{2m_{ox}^2 V_e}{\hbar^2}R^2}$ and $x = \sqrt{\frac{2m_{ox}^e}{\hbar^2}R^2\epsilon_i}$. The energy eigenvalues ϵ_i (the E_0 used previously) can be obtained solving Eq. 3.9. This equation does not have an analytical solution and has to be solved using numerical techniques, such as the Newton-Raphson method. The solutions of Eq. 3.9 form the discrete binding energy levels of the QD. For the hole case, the discrete binding energy levels can be obtained in a similar form.

Finally, in order to obtain the correct description of the electron and hole states we have to include the bulk band gap E_g, since we have solved the Schrödinger equation assuming that the zero energy origin is located at the bottom of the well and the solutions have to be energy shifted.

3.1.2 From discrete energy states to the continuum DOS

Up to now, the QD energy spectra is formed by electron and hole discrete energy levels and the density of states (DOS) can be written as

$$\rho(E) = \sum_{i}^{n} \delta(E - \epsilon_i) \tag{3.10}$$

where n is the total number of binding states (holes and electrons). These binding states are the solution of the isolated QD in the weak coupling regime in which we consider that the electronic properties of the QDs can be explained independently to the surrounding elements. However, the couplings between the QD and an external element (electrodes or other QDs) make energy levels acquire a finite lifetime, since an electron inserted at $t = 0$ in the state $E = \epsilon_i$ will gradually scape from this state. Therefore, the time evolution of the wave function is

$$\underbrace{exp(-i\epsilon_i t/\hbar)}_{\text{isolated QD}} \rightarrow \underbrace{exp(-i\epsilon_i t/\hbar)\ exp(-|t|/2\tau)}_{\text{coupled QD}} \tag{3.11}$$

where τ is the life time. This corresponds to a Fourier transform of a Lorentzian function centered in ϵ_i with width $\hbar/\tau$ [13, 14]. In general, the scape of electrons from a level does not follow a simple exponential law and the corresponding lineshape is not a Lorentzian function. However as we will see latter, for tunneling processes, this is the case.

Therefore, instead of a series of discrete energy levels, the QD DOS can be written as a sum of Lorentzian functions centered in each binding state forming a quasi-continuous DOS

$$\rho(E) = \sum_{i}^{n} \frac{\frac{\gamma}{2\pi}}{(E - \epsilon_i)^2 + (\frac{\gamma}{2\pi})^2}, \tag{3.12}$$

where γ is the broadening of the level. Although we have written the total DOS of the QD, for the electronic transport purpose we need to take into account if the energy level belongs to an electron or hole state since the transport coefficients are not equal for both types of carriers.
From a computational point of view, the approximation of a continuous DOS avoids several numerical problems that arise from the discreteness nature of the energy levels.

3.2 Electron & Holes

Before describing the transmission coefficients, we are going to focus on the distinction between electrons and holes.

In standard bulk semiconductor theory [15], two kinds of energy bands are defined: the conduction and the valence bands separated by an energy range called energy gap

(E_g). They are defined as a function of their position respect to the energy Fermi level (E_f): the valence band is below, whereas the conduction band is above E_f. The intrinsic characteristic of semiconductor is that E_f falls within the energy gap at room temperature. This means that the valence band is almost filled, whilst the conduction band is almost empty. For this reason, an intrinsic semiconductor at room temperature has bad conductivity since there are few mobile carriers. In order to explain the mobile carriers, the electron-hole scheme is used. The holes are defined as the absence of electrons in the valence band, whereas the electrons are only computed in the conduction band (Fig. 3.1(a)). Thus, the conductivity has two contributions: electrons and holes terms.

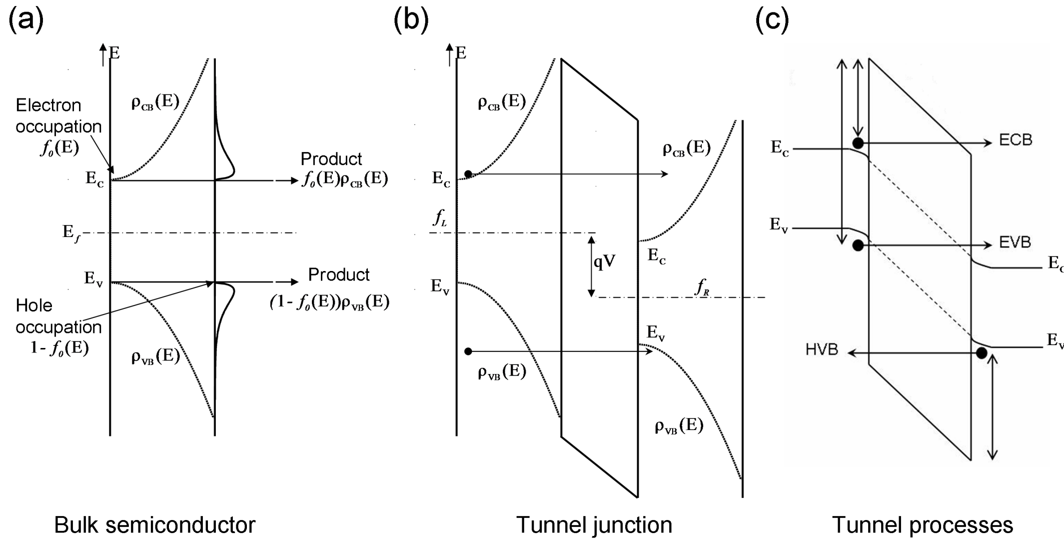

FIGURE 3.1: (a) Electron (f_0) and hole ($1 - f_0$) distribution functions, Fermi level (E_f), DOS (ρ_{CB} and ρ_{VB}) and electron ($f_0\rho_{CB}$) and hole populations ($(1 - f_0)\rho_{VB}$) for an intrinsic bulk semiconductor. (b) Scheme of the tunneling junction and the tunneling transitions under external polarization. (c) Schematics of the different tunneling processes in bulk materials. Electron from conduction band to conduction band (ECB), electron from valence band to conduction band (EVB) and tunneling from valence band to valence band (HVB) processes.

From the Transfer Hamiltonian formalism, we can write the tunnel current as $I \propto \int (f_L - f_R) dE$, this means that if there are energy states at both sides of the barrier the carriers will move from filled to emptied states. Therefore, we can neglect the distinction between electrons and holes and treat all the carriers as electrons that move through different energy levels. Nevertheless, we have to include the different parameters of electrons and holes associated to the tunnel transport as the different effective masses and the barrier heights. Thus, we can treat the hole conduction as electron conduction restricted to the valence band (see Fig. 3.1(b)).

In comparison to the bulk semiconductor theory in which we talk about conduction and valence bands, in QD we have discrete energy states and we talk about electron and hole energy states.

3.2.1 Transport tunneling processes

A variety of tunneling processes can be identified in a semiconductor-dielectric- semiconductor structure. Several studies have been done in N/P-MOS structures in inversion and accumulation regimes and three main processes were observed [16, 17, 18]: electron tunneling from conduction band to conduction band (ECB), hole tunneling from valence band to valence band (HVB), and hole tunneling from valence band to conduction band (EVB). Since the transmission coefficients are symmetric, the EVB process also involves the inverse case, tunneling from conduction band to valence band. Fig. 3.1(c) shows an scheme of these tunneling processes. We must note that the N/P-MOSFET was experimentally used in order to obtain a dominant current component (electrons or holes) doping the semiconductor contact, but, the same transport mechanisms are present in undoped systems.

We include the three tunneling mechanisms in the rate equation via the Transfer Hamiltonian Formalism using the appropriate DOS and transmission coefficient for each process.

3.3 Transmission coefficients

This section aims to present a brief description of the transmission coefficients. The invention of scanning tunneling microscopy (STM) by Binning, Rohrer, Gerber and Weibel [19] stimulated additional interest in the theory of tunneling. The Transfer Hamiltonian formalism was used to explain the three dimensional tunneling in STM measurements [20, 21, 22, 23]. With the advance of the atomic spatial resolution, many authors [22, 24] concluded that in the general case of three-dimensional tunneling current cannot be calculated using the simple formula described by the Transfer Hamiltonian Formalism. This simple relation is only valid in the one-dimensional case.

The carriers in the QD are confined by a potential barrier created by band offsets of the QD material and the surrounding matrix. Thus, in order to extract it, they have to cross through the oxide. Assuming elastic processes, the carriers scape via tunneling. Therefore, a realistic description of these tunneling processes are desirable. Moreover, as we saw in the previous chapter, the final electrical response of the system is strongly dependent on these coefficients.

Here, we present two methodologies in order to obtain the one-dimensional transmission coefficients: the transfer matrix approach and the Wentzel Kramers Brillouin (WKB)

approximation. We consider only one dimensional tunneling since we expect that the tunnel process takes place along the direction that minimizes the tunneling distance.

3.3.1 The transfer matrix approach

There are a few cases in which we can obtain an exact solution of the Schrödinger equation that involves a spatial varying potential. Thus, numerical methods or approximate solutions are needed in order to solve it and obtain the transmission coefficient.

The transfer matrix is a fruitful object that it has been used in the treatment of layered systems or supperlatices [25, 26, 27]. It is based on a very simple strategy: the discretization of the spatial varying potential. Since we can obtain the exact solution for a constant potential, it is decomposed in spatial regions in which its value is constant. From this simple and elegant idea, and imposing the usual wave function boundary conditions, the transmission coefficient can be easily evaluated.

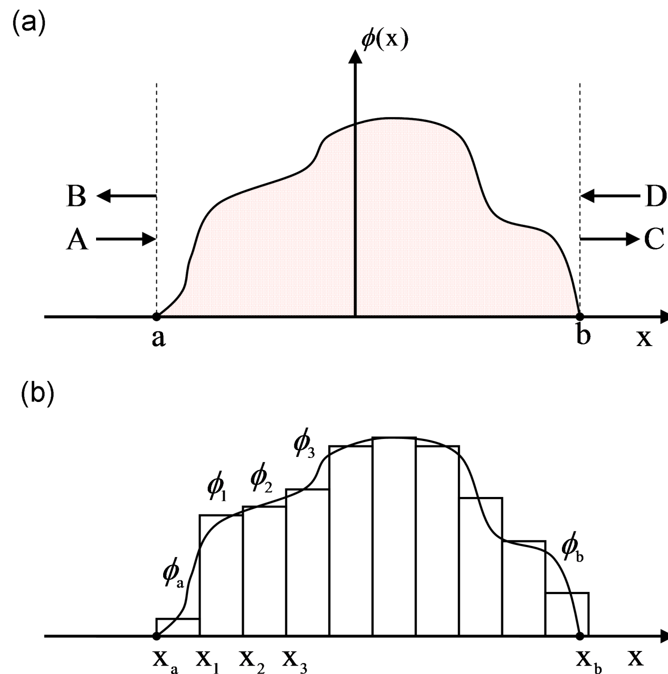

FIGURE 3.2: (a) Scheme of arbitrary spatial varying potential $\phi(x)$ barrier and the input (A and D) and output (B an C) amplitudes. (b) Scheme of the spatial discretization of the previous presented potential barrier.

Let us start describing one dimensional incident planar wave that transmit through the space in which there is a spatial varying potential barrier, Fig. 3.2(a). The transmission coefficient is defined as $|T|^2 = t^*t$ where $t = C/A$, where the parameters C and A are the wave amplitudes in each side of the barrier. In a general form, the solution of the

Schrödinger equation can be expressed as

$$\psi(x) = \begin{cases} Ae^{ik(x-a)} + Be^{-ik(x-a)} & x < a \\ \psi_{ab}(x) & a < x < b \\ Ce^{ik(x-b)} + De^{-ik(x-b)} & x > b \end{cases}. \tag{3.13}$$

Where $k = \sqrt{\frac{2mE}{\hbar}}$, E is the energy of the incident particle. The positive and negative exponential terms indicate the propagation of the waves to the right and to the left, respectively.

To solve the problem in a closed form, we must work out the Schrödinger equation in the $x \in (a, b)$ region to compute $\psi_{ab}(x)$ and impose the appropriate boundary conditions: the continuity of $\psi(x)$ and also of its derivative. Thus, two linear relations among the coefficients A, B and C, D appear which can be solve for any amplitude pair in terms of the other two: the result can be expressed as a matrix equation, which translates the linearity of the problem. The linear relation between the wave amplitudes on both sides of the barrier can be written as

$$\begin{pmatrix} A \\ B \end{pmatrix} = M \begin{pmatrix} C \\ D \end{pmatrix}. \tag{3.14}$$

The transmission coefficient can be easily obtained assuming that we have only incident waves in the left side ($A \neq 0$ and $D = 0$), therefore the transmission is $t = \frac{C}{A} = \frac{1}{M(1,1)}$. Now, it is time to describe the M matrix.

The M matrix takes into account the boundary conditions of the wave function in the space. This means, if we use the strategy presented before, discretization of the potential in small regions with constant potential (see Fig. 3.2(b)), we have to solve the Schrödinger equation in each region. The wave function is described by plane waves $\psi_N = A_N^+ e^{ik_N x} + A_N^- e^{-ik_N x}$ where $k_N = \sqrt{\frac{2m(E-\phi_N)}{\hbar}}$ in the Nth region. From the boundary conditions between the Nth region and the $(N+1)^{th}$ region, we can write

$$S(N) = \frac{1}{2} \begin{pmatrix} 1 + \frac{k_{N+1}}{k_N} & 1 - \frac{k_{N+1}}{k_N} \\ 1 - \frac{k_{N+1}}{k_N} & 1 + \frac{k_{N+1}}{k_N} \end{pmatrix}. \tag{3.15}$$

We need to include a phase factor that takes into account the new origin of the space coordinate $x + x_N \rightarrow x$ and it reads as

$$P(N) = \begin{pmatrix} e^{-ik_N(x_{N+1}-x_N)} & 0 \\ 0 & e^{ik_N(x_{N+1}-x_N)} \end{pmatrix}. \tag{3.16}$$

From Eq. 3.15 and Eq. 3.16, we can build the matrix propagation across the space in an easy way

$$M = S(x_a)P(x_a)S(x_1)P(x_1)...S(x_b). \tag{3.17}$$

Thus, the transmission coefficient is $|T|^2 = \frac{1}{|M(1,1)|^2}$. From this presented methodology, the transmission coefficient can be obtained numerically. Regrettably, we can not write an analytical expression.

Now, we are going to present another approximation that allows us to evaluate the transmission coefficient in a simple form, and it provides an analytical expression.

3.3.2 Wentzel Kramers Brillouin approximation

The Wentzel Kramers Brillouin (WKB) approximation is a method for finding approximate solutions to linear partial differential equations with spatially varying coefficients. In quantum mechanics, it is used to expand semiclassically the wave function in which the amplitude and the phase varies slowly compared to the de Broglie wavelength. This method allows to obtain approximate solutions to the time-independent Schrödinger equation in one dimension and it is widely used to calculate the tunneling probabilities.

The WKB is based on the solution of the wave function for a constant potential (ϕ_B), it reads

$$\psi(x) = Ae^{\pm ikx} \text{ where } k = \sqrt{\frac{2m(E-\phi_B)}{\hbar^2}}. \tag{3.18}$$

If the potential ($\phi_B \rightarrow \phi_B(x)$) changes slowly with x, we assume that the solution of the Schrödinger equation has the form

$$\psi(x) = A(x)e^{i\phi(x)}, \tag{3.19}$$

where $\phi(x) = xk(x)$ and $A(x)$ is the amplitude. In a slowly varying potential, $\phi(x)$ should vary slowly from the linear case, $\pm kx$. The wave vector as a function of the energy can be written as

$$\begin{aligned} k(x) &= \sqrt{\tfrac{2m(E-\phi_B(x))}{\hbar^2}} \text{ for } E > \phi_B(x) \\ k(x) &= -i\sqrt{\tfrac{2m(\phi_B(x)-E)}{\hbar^2}} \text{ for } E < \phi_B(x). \end{aligned} \tag{3.20}$$

Using this *ansatz* (Eq. 3.19),the Schrödinger equation becomes

$$A'' + 2i\phi' A' + iA\phi'' - A\phi'^2 = -kA. \tag{3.21}$$

The set of equations is

$$A'' - A\phi'^2 = -kA \tag{3.22}$$

$$2\phi' A' + A\phi'' = 0. \tag{3.23}$$

From the second equation we obtain $A = C\ \sqrt{\phi'}$ where C is a real constant. In order to solve the first term, we assume that the amplitude varies slowly. Thus, the term A'' is

negligible. The final wave function solution is

$$\psi(x) \approx \frac{C}{\sqrt{\phi'}} e^{\pm i \int k(x)dx}. \tag{3.24}$$

In order to calculate the transmission coefficient trough a potential barrier, and taking into account that the wave function (Eq. 3.24) conserves the density probability $|\psi(x)|^2 = |\psi_0|^2$, we are going to separate the wave function in each part of the potential barrier. Let us assume that the barrier extends from x_1 to x_2 and $\phi_B(x) > E$ inside the barrier. The solution is written as

$$\psi(x) = \underbrace{\psi_0 exp\left\{\int_0^{x_1} ik(x)dx\right\}}_{\psi_1} exp\left\{-\int_{x_1}^{x_2} |k(x)|dx\right\}, \tag{3.25}$$

where we have neglected the growing exponential solution for physical reasons. The ψ_1 term can be viewed as the wave function in the left part outside the barrier. It is readily shown that the probability decays exponentially inside the barrier. The probability in the other side of the barrier is

$$|\psi_2|^2 = |\psi_1|^2 exp\left\{-2\int_{x_1}^{x_2} |k(x)dx\right\}. \tag{3.26}$$

The ratio of the probability densities to the right and to the left side of the barrier is the tunnel probability $|T|^2$ and it is written as

$$|T|^2 = \frac{|\psi_2|^2}{|\psi_1|^2} = exp\left\{-2\int_{x_1}^{x_2} |k(x')|dx'\right\}, \tag{3.27}$$

where x_1 and x_2 are the classical turning points defined by the region where $\phi_B(x) > E$. We must note that the difference $x_2 - x_1$ defines the actual tunnel distance covered by the carriers through the barrier. It is worth noting that two important assumptions have been taken in Eq. 3.27: (i) the energy momentum dispersion relation is considered as parabolic, (ii) the electron mass is isotropic (effective mass approximation in the oxide).

The derived formulas using the WKB approximation are valid when the de Broglie wavelength (λ) of the electron is much smaller than the characteristic length over which the potential varies appreciably [28]. For the Si/SiO_2 electron barrier, λ can be estimated as follows:

$$\lambda = \frac{1}{k} = \frac{\hbar}{\sqrt{2m_{ox}\phi_B}} \approx 1.5 - 2\text{Å}. \tag{3.28}$$

Where we have used the electron and hole tunneling parameters: $\phi_{Be} = 3.1$ eV, $\phi_{Bh} = 4.5$ eV, $m_{ox}^e = 0.3m_o$ and $m_{ox}^h = 0.3m_o$ for electrons and holes, respectively. This result shows that the WKB approximation should be valid for oxide thickness as thin as 10-15 Å which is 6-10 times larger than the electron de Broglie wavelength [29].

Finally, we consider that the tunneling barrier is bended when there is a potential

difference between its sides. This potential difference creates an electric field across the barrier, assuming that the barrier has a linear dependence on the applied electric field, $\phi_B(x)$ can be expressed as

$$\phi_B(x) = \phi_0 - qE_{diel}x, \tag{3.29}$$

where ϕ_0 is the unmodified barrier height, $E_{diel} = V/d$ is the created electric field defined as the drop voltage V and the width of the tunnel junction d. To obtain an analytical expression of the tunnel probability, still it is necessary to distinguish between the regions where direct tunneling or Fowler-Nordheim conduction take place. The main difference between these two types of tunneling processes is the shape of the barrier that the carriers have to overcome. In direct tunneling, the carriers see a trapezoidal barrier, whereas in Fowler-Nordheim there is a triangular barrier. In the next section, we are going to derive the expressions used for these two tunneling mechanisms.

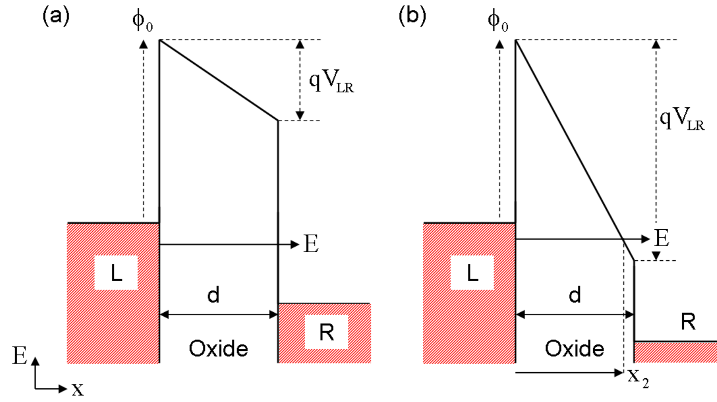

FIGURE 3.3: Scheme of the band diagram for the: (a) direct tunnel and, (b) the Fowler-Nordheim processes.

3.3.2.1 Direct tunneling

The direct tunneling (DT) takes place when $E \leq \phi(d)$. If the barrier has a linear dependence on the applied field, $\phi_B(x) = \phi_0 - qE_{diel}$, the electric field through the dielectric layer is $E_{diel} = \frac{V}{d}$ where, d is its overall thickness. Thus, the transmission probability

$$|T|^2 = exp\left(-\frac{2}{\hbar}\int_0^d \sqrt{2m_{ox}(\phi_0 - qE_{diel}x - E)}dx\right) \tag{3.30}$$

leads to

$$|T|^2 = exp\left[-\frac{4\sqrt{2m_{ox}}}{3\hbar qE_{diel}}\left((\phi_0 - E)^{3/2} - (\phi(d) - E)^{3/2}\right)\right]. \tag{3.31}$$

Here, E is the energy of the incident carrier. Fig. 3.3(a) shows the band diagram scheme for the DT process.

3.3.2.2 Fowler-Nordheim tunneling

The Fowler-Nordheim (FN) tunneling takes place when $E \geq \phi(d)$ and the turning point x_2 is given by the relation

$$\phi(x_2) = E = \phi_0 - qE_{diel}x_2. \tag{3.32}$$

This means that the carrier has enough energy to overcome the barrier before tunneling the overall barrier thickness. Thus, the carrier sees a triangular barrier. The transmission probability is expressed as

$$|T|^2 = exp\left(-\frac{2}{\hbar}\int_0^{x_2}\sqrt{2m_{ox}(\phi_0 - qE_{diel}x - E)}dx\right) \tag{3.33}$$

which leads to

$$|T|^2 = exp\left[-\frac{4\sqrt{2m_{ox}}}{3\hbar qE_{diel}}(\phi_0 - E)^{3/2}\right], \tag{3.34}$$

where E is the energy of the incident carrier. Fig. 3.3(b) shows the band diagram scheme for the FN tunneling.

It should be noted that the observation of DT or FN processes strongly depends on the thickness of the energy barrier, the applied electric field and the energy of the incident carrier.

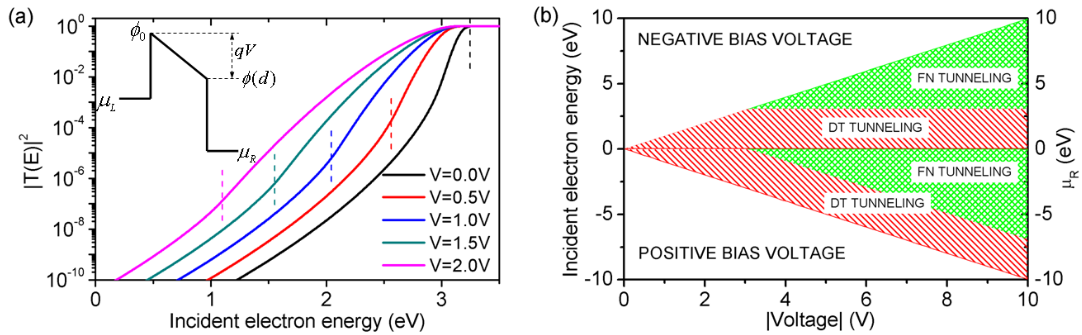

FIGURE 3.4: (a) Transmission coefficient as a function of the energy of the incident carrier for different polarization voltages. An scheme of the band bending is also shown in the inset. The value of the potential barrier is $\phi_0 = 3.1$ eV, $m_{ox} = 0.3m_o$ and barrier width $d = 3$ nm. The vertical dashed lines represent the transition from DT to FN tunneling processes. (b) Representation of the different tunneling process as a function of the voltage and the incident carrier energy for the previous barrier. We must note that the transport only occurs when the carrier is inside the transport window created by μ_L and μ_R. We fix $\mu_L = 0$ and $\mu_R = -qV$.

In Fig. 3.4(a), we show the evolution of the transmission coefficient for different applied voltages. The carrier must lie between μ_L and μ_R in order to obtain a net current. If we fix $\mu_L = 0$ and $\mu_R = -qV$, the different regions in which each transport regime occurs can be observed in Fig. 3.4(b).

3.3.3 Transfer matrix vs. WKB approximation: a comparison

In this section, we are going to present the different obtained curves using the two methodologies described before, the transfer matrix an the WKB approximation. A comparison to an exact solution of the problem for a rectangular potential is also shown. The systems under study are a potential barrier of 3.1 eV height and 1 nm and 3 nm width. We have used $m_{ox} = 0.3m_0$.

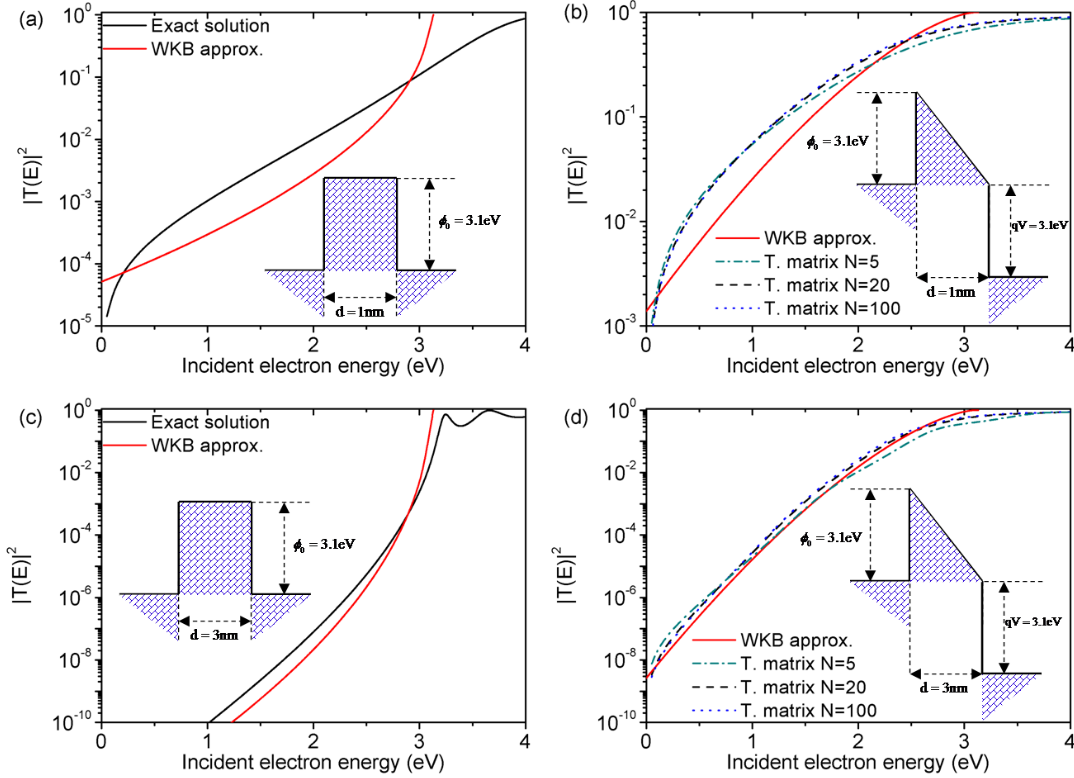

FIGURE 3.5: (a-b) Transmission coefficients for a rectangular and triangular potential barrier of $1nm$ width, respectively. The exact solution and the WKB approximation are shown for the rectangular barrier. The solution for the triangular case using the transfer matrix with different space discretization and the WKB approximation are also shown. In the inset, an scheme of the system is presented. (c-d) Transmissions coefficient for a rectangular and triangular potential barrier of 3 nm width, respectively.

In Fig. 3.5(a), we compared the transmission coefficient as a function of the incident energy for a rectangular potential barrier of 1 nm width. The WKB approximation and the exact solution are also presented. For this case, the transfer matrix approach coincides with the exact solution of the Schrödinger equation.

The comparison between WKB and the transfer matrix approach for the triangular case is also presented in Fig. 3.5(b) for different space discretization. In order to obtain a triangular barrier, a voltage $V = 3.1$ V has been applied. The limitations of the WKB approximation are clearly presented in Fig. 3.5(b) since the assumptions of this approach

are not fulfilled ($\lambda << d$). We can also note the differences in the classical turning point, when the incident electron energy equals the height of the barrier $E = \phi_B = 3.1$ eV.

In Fig. 3.5(c) and (d), the transmission is presented for the same cases as before but using a wider barrier (3 nm). In this structure, the WKB solution is closer to the exact and the transfer matrix solutions since the barrier is wider than in the previous case.

In order to develop a suitable methodology capable to deal with several QDs, we have to sacrifice some accuracy in the calculation of the transmission coefficients. Although we have observed differences between the WKB, the exact and the transfer matrix solutions, the major ones appear for the rectangular barrier. However, we must note that the transport trough a rectangular barrier represents that there is no voltage difference between the two sides of the barrier being the net current equal to zero. Thus, the oxide band will be bended when we calculate the net currents. Therefore, we can use the WKB approximation without lack of much precision.

3.4 Capacitive couplings

As we have seen in the solution of the Poisson equation, the local potential in each QD can be decomposed in two terms: the Laplace term plus the charge term. Concerning the Laplace term, the solution is expressed as a function of the capacitive couplings between the QD and the rest of the elements of the system. Moreover, we have demonstrated the importance of these capacitive couplings in the final current trend since the Laplace term is the dominant term in the local potential. Therefore, these capacitive couplings govern the movement of the DOS changing the number of energy levels that can contribute to the transport processes.
For this reason, we are going to present a realistic modelization of these couplings. Using the image charge method, the capacitance among the QDs and the leads and between the QDs can be obtained as the sphere-to-conducting-plane capacitance and sphere-sphere, respectively.

3.4.1 Image charge method

In order to obtain the different capacitive couplings among the parts of the system, we are going to describe briefly the image charge method.

The essence of this method consists in the replacement of the boundary conditions effects by imaginary charges which replicate the boundary conditions of the problem. The validity of the image charges method rests upon a corollary of the uniqueness theorem, which states that the electric potential in a volume is uniquely determined if

both the charge density throughout the region and the potential value on all boundaries are specified.

We focus on the sphere-to-conducting-plane case. The two elements are subjected to a potential difference V. The conducting plane is placed at $z = 0$ and grounded. The sphere radius is R and its center is placed at a distance $z = z_0$ from the infinite plane. The minimum distance between the sphere and the grounded plane is $d = z_0 - R$. We start considering the isolated sphere with charge q_0 that generates the potential V at the surface. This charge can be expressed as

$$q_0 = 4\pi\varepsilon_0\varepsilon_r RV, \tag{3.35}$$

where ε_r is the relative dielectric constant of the material and ε_0 is the vacuum permittivity. This charge generates an image charge with $-q_0$ located at $z = -z_0$. The image charge also creates an image charge in the sphere with position and magnitude given by

$$z_1 = z_0 - \frac{R^2}{2z_0} \tag{3.36}$$

$$q_1 = \frac{R}{2z_0} q_0. \tag{3.37}$$

If the process is repeated and for the ith charge, we can write

$$z_i = z_0 - \frac{R^2}{z_0 + z_{i-1}} \tag{3.38}$$

$$q_i = \frac{R}{z_0 + z_{i-1}} q_{i-1}. \tag{3.39}$$

The derivation of Eqs. 3.36 to 3.39 can be found in many textbooks [30]. It is convenient to define the normalized charge $\xi_i = q_i/q_0$.
The potential for the sphere-plane is equivalent to the potential of these two groups of charges

$$\phi(r,z) = \frac{1}{4\pi\varepsilon_0\varepsilon_r} \sum_{i=0}^{\infty} \frac{q_i}{\sqrt{r^2 + (z_i - z)^2}} - \frac{q_i}{\sqrt{r^2 + (z_i + z)^2}} \tag{3.40}$$

where, we have used polar coordinates. We must note that Eq. 3.40 is a solution for point charges, which is not the actual system of a sphere-plane. Both solutions are equal only for $(z - z_0)^2 + r^2 \geq R^2$ (outside the sphere) and for $z \geq 0$ (above the plane). Inside the sphere $\phi = V$ at any point and beneath the plane $\phi = 0$ at any point.

Once ϕ is given, the electric field can be obtained. From $\vec{E}(r,z) = -\nabla\phi$ it reads as

$$E_z(r,z) = RV \sum_{i=0}^{\infty} \frac{\xi_i(z - z_i)}{[(z - z_i)^2 + r^2]^{3/2}} - \frac{\xi_i(z + z_i)}{[(z + z_i)^2 + r^2]^{3/2}}, \tag{3.41}$$

where we have omitted the r-component of the field since the electric field on a conductor surface is perpendicular to it. Evaluating the electric field at $z = 0$ we can write

$$E_z(r, z = 0) = RV \sum_{i=0}^{\infty} \frac{-2\xi_i z_i}{(r^2 + z_i^2)^{3/2}}. \tag{3.42}$$

Using the Gauss theorem, we can obtain the charge in the plane as $\int \vec{E} \cdot \vec{ds} = Q/\varepsilon_r\varepsilon_0$. The capacitance is expressed as $C = Q/V$, thus, the capacitance can be written as

$$C = \frac{-2\pi\varepsilon_0\varepsilon_r}{V} \int_0^{\infty} E_z(r, z = 0) r dr. \tag{3.43}$$

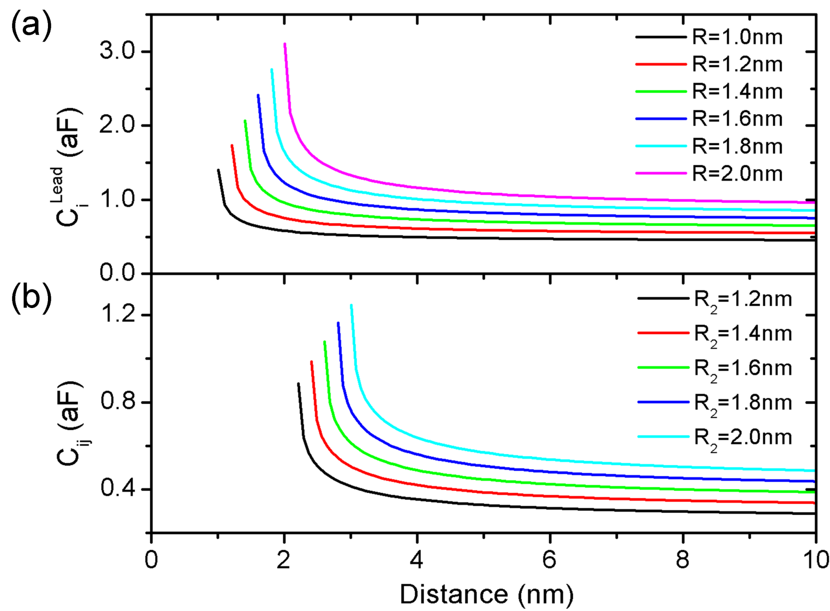

FIGURE 3.6: (a) Lead-QD capacity for different QDs radii as a function of the distance. (b) QD-QD capacity for different R_2 radii, the radius of one QD is hold at $R_1 = 1$ nm. In both cases, we have used $\varepsilon_r = 3.9$.

3.4.2 QD-lead coupling

Using the image charge method the coupling between the QD and the lead is obtained as the sphere-to-conducting-plane capacitance. From Eq. 3.43, it is derived an analytical solution that it is written as [31]

$$C_i^{Lead} = 4\pi\varepsilon_r\varepsilon_0\sqrt{r^2 - R^2} \sum_{n=1}^{\infty} \frac{1}{sinh(n \cdot arccosh(\frac{r}{R}))}. \tag{3.44}$$

Where, r is the distance among the center of the QD and the lead and R is the QD radius. The value of the capacitance is shown in Fig. 3.6(a) as a function of the distance and QD radius.

3.4.3 QD-QD coupling

For the QD-QD capacitance, sphere-to-sphere coupling, we also need to use the image charge method but there is not an analytical solution. Therefore, the evaluation must be numerically, which converges to the desired value within an acceptable number of iterations [32]. The value of the capacitance is shown in Fig. 3.6(b) as a function of the distance among the QDs and the QDs radii.

3.5 Putting all together: final equations

Summarizing the theory exposed in the previous sections and including the realistic parametrization that was done in this chapter (DOS, transmission coefficients and capacities) and the inclusion of the different transport mechanisms (ECB, EVB, HVB), the rate equation for each QD in a general system can be written as

$$
\begin{aligned}
q\frac{dN_i}{dt} = \; & \underbrace{\frac{4\pi q}{\hbar}\int_{-\infty}^{+\infty}|T_{ECB}|^2\rho_L\rho_i^e(f_L-n_i)dE + \frac{4\pi q}{\hbar}\int_{-\infty}^{+\infty}|T_{HVB}|^2\rho_L\rho_i^h(f_L-n_i)dE}_{\text{Left lead contribution}} \\
& \underbrace{+\frac{4\pi q}{\hbar}\int_{-\infty}^{+\infty}|T_{ECB}|^2\rho_R\rho_i^e(f_R-n_i)dE + \frac{4\pi q}{\hbar}\int_{-\infty}^{+\infty}|T_{HVB}|^2\rho_R\rho_i^h(f_R-n_i)dE}_{\text{Right lead contribution}} \qquad (3.45) \\
\begin{matrix}\text{Neighboring}\\ \text{QDs}\\ \text{contribution}\end{matrix} & \left\{\begin{matrix} +\frac{4\pi q}{\hbar}\sum_{j,j\neq i}^{N}\left\{\int_{-\infty}^{+\infty}|T_{ECB}|^2\rho_i^e\rho_j^e(n_j-n_i)dE + \int_{-\infty}^{+\infty}|T_{HVB}|^2\rho_i^h\rho_j^h(n_j-n_i)dE\right\} \\ +\frac{4\pi q}{\hbar}\sum_{j,j\neq i}^{N}\left\{\int_{-\infty}^{+\infty}|T_{EVB}|^2\rho_i^e\rho_j^h(n_j-n_i)dE + \int_{-\infty}^{+\infty}|T_{EVB}|^2\rho_j^e\rho_i^h(n_j-n_i)dE\right\}\end{matrix}\right.
\end{aligned}
$$

where $i = 1 \ldots N$, being N the number of QDs. We have written explicitly all the current contributions for an arbitrary i^{th} QD. The first pair of terms is related to the left lead contribution, the electron and the hole contributions. For simplicity, we assume infinite metallic leads therefore we only write the continuum DOS of the leads (ρ_L), meanwhile in the QD we write the DOS in separately terms: electron (ρ_i^e) and hole (ρ_i^h) DOS. Similar contribution is obtained for the right lead. In these two contributions, we use the Fermi Dirac distribution function to describe the leads with $\mu_L - \mu_R = qV$ electrochemical potentials. In each current term, we use the appropriate transmission coefficient. The last two pairs of current terms represent the current from the neighbor QDs. The subscript j runs over all the QDs except the QD that we are considering. In these terms, we take into account the different processes: tunneling from the electron to electron states and tunneling from hole to hole states. We also need to describe the tunneling that mix electron and hole states (EVB process).

The set of Eqs. 3.45 (one per QD) can be solved for the steady state. Under our assumption that there is no inelastic scattering, the system can be written in a matrix

form and solved for each energy step to obtain the non-equilibrium distribution function for each QD (n_i).

On the other hand, from the solution of the Poisson equation, the capacitive coupling term (Laplace solution) can be expressed in a matrix form for a general system. It reads as

$$\begin{pmatrix} U_1^L \\ \vdots \\ U_N^L \end{pmatrix} = \begin{pmatrix} 1/C_{tot,1} & 0 & 0 \\ 0 & \vdots & 0 \\ 0 & \dots & 1/C_{tot,N} \end{pmatrix} \times \left[\begin{pmatrix} C_1^{Lead} \\ \vdots \\ C_N^{Lead} \end{pmatrix} (-qV) - \begin{pmatrix} 0 & C_{1,2} & \dots & C_{1,N} \\ C_{2,1} & 0 & \dots & C_{2,N} \\ \vdots & \vdots & \vdots & \vdots \\ C_{N,1} & C_{N,2} & \dots & 0 \end{pmatrix} \begin{pmatrix} qV_1 \\ \vdots \\ qV_N \end{pmatrix} \right]. \tag{3.46}$$

C_{ij} is the capacitive coupling between the different components, QD-lead and QD-QD capacities, and $C_{tot,i} = \sum_{j,j\neq i} C_{ij}$ is the total capacitive coupling of the ith QD, where the subscript j runs over all the components of the system except the ith QD. The first term in the previous equation is the electrostatic influence of the lead in which the bias voltage (V) is applied, whereas the second term is the electrostatic coupling with the neighboring QDs. The neighbors capacitive matrix is defined as $N \times N$ symmetric matrix with zero in the diagonal terms. Both terms are multiplied by the inverse of the total QD capacity.

The general solution of the Poisson equation for each QD can be written as

$$U_i = U_i^L + \frac{q^2}{C_{tot,i}} \triangle N_i, \tag{3.47}$$

where the first term is the capacitive coupling described before and the second term reflects the charge increasing in the QD respect to the original charge.

Summarizing the here presented methodology:

1. For a given external bias voltage, Eqs. 3.45 are solved and the distribution functions are obtained. The electron number in each QD is computed as $N_i = 2\int \rho_i(E) n_i(E) dE$.

2. The local potential in each QD is obtained using Eq. 3.47.

3. The DOS are modified $\rho_i(E) \rightarrow \rho_i(E - U_i)$ and the transmission coefficients also change.

4. Repeat step 1 and 2 until the potential converge.

3.6 Code implementation: the SimQD simulator

Here, we are going to describe briefly the code implementation and some computational strategies that we have used in order to create a computational tool capable to simulate these devices, the SimQD simulator. The previous formalism has been implemented in MATLAB© code taking advantage of its matrix-oriented syntax. In Fig. 3.7 we show the SimQD scheme flowchart and the general strategy behind the code is presented below.

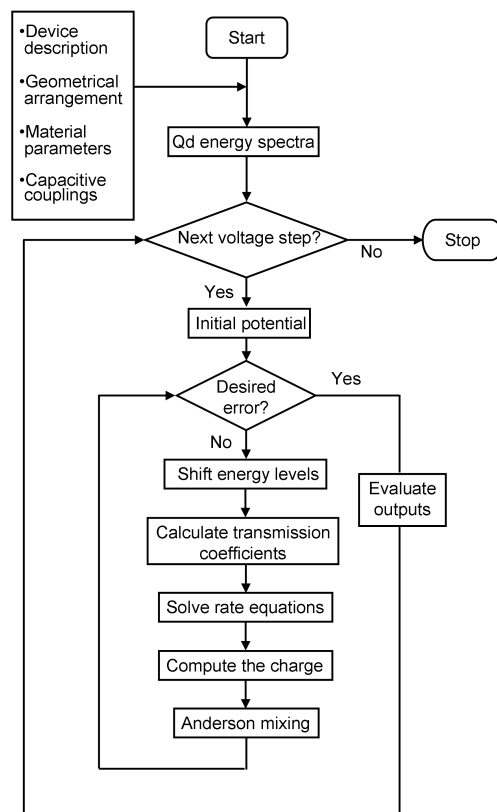

FIGURE 3.7: Scheme flowchart of the SimQD that implements the methodology described in this chapter.

The code is divided in 3 main parts:

1. *Input parameters:* Define the geometrical and the material parameters that form the device. The number of QDs is also defined. Calculate all the voltage independent parameters.

2. *SCF process:* Start the voltage loop. For each voltage point, the SCF process is repeated until it converges to the desired error.

3. *Output:* Calculate the output values.

3.6.1 Input parameters

First of all, we start describing the input parameters that define the system under study. They can be decomposed in two types: material and geometric constants. The code inputs are shown in Fig. 3.8.

Material parameters

Energy barriers

ϕ_b^{ECB} m_{ox}^{ECB}

ϕ_b^{EVB} m_{ox}^{EVB}

ϕ_b^{HVB} m_{ox}^{HVB}

Dielectric

Oxide dielectric constant

Device temperature

QD material

Band gap

QD dielectric constant

Effective masses

- Electron
- Hole

Geometrical inputs

Device description:

Device area

Number of layers

QDs per layer

Number of QDs

Layer spacing

QD position distribution:

- Fixed position
- Random...

QD mean size

QD size Std. Dev.

FIGURE 3.8: List of the input parameters that describe the device.

After the system is described, the QD array can be generated both randomly or in a fixed positions. The QD size is also generated using a normal distribution with a mean radius and standard deviation. However, in both cases all the QDs must fulfill two conditions: (1) no overlapping between QDs and (2) the QDs must lie entirely in the oxide matrix. The distances between all the elements of the system are also calculated.

The capacitive couplings are calculated at this point. The electron and hole energy levels are also obtained, since they only suffer a shift when an external voltage is applied. The Newton-Raphson method is used to compute the electron/hole binding states.

As we pointed out previously, the set of rate equations can be described for each energy step. Since we are describing ballistic transport, the electron/hole always has the same energy. Therefore, an energy grid is created and the rate equations are solved for each energy grid point.

3.6.2 Self-consistent field process

For each voltage step the SCF process is initiated. The Laplace term of the local potential is evaluated using the capacitance matrix. The energy levels of each QD is shifted by the local potential. The transmission coefficients are calculated for each QD

in each point of the energy grid taking into account the voltage difference among the two sides of the barrier. Thus, the rate equations can be written: one equation per QD and evaluated at each energy point of the grid. In order to solve this set of equations, the Moore-Penrose pseudoinverse method [33] is used since the matrix is not always directly invertible. Thus, the non-equilibrium distribuion function is obtained and the stored charge in each QD can be evaluated. The charge term in the local potential is added and the process is repeated until the system converges to a desired error. In order to accelerate this process, the Anderson mixing method is implemented.

3.6.2.1 Computational strategies: Anderson mixing

The self-consistent solution of coupled, nonlinear equations is a treasured topic in numerical analysis for obtaining stable and computationally efficient convergence for iterative solutions. It is interesting to know that this kind of computational strategy is widely used in electronic-structure calculations since the Kohn-Sham equations [34] have to be solved self-consistently. The charge density $n(\mathbf{r})$ depends on the potential $V(\mathbf{r})$ which depends nonlinearly on $n(\mathbf{r})$. The prescription for obtaining $V(\mathbf{r})$ from $n(\mathbf{r})$ is given within density-functional theory via Poisson's equation. The self-consistency condition for this type of calculations can be written as $F(n) = n_{out}(n) - n = 0$, where n is the input density. Therefore, in essence, one is just solving a system of simultaneous non-linear equations $F(n) = 0$. This kind of equations is also obtained by the Schrödinger Poisson solvers [35]. From the previous developed rate equation model, we have to solve simultaneously the charge in each QD and the Poission equation.

In an iterative procedure, convergence can be defined as continuously minimizing the "distance" between the input and the output potential. The terms input and output refer to the potential before and after the solution of the system of equations. When this distance is zero, i.e. input and output potentials are equal, the system has converged to the fixed-point solution. The simplest definition of distance between the input (U_{in}) and output (U_{out}) potential is

$$D[U_{out}, U_{in}] = (< U_{out} - U_{in}|U_{out} - U_{in} >)^{1/2} =< F|F >^{1/2}, \quad (3.48)$$

where $< U_{out} - U_{in}|$ is the vector of the differences for each QD.

Now, we are going to describe the used method to solve simultaneously the charge and the Poission equation in each QD. It is based on the Anderson's method [36, 37]. Two "average" mixed potentials are defined for each iteration step as

$$|\bar{U}_{in(out)} >= (1 - \beta)|U^{(m)}_{in(out)} > +\beta|U^{(m-1)}_{in(out)} >, \quad (3.49)$$

where m is the current iteration. The aim is to obtain the "best" β value for the current iteration that minimizes the distance between these two average quantities. It reads as

$$\beta = \frac{< F^{(m)}|F^{(m)} - F^{(m-1)} >}{D^2[F^m, F^m]}. \tag{3.50}$$

Finally, to obtain the new guess for the next iteration, we simply mix the average $\bar{U}_{in}$ and $\bar{U}_{out}$ potentials

$$|U^{(m+1)} >= (1-\alpha)|\bar{U}^m_{out} > +\alpha|\bar{U}^m_{in} >, \tag{3.51}$$

where α is chosen empirically.

This method is implemented in the code as following:

1. Initialize the variables with the last value of the previous voltage point. For the first voltage point, the variables start in zero.
2. Calculate the solution of the Poisson equation U_{out} for given U_{in}.
3. Calculate the value of β.
4. Calculate the average mixing for the input $\bar{U}_{in}$.
5. Calculate the average value for the output $\bar{U}_{out}$.
6. Do the simple mixing between the input and output average potentials.
7. Save values for the next iteration.
8. Repeat steps 2-7 until the desired convergence is achieved.

3.6.2.2 From equations to code: oriented matrix language

Previously we have presented the two main set of equations that govern the response of the system: the rate equations and the solution to the Poisson equation. Since for each QD we have to write a rate equation and a solution of the Poisson equation, we can write them in a matrix form.

Concerning the rate equations, we have to solve them numerically, since no analytical solution of the distribution function of each QD can be obtained. As the transport is ballistic, we can write a set of rate equations for each energy point. Thus, an energy grid discretization has been done and the distribution function is obtained at each grid point. Therefore, the problem is decomposed in a set of N equations (where N is the number of QDs) that has to be solved N_E times (where N_E is the number of the energy grid points). Obtaining the distribution function of each QD at each energy point of the grid. To compute the currents and the charge we sum over all the energy grid.

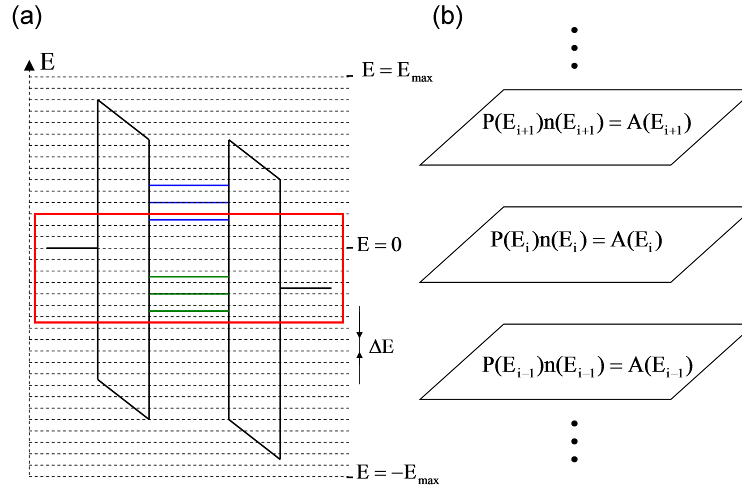

FIGURE 3.9: (a) Band diagram scheme of a single QD and the energy grid. All the energy dependent parameters are evaluated at these grid energy points. Moreover, the "interesting" transport region is highlighted by the red square. As we saw previously, the transport only occurs in the energy window created by μ_L and μ_R. Since we are doing the transport calculus at room temperature, we also include an energy region above and below the electrochemical potentials. (b) Computing strategy to obtain the distribution function at each energy grid point. The set of rate equations are solved for each energy being P and A the transport matrices.

In Fig. 3.9(a) we show a band energy scheme of a single QD connected to the leads. The energy grid is also shown. Following the previous strategy, the transmission coefficients and the DOS of the QD are evaluated at each energy point. Thus, the we need to solve the rate equation for each energy point to obtain the distribution function (see Fig. 3.9(b)).

Finally, from the Poisson solution we compute the variation of the charge respect to the initial value. The easiest way to obtain the initial charge is to perform the summation of the DOS up to the common electrochemical potential at zero bias. However, when the local potential raises or lowers the DOS, a fraction of the DOS enters or leaves the fix energy grid changing "artificially" the charge. In order to avoid this effect, we restrict the calculations of the charge to the transport energy window and a small energy region above and below it (red square in Fig. 3.9).

3.6.3 Code outputs

In the final stage, the code calculates the outputs for each voltage point. Occupancy of each QD respect the initial charge as a function of the applied voltage, the individual current voltage curve, as well as the total device I(V) curve and the local potential in each dot for the applied voltage.

The total current is decomposed into electron and hole terms for a system of N QDs and reads as

$$I_{Total}(V) = \frac{4\pi q}{\hbar}\sum_{i=1}^{N}\left\{\int_{-\infty}^{+\infty}|T_{ECB}|^2\rho_L\rho_i^e(f_L - n_i)dE + \int_{-\infty}^{+\infty}|T_{HVB}|^2\rho_L\rho_i^h(f_L - n_i)dE\right\}. \quad (3.52)$$

The electron number in the ith QD under external polarization can be obtained using

$$N_i(V) = 2\int_{-\infty}^{+\infty}\rho^e n_i dE + 2\int_{-\infty}^{+\infty}\rho^h n_i dE, \quad (3.53)$$

where we have decomposed explicitly the DOS in the electron (ρ^e) and hole (ρ^h) parts. Here, we must note that we are summing for all the electrons of the QD since n_i gives the occupation of the energy levels. Therefore, to compute the electron increment ($\triangle N$) we have to subtract the electrons in the QD in the equilibrium state (N_i^0), which reads as

$$N_i^0 = 2\int_{-\infty}^{+\infty}\rho^h f(E)dE, \quad (3.54)$$

where, $f(E)$ is the equilibrium Fermi Dirac distribution function and we have neglected the filled electron states.

3.6.4 Computational performance

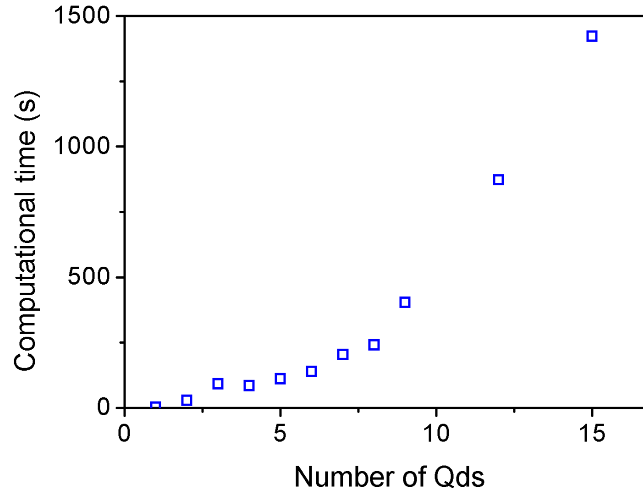

FIGURE 3.10: Computational time vs. number of simulated QDs. The time is referred for a single voltage point. Simulations were done in a dual core 2.60 GHz.

To conclude, we present here the computational efficiency of the code. In Fig. 3.10 we show the computational time needed to obtain results for one voltage point as a function of the number of QDs. The computational time grows with the number of QDs but it is still reasonable and allows to simulate large QD arrays. The most computational time is

spend in the recursive calculation of the transmission coefficients that is a $N \times N \times N_E$ matrix, where N is the number of QD and N_E is the number of energy grid points. This matrix has to be obtained in each iteration of the SCF process.

Besides, in order to increase the computational efficiency of the code and accelerate the SCF convergence, the simulation at each non-zero voltage is started using the potential solution obtained at the previous voltage as initial guess

MATLAB© allows to execute the code in parallel using computers with several cores. Thus, the simulations can be run in a parallel cluster decreasing further the computational time.

3.7 Conclusions

In this chapter, we have extended the rate equation transport methodology. In order to create a simulator tool, we have described as realistically as possible the main parameters that govern the final response of the system.

Concerning the energy level spectra of the QDs, we have seen that play an important role in the final response. Therefore, a realistic DOS that takes into account the discrete energy spectrum of the QDs has been obtained using the EMA. As a first order approximation, we have used a finite spherical potential well within the EMA. This framework allow us to describe the internal structure of the QDs as a function of three basic parameters: the confinement potentials, the effective masses and the QD radius.
Besides, we have also included the hole carriers so; the DOS is decomposed in hole and electron energy levels. Therefore, a new contribution to the current is included. Thus, different tunneling processes are described for electron and holes.

Since the tunneling junctions dominates the final response of the system, an effort has been done in order to describe accurately the tunneling transmission coefficients. Regrettably, the exact solution can not be obtained analytically. Therefore, two different approaches has been studied: the transfer matrix and the WKB approximation. A comparison between the two approaches was done and finally, the WKB was chosen for computational reasons to describe the tunneling probabilities.
Two different tunneling regimes have been considered as a function of the deformation of the oxide barrier and the incident energy electron: direct tunneling and Fowler-Nordheim for trapezoidal and triangular barriers, respectively.

On the other hand, the capacitive couplings have been described using the image charge method: a sphere-to-conducting-plane for the QD-lead and sphere-sphere for QD-QD couplings, respectively.

To conclude, we have presented the implementation of the transport model in a MATLAB© code. The computational issues, numerical strategies to achieve the convergence, as well as the code implementation were also discussed. Probably, the code implementation is one of the most important part of this thesis since it allowed us to simulate realistically different kind of systems as we will see in the following chapters.

Bibliography

[1] P. Michlerl. *Single Quantum dots.* Springer, 2003.

[2] Nizami Z. Vagidov Vladimir V. Mitin, Dimitryi I. Sementsov. *Quantum Mechanics for Nanostructures.* Cambridge university press, 1994.

[3] P. Yu and M. Cardona. *Fundamentals of Semiconductors: Physics and Materials Properties.* NanoScience and Technology. Springer, 2005.

[4] C. Kittel. *Quantum Theory of Solids.* NanoScience and Technology. Wiley, 1987.

[5] C. Delerue and M. Lanno. *Nanostructures: Theory and Modelling.* NanoScience and Technology. Springer-Verlag, 2004.

[6] Supriyo Datta. *Electronic Transport in Mesoscopic Systems.* Cambridge University Press, 1995.

[7] W. G. van der Wiel, S. De Franceschi, J. M. Elzerman, T. Fujisawa, S. Tarucha, and L. P. Kouwenhoven. Electron transport through double quantum dots. *Rev. Mod. Phys.*, 75:1–22, Dec 2002.

[8] J. Oshinowo, M. Nishioka, S. Ishida, and Y. Arakawa. Highly uniform InGaAs/-GaAs quantum dots ($15nm$) by metalorganic chemical vapor deposition. *Applied Physics Letters*, 65(11):1421–1423, 1994.

[9] D. Leonard, M. Krishnamurthy, C. M. Reaves, S. P. Denbaars, and P. M. Petroff. Direct formation of quantum sized dots from uniform coherent islands of InGaAs on GaAs surfaces. *Applied Physics Letters*, 63(23):3203–3205, 1993.

[10] M. Bayer, P. Hawrylak, K. Hinzer, S. Fafard, M. Korkusinski, Z. R. Wasilewski, O. Stern, and A. Forchel. Coupling and entangling of quantum states in quantum dot molecules. *Science*, 291(5503):451–453, 2001.

[11] Stephan W. Koch Hartmut Haug. *Quantum Theory of the Optical and Electronic Properties of Semiconductors.* World Scientific, 2004.

[12] G. Bastard. Superlattice band structure in the envelope-function approximation. *Phys. Rev. B*, 24:5693–5697, Nov 1981.

[13] Inder P Batra. From uncertainty to certainty in quantum conductance of nanowires. *Solid State Communications*, 124(12):463 – 467, 2002.

[14] Supriyo Datta. Electrical resistance: an atomistic view. *Nanotechnology*, 15(7):S433, 2004.

[15] John P. McKelvey. *Solid State and Semiconductor Physics.* Harper's physics series. Robert E. Krieger Phublising company, 1996.

[16] Wen-Chin Lee and Chenming Hu. Modeling CMOS tunneling currents through ultrathin gate oxide due to conduction- and valence-band electron and hole tunneling. *Electron Devices, IEEE Transactions on*, 48(7):1366–1373, Jul 2001.

[17] Yee-Chia Yeo, Tsu-Jae King, and Chenming Hu. MOSFET gate leakage modeling and selection guide for alternative gate dielectrics based on leakage considerations. *Electron Devices, IEEE Transactions on*, 50(4):1027–1035, April 2003.

[18] Yee Chia Yeo, Qiang Lu, Wen-Chin Lee, Tsu-Jae King, Chenming Hu, Xiewen Wang, Xin Guo, and T-P Ma. Direct tunneling gate leakage current in transistors with ultrathin silicon nitride gate dielectric. *Electron Device Letters, IEEE*, 21(11):540–542, Nov 2000.

[19] G. Binnig, H. Rohrer, Ch. Gerber, and E. Weibel. Surface studies by scanning tunneling microscopy. *Phys. Rev. Lett.*, 49:57–61, Jul 1982.

[20] J. Tersoff and D. R. Hamann. Theory and application for the scanning tunneling microscope. *Phys. Rev. Lett.*, 50:1998–2001, Jun 1983.

[21] N. García, C. Ocal, and F. Flores. Model theory for scanning tunneling microscopy: Application to Au(110) (12). *Phys. Rev. Lett.*, 50:2002–2005, Jun 1983.

[22] J. Bono and R.H. Good Jr. Theoretical discussion of the scanning tunneling microscope. *Surface Science*, 151(2–3):543 – 552, 1985.

[23] N. D. Lang. Vacuum tunneling current from an adsorbed atom. *Phys. Rev. Lett.*, 55:230–233, Jul 1985.

[24] A. Selloni, P. Carnevali, E. Tosatti, and C. D. Chen. Voltage-dependent scanning-tunneling microscopy of a crystal surface: Graphite. *Phys. Rev. B*, 31:2602–2605, Feb 1985.

[25] E. H. Hauge and J. A. Støvneng. Tunneling times: a critical review. *Rev. Mod. Phys.*, 61:917–936, Oct 1989.

[26] L. R. Ram-Mohan, K. H. Yoo, and R. L. Aggarwal. Transfer-matrix algorithm for the calculation of the band structure of semiconductor superlattices. *Phys. Rev. B*, 38:6151–6159, Sep 1988.

[27] R. Tsu and L. Esaki. Tunneling in a finite superlattice. *Applied Physics Letters*, 22(11):562–564, 1973.

[28] J. J. Sakurai. *Modern Quantum Mechanics*. Addison–Wesley, 1994.

[29] Jin Cai and Chih-Tang Sah. Gate tunneling currents in ultrathin oxide metal–oxide–silicon transistors. *Journal of Applied Physics*, 89(4):2272–2285, 2001.

[30] P. J. Lawrenson K. J. Binns and C. W. Trowbridge. *The Analytical and Numerical Solution of Electric and Magnetic Fields*. John Wiley Sons, 1992.

[31] Josep Carreras, O Jambois, S Lombardo, and B Garrido. Quantum dot networks in dielectric media: from compact modeling of transport to the origin of field effect luminescence. *Nanotechnology*, 20(15):155201, 2009.

[32] A. Basu, Sheng-Chih Lin, C. Wasshuber, A.-M. Ionescu, and K. Banedee. A comprehensive analytical capacitance model of a two dimensional nanodot array: cellular neural net application. In *Quality Electronic Design, 2004. Proceedings. 5th International Symposium on*, pages 259–264, 2004.

[33] R. Penrose. A generalized inverse for matrices. *Mathematical Proceedings of the Cambridge Philosophical Society*, 51:406–413, 7 1955.

[34] W. Kohn and L. J. Sham. Self-consistent equations including exchange and correlation effects. *Phys. Rev.*, 140:A1133–A1138, Nov 1965.

[35] X. Gao, D. Mamaluy, E. Nielsen, R. W. Young, A. Shirkhorshidian, M. P. Lilly, N. C. Bishop, M. S. Carroll, and R. P. Muller. Efficient self-consistent quantum transport simulator for quantum devices. *Journal of Applied Physics*, 115(13):–, 2014.

[36] D. D. Johnson. Modified broyden's method for accelerating convergence in self-consistent calculations. *Phys. Rev. B*, 38:12807–12813, Dec 1988.

[37] Donald G. Anderson. Iterative procedures for nonlinear integral equations. *J. ACM*, 12(4):547–560, oct 1965.

Chapter 4

Study of the electronic transport in Silicon QDs

In this chapter, we use the previous developed formalism and its code implementation, the SimQD code, to simulate different systems based on silicon quantum dots (Si QDs) embedded in a SiO_2 matrix (Si/SiO_2 QDs). First of all, we show the shape of the obtained density of states (DOS) using the Effective Mass Approximation (EMA). As this approximation has several limitations and can not reproduce exactly realistic DOSs, we introduce the possibility to use the density functional theory (DFT) to describe the electronic properties of the QDs; opening the possibility to use the DOS of the QDs as an input parameter. In the second part, we obtain the I(V) and the accumulated charge curves for a single QD in different configurations. The simulations of large systems based on multilayer structures are also presented reflecting the capability of the here presented transport model to deal with experimentally relevant structures. Once the transport features for Si/SiO_2 systems are explained, potential applications of these systems are studied: the single electron transistor and the double gate transistor. In the last section, a comparison with experimental results and with other macroscopic transport models is done. Moreover, we present the possibility to use the transport model to describe ballistic transport through material traps or defects.

4.1 From DOS to current: preliminary discussion

In Chapter 2, we have described a general theoretical framework to calculate the electrical response of a system based on QDs. The total tunneling current incoming from left lead to all the QDs can be written as

$$I = \frac{4\pi q}{\hbar} \sum_i \int T_{Li}(E)\rho_L(E)\rho_i(E)(f_L(E) - n_i(E))dE, \tag{4.1}$$

where the subscript i corresponds to the ith QD. The total current that crosses the whole device can be obtained summing all the individual currents through each QD, since we do not consider direct current between the two electrodes.

Up to now, we have not introduced the nature of the leads. The final response of the system is strongly dominated by the injection properties of the carrier reservoirs (leads). As we are interested in the transport properties of the QDs and in order to present clearly the different features of these systems, we treat the electrodes as infinite metallic contacts well described using the Fermi Dirac distribution function. Moreover, we assume a constant DOS in the leads.
Concerning the DOS of the QDs, we have used the approximation described in the previous chapter, the EMA. Although this approximation gives a discrete spectrum of energy states, it fails to reproduce all the internal structure of the QD, and the most important issue is how to include the degeneracy of the energy levels. Up to now, we only considered spin degeneracy but it is well known that there are other degeneracies associated to the quantum numbers, i.e. for the $l \neq 0$ cases, each state is $2l + 1$ degenerated.

Since the values of the used DOS (lead and QD) are only qualitative and not quantitative, the obtained current values can not be directly compared to experimental results. We restrict our calculations to a number of QDs embedded in an oxide block of given dimensions. Therefore, to compare directly the simulations and the experimental results the QD density has to be known. Thus, although Eq. 4.1 has units of current (A), it can not be directly compared to experimental current values. Then, we try to reproduce the measured experimental trends and features instead of the measured values.

4.2 Running the simulations

In this chapter, we are going to show several results from different QD arrangements simulated using the implemented code, the SimQD. As we saw, the code only needs two types of inputs: the device description (oxide size, disposition and QD number) and the material parameters to describe the QDs, the oxide matrix and the tunneling processes.

4.2.1 Device description

First of all, we must define the system: the geometrical disposition of the QDs and the size of the embedding oxide. Here, the most important dimension, which will dominate the value of the current, is the length of the device, since the tunneling current decreases exponentially with the tunneling distance. In order to avoid future confusion we assume: x-direction (length), y-direction (width) and z-direction(height). The transport direction

is in the x-direction and the leads are placed in the y-z plane ($x = 0$ and $x = L$ where L is the device length).

4.2.2 Material parameters

Up to now, we have proposed a transport model to simulate the electrical behavior of a device based on QDs. Here, we are going to focus on the specific case of silicon QDs (Si QDs) embedded in a SiO_2 matrix (Si/SiO_2 QDs). The inputs needed to describe this system are the material constants given in Table. 4.1.

m^*_{ECB} (m_0)	0.40 [1, 2]	$\phi_{1,ECB}$ (eV)	3.1 [3, 4]
m^*_{EVB} (m_0)	0.30 [1]	$\phi_{1,HVB}$ (eV)	-4.5 [3, 4]
m^*_{HVB} (m_0)	0.32 [1]	E_{gap} (eV)	1.12 [3, 4]
$m^*_{Qd,CB}$ (m_0)	0.33 [5]	ε_{rSiO_2} (ε_0)	3.9 [4, 6]
$m^*_{Qd,VB}$ (m_0)	0.28 [5]	$\varepsilon_{rSi}(\varepsilon_0)$	11.7 [4, 6]

TABLE 4.1: Parameters used in the simulation in order to describe Si QDs embedded in SiO_2 insulator matrix.

m^*_{ECB}, m^*_{EVB} and m^*_{HVB} are the effective masses for the different tunneling processes (see the previous Chapter). $m^*_{Qd,CB}$ and $m^*_{Qd,VB}$ are the geometric averages of the anisotropic Si bulk effective masses for the electrons and holes [7]. $\phi_{1,ECB}$ is the electron confinement potential whereas $\phi_{1,HVB}$ is the one for the holes. E_{gap} is the bulk Si band gap and we assume that the Fermi level is placed in the middle. We must note that the position of the Fermi level is an important point, since it modifies the energetic distance between the zero energy level and the first electron and hole energy levels.

Although the electron and hole energy levels position depends on the parameters presented in Table. 4.1, the HOMO (first hole energy level) and the LUMO (first electron energy level) are placed approximately at the same energy distance respect to the Fermi level. This means that when an external voltage is applied both energy levels will start to conduct at the same time. Moreover, in these energy levels the charge will change (filling the electron level and emptying the hole one). This effect can be changed moving the position of the Fermi level, if the Fermi level is close to an electron state it will start to conduct before the hole state. The similar case is obtained for the Fermi level close to the hole state, the hole state will conduct before the electron one. Thus, the alignment of the QD Fermi level and the leads is not a trivial question and will govern the current and charge trends.
On the other hand, the difference position between the Fermi levels of the leads and the oxide matrix defines the electron and hole energy barrier. Thus, the material parameters have to be changed as a function of the simulated system.
Finally, ε_{rSiO_2} and ε_{rSi} are the dielectric constants of the bulk SiO_2 and Si, respectively.

In order to focus on the intrinsic properties of the electron transport through the QD array, we have assumed a continuous DOS for the leads. Therefore, the leads act as an infinite carrier reservoir.

4.2.3 Example with the Effective Mass Approximation DOS

Since the materials that form the QDs (Si) and the surrounding insulator matrix (SiO_2) are well described, we can use the EMA and the finite spherical confinement potential to obtain the energy binding states that define the discrete energy spectra of the QDs. From the previous chapter, we use the following equation to obtain the electron binding energy levels

$$\cot x = -\sqrt{\frac{m^*_{ECB}}{m^*_{Qd,CB}}}\sqrt{\left(\frac{\sigma_0}{x}\right)^2 - 1}, \tag{4.2}$$

where $\sigma_0 = \sqrt{\frac{2m^*_{ECB}\phi_{1,ECB}}{\hbar^2}R^2}$ and $x = \sqrt{\frac{2m^*_{ECB}E_0}{\hbar^2}R^2}$. E_0 is the electron energy binding states. For the hole case, we use m^*_{HVB}, $\phi_{1,HVB}$ and $m^*_{Qd,VB}$.
An example of the obtained DOS for a QD of radius $R = 1$ nm, where the discrete energy levels have been broadened, is presented in Fig. 4.1. The confinement potentials, the bulk Si band gap and the position of the equilibrium Fermi level are also shown. Moreover, as a first approximation we have assumed a continuous DOS for energies above the confinement potentials of the insulator matrix. This fact reflects the continuous energy level spectra out of the confinement region.

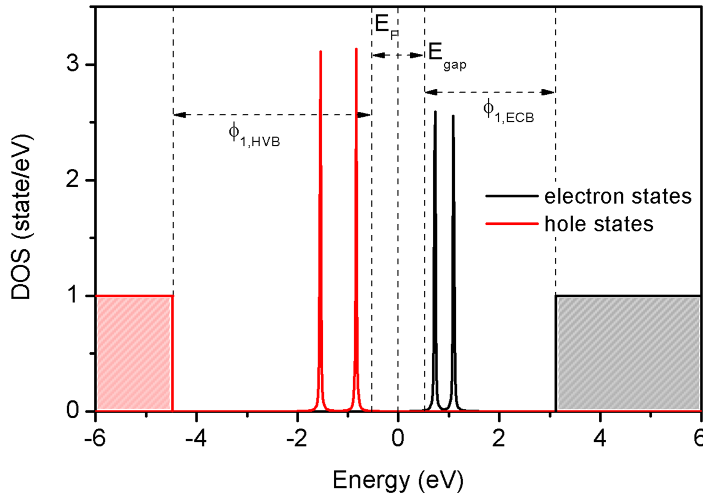

FIGURE 4.1: Obtained DOS for a QD of R=1nm. The broadened binding electron and hole states are shown. The position of the Fermi level E_F (zero energy point), the confinement potentials $\phi_{1,ECB}$ and $\phi_{1,HVB}$ and the Si bulk band gap E_{gap} are also shown. For energies above the confinement potentials, continuous DOSs are assumed.

On the other hand, from Eq. 4.2 the energy position of the electron and hole energy levels are dependent on the QD radius. Obtaining the well know relation between the

QD energy gap and the QD radius. Besides, the number of binding states increases with the QD radius.

4.2.4 Example with Density Functional Theory inputs

Up to now, we have described the electrical properties of the QDs using the simply model based on the finite spherical potential well within the EMA. As we have seen, this approximation allows us to deal with discrete energy levels. This approximation also reproduces the well know dependence of the E_{gap} with the QD radius, as we will see in the next chapter.
From the proposed transport model, the DOS of the QDs (the energy level spectra) only appears in the calculation of the tunneling currents and the QDs charge. In fact, since we have presented a general carrier transport method the QD DOSs can also be viewed as another input parameters. Hence, we can use other approaches in order to describe the QDs electronic properties.

Here, we discuss briefly the inclusion of Density Functional Theory (DFT) outputs as inputs for our transport model. This work has been presented in Ref. [8] and all the details of the DFT simulations conform the PhD Thesis of Dra. Núria García-Castelló.

As in any atomistic calculation, the main work can be decomposed in two fundamental parts: the construction of the structure under simulation and the structure relaxation. The relaxation process moves the initial atomic positions in order to find the minimum energy configuration of the system. Two types of structures have been studied: the β-cristobalite SiO_2 and amorphous SiO_2. All the structures have been obtained from the supercell $Si_{216}O_{432}$. The QD is created removing all the O atoms inside a cutoff sphere of given radius. The relaxations of all the systems and the calculation of the DOS have been computed with the DFT code SIESTA [9, 10]. Due to the large computational time needed to relax these structures, only a few cases have been studied. Different QDs have been created in the crystalline and amorphous SiO_2 matrices ranging from $1.27nm$ to $1.60nm$ of QD diameter.

The projected density of states in the atoms that forms the QDs has been calculated and it was compared to the embedding SiO_2 matrix DOS. From this direct comparison, the confinement potentials (band offsets between the conduction and valence bands of the Si/SiO_2 interface) can be obtained. The main results as functions of the QD diameter can be summarized as:

- The band offsets increase with the QD size (more pronounced for valence band than for conduction band) consistently with the planar value corresponding to the bulk case.

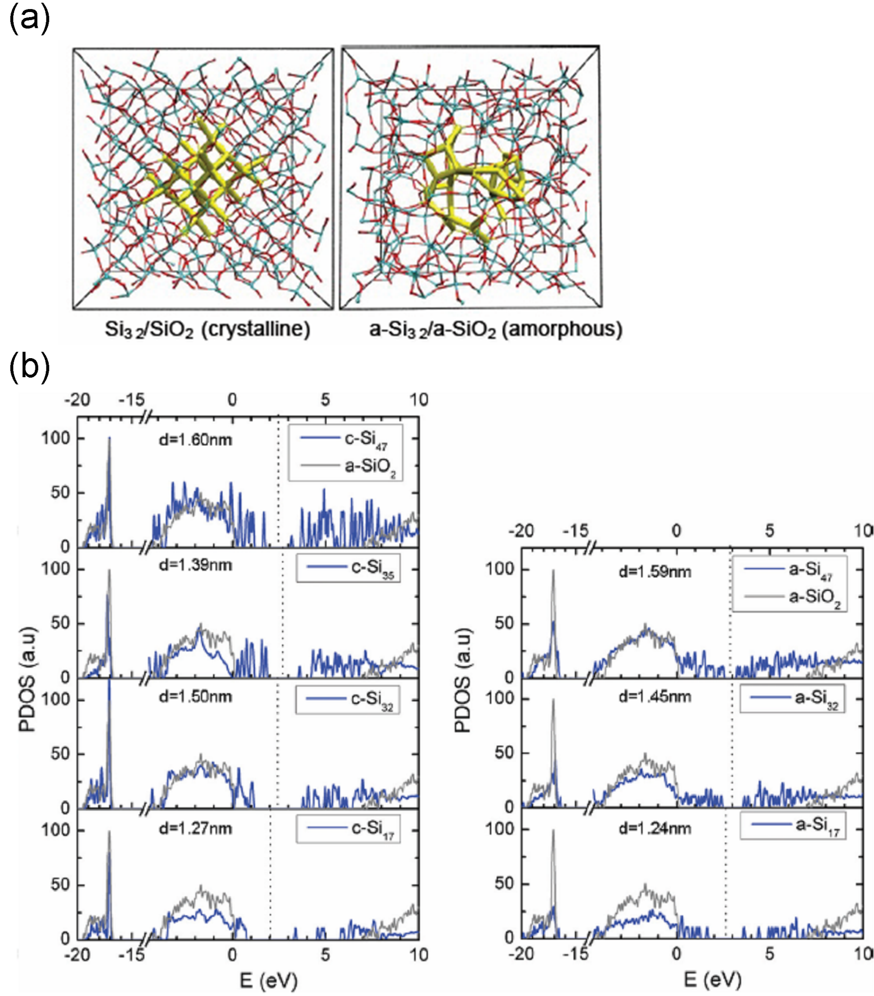

FIGURE 4.2: (a) Relaxed structure of the QD of 32 Si atoms in crystalline (left panel) and amorphous (right panel) SiO_2 matrix. Red spheres are O atoms, green spheres are Si atoms and the yellow thick sticks represents the Si atoms that form the Qd. (b) Simulated DOS using DFT for different Si QD sizes embedded in amorphous a- or crystalline c- SiO_2 matrix. The subscript is the number of Si atoms that form the QD. For comparison, the amorphous silica (a-SiO_2) is shown in all the plots. From this comparison, the band offsets for each QD radius can be obtained. The figures have been taken from Ref. [8]. The position of the Fermi level is the vertical dashed line and it is located in the middle of the QD E_{gap}.

- In crystalline systems, the valence band offsets are lower than in the amorphous ones for similar QD diameters. In contrast, for the conduction band offsets, a clear trend is not observed.

- In a general trend, E_{gap} decreases when the QD size increases. Some fluctuations in the expected trend were found due to the oxidation degree at the interface and the strain induced by the embedding matrix. Due to the small size of the QDs, they are basically formed by surface atoms and the embedding matrix has a strong influence in the QD properties.

To conclude the DFT study, the obtained DOS (see Fig. 4.2) have been used to simulate the charge transport in a single QD. We are not going to reproduce here again the obtained results because, as we have seen previously, the current basically represents the DOS of the QD. The I(V) curves are presented in Ref. [8].

Thus, we have shown the possibility to combine two different simulation techniques to obtain the electronic transport. We use the realistic and complete description that the DFT provides of the electronic structure of the QD and then, the obtained DOS is used as an input to the here presented transport methodology. Although there are other codes that treat to solve the electronic transport from DFT calculations using NEGFF, such as TRANSIESTA [11], and the transport module of GPAW [12], the atomistic procedure is infeasible for large systems. Thus, our model is perfect to combine the realistic description of the QDs within DFT codes and the large system capability of the transport model in order to simulate devices based on QDs.

4.3 One single Si/SiO_2 QD

Before simulating a complete device based on large arrays of QDs, we are going to describe a single Si/SiO_2 QD in different configurations. From this small system, we will show the general trends obtained for the current voltage curves (I(V)) and the accumulated charge.

In Fig. 4.3, we present the obtained I(V) curves and the accumulated charge for a system composed of: two leads separated by 5nm and a single QD of $R = 1.5$ nm connected to them at different positions. The position of the QD x is measured from the left lead. An external bias voltage is applied to the right lead, whereas the left one is kept as a reference, this means $\mu_L = 0$ and $\mu_R = -qV$. Concerning the variation of the number of electrons ($\triangle N = N - N_0$), it reflects the variation of electrons (N) respect to the initial number (N_0). Therefore, if the variation is negative, it implies that the system looses charge (hole accumulation). If the variation is positive, this implies that the system increases its charge (electron accumulation). Concerning the values of the charging energy U_0, it is around tens of meV similar to the thermal energy ($T = 300$ K) being in the self-consistent field regime.

Fig. 4.3(a) shows the total I(V) curve and the hole and electron currents for a QD connected symmetrically to both leads, $x = 2.5$ nm. Concerning the partial currents (electron and hole contributions), the electron current is the dominant term since the electron barrier (3.1 eV) is smaller than the hole barrier (4.5 eV). Besides, the opening of the discrete electron/hole conductive channels are clearly visible in the current steps at different voltages due to the position of the discrete electron/hole energy levels. Since the system is symmetrically coupled to the leads, the total current is symmetric in both polarization directions. From the I(V) curves, we must note that negative differential

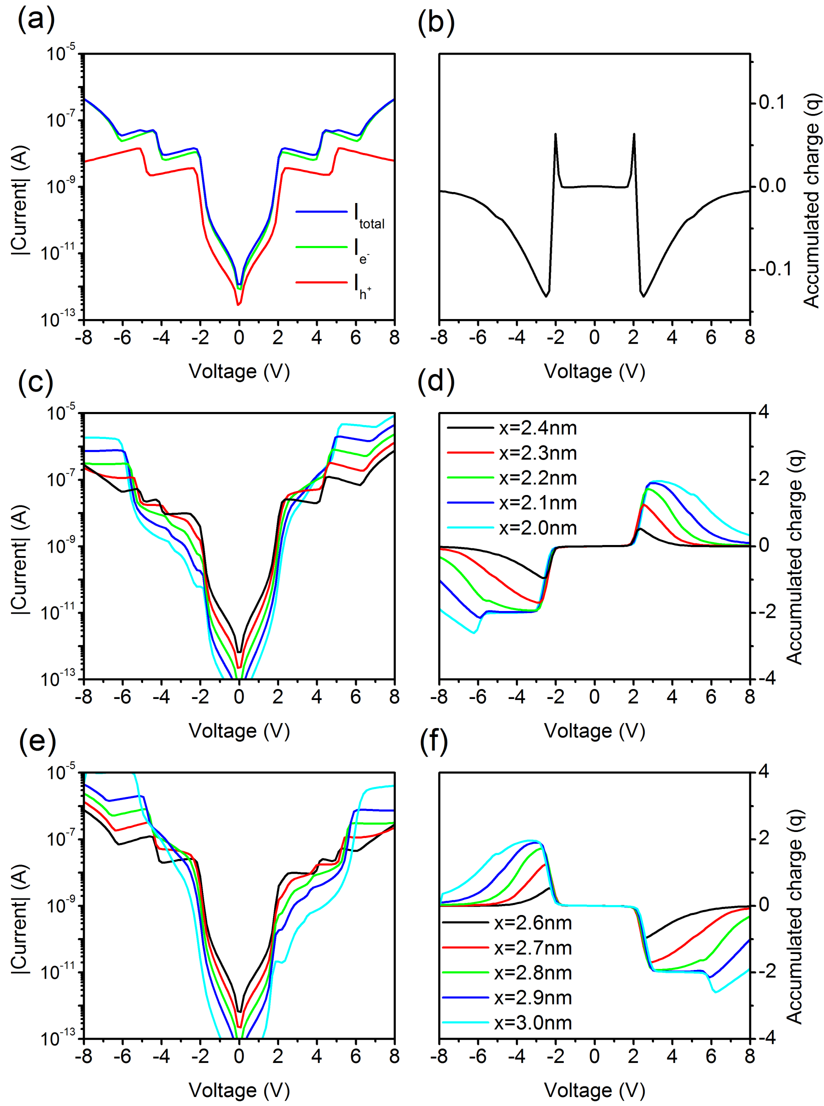

FIGURE 4.3: A single Si/SiO_2 QD of $R = 1.5$ nm placed in different positions between the two leads. x is the distance from the left lead to the center of the QD. The separation among the leads is 5 nm. (a-b) I(V) curve and accumulated charge for a centered QD. The hole and electron currents are also shown. (c-e) I(V) curves for different QD positions and (e-f) accumulated charge in the same cases.

resistances (NDR) are obtained. The nature of this effect is different from the other cases that we have seen previously (the decreasing of the QD DOS overlap). In this case, the NDR is obtained because the transmission coefficients are energy dependent and the ratio between the right and left lead couplings changes as a function of the applied bias voltage.

Regarding to the accumulated charge, Fig. 4.3(b), the QD remains practically uncharged. The obtained trend reflects the position of the electron and hole energy states respect to the equilibrium Fermi level and the effect of the self-charge. An electron state is the first energy level that starts to be conductive but a hole conductive channel is

opened immediately being the accumulated charge the difference of the electron/hole filled states.

The I(V) curves and the accumulated charge are shown in Fig. 4.3(c-d) and Fig. 4.3(e-f) for different non-symmetric configurations $x < 2.5$ and $x > 2.5$, respectively. As can be seen, the symmetry in the total I(V) curve has been broken due to the different capacitive coupling among the leads, as we studied in Chapter 2. The QD gains/losses net charge. We are going to explain this effect in the next section. Besides, we must note that the obtained trends for the $x < 2.5$ cases are complementary to the $x > 2.5$ cases.

4.3.1 Accumulated charge trends

From the band diagram scheme of the system under study, and taking into account that the transmission coefficients are strongly dependent on the width and the height of the barrier, the accumulated charge trends obtained in the previous section can be explained.

As we have seen before, when an external polarization is applied different incoming/outgoing fluxes are created and the occupation of the states differ from the initial case. Besides, the transport only takes place in the energy region between μ_L and μ_R. Thus, only the energy states placed in this energy region can gain or lose charge.
From the rate equation, the QD steady state distribution function can be viewed as a balance between the two leads that strongly depends on the transmission coefficients and the occupation of the leads. Since the leads occupation are well described by the electrochemical potentials $\mu_{L(R)}$, the QD energy level occupation is dominated by the highest transmission coefficient. Therefore, the lead connected to the QD with the highest transmission coefficient dominates the QD occupation.

In Fig. 4.4(a-b), the band diagram schemes for both polarization regimes ($V > 0$ and $V < 0$) and $x < 2.5$nm are shown. The discrete electron (blue) and hole (green) states are also represented. In equilibrium, the hole states are filled, whereas the electron states are emptied. However, under external bias polarization net fluxes are created. Therefore, for low voltages, the width of the barrier dominates the transmission since the oxide bands are still not enough bended. Thus, the position of the QD (x) is crucial. In the band scheme, the highest transmission coefficient is represented by wider arrows. For the $x < 2.5$ nm case, the QD is strongly connected to the left lead and its occupation is governed by μ_L: increasing the QD charge (electron accumulation) for $V > 0$ and loosing charge (hole accumulation) for $V < 0$ case.
The $x > 2.5$ nm case can be explained using the same arguments but now, the occupation of the QD is governed by μ_R (Fig. 4.4(c-d)). The hole accumulation is obtained for the $V > 0$ case, whereas the electron accumulation appears for $V < 0$.

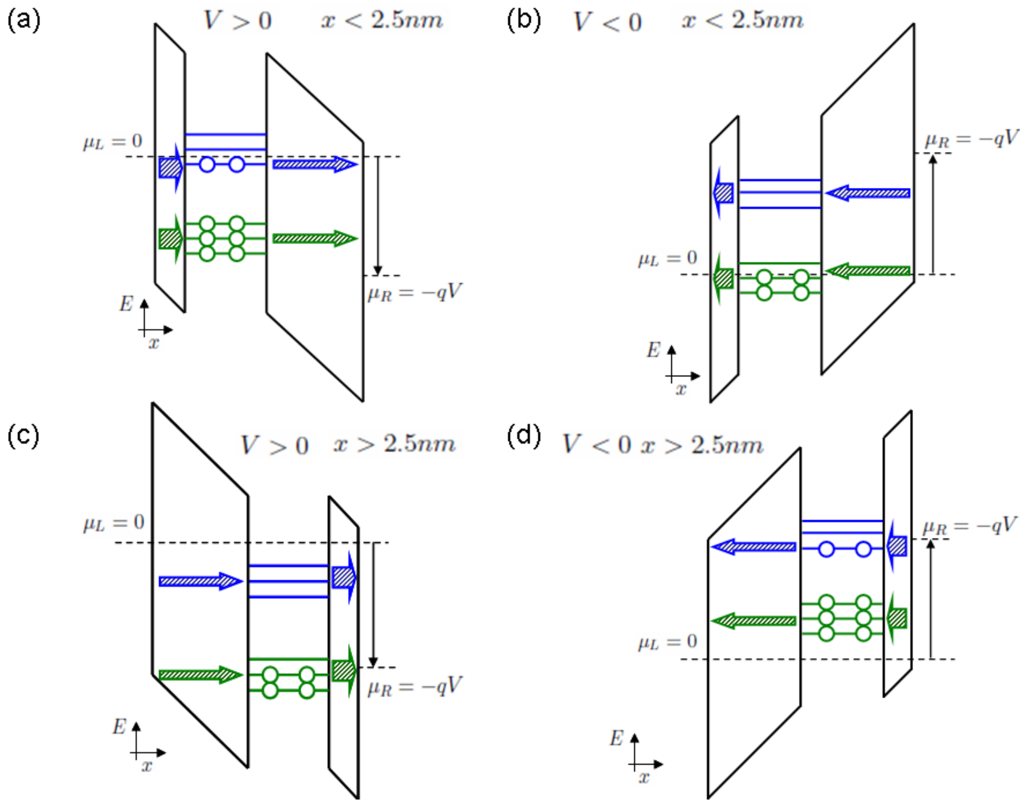

FIGURE 4.4: Band diagram scheme of the single Si QD in different positions (x) and bias polarizations ($V < 0$ and $V > 0$). The thinnest arrows represent a lower transmission probabilities whereas the widest ones are the most probable transmissions. The conduction window, $\mu_L - \mu_R$, and the several electron (blue lines) and hole (green lines) energy levels are also shown. (a) and (d) reflect an electron accumulation regime whereas in (b) and (c) the QD losses part of its initial charge (hole accumulation).

From these analysis, the obtained accumulated charge curves presented previously (Fig. 4.3(d-f)) can be explained. Nevertheless, for larger voltages the band bending of the wider oxide increases giving an smaller effective tunneling distance and being that the dominant process. Thus, the QD recovers its initial charge.

4.4 Multilayered structures

In order to present the capabilities of the here presented methodology and the possibility to simulate realistic devices based on large arrays of QDs, we are going to present several simulations of QDs distributed in a multilayer structure. We focused on this arrangement because from the fabrication process it emerges as the most fundamental structure.

From the experimental point of view, in the last decade, the superlaticce approach (SL) [13] was developed to create Si QDs embedded in SiO_2 matrices. Thin silicon

rich oxide and thin pure SiO_2 layers are deposited alternatively by means of plasma-enhanced chemical-vapor deposition (PECVD) making feasible that the SiO_2 layers act as a diffusion barrier. In a latter temperature annealing process, the Si atoms of the silicon rich oxide layer aggregate and form the QDs. The different growth stages of the Si QDs are well described in Ref. [14, 15, 16], being the final physical properties of the layers strongly dependent on the annealing conditions [14, 15, 17]. Overall, a relative broad Si QD size distribution is obtained and it is usually fitted with Gaussian or log-normal distributions [17, 18]. Therefore, a tight control of the Si QD size can be easily obtained by adjusting the inter-distance of the SiO_2 diffusion barriers, allowing for a self-organized array of size-controlled Si QDs embedded in a SiO_2 matrix.

Here, we present the I(V) and the total accumulated charge for two simulated systems in a multilayer structure. The structure is formed by 2 Si QD layers. The leads are placed perpendicular to them, therefore, the electronic transport takes place laterally. Both layers are spaced 5nm and the layer size is 20 nm length and 20 nm width. We simulate 10 randomly distributed QDs per layer and a normal distribution with 1.75 nm mean value, and 0.3 nm standard deviation for the QDs radii. The Qds layers are separated by 3 nm of SiO_2.

In Fig. 4.5, the obtained results are shown for the two different systems. The I(V) curves and the electron and hole currents are presented in Fig. 4.5(a-c); in the inset, we also show the QD radius distribution for each system. Besides, in Fig. 4.5(b-d) the accumulated charge and a top view of the structure (inset) are presented.

Before explaining in detail each case, we are going to focus on the common aspects of the obtained results. Concerning the I(V) curves, the step-like current shape is still present since it is a consequence of the opening of the conductive channels. In these cases, the transport involves several tunneling processes between the QDs. Therefore, the energy level alignment is necessary. However, the NDR is not clearly visible since there are many electron/hole pathways and the sum of the different conduction channels masks this effect.
From the I(V) curves, two different regimes are obtained. For low and medium voltage ranges, the current reflects the discrete nature of the QDs energy spectra. However, for the largest voltages, the continuous part of the QD DOS begins to be conductive and the current increases in a continuous form loosing its step-like shape. Concerning the electron/hole current components, the electron term dominates since its potential barrier is lower than the hole one.

Regarding the accumulated charge plotted in Fig. 4.5(b-d), it is the total sum of the accumulated charge in each QD (q $\sum_i \triangle N_i$ where i=1..20). The geometrical disposition of the QDs strongly affects the final response of the system. However, the two main trends discussed in the previous section are obtained: electron accumulation for positive voltages (first system) and hole accumulation for positive voltages (second systems).

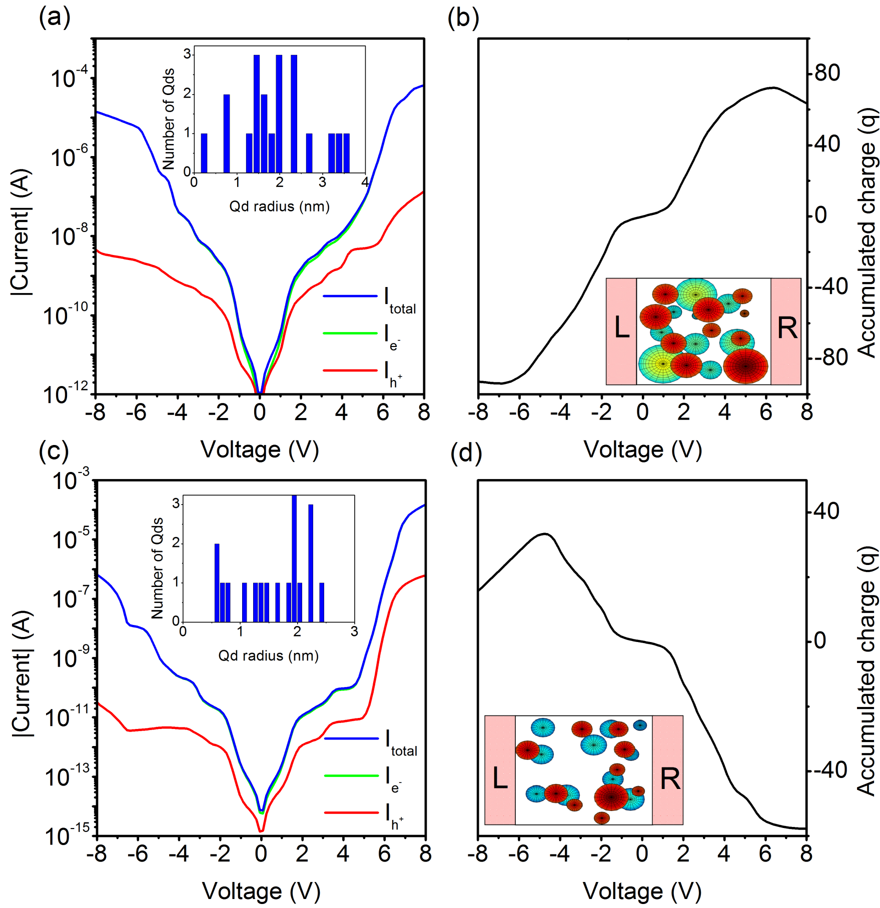

FIGURE 4.5: (a-c) Obtained I(V) curves for two layers of Si/SiO_2 QDs (the systems details are described in the text). The total current as well as the electron and hole partials currents are also shown. In the inset, the QD radius distributions are shown. (b-d) Total accumulated charge ($\sum_i \triangle N_i$, where $i = 1..20$) of the structures as a function of the external bias voltage. In the inset, a top view of the systems are presented where the left and right leads are L and R, respectively.

For these systems, since there are many electronic conduction channels and a complex capacitive interaction between the QDs, it is hard to explain clearly the accumulated charge trends. Reflecting that, the geometrical disposition of the QDs influences directly in the final response of the system.

4.5 Electronic devices based on QD

Up to now, we restrict our simulations to systems in witch the QDs are connected to two electrodes (source and drain). However, it is possible to include a third electrode (gate) to create a gate controlled or gated QDs. These systems have attracted much interest in both physics [19, 20, 21, 22] and quantum engineering [23, 24, 25] since the properties of the confined electrons can be modified by the external gate voltage. The gated QD

is a very important nanoelectronic device because it is a prototype of a single-electron transistor (SET) [23, 26, 27, 28]. Possible applications of SETs are expected to yield an extremely high speed of nanoelectronic devices at low power consumption. Another exciting field of future applications of electrostatics QDs is quantum computation [29, 30, 31, 32]. The QDs can be used to represent quantum bits (qubits) [33, 34, 35] and to perform a readout of qubits as well as logic operations on the qubits, the so-called logic gates [36, 37, 38]. Other possible applications of these kind of systems are: as a single electron pumps [28, 39], as a temperature standards [40, 41], resistance standards [42] and supersensitive infrared radiation detectors [43, 44].

Concerning the SET, it is a highly charge-sensitive device capable to detect charge variations of one electron. This remarkable property allows SETs to be used as extremely responsive electrometers, making them a useful tool in experiments where very high charge sensitivity is required [45, 46]. A SET fabricated on the tip of a scanning probe has been reported [47] creating a new type of scanning microscopy, combining submicron spatial resolution with sub-single-electron sensitivity. This technique has been used to observe single charged impurities in GaAs/AlGaAs heterostructures. Another attractive possibility is the ability to measure addition energies (and hence the energy level distribution) in QDs and other nanoscale objects [48]. Respect to the applicability of this device to digital electronics, the basic application is use it as a usual FET transistor controlling with the gate voltage the high/low current states. Moreover, several concept memories have been developed taking advantage of the transport properties of this system [49].
While in the previous section we have described the transport processes in an extended array of QDs, now, we are going to deal with a prototypical application of these kind of systems: the SET.

4.5.1 Transistor structure: the single electron transistor

The transistor structure includes metallic source and drain electrodes bridged by a QD (metallic, semiconductor or a molecule) plus a gate electrode. Although we consider the QDs as particles created inside an embedding matrix, the first device was created using two confining electrodes and a MOS type structure, in order to achieve the 3D confinement of the carriers in a small space region [23].

The electron transport is carried by sequential tunneling through the QD coupled by tunneling junctions to the source and drain. Besides, the QD is capacitive coupled to the gate electrode which is used to shift the QD energy levels and control the charge transfer. The electron transfer between the QD and the gate electrode is assumed negligible. Two main approaches have been used to describe the device working principle: the classical Coulomb blockade regime and the quantum Coulomb blockade [50], for metallic

or semiconductor respectively. In the quantum Coulomb blockade, the discrete energy spectra of the QD is also included [23, 51].

The transport mechanism in the transistor is as follows: when there is no energy level of the QD between the Fermi levels of the source and drain leads, electron transport through the device is blocked, leaving the number of electrons, N, in the QD unchanged. In the quantum Coulomb blockade, in which the charge is an integer, when the energy level plus the charging energy lies in the conductive region the electron transport takes place, and the charge is increased (N+1). The resultant transport suppression is called the Coulomb blockade. However, the Coulomb blockade may be lifted by applying voltage to the gate electrode, which adjusts the QD electrostatic potential. However, as we discussed in chapter 1, in the SCF regime the condition that the charge is an integer is not considered being the transport condition less restrictive and the current is not suppressed. Nevertheless, the charging energy is included in the solution of the Poisson equation being the local potential in the QD the same when the charge is an integer value.
The main differences between our model and the orthodox Coulomb blockade is seen in metallic QDs in which the energy levels form a continuous spectra. In this situation, each time that one electron crosses through the QD it has to overcome the charging energy and the current increases once this condition is reached. This situation plus the condition of the charge has to be an integer make that the current increases in discrete steps, i. e., the current is blocked until the condition is satisfied.

4.5.2 Device simulation

In order to simulate a transistor device based on QDs, we need to include the third electrode: the gate. We consider that the gate electrode only changes the local potential (i.e, moves the DOS) of the QD and injects no current. This new term in the Laplace solution is included as $-C_{gate,i}/C_{tot,i}(-qV_{gate})$, where V_{gate} is the applied gate polarization and $C_{gate,i}$ is the capacity coupling between the gate electrode and the ith QD. Moreover, $C_{gate,i}$ is also included in the $C_{tot,i}$.

What follows is the discussion of the transistor structure in a device formed by a single Si/SiO_2 QD. The scheme of this structure is shown in Fig. 4.6(a), the band diagram is shown in Fig. 4.6(b) under no external polarizations and in Fig. 4.6(c-d) under negative and positive gate polarization, respectively. The local potential in the QD can be written as

$$U = \frac{C_s}{C_{tot}}(-qV_{ds}) + \frac{C_{gate}}{C_{tot}}(-qV_{gate}) + \frac{q^2}{C_{tot}}\triangle N, \tag{4.3}$$

where C_s is the capacity coupling to the source (we consider that the drain is fixed to the ground). As we have studied in the chapter 2, the transport takes place when an

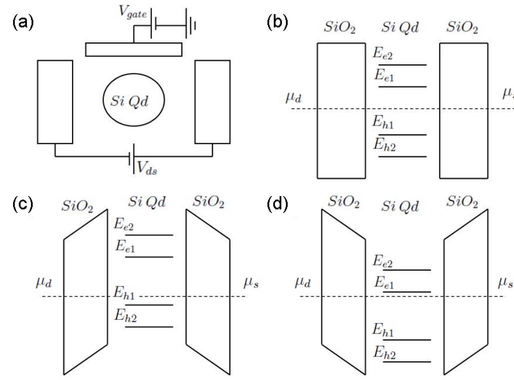

FIGURE 4.6: (a) Structure of the system under consideration. The scheme shows the three electrodes (source, drain and gate) and the QD is placed in the middle. The QD is connected with the source and drain by 1nm and 2nm tunnel junctions respectively. The QD radius is 1nm. The gate electrode is placed at 7.5nm distance from the center of the QD. This tunneling distance justifies the assumption that the current between the QD and the gate is negligible. (b) Band diagram of the structure without applied voltage, under negative gate polarization (c) and under a positive gate polarization (d). The oxide barriers, the equilibrium Fermi level and the electron and hole energy levels are also shown.

energy level of the QD lies in the conductive channel ($\mu_d - \mu_s = qV_{ds}$). Thus, from Eq. 4.3 this condition can be achieved by combination of V_{ds} and V_{gate}.

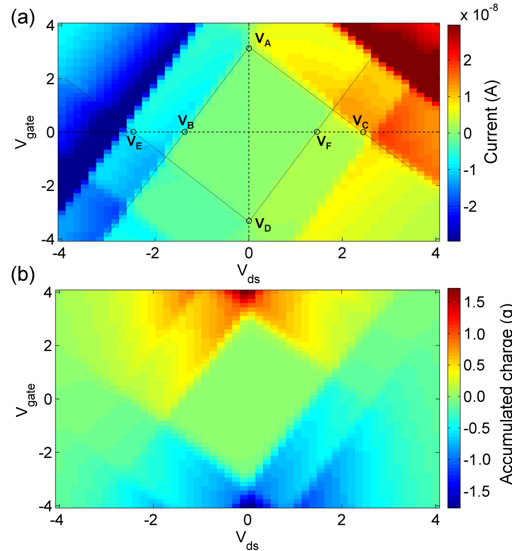

FIGURE 4.7: (a) Current map as a function of the applied V_{ds} and V_{gate}. Current suppression is obtained until the energy levels are placed between the electrochemical potentials of the drain and source (μ_d and μ_s). Once a conducting energy level is open the current increases dramatically. Important voltage points are also highlighted. (b) Accumulated charge ($q\triangle N$) in the QD map as a function of the applied voltages.

In Fig. 4.7(a), the current is shown as a function of V_{ds} and V_{gate}. For small $V_{ds} \approx 0$, the current is blocked until the first energy level is placed between the electrochemical potentials as a result of the applied V_{gate}. For the $V_{gate} \approx 0$ case, the explanation is

similar but in this case only V_{ds} contributes to the local potential. Therefore, the current is blocked until the previous condition is achieved. This effect corresponds to the central *diamond*. The shape of the current *diamonds* is related to the relationship between the different capacity values and the position of the energy levels. Once an energy channel is open, the current increases. Several *diamond* structures are obtained when the electron, hole and both energy levels contributes to the current [23, 52].

Several important voltage points are remarked in the current map (A, B, C, D, E, F). We can write the evolution of the first electron and hole energy level for these voltage points neglecting the charge term of the Poisson solution as

$$\begin{aligned}
(A)\;\; E_e - \frac{C_{gate}}{C_{tot}} V_A = 0 \\
(B)\;\; E_e - \frac{C_s}{C_{tot}} V_B = -V_B \\
(C)\;\; E_e - \frac{C_s}{C_{tot}} V_C = 0 \\
(D)\;\; E_h - \frac{C_{gate}}{C_{tot}} V_D = 0 \\
(E)\;\; E_h - \frac{C_s}{C_{tot}} V_E = -V_E \\
(F)\;\; E_h - \frac{C_s}{C_{tot}} V_F = 0
\end{aligned} \tag{4.4}$$

where E_e and E_h are the first electron and hole energy levels, respectively. The (V_A) and (V_D) points correspond to the energy levels cross the equilibrium electrochemical potentials of the leads whereas the other points reflect that the energy levels enter in the conductive channel for positive (V_C, V_F) and negative (V_B, V_E) bias voltages. From these voltage points, the value of the first electron and hole energy levels as the different capacitive couplings can be obtained. Therefore, this kind of structures can be used to make an energy level spectroscopy of the QD [23].

We also show the QD accumulated charge ($q\triangle N$), Fig. 4.7(b). The QD remains uncharged in a large region since the energy value of the electron and hole energy levels are similar. Therefore, the QD begins to charge when the electron transport is the dominant processes. If the hole conduction is preferred, the QD losses its initial charge. Applying V_{gate} the charge in the QD is also changed. The physical process is different, as V_{gate} moves upward/downward the energy levels across the electrochemical potentials of the leads and the QD losses/gains charge [23].

4.5.3 QD array transistor

Now, we present the results for an array of QDs in a transistor structure. Since the the single QD transistor and the electron transport through an array of QDs embedded in the dielectric matrix have been previously presented, the following step is create a transistor structure but using several QDs. From an experimental point of view, the fabrication of this device (many QDs in a transistor structure) is easier than the single QD structure.

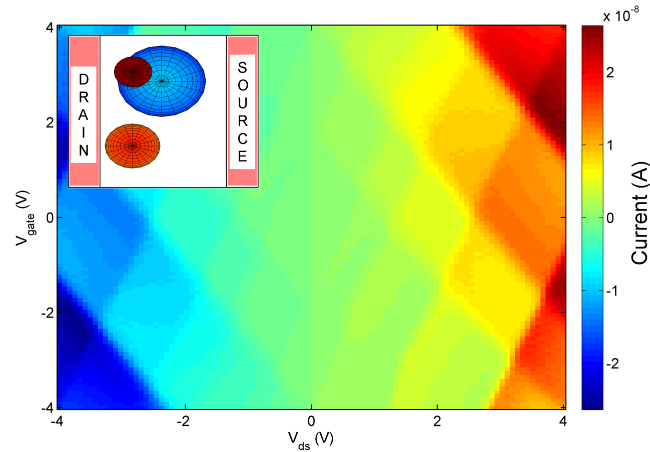

FIGURE 4.8: Obtained current map as a function of V_{ds} and V_{gate}. The single current diamonds corresponding to each QD are overlapped but they are still recognizable. In the inset, an scheme of the transistor device is presented. The system is formed by 3 Si QDs randomly generated inside the SiO_2 insulator matrix.

Keeping our model as general as possible, we assume a SiO_2 block of $15nm$ width, 4 nm length and 15 nm high where three Si QDs are embedded. The dielectric matrix is placed between two electrodes, source and drain, and a gate electrode is located at 15 nm on the top. A top view of the system is shown in the inset of Fig. 4.8. The current crosses the 4 nm of oxide where the QDs are placed and we neglect current from/to the gate electrode. The simulated current as a function of V_{ds} and V_{gate} is presented in Fig. 4.8. As we can see from the scheme of the system, the QDs are placed in a parallel configuration thus, the obtained current map is very similar to the single transistor structure. The single current diamonds corresponding to each QD are overlapped but they are still recognizable.

As we have demonstrated that the spatial arrangement of the QDs is a fundamental parameter that governs the final response of the system, we simulated different QD arrangements. In Fig. 4.9, we present another system composed by four Si/SiO_2 QDs. The size of the system is: 10 nm width, 9 nm length and 15 nm high. The gate electrode is located at $15nm$ on the top of the oxide. An scheme of the system is shown in the inset of Fig. 4.9. The current crosses the 9 nm of oxide where the QDs are placed and we neglect current from/to the gate electrode. Current suppression is obtained until

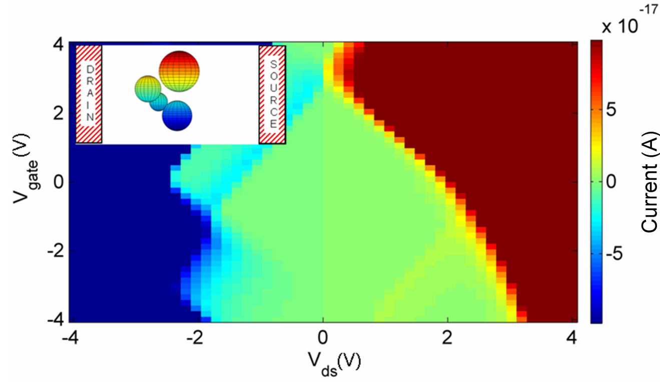

FIGURE 4.9: Obtained current map as a function of V_{ds} and V_{gate}. Current suppression is obtained until the energy levels lie between the electrochemical potentials of the drain and source. Once a conducting energy level is open, the current increases dramatically. In the inset, an scheme of the transistor device is presented. The system is formed by 4 Si QDs randomly generated inside the SiO_2 insulator matrix.

the energy levels lie in the conduction window. However, for this spatial configuration, the complete *diamond* structure is not recovered due to the many electronic transport pathways and the DOS overlapping condition.

4.5.4 Double gate transistor

To conclude the transistor-like structures based on QDs, we are going to study the next logical step: a transistor structure based on two QDs and two electrodes.

From a theoretical point of view, a complete review of the physics behind this kind of system is presented by van der Wiel *et al.* [53]. They described the electrical response for metallic and semiconductor double gate transistor in the linear transport regime using the classical theory (Coulomb blockade and quantum Coulomb blockade).

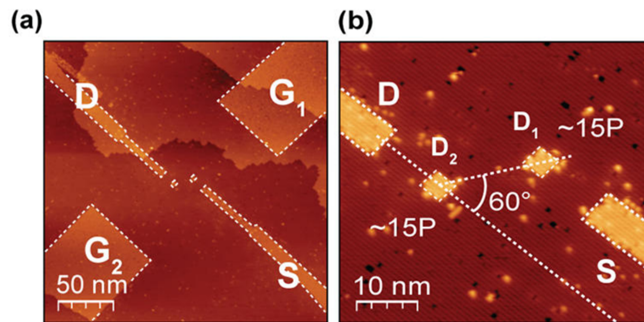

FIGURE 4.10: (a) STM image of the device showing the two QDs $D_{1(2)}$, tunnel-coupled to the source and drain (S/D) leads and capacitively coupled to the gates $G_{1(2)}$. (b) Close-up of the two QDs. Both figures have been extracted from Ref. [54]. Reprinted with permission from ACS.

From the experimental perspective, Bent Weber *et al.* [54] showed the possibility to create a double gate transistor based on QDs using lithographicall techniques [55]. Two QDs of ≈ 4 nm diameter separated by ≈ 10 nm from the drain and source, as well as two gate electrodes conform the whole experimental device. See Fig. 4.10(a) and (b) for a close-up image of the QDs. They demonstrated that each QD is electrically coupled to one gate and studied the best QD geometrical configuration. This structure is based on Si(001) layer in which the two QDs are created by selective P doping. The possibility to control the doping position and the limited diffusion of these atoms create the Si:P QDs. In order to fabricate the four electrodes, a process based on selective etching of the hydrogen resist monolayer that covers the whole structure and a subsequent exposure of this surface to phospine (PH_3) gas and posterior annealing treatment allows to create quasi-metallic leads.

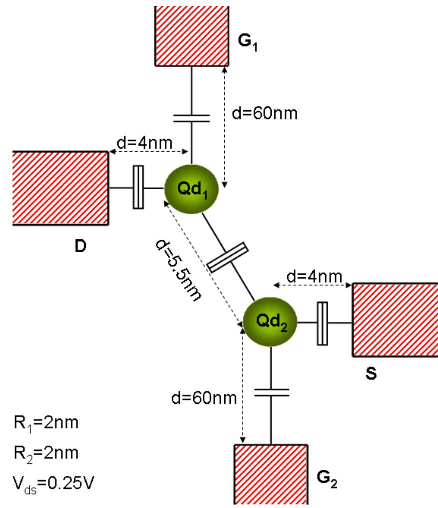

FIGURE 4.11: Scheme of the double gate transistor under simulation. The tunnel junctions and the capacity couplings are also shown. Due to the QD configuration, we assume that each QD is only coupled to one gate and one lead. Thus, the electronic transport occurs as in the serial QDs cases studied before. The QDs radii are 2 nm and $V_{ds} = 0.25$ V.

To present here the possibilities of this methodology and how it can be used to simulate realistic devices, we studied a double gate transistor. A second gate electrode was included modifying independently the potential of each QD. We used two Si/SiO_2 QDs described by the material parameters presented before (Table. 4.1) in order to focus on the physics behind the structure and not on constant material parameters. The structure under study is presented in Fig. 4.11. Within this configuration, each QD is only coupled to one gate and one lead. Therefore, each gate tune independently the potential of each QD and the QDs are placed in serial configuration.

We must note here that, one of the seminal result of the Bent Weber work is the individual control of the electrostatic potential of each QD. This fact is accomplished by the QD spatial configuration that minimizes the influence of the cross gate capacitive coupling (G_1 against QD_2 and G_2 against QD_1). This can be directly related to some QD capacitive screening that it is not included in our simple capacitance model calculation.

Therefore, we need to skip "manually" these couplings. The applied bias voltage among the drain (D) and the source (S) leads is $V_{ds} = 0.25$ V. Thus, the Laplace solution in each QD can be written as

$$U_{L1} = -\frac{C_{12}(qV_2)}{C_1} - \frac{C_{G_1}(qV_{G1})}{C_1} \tag{4.5}$$

$$U_{L2} = -\frac{C_s qV_{ds}}{C_2} - \frac{C_{12}(qV_1)}{C_2} - \frac{C_{G_2}(qV_{G2})}{C_2}, \tag{4.6}$$

where C_1 and C_2 take into account all the capacitive couplings of QD_1 and QD_2, respectively. In these expressions, we can see the capacitive coupling among the QDs (C_{12}) and the couplings to the four electrodes. V_1 and V_2 are the potential of each QD.

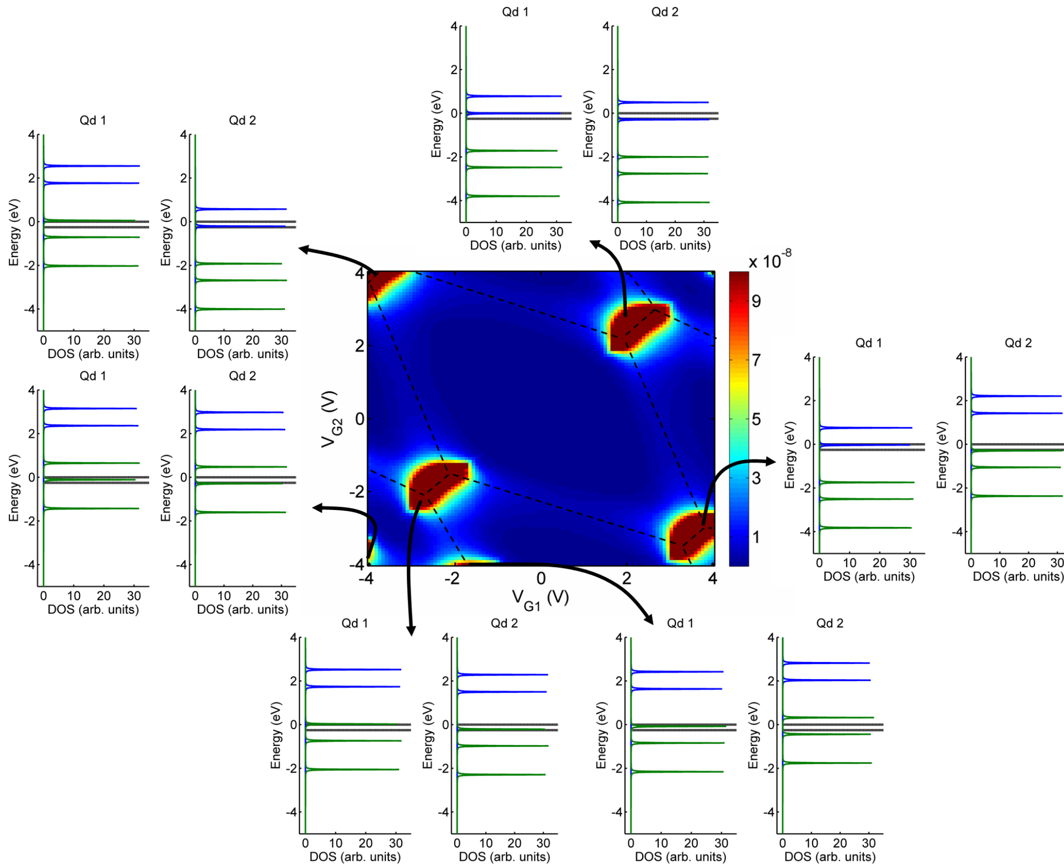

FIGURE 4.12: Simulated current map for the previous presented structure as a function of the applied gate voltages, V_{G1} and V_{G2}, for $V_{ds} = 0.25$ V. Moreover, in the insets an intuitive explanation of the obtained current trend are also presented as a function of the DOS of each QD. The conduction window is also shown (dotted line).

Once the system is described, in Fig. 4.12 we present the simulated current map as a function of the two gate voltages, V_{G1} and V_{G2}. The obtained current trend can be easily explained thinking in terms of the energy level overlapping between the two QDs. Each time that one energy level of the first QD (either electron or hole energy level) is aligned with an energy level of the second QD (either electron or hole energy level) and both

levels lie in the conduction window a charge transport process occurs. This necessary condition can be achieved by a combination of V_{G1} and V_{G2} obtaining the hexagonal current structure. The previous explanation is consistent with the theory reported in Ref. [53].

4.6 Carrier transport mechanisms in Si/SiO_2 structures

In this section, we are going to compare the previous developed formalism to experimental measurements. First of all, a brief description of the most relevant transport mechanisms is presented. Then, using the same ballistic transport mechanism and modeling the defects as punctual QDs described by a single energy level, a methodology capable to explain the transport between QDs and defects are presented. Moreover, for thin oxides and large voltages the direct current between the leads is included. Finally, the complete approach has been used to compare to experimental measurements.

4.6.1 Si/SiO_2 transport mechanisms

Up to now, we have described and proposed an elastic transport model based on rate equations in order to describe the electrical response of a system based on QDs embedded in a dielectric matrix. However, there are several transport models that describe the different transport mechanism observed from the experiments. There was during the development of the MOS technology, specially the Si/SiO_2 technology, when the MIM (metal-insulator-metal) and MOS (metal-oxid-semiconductor) structures have been exhaustive studied and different transport mechanisms have been observed and described.

As we described previously, when two different materials are placed in contact due to the band offsets differences between the materials, a potential barrier is created. For a metal insulator junction, we can describe two main situations: the oxide is thick enough to govern the transport mechanism of this system and the transport is related to the bulk properties of the oxide (bulk limited current). For thinner oxides, the transport are governed by properties of the metal-oxide interface (electrode limited). Thus, the conductivity in such system is dominated by the interface properties of the junction.

Here, we are going to present and describe briefly the usual transport mechanism used to model the experimental I(V) curves in MOS structures.

4.6.1.1 Poole-Frenkel emission

The Poole-Frenkel (PF) conduction consist in the successive emission of trapped electrons into the dielectric conduction band, where they can freely move for a certain time

before relaxing in other localized state [56, 57]. The emission process, governed by thermal excitation, is enhanced by the presence of a uniform electric field since it lowers the trap barrier height. The PF current density can be written as

$$J_{PF} \approx \frac{V}{d} exp \left(-\frac{\left(\phi_t - \sqrt{q^3 V/(d\pi\varepsilon_r)}\right)}{k_B T} \right), \tag{4.7}$$

where V is the applied voltage, d the total oxide thickness, ϕ_t is the trap energy taken from the bottom of the conduction band, k_B is the Boltzmann constant, T is the temperature and ε_r is the relative material permittivity in units of the absolute permittivity (ε_0).

This transport mechanism is usually used [58, 59, 60] to explain the electrical conduction in systems where trap states are induced by the Si/SiO_2 interface defects, or even the embedded QDs themselves assuming a thermal hopping through these shallow trap states. This mechanism is a clear example of the bulk limited mechanism. The energy levels of the traps are inherent to the oxide properties.

4.6.1.2 Schottky emission

This mechanism is usually observed for low energy barriers or when the barrier is too thick to allow carrier tunneling processes. This mechanism consist in the thermionic emission of carriers over the insulator potential barrier. The Richardson-Schottky equation, the expression for the thermionic emission, reads as [61]

$$J_s \approx T^2 exp \left(-\frac{\phi_0}{k_B T} \right) exp \left(\frac{\sqrt{\frac{q^3 V}{4\pi\varepsilon_0\varepsilon_\infty d}}}{k_B T} \right), \tag{4.8}$$

where ϕ_0 is the barrier height and ε_∞ is the high frequency dielectric constant. This mechanism is an example of electrode limited mechanism since the barrier is created in the junction interface.

4.6.1.3 Tunneling processes

In general, in MIM or MOS structures, two different tunneling processes may be observed depending of the shape of the injection barrier. Previously, we have described the transmission coefficients among the different parts of the system as a function of the shape of the barrier: trapezoidal, direct tunneling (DT), or triangular, Fowler-Nordheim (FN). In this case, the tunneling process takes place directly between the two leads.

Assuming that: (i) the energy momentum dispersion is considered as parabolic; (ii) in each of three regions of the space the electron mass has the same value m^* and (iii) the

validity of the Tsu-Esaki formula [62, 63], the expression for the DT tunneling reads as [64]

$$J_{DT} \approx (V/d)^2 exp\left(-\frac{4\sqrt{2m^*}\phi_0^{3/2}}{3\hbar qV/d}\left[1-\left(1-\frac{qV}{\phi_0}\right)\right]\right). \tag{4.9}$$

In the same way, the FN tunneling current can be written as [65]

$$J_{FN} \approx (V/d)^2 exp\left(-\frac{4\sqrt{2m^*}\phi_0^{3/2}}{3\hbar qV/d}\right). \tag{4.10}$$

It should be noted that both mechanisms are grounded on the same assumptions and the only difference appears in the transmission probability through the insulator barrier. Hereon, we are going to refer the tunneling between the two leads as direct tunneling including the appropriate transmission coefficient as a function of the barrier shape.

4.6.1.4 Trap assisted tunneling

This mechanism can be described as a charge carrier tunneling between two electrodes assisted by an intermediate traps [66, 67]. These intermediate traps can be inherent to the dielectric material or can induced by the nanostructures embedded in the oxide. The trap assisted tunneling (TAT) takes into account the multistep tunneling among the traps being strongly dependent on the trap concentration. Several authors have studied the elastic [77] and inelastic [69] TAT processes assuming different traps distributions being the energy level and the trap concentration the main parameters that describe the process [70]. If an uniformly distributed trap concentration is assumed with a mean trap energy ϕ_t, the TAT current can be written as[71]

$$J_{TAT} \approx exp\left(-\frac{4\sqrt{2m^*}\phi_t^{3/2}}{3\hbar qV/d}\right). \tag{4.11}$$

4.6.2 Beyond the QD model

Now, we include the direct tunneling process between the leads and the trap assisted processes. As shown in Fig. 4.13, all the possible elastic tunneling transport processes are: (I and II) through the total oxide, (III) assisted by an intermediate trap and (IV) assisted by a QD. Since we considered that the electrodes act as an infinite electron source, the total current that crosses the structure will be the sum of the different current contributions. The total current trough the structure (I_{total}) can be expressed as

$$I_{total} = I_{FN} + I_{Traps} + I_{QD}. \tag{4.12}$$

We must note here that we are neglecting the interaction between the QDs and the traps since we have considered both processes as independent transport channels. This

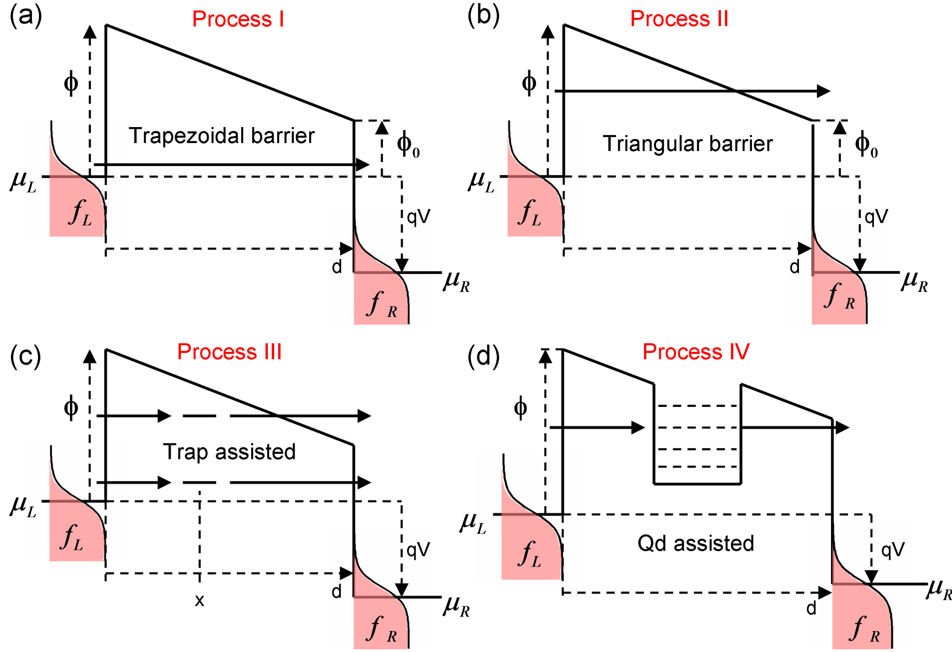

FIGURE 4.13: Energy band diagram of the system under external electric field. The different elastic tunneling transport processes are also shown: (I and II) tunneling through the oxide from the left to right leads, (III) elastic trap assisted tunneling and (IV) tunneling through the discrete energy levels of the embedded QD. The Fermi levels of each lead (μ_L and μ_R) and the Fermi functions (f_L and f_R) are also shown. μ_L is fixed as a energy reference.

assumption, that seems dramatic, can be justified thinking in terms of the tunnel current values. The tunnel current depends on the DOS at both sides of the barrier. Therefore, the current among a QD and a single trap is lower than the current among QDs. Thus, the first can be neglected. For the same reason, the current between traps is not considered (i.e. the transport processes that involves two or more intermediate traps). Using this approximation, the current through the traps can be easily obtained and in the QD rate equations we avoid to include extra terms.

4.6.2.1 Tunneling through the total oxide

The expression for the current associated to the tunneling mechanism (Fig. 4.13(a-b)) can be written using the Transfer Hamiltonian formalism as

$$I_{FN} = \frac{4\pi q}{\hbar} \int_{-\infty}^{+\infty} T(E)\rho_R(E)\rho_L(E)(f_L(E) - f_R(E))dE, \quad (4.13)$$

where $\rho_L(E)$ and $\rho_R(E)$ are the density of states (DOS) of the left and right lead. The occupation distribution functions of the leads are well described by the Fermi functions, $f_L(E)$ and $f_R(E)$, with the corresponding electrochemical potential for the left and right

leads, μ_L and μ_R respectively. We choose the Wentzel-Kramers-Brillouin approximation to describe the tunneling probability $T(E)$ (as we have done in previous simulations). As a result of the external applied bias voltage, the oxide bands are bended and the tunneling probability is written as

$$T = \begin{cases} exp\left\{-4\frac{\sqrt{2m^*_{diel}}}{3\hbar qF}((\phi - E)^{3/2} - (\phi_0 - E)^{3/2})\right\} \text{for } \phi_0 \geq E \\ exp\left\{-4\frac{\sqrt{2m^*_{diel}}}{3\hbar qF}(\phi - E)^{3/2}\right\} \text{for } \phi \geq E \geq \phi_0 \end{cases} \tag{4.14}$$

where, the electric field is defined as $F = \frac{\mu_L - \mu_R}{qd}$, ϕ is the potential barrier height, ϕ_0 is the modified potential barrier height ($\phi(d)$), d is the tunneling distance and m^*_{diel} is the electron oxide effective mass. $\mu_L - \mu_R = qV$ reflects the different applied bias voltage in each side of the barrier. From Eq. 4.14, the tunneling probability is decomposed in two regimes as a function of the modified potential barrier height and the carrier incident energy (E): trapezoidal (process I) and triangular barrier (process II).

We must note that in the previous expression the image force effects are neglected. The image force correction is introduced to explain the positive charge created at the interface acting like an image charge within the layer when an electron approaches to the dielectric layer. There is some controversy about the inclusion of the image force in the calculation of the tunnel current. Some authors argue that its inclusion overestimates the tunneling current [72, 73] and other authors claim for its inclusion in order to avoid the thickness-dependent tunneling mass [74, 75]. In any case, the inclusion of the image force is known to lower and round the barrier [76] an it can be included changing the barrier height. Thus, in principle, we can avoid the image force, specially if the barrier height is used as a fitting parameter.

Two main current expressions appear as a function of the energy of the incident electrons and the band bending of the oxide: a trapezoidal barrier for low fields (process I) and triangular barrier for high fields (process II), analogous to the DT and FN processes described previously. We refer to both processes as a I_{FN}.

4.6.2.2 Defect inclusion

The defects are included in a similar way as we have described the carrier transport in the QDs. The elastic trap-assisted tunneling (process III in Fig. 4.13) is described as a two-step process. The electrons come from one lead to the trap and go out to the second lead. Writing the occupation of a single mono-energetic trap as a net flux between incoming and outgoing current, and assuming a steady state condition, the net current that crosses the oxide through the trap from lead to lead can be written as

$$I(E_t, V) = 2\frac{q}{h}\frac{T_L(E_t)T_R(E_t)}{T_L(E_t) + T_R(E_t)}(f_L(E_t) - f_R(E_t)) \tag{4.15}$$

where we used the Transfer Hamiltonian formalism to describe the partial fluxes. The occupation functions of the leads are described by the Fermi function $f_L(E_t)$ and $f_R(E_t)$ with the corresponding electrochemical potential for the left and right leads, respectively. $T_L(E_t)$ and $T_R(E_t)$ are the tunneling probabilities for the left and right contacts. We have used Eq. 4.14 to describe these tunneling probabilities. We must note here that all these parameters are evaluated at the energy level of the trap E_t since we consider that the trap is mono-energetic.

On the other hand, the energy level of the trap is located at a constant energy position from the bottom of the oxide conduction band. We assume that when an external bias voltage V is applied, the voltage drops uniformly through the oxide, bending the conduction band and modifying the energy level position of the trap. The position of the trap energy level is described by

$$E_t(x, V) = E_0 - \frac{qV}{d}x, \tag{4.16}$$

where x is the distance respect to the left lead and d is the total oxide thickness. The unbiased trap energy level E_0 is usually measured from the bottom of the conduction band but for our notation we redefine it and we measure it from the position of the equilibrium Fermi level.

In Eq. 4.15 the current through a single trap has been presented but, we can use it to simulate an energy and position trap distribution described by a distribution function $f_t(E_0, x)$ and the total trap current is written as

$$I_{Traps}(V) = \int_0^d \int_{E_{0min}}^{E_{0max}} f_t(E_0, x) I(E_t, V) dx\ dE_0 \tag{4.17}$$

where d is the oxide thickness and E_{0min} and E_{0max} are the minimum/maximum energy distance between the traps and the bottom of the oxide conduction band. From Eq. 4.17 and the single trap current Eq. 4.15, we must note that the two main parameters that govern the final current value, for an externally applied bias voltage, are the trap position x and the energy level distribution (E_0).

4.6.3 Transport simulations: experimental validation

In this section, we present the comparison between the here developed transport methodology and the experimental results. The previous model was used to reproduce the experimental electrical measurements for three different Si/SiO_2 structures, which are basically a MOS structure: a P-type Si substrate and a highly N-type doped polycrystalline silicon (Polysilicon) acting as a gate electrode separated by the SiO_2 layer (active layer). The different active layers embedded between the electrodes are: (1) a SiO_2 layer of different thicknesses (SiO_2), (2) Si QDs randomly distributed embedded in a SiO_2

matrix (Si QD/SiO_2) and (3) a superlattice structure of 6 SRO/SiO_2 bilayers (SL Si QD/SiO_2).

Usually, the experimental current measurements are presented as a function of the applied electric field since from this representation, several curve fittings can be done using the previous described transport mechanisms (Poole-Frenkel, Schottky, tunneling or trap assisted tunneling). The applied electric field is defined as $F = V/d$ where V is the external bias voltage and d is the total active layer thickness.

4.6.3.1 SiO_2 layer: pure defects conduction

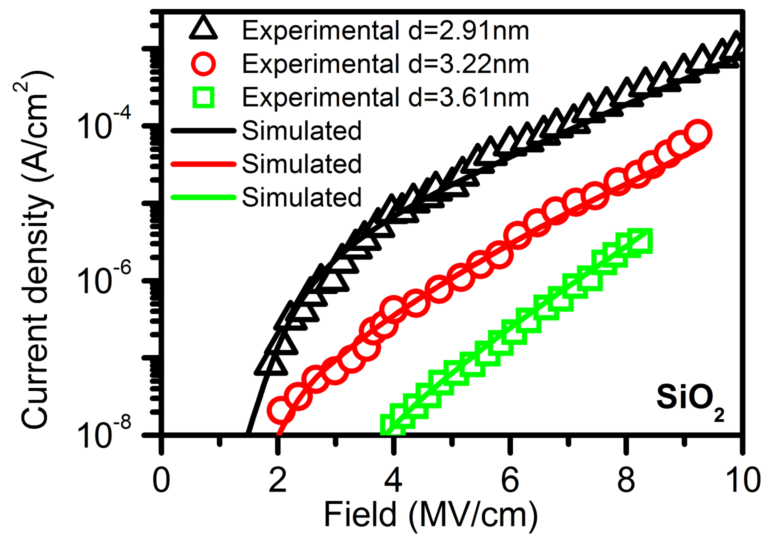

FIGURE 4.14: Experimental and simulated tunnel current density for different SiO_2 active layer thicknesses. The direct current among the leads is not considered. Experimental data has been extracted from Ref. [77].

First of all, we studied the tunnel transport processes through a pure SiO_2 film with different thicknesses in order to validate the here presented trap assisted model. Fig. 4.14 shows the simulated and the experimental tunnel current density through SiO_2 for different thicknesses. Experimental current density measurements were taken from Jimenez *et al.* [77]. We have used the SiO_2 parameters to explain the tunneling processes, whereas the traps were distributed uniformly in space and a Gaussian distribution function in energy has been assumed to describe the mono-energetic trap distributions, following

$$f_t(E_0, x) = \begin{cases} N_0 \cdot exp\left\{-(\frac{E_0 - \langle E_0 \rangle}{\sigma_{E_0}})^2\right\} \text{for } E_0 \in [E_{0min}, E_{0max}] \\ 0 \text{ for } E_0 \notin [E_{0min}, E_{0max}] \end{cases} \tag{4.18}$$

where N_0 is the trap density, $\langle E_0 \rangle$ is the average of the distribution and the width is controlled by σ_{E_0}. The best fitted parameters are presented in Table 4.2. Besides, we compared our fits and the parameters obtained using the approach presented by

d (nm)	$N_0(cm^{-3})$	$\langle E_0\rangle(eV)$	$\sigma_{E_0}(eV)$	
$2.91nm$	6.87×10^{13}	1.25	0.48	This work
	4×10^{14}	1.0	0.65	Ref. [77]
$3.22nm$	1.24×10^{13}	1.25	0.48	This work
	1×10^{14}	0.8	0.65	Ref. [77]
$3.61nm$	5.54×10^{12}	1.40	0.39	This work
	3×10^{13}	1.1	0.65	Ref. [77]

TABLE 4.2: Parameters of the trap distribution used to fit the experimental data and its comparison to other theoretical approach. We have used $E_{0min} = 0.3eV$ and $E_{0max} = 3eV$ for all the fits.

Ref. [77]. They presented a complete theoretical model based on the Transfer Hamiltonian formalism to study the trap-assisted elastic tunneling and analyzed the role of the image force. Detailed expressions for the tunneling probabilities were also presented. In order to make a direct comparison between both approaches, we have used their fitted active layer thicknesses: 2.91 nm, 3.22 nm and 3.61 nm.

As we can see, our elastic tunneling trap assisted model reproduces successfully experimental results and the fitted parameters (see Table. 4.2) used to describe the position and energy trap distribution function are similar to the ones used in Ref. [77]. We have focused on the thickest active layers since, as they claimed for the thinner ones, the experimental data were well reproduced taking into account only the tunneling from one lead to the other without intermediate tunneling processes. In the thickest ones, the tunnel current through the total oxide underestimates the experimental current and the inclusion of elastic tunneling assisted by traps are needed to reproduce experimental measurements.

Small discrepancies arise since they use an energy dependent oxide effective mass whereas we use the previous constant value. However, both models describe the elastic trap-assisted tunneling using similar trap densities and energy distribution function. From this comparison, in the next simulations we consider a fixed value of $\langle E_0\rangle = 1.3$ eV and $\sigma_{E_0} = 0.45$ eV for the energy trap distribution.

From the general transport condition, the traps contribute to the current when their energy level lie in the conduction channel. From Eq. 4.16, this condition can be achieved as a function of the trap energy level (E_0) and its position respect to the left lead (x). Traps with deep energy levels will start to conduct before than the shallow traps. However, the transmission coefficients of these deep traps will be smaller than the shallow ones being the current practically zero. The position of the trap controls the influence of the external potential, Eq. 4.16. This compromise is clearly visible in a current map as a function of the trap energy level (E_0) and its distance respect to the left lead (x) for different electric fields (Fig. 4.15). Here, we use the fitted parameters obtained for the thickest SiO_2 layer ($d = 3.61$ nm).

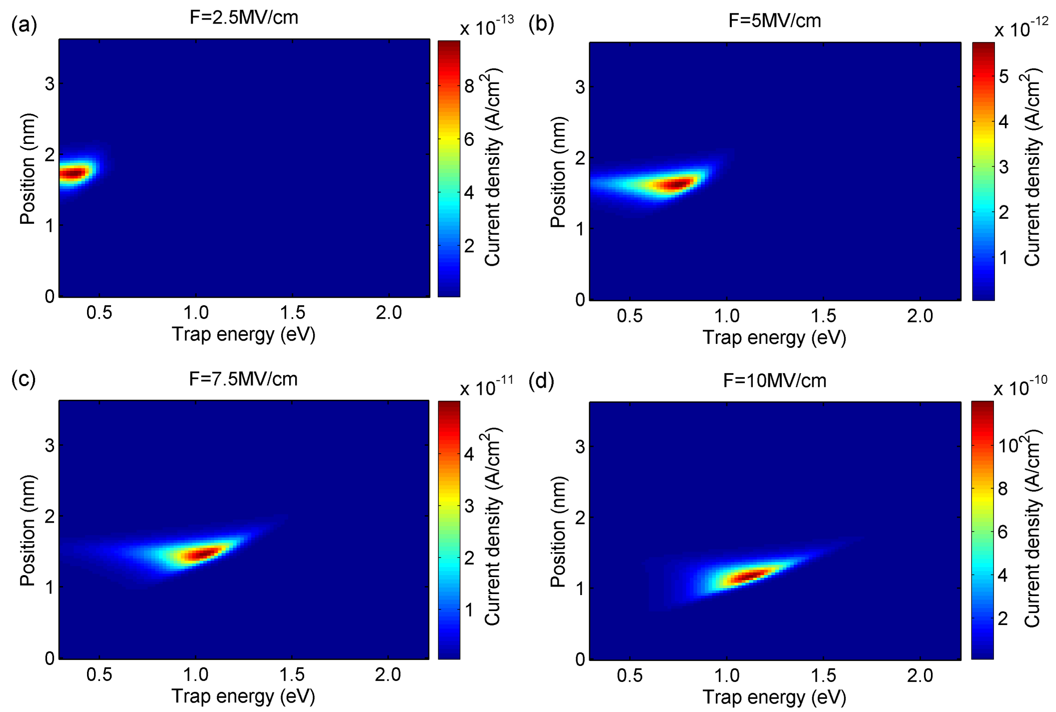

FIGURE 4.15: Current map for a single trap as a function of the distance to the left lead and the energy trap level for different electric fields: (a) $F = 2.5$ MV/cm, (b) $F = 5$ MV/cm, (c) $F = 7.5$ MV/cm and (d) $F = 10$ MV/cm.

In Fig. 4.15, the dominant trap current is shown for different applied electric fields. When the field increases, the band bending of the oxide increases and the dominant traps progressively become those closer to the left lead with higher energy levels, since they see lower potential barriers.

4.6.3.2 SiO_2 layer: defect and direct tunneling

Now, we simulate another SiO_2 structure, but thicker than the previous one. The experimental data has been taken from Ramírez *et al.* [6] and corresponds to a SiO_2 active layer of $50nm$ thickness. The experimental current density is given as a function of the electric field.

The simulated current and the experimental data are shown in Fig. 4.16. For low and moderate fields the elastic trap assisted tunneling mechanism dominates transport and for high fields the oxide band bending allows direct tunneling from the left to the right lead. Thus, two different transport processes are observed and this effect is observed in the current. It is worth to mention that the used trap energy level for our simulations (1.3 eV, see previous simulations) correlates well with the one fitted by the authors (1.2

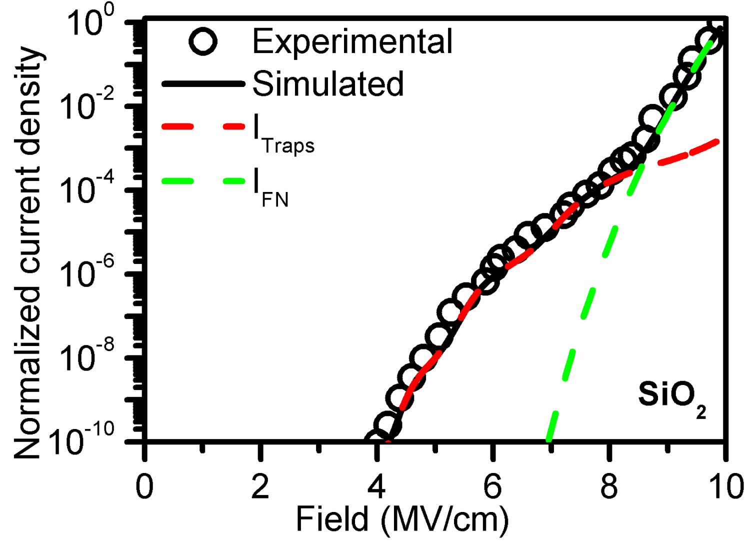

FIGURE 4.16: Experimental normalized current density and simulated current for the SiO_2 structure. Trap (I_{Traps}) and direct tunnel (I_{FN}) currents are also shown. Experimental data has been extracted from Ref. [6].

eV). Concerning the tunneling through the total oxide, we assume a continuous and constant lead density of states.

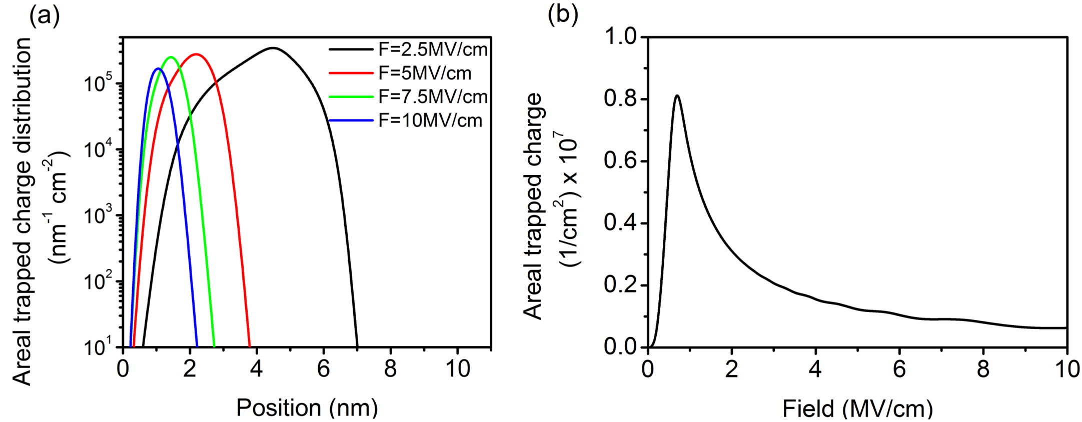

FIGURE 4.17: Trapped charge studies for the $50nm$ SiO_2 layer. (a) Trapped charge distribution in the oxide layer for different electric fields and (b) trapped charge as a function of the applied electric field.

Besides, we present the trapped charge distribution in space for different electric fields in Fig. 4.17(a) and (b), respectively. The charge injection in the oxide is a balance between the incoming and the outgoing carrier fluxes to/from the leads and it is strongly dominated by the transmission coefficients that depend on the position of the trap and the applied electric field.

Following the derivation that we have done in the second chapter, the number of electrons in a mono-energetic trap can be written as

$$N = \frac{T_L(E_t)f_L(E_t) + T_R(E_t)f_R(E_t)}{T_L(E_t) + T_R(E_t)}. \tag{4.19}$$

As can be observed in Fig. 4.17(a), when the field increases, all the charge is concentrated in the interface between the left lead and the oxide layer being possible to create internal electric field that reduces the contact potential barrier (image charge effects). However, in Fig. 4.16 the simulated curves matched the experimental trends reflecting that the image charge effects are not a dominant effect.
The trapped charge as a function of the applied electric field, Fig. 4.17(b), shows a maximum trapped charge when $T_L(E_t) > T_R(E_t)$ and E_t lies between μ_L and μ_R ($f_L(E_t) \approx 1$ and $f_R(E_R) \approx 0$).

4.6.3.3 Si QD/SiO_2 structure

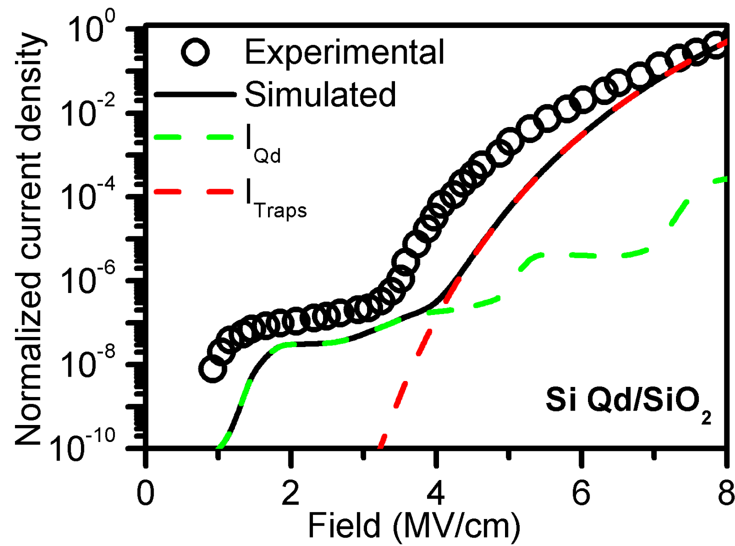

FIGURE 4.18: Experimental normalized current density and simulated current for the Si QD/SiO_2 structure. Current through the QDs (I_{QD}) and the traps (I_{Traps}) are shown. Experimental data has been extracted from Ref. [6].

Regarding the Si QD/SiO_2 structure, it is basically a SiO_2 layer in which the silicon excess aggregates forming Si QDs. These QDs are randomly created inside the oxide matrix. We used the QD transport model in combination with the elastic trap assisted tunneling.
According to microscopic measurements from Ref. [6], we simulated an arrangement of QDs in random positions and normal radius distribution with $\langle R \rangle = 1.5$ nm of mean radius and $\sigma_R = 0.2$ nm of standard deviation. We used the same mono-energetic trap distribution as in the previous case. The simulated current and the experimental data Ref. [6] are shown in Fig. 4.18. This figure also shows the different current contributions due to the transport: through the QDs and through the traps. We distinguish two main regimes: the QD term displays the step-like behavior in the current as a consequence of the discrete nature of the QD energy levels and it is the dominant transport mechanism for low fields, whereas for intermediate and high fields the trap assisted tunneling dominates. We must note that these results can not be achieved by considering direct

tunneling between the leads, so we concluded that the electron transport process is assisted by an intermediate QD or a trap.

In this case, the authors of Ref. [6] fitted a TAT expression with energy trap value (1.8 eV) for moderate and high fields. The fitted value is different to the one used in the SiO_2 structure and they claim that the transport is assisted by Si QDs and SiO_2 traps. However, a further explanation is needed for the obtained current behavior at low fields. Our simulations reproduce this low field regime and give an explanation as a pure transport through the discrete energy states of the QDs as we have described previously. However, some discrepancies appear for higher voltages. We must note here that we have used the previous trap energy distribution neglecting the possibility that the QDs change the energy levels of the traps.

4.6.3.4 Superlatice Si QD/SiO_2 structures

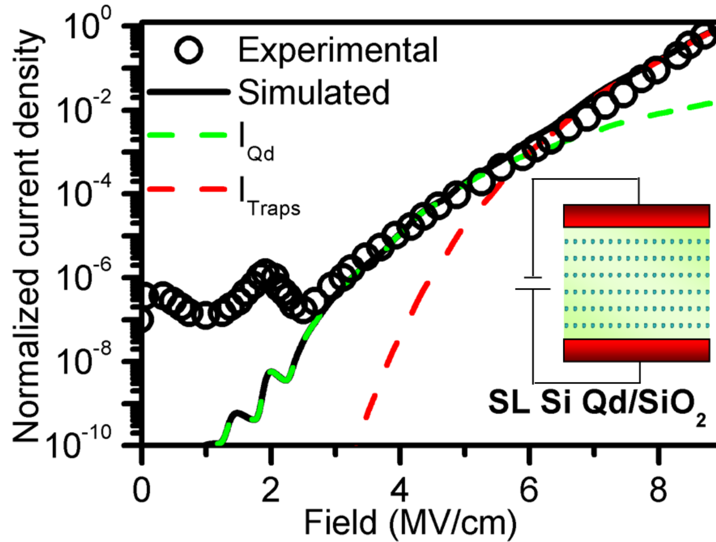

FIGURE 4.19: Experimental normalized current density and simulated current for the SL Si QD/SiO_2 structure. Different current contributions, through the QDs (I_{QD}) and traps (I_{Traps}), are also shown. In the inset, the cross section of the structure is presented. Experimental data has been extracted from Ref. [6].

Finally, the simulated current and the experimental results for the SL Si QD/SiO_2 are shown in Fig. 4.19. An scheme of the structure is also presented in the inset. In order to properly describe the structure presented by Ramírez *et al.* [6], we considered 6 layers of Si QDs with a normal distribution of radius, $\langle R \rangle = 1.5$ nm of mean radius and $\sigma_R = 0.2$ nm of standard deviation. The QDs are distributed in a perpendicular plane respect to the transport direction reflecting the layer structure and the layers are spaced 2.5 nm between them. As in the previous case, we used the QD transport model and the trap assisted tunneling.

Concerning the experimental and simulated results: for low and moderate field regime, we reproduced the experimental current trend as a QD pure transport. For the highest fields, a pure trap mechanism is enough to explain the experiments. In Ref. [6], the authors fitted a PF expression for moderate fields and a pure TAT for highest fields with mean energy trap value (1 eV) neglecting the current peaks at low fields. This value is close to the one obtained for the SiO_2 structure and the authors conclude that the tunneling in both structures is mediated by deep traps inherent to the SiO_2 and not by states created ad-hoc when including Si QDs. This fact is reflected here since we considered a fixed value for the energy level trap distribution.

4.7 Conclusions

In this chapter, we have used the previously developed transport formalism and its code implementation to simulate different QDs arrangements using realistic parameters. We have focused on the Si/SiO_2 QDs since these kind of systems have been widely studied in previous chapters. Since an approximate DOS that describes the Si QD is obtained and the oxide barriers are parametrized, the transport was done. We started studying the simplest case, a single QD placed between two leads. As we pointed out in the first chapter, the current reflects directly the internal discrete energy level structure of the QD. The current increases in step-like behavior every time that an energy level (either electron or hole) lies in the conduction windows. From the parameters used to describe the oxide, the hole current is weaker than the electron one since the hole has to cross a higher barrier. A NDR has also been obtained and it is explained as a function of the energy and voltage dependence of the transmission coefficients that change the coupling among the right and left leads.

From this simple system, the accumulated charge trends have also been studied. As we saw in the first chapter, the accumulated charge reflects directly the ratio among the incoming and outgoing fluxes from/to the QD. Now, these fluxes are strongly dominated by the transmission coefficients. Thus, when an energy level lies in the conduction window its charge changes. The new charge state is dominated by the lead which is strongly coupled to the QD. Therefore, the electron energy levels can be filled whereas the hole energy levels can be emptied. A systematic study of the transmission coefficients was done changing the coupling distance between the QD and the leads obtained electron or hole charge accumulation as a function of the QD position. Besides, the discrete nature of the QD energy levels is also viewed in the charge increment.

To conclude the general transport simulations and show the capabilities of the code, large systems based on QD multilayer structure have been simulated. These structures have crucial importance since the bilayer QDs arrangement is usually obtained from experimental fabrication methods. The total current and accumulated charge curves

were obtained but due to the many charge transport channels, the specific QDs positions and their interaction a generalized analysis can not be obtained. However, the hole current is lesser than the electron component as we explained before.

Once the structures based on two electrodes have been presented, we studied the transistor device. It is based in a third electrode (gate) located on the top of the structure which is capacitive coupled to the QDs but does not injects current. Thus, this gate electrode can tune the position of the QD energy levels independently increasing the QD charge and moving the energy levels trough the conduction window. Current and charge maps were obtained as a function of the gate and drain source voltages. The discrete energy spectra of the QDs are reflected in the current and charge curves creating diamond behaviors. This structure has been studied for a single QD case and for many QDs. Moreover, the double gate electron transistor has also presented. It is based on two QDs independently coupled to two different gate electrodes. Thus, each gate electrode controls its respective QD. From the current map as a function of the two gate potentials a hexagonal behaviors is obtained. Its explanation is related to the electron and hole energy level alignment.

Finally, a comparison to experimental measurements and other transport mechanism has been done. The basic transport mechanisms usually observed in the experiments are described. Our QD transport model has completed including the current term from direct transmission between the leads (for thinner oxides or high electric fields) and a defect component. The defects current was included describing the trap as a non-interacting mono-energetic level. These three transport mechanisms was used to describe experimental results obtained from different Si/SiO_2 structures. The transport in these structures can be summarized as: for narrow pure SiO_2 layers, the trap assisted tunneling dominates at low and moderate fields whereas for high fields the direct tunnel between the leads is the most important process. In the presence of QDs, the current reflects the discrete nature of the energy levels for low electric fields and the trap assisted tunneling appears for moderate and high fields.

Bibliography

[1] Wen-Chin Lee and Chenming Hu. Modeling CMOS tunneling currents through ultrathin gate oxide due to conduction- and valence-band electron and hole tunneling. *Electron Devices, IEEE Transactions on*, 48(7):1366–1373, Jul 2001.

[2] Yee-Chia Yeo, Tsu-Jae King, and Chenming Hu. MOSFET gate leakage modeling and selection guide for alternative gate dielectrics based on leakage considerations. *Electron Devices, IEEE Transactions on*, 50(4):1027–1035, April 2003.

[3] Gavin Conibeer, Martin Green, Richard Corkish, Young Cho, Eun-Chel Cho, Chu-Wei Jiang, Thipwan Fangsuwannarak, Edwin Pink, Yidan Huang, Tom Puzzer, Thorsten Trupke, Bryce Richards, Avi Shalav, and Kuo lung Lin. Silicon nanostructures for third generation photovoltaic solar cells. *Thin Solid Films*, 511–512(0):654 – 662, 2006. {EMSR} 2005 - Proceedings of Symposium F on Thin Film and Nanostructured Materials for Photovoltaics {EMRS} 2005- Symposium F {EMSR} 2005 - Proceedings of Symposium F on Thin Film and Nanostructured Materials for Photovoltaics.

[4] S. Okhonin, P. Fazan, G. Guegan, S. Deleonibus, and F. Martin. Two-band tunneling currents in metal-oxide-semiconductor capacitors at the transition from direct to fowler x2013;nordheim tunneling regime. *Applied Physics Letters*, 74(6):842–843, Feb 1999.

[5] S. M. Sze. *Semiconductor Devices, Physics and Technology.* Wiley. Hoboken, NJ, 2001.

[6] J. M. Ramírez, Y. Berencén, L. López-Conesa, J. M. Rebled, F. Peiró, and B. Garrido. Carrier transport and electroluminescence efficiency of erbium-doped silicon nanocrystal superlattices. *Applied Physics Letters*, 103(8):–, 2013.

[7] P. Löper, R. Müller, D. Hiller, T. Barthel, E. Malguth, S. Janz, J. C. Goldschmidt, M. Hermle, and M. Zacharias. Quasi-fermi-level splitting in ideal silicon nanocrystal superlattices. *Phys. Rev. B*, 84:195317, Nov 2011.

[8] Nuria Garcia-Castello, Sergio Illera, Roberto Guerra, Joan Daniel Prades, Stefano Ossicini, and Albert Cirera. Silicon quantum dots embedded in a SiO_2 matrix: From structural study to carrier transport properties. *Phys. Rev. B*, 88:075322, Aug 2013.

[9] José M Soler, Emilio Artacho, Julian D Gale, Alberto García, Javier Junquera, Pablo Ordejón, and Daniel Sánchez-Portal. The siesta method for ab initio order-n materials simulation. *Journal of Physics: Condensed Matter*, 14(11):2745, 2002.

[10] Pablo Ordejón, Emilio Artacho, and José M. Soler. Self-consistent order-n density-functional calculations for very large systems. *Phys. Rev. B*, 53:R10441–R10444, Apr 1996.

[11] Mads Brandbyge, José-Luis Mozos, Pablo Ordejón, Jeremy Taylor, and Kurt Stokbro. Density-functional method for nonequilibrium electron transport. *Phys. Rev. B*, 65:165401, Mar 2002.

[12] A. H. Larsen, M. Vanin, J. J. Mortensen, K. S. Thygesen, and K. W. Jacobsen. Localized atomic basis set in the projector augmented wave method. *Phys. Rev. B*, 80:195112, Nov 2009.

[13] M. Zacharias, J. Heitmann, R. Scholz, U. Kahler, M. Schmidt, and J. Blasing. Size-controlled highly luminescent silicon nanocrystals: A SiO/SiO_2 superlattice approach. *Applied Physics Letters*, 80(4):661–663, Jan 2002.

[14] C. Bonafos, B. Colombeau, A. Altibelli, M. Carrada, G. Ben Assayag, B. Garrido, M. López, A. Pérez-Rodríguez, J.R. Morante, and A. Claverie. Kinetic study of group {IV} nanoparticles ion beam synthesized in SiO_2. *Nuclear Instruments and Methods in Physics Research Section B: Beam Interactions with Materials and Atoms*, 178(1–4):17 – 24, 2001. Materials Science with Ion Beams.

[15] B. Garrido Fernandez, M. López, C. García, A. Pérez-Rodríguez, J. R. Morante, C. Bonafos, M. Carrada, and A. Claverie. Influence of average size and interface passivation on the spectral emission of Si nanocrystals embedded in SiO_2. *Journal of Applied Physics*, 91(2), 2002.

[16] Daria Riabinina, Christophe Durand, Joëlle Margot, Mohamed Chaker, Gianluigi A. Botton, and Federico Rosei. Nucleation and growth of Si nanocrystals in an amorphous SiO_2 matrix. *Phys. Rev. B*, 74:075334, Aug 2006.

[17] Fabio Iacona, Giorgia Franzò, and Corrado Spinella. Correlation between luminescence and structural properties of Si nanocrystals. *Journal of Applied Physics*, 87(3):1295–1303, 2000.

[18] R. Lockwood V. A. Belyakov, V. A. Burdov and A. Meldrum. Silicon nanocrystals: Fundamental theory and implications for stimulated emission. *Advances in Optical Technologies*, pages 279502–32, 2008.

[19] A.D. Yoffe. Low-dimensional systems: quantum size effects and electronic properties of semiconductor microcrystallites (zero-dimensional systems) and some quasi-two-dimensional systems. *Advances in Physics*, 42(2):173–262, 1993.

[20] N F Johnson. Quantum dots: few-body, low-dimensional systems. *Journal of Physics: Condensed Matter*, 7(6):965, 1995.

[21] Stephanie M. Reimann and Matti Manninen. Electronic structure of quantum dots. *Rev. Mod. Phys.*, 74:1283–1342, Nov 2002.

[22] L P Kouwenhoven, D G Austing, and S Tarucha. Few-electron quantum dots. *Reports on Progress in Physics*, 64(6):701, 2001.

[23] M. A. Kastner. The single-electron transistor. *Rev. Mod. Phys.*, 64:849–858, Jul 1992.

[24] Chao Wang and Stephen Y. Chou. Integration of metallic nanostructures in fluidic channels for fluorescence and raman enhancement by nanoimprint lithography and lift-off on compositional resist stack. *Microelectronic Engineering*, 98(0):693 – 697, 2012. Special issue {MNE} 2011 - Part {II}.

[25] M. Koltonyuk, D. Berman, N. B. Zhitenev, R. C. Ashoori, L. N. Pfeiffer, and K. W. West. Single-electron capacitance spectroscopy of vertical quantum dots using a single-electron transistor. *Applied Physics Letters*, 74(4), 1999.

[26] Michel H. Devoret, Daniel Esteve, and Cristian Urbina. Single-electron transfer in metallic nanostructures. *Nature*, 360(6404), 1992.

[27] N.D. Akhavan, A. Afzalian, Chi-Woo Lee, Ran Yan, I. Ferain, P. Razavi, Ran Yu, G. Fagas, and J. Colinge. Nanowire to single-electron transistor transition in trigate SOI MOSFETs. *Electron Devices, IEEE Transactions on*, 58(1):26–32, Jan 2011.

[28] D.V. Averin and K.K. Likharev. Coulomb blockade of single-electron tunneling, and coherent oscillations in small tunnel junctions. *Journal of Low Temperature Physics*, 62(3-4):345–373, 1986.

[29] Daniel Loss and David P. DiVincenzo. Quantum computation with quantum dots. *Phys. Rev. A*, 57:120–126, Jan 1998.

[30] Rutger Vrijen, Eli Yablonovitch, Kang Wang, Hong Wen Jiang, Alex Balandin, Vwani Roychowdhury, Tal Mor, and David DiVincenzo. Electron-spin-resonance transistors for quantum computing in silicon-germanium heterostructures. *Phys. Rev. A*, 62:012306, Jun 2000.

[31] Mark Friesen, Paul Rugheimer, Donald E. Savage, Max G. Lagally, Daniel W. van der Weide, Robert Joynt, and Mark A. Eriksson. Practical design and simulation of silicon-based quantum-dot qubits. *Phys. Rev. B*, 67:121301, Mar 2003.

[32] Adriano Barenco, David Deutsch, Artur Ekert, and Richard Jozsa. Conditional quantum dynamics and logic gates. *Phys. Rev. Lett.*, 74:4083–4086, May 1995.

[33] Daniel Loss and David P. DiVincenzo. Quantum computation with quantum dots. *Phys. Rev. A*, 57:120–126, Jan 1998.

[34] G. D. Sanders, K. W. Kim, and W. C. Holton. Scalable solid-state quantum computer based on quantum dot pillar structures. *Phys. Rev. B*, 61:7526–7535, Mar 2000.

[35] J. H. Jefferson, M. Fearn, D. L. J. Tipton, and T. P. Spiller. Two-electron quantum dots as scalable qubits. *Phys. Rev. A*, 66:042328, Oct 2002.

[36] Tetsufumi Tanamoto. Quantum gates by coupled asymmetric quantum dots and controlled-not-gate operation. *Phys. Rev. A*, 61:022305, Jan 2000.

[37] Hirotaka Sasakura, Satoru Adachi, and Shunichi Muto. Quantum gates based on electron spins of triple quantum dot. *Japanese Journal of Applied Physics*, 42(10R):6308, 2003.

[38] Filippo Troiani, Elisa Molinari, and Ulrich Hohenester. High-finesse optical quantum gates for electron spins in artificial molecules. *Phys. Rev. Lett.*, 90:206802, May 2003.

[39] K.K. Likharev and A.B. Zorin. Theory of the bloch-wave oscillations in small josephson junctions. *Journal of Low Temperature Physics*, 59(3-4):347–382, 1985.

[40] J. P. Pekola, K. P. Hirvi, J. P. Kauppinen, and M. A. Paalanen. Thermometry by arrays of tunnel junctions. *Phys. Rev. Lett.*, 73:2903–2906, Nov 1994.

[41] Sh. Farhangfar, K.P. Hirvi, J.P. Kauppinen, J.P. Pekola, J.J. Toppari, D.V. Averin, and A.N. Korotkov. One dimensional arrays and solitary tunnel junctions in the weak coulomb blockade regime: Cbt thermometry. *Journal of Low Temperature Physics*, 108(1-2):191–215, 1997.

[42] K. K. Likharev and A. B. Zorin. Simultaneous bloch and josephson oscillations, and resistance quantizations in small superconducting double junctions. *Japanese Journal of Applied Physics*, 26(S3-2):1407, 1987.

[43] L. P. Kouwenhoven, S. Jauhar, K. McCormick, D. Dixon, P. L. McEuen, Yu. V. Nazarov, N. C. van der Vaart, and C. T. Foxon. Photon-assisted tunneling through a quantum dot. *Phys. Rev. B*, 50:2019–2022, Jul 1994.

[44] Akira Fujiwara, Yasuo Takahashi, and Katsumi Murase. Observation of single electron-hole recombination and photon-pumped current in an asymmetric Si single-electron transistor. *Phys. Rev. Lett.*, 78:1532–1535, Feb 1997.

[45] P. Lafarge, H. Pothier, E.R. Williams, D. Esteve, C. Urbina, and M.H. Devoret. Direct observation of macroscopic charge quantization. *Zeitschrift für Physik B Condensed Matter*, 85(3):327–332, 1991.

[46] David Berman, Nikolai B. Zhitenev, Raymond C. Ashoori, Henry I. Smith, and Michael R. Melloch. Single-electron transistor as a charge sensor for semiconductor applications. *Journal of Vacuum Science Technology B*, 15(6), 1997.

[47] M. J. Yoo, T. A. Fulton, H. F. Hess, R. L. Willett, L. N. Dunkleberger, R. J. Chichester, L. N. Pfeiffer, and K. W. West. Scanning single-electron transistor microscopy: Imaging individual charges. *Science*, 276(5312):579–582, 1997.

[48] P. L. McEuen, E. B. Foxman, U. Meirav, M. A. Kastner, Yigal Meir, Ned S. Wingreen, and S. J. Wind. Transport spectroscopy of a coulomb island in the quantum hall regime. *Phys. Rev. Lett.*, 66:1926–1929, Apr 1991.

[49] K.K. Likharev. Single-electron devices and their applications. *Proceedings of the IEEE*, 87(4):606–632, Apr 1999.

[50] P. L. McEuen S. Tarucha L. P. Kouwenhoven, C. M. Marcus and M. Robert. *NATO ASI Conf. Proc.* Norwell, MA: Kluwer Academic Publishers, 1997.

[51] U Meirav and E B Foxman. Single-electron phenomena in semiconductors. *Semiconductor Science and Technology*, 11(3):255, 1996.

[52] L. P. Kouwenhoven, T. H. Oosterkamp, M. W. S. Danoesastro, M. Eto, D. G. Austing, T. Honda, and S. Tarucha. Excitation spectra of circular, few-electron quantum dots. *Science*, 278(5344):1788–1792, 1997.

[53] W. G. van der Wiel, S. De Franceschi, J. M. Elzerman, T. Fujisawa, S. Tarucha, and L. P. Kouwenhoven. Electron transport through double quantum dots. *Rev. Mod. Phys.*, 75:1–22, Dec 2002.

[54] Bent Weber, Suddhasatta Mahapatra, Thomas F. Watson, and Michelle Y. Simmons. Engineering independent electrostatic control of atomic-scale silicon double quantum dots. *Nano Letters*, 12(8):4001–4006, 2012.

[55] Gabriel P. Lansbergen. Nanoelectronics: Transistors arrive at the atomic limit. *Nature Nanotechnology*, 7:209–210, 2012.

[56] J. Frenkel. On pre-breakdown phenomena in insulators and electronic semiconductors. *Phys. Rev.*, 54:647–648, Oct 1938.

[57] J G Simmons. Conduction in thin dielectric films. *Journal of Physics D: Applied Physics*, 4(5):613, 1971.

[58] Tim Creazzo, Brandon Redding, Elton Marchena, Janusz Murakowski, and Dennis W. Prather. Tunable photoluminescence and electroluminescence of size-controlled silicon nanocrystals in nanocrystalline-Si/SiO_2 superlattices. *Journal of Luminescence*, 130(4):631 – 636, 2010.

[59] Alessia Irrera, Fabio Iacona, Isodiana Crupi, Calogero D Presti, Giorgia Franz, Corrado Bongiorno, Delfo Sanfilippo, Gianfranco Di Stefano, Angelo Piana, Pier Giorgio Fallica, Andrea Canino, and Francesco Priolo. Electroluminescence and transport properties in amorphous silicon nanostructures. *Nanotechnology*, 17(5):1428, 2006.

[60] S. Prezioso, A. Anopchenko, Z. Gaburro, L. Pavesi, G. Pucker, L. Vanzetti, and P. Bellutti. Electrical conduction and electroluminescence in nanocrystalline silicon-based light emitting devices. *Journal of Applied Physics*, 104(6):–, 2008.

[61] E. H. Rhoderick. *Metal-Semiconductor Contacts.* Clarendon, Oxford, 1978.

[62] R. Tsu and L. Esaki. Tunneling in a finite superlattice. *Applied Physics Letters*, 22(11), 1973.

[63] C. B. Duke. *Tunneling in Solids.* Academic Press, 1969.

[64] T. Hori. *Gate dielectrics and MOS ULSIs: Principles, Technologies and Applications.* Springer, 1997.

[65] R. H. Fowler and L. Nordheim. Electron emission in intense electric fields. *Proceedings of the Royal Society of London. Series A, Containing Papers of a Mathematical and Physical Character*, 119(781):173–181, 1928.

[66] Ingemar Lundström and Christer Svensson. Tunneling to traps in insulators. *Journal of Applied Physics*, 43(12), 1972.

[67] D. Ielmini, AS. Spinelli, M.A Rigamonti, and AL. Lacaita. Modeling of SILC based on electron and hole tunneling. i. transient effects. *Electron Devices, IEEE Transactions on*, 47(6):1258–1265, Jun 2000.

[68] F. Jiménez-Molinos, F. Gámiz, A. Palma, P. Cartujo, and J. A. López-Villanueva. Direct and trap-assisted elastic tunneling through ultrathin gate oxides. *Journal of Applied Physics*, 91(8), 2002.

[69] F. Jiménez-Molinos, A. Palma, F. Gámiz, J. Banqueri, and J. A. López-Villanueva. Physical model for trap-assisted inelastic tunneling in metal-oxide-semiconductor structures. *Journal of Applied Physics*, 90(7), 2001.

[70] M. Specht, M. Städele, S. Jakschik, and U. Schröder. Transport mechanisms in atomic-layer-deposited Al_2O_3 dielectrics. *Applied Physics Letters*, 84(16), 2004.

[71] Wai-Jyh Chang, Mau-Phon Houng, and Yeong-Her Wang. Electrical properties and modeling of ultrathin impurity-doped silicon dioxides. *Journal of Applied Physics*, 90(10), 2001.

[72] Z.A. Weinberg and A. Hartstein. Photon assisted tunneling from aluminum into silicon dioxide. *Solid State Communications*, 20(3):179 – 182, 1976.

[73] A Hartstein and Z A Weinberg. On the nature of the image force in quantum mechanics with application to photon assisted tunnelling and photoemission. *Journal of Physics C: Solid State Physics*, 11(11):L469, 1978.

[74] G. Binnig, N. Garcia, H. Rohrer, J. M. Soler, and F. Flores. Electron-metal-surface interaction potential with vacuum tunneling: Observation of the image force. *Phys. Rev. B*, 30:4816–4818, Oct 1984.

[75] Andreas Schenk and Gernot Heiser. Modeling and simulation of tunneling through ultra-thin gate dielectrics. *Journal of Applied Physics*, 81(12), 1997.

[76] J. G. Simmons. Generalized Formula for the Electric Tunnel Effect between Similar Electrodes Separated by a Thin Insulating Film. *Journal of Applied Physics*, 34:1793–1803, June 1963.

[77] F. Jiménez-Molinos, F. Gámiz, A. Palma, P. Cartujo, and J. A. López-Villanueva. Direct and trap-assisted elastic tunneling through ultrathin gate oxides. *Journal of Applied Physics*, 91(8), 2002.

Chapter 5

Interaction with Light

Semiconductor QDs have attracted a great deal of attention for their application in the field of silicon optoelectronics [1, 2, 3], and as a light absorbing component in the third generation solar cells [4, 5]. The most well-known property of QDs is that the optical band gap depends strongly on their size, which means that their absorption and emission properties can be tuned.

Considerable material fabrication work has been done on the growth and characterization of Si QDs embedded in dielectric matrices such as oxides [6], nitrides [7] and carbides wide band gap material matrices [8]. In indirect band gap semiconductors, optical transitions are allowed only if phonons are absorbed or emitted to conserve the momentum. The localization of electrons and holes inside a QD relaxes the k-conservation requirement and creates a quasi-direct band gap.

Several optical effects have been reported under illuminating conditions as: carrier multiplication [9], the presence of multiexcitons [10] and auger recombination [11] processes. Therefore, the analysis of the electron hole lifetime is complicated due to the large number of different generation/recombination processes that can occur in semiconductors. Instead to consider all these effects, we simplify the problem to a simple and easily understandable system that takes into account the transport properties described before and the optical transitions generated by external photon field (i.e. stimulated emission/recombination).

The term "optoelectronics" is often used to discuss the study and development of electronic devices that can control, or can be controlled by, the electromagnetic field. The system response is a non-equilibrium state that results from two different driving processes: an electron flux induced by an external potential bias, and a photon flux associated with an incident radiation field. Since both processes are strongly correlated, one of these fluxes can appear as a response to the other. Thus, we can encounter

phenomena where light appears in response to electrical driving (bias potential) or, conversely, electronic current appears in response to optical illumination. These multitude of inter-related phenomena create a rich, and in many aspects still open, field of study.

Here, we describe the inclusion of the light terms in the electronic transport model developed before. We focus on the optical transitions between the electron and the hole states, stimulated generation and recombination, and the electrical response of the system under external perturbations: light and bias voltage.

This chapter is organized as follows: first of all we rewrite the rate equations to include the optical generation/recombination processes. Then, a toy example is also studied in order to understand and recognize the physical parameters that govern the electrical response of the system. In the second section, we recalculate the densities of states (DOS) and the energy levels assuming $l \neq 0$ because as we will see in the next section, the optical transitions involve states with different l quantum numbers. In the third part, a formal derivation of the QD optical properties is presented: the intraband and interband transitions. The optical properties are summarized in the absorption coefficient. Device simulations based on Si/SiO_2 QDs have been done in the fourth section. To conclude, a comparison with an experimental device is presented.

5.1 Modifying the rate equations: the light terms

The model developed in the previous chapter was used to evaluate the electrical response of the system under external bias voltage. Now, we introduce the light effects in this approach.

Following with the rate equation model, the new processes that govern the occupancy of the energy levels can be included as net fluxes. The movement of the electrons under illumination in the QDs is governed by three basic mechanisms: (i) promotion to an excited state assisted by a photon (photon absorption); (ii) relaxation transitions from excited states to the ground state (stimulated photon emission) and (iii) tunneling processes to the neighbor QDs or electrodes. We must note that the first mechanism involves intraband processes, excitation of electrons to other state of the same type (electron or hole energy states), and interband transitions that includes promotion from hole state to electron state. We only consider optical transitions between binding states neglecting the continuous DOS above/below the valence/conduction band offsets.

In the spirit of the rate equation type model [12, 13], we assume that the optical and transport processes are independent. Therefore, the rate equations have been modified in order to reflect the stimulated generation/recombination carrier processes. For each

energy level, they read as

$$q\frac{dn_j^i}{dt} = \underbrace{\frac{2\pi q}{\hbar}|T_{Lj}|^2\rho_L\rho_j^i(f_{Lj}-n_j^i)}_{\text{Left lead contribution}} + \underbrace{\frac{2\pi q}{\hbar}|T_{Rj}|^2\rho_R\rho_j^i(f_{Rj}-n_j^i)}_{\text{Right lead contributions}}$$

$$+ \underbrace{\sum_{k,i'\neq i}\frac{2\pi q}{\hbar}|T_{jk}^{ii'}|^2\rho_j^i\rho_k^{i'}(n_k^{i'}-n_j^i)}_{\text{Neighboring QDs contribution}} + \underbrace{\sum_k qR_{kj}\frac{\rho_k^i}{\rho_j^i}n_k^i(1-n_j^i) - \sum_k qR_{jk}n_j^i(1-n_k^i)}_{\text{Light terms}}, \quad (5.1)$$

where the superscript i and i' refers to the ith and i'^{th} QDs, respectively. j and k refer to the jth and k^{th} energy level of the corresponding QD. n_j^i is the non-equilibrium distribution function of the jth level in the ith QD. ρ_L and ρ_R are the DOS of the leads evaluated at the energy of the energy level j, and ρ_j^i is the degeneracy of the jth energy level of the ith QD. f_{Lj} and f_{Rj} are the distribution functions of the leads described by the Fermi Dirac distribution function. $|T_{Lj}|$ and $|T_{Rj}|$ are the transmission coefficients between the QD and the leads. If the jth energy level belongs to the electron binding states, we will use the barrier for electrons otherwise we will use the barrier for holes.

In Eq. 5.1, we have reordered the different contributions as a function of their physical "nature": the left and right lead contributions reflect the charge injection from the leads, whereas the neighboring QDs contribution is the tunneling between the QDs. The light processes are included in the two last terms. The first light term represents the stimulated carrier generation/excitation. We describe it as the optical transition probability R_{jk} that an electron in an occupied initial state k interacts with a photon. Therefore, it is promoted to an empty state j. The product of the occupancy of the energy levels involved in the optical transitions takes into account the Pauli exclusion principle [14, 15, 16]. The second light term represents the stimulated carrier relaxation/recombination and can be described in the same way as the previous one.

From the light terms in Eq. 5.1, it is derived that the incoming flux of electrons due to optical generation/excitation (positive contribution) in the final state has to be equal to the outgoing flux (negative contribution) in the initial state.

Now, we are going to focus on the physical differences between the generation and excitation processes. Up to now, we have treated the hole and the electrons indistinctly but taking into account the corresponding material parameters to describe the tunneling processes. In the previous section, we refereed to the hole current as electrons that move in hole states. This treatment is possible since the difference of the occupation functions in the tunneling current expression appears explicitly. When we include the light interaction, we use a similar treatment. The excitation process is easily explained as a "vertical" transitions in energy (involving states of the same type), either for holes or electrons. The generation process is usually explained as a creation of an electron-hole pair but, in our description, it can also be viewed as an excitation process of an electron

from a hole state to an electron state. From a point of view of the electron distribution function, the hole state empties (equivalent to generate a hole) and the electron state fills (electron generation). Thus, the previous rate equations include these two processes in an easy way.

Before describing in detail the transition probabilities R_{jk}, we focus our attention on Eq. 5.1 and on the different scenarios that are derived from it. As in the previous chapter, this set of non-lineal equations has to be solved simultaneously with the local potential in the SCF regime.

5.1.1 Toy examples: the role of each coefficient

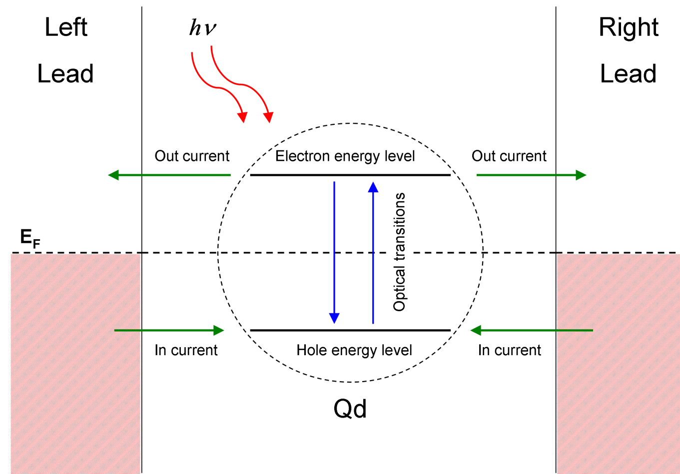

FIGURE 5.1: Scheme of the simplest system under study composed by a single QD with two energy levels. The QD is connected by tunnel junctions to the leads. The sense of the different currents terms are also shown for illumination conditions and no external bias voltage applied.

Now, we are going to simulate a single illuminated QD with a single electron and hole energy level in order to study the electrical response of this basic system as a function of the ratio between the electrical and optical terms. This QD is connected by tunnel junctions to the leads. We rewrite the rate equation for each energy level of the QD as

$$q\frac{n_e}{dt} = \frac{2\pi q}{\hbar}g_{Le}(f_{Le} - n_e) + \frac{2\pi q}{\hbar}g_{Re}(f_{Re} - n_e) + q\gamma n_h(1 - n_e) - q\gamma n_e(1 - n_h) \quad (5.2)$$

$$q\frac{n_h}{dt} = \frac{2\pi q}{\hbar}g_{Lh}(f_{Lh} - n_h) + \frac{2\pi q}{\hbar}g_{Rh}(f_{Rh} - n_h) + q\gamma n_e(1 - n_h) - q\gamma n_h(1 - n_e), \quad (5.3)$$

where the coefficients g_{Le}, g_{Re}, g_{Lh} and g_{Rh} correspond to the electron/hole tunneling transmission to the left and right lead, respectively. The optical transition probability is called γ. The scheme of the system is shown in Fig. 5.1. We have assumed the same capacitive coupling between the QD and the left and right leads. Several scenarios

appear as a function of the ratio between the optical and tunneling terms in the steady state:

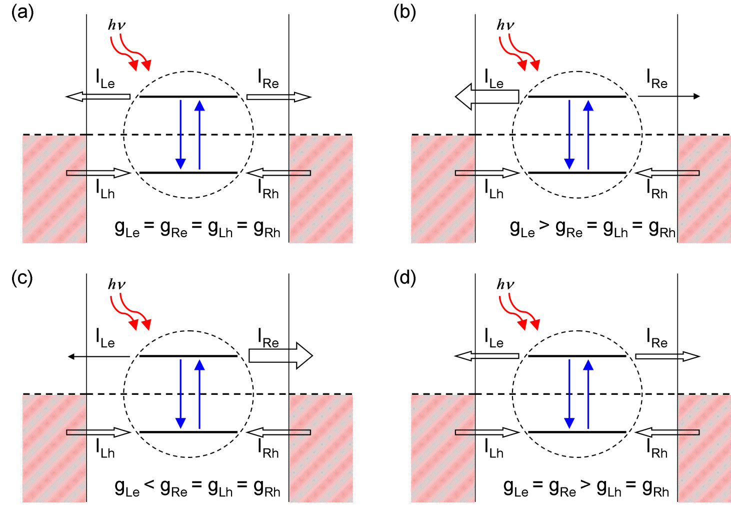

FIGURE 5.2: Scheme of a single QD under external illumination conditions and no external polarization. The QD is composed by two discrete energy levels. The magnitudes of the current components (the arrow size) and their direction are represented for different values of the tunneling transmissions: (a) $g_{Le} = g_{Re} = g_{Lh} = g_{Rh}$, (b) $g_{Le} > g_{Re} = g_{Lh} = g_{Rh}$, (c) $g_{Le} < g_{Re} = g_{Lh} = g_{Rh}$ and (d) $g_{Le} = g_{Re} > g_{Lh} = g_{Rh}$.

- $g_{Le} = g_{Re} = g_{Lh} = g_{Rh} > \gamma$: In this case, the optical terms are smaller than the electrical ones and we can neglect them. Thus, the electrical response of the system does not change much respect to the dark case studied in the previous chapter.

- $g_{Le} = g_{Re} = g_{Lh} = g_{Rh} < \gamma$: The optical terms dominate the rate equation. Let's focus on the $V = 0$ case. In dark conditions, the hole energy level is fill whereas the electron one is empty. The light interaction creates a new flux between these two levels, filling the electron level and emptying the hole one. However, there are also fluxes from the leads to the hole state in order to keep filled the energy level. Moreover, the promoted electrons go out to the empty states in the leads generating a current flux. A simple analysis of the current (using basic Kirchhoff's law) can be done: $I_{opt} - I_{Le} - I_{Re} = 0$ for electrons and $I_{Lh} + I_{Rh} - I_{opt} = 0$ for holes, respectively; where I_{opt} is the optical flux and I_{Le} and I_{Re} are the electron fluxes whereas I_{Lh} and I_{Rh} are the hole fluxes to the left and right leads, respectively. We have assumed that the incoming currents to the QD are positive. Since the tunneling coefficients for electrons and holes are equal, we obtain that the electron and hole currents compensate each other being zero the net current. In Fig. 5.2(a) we show the scheme of the different current contributions.

- $g_{Le} \neq g_{Re} = g_{Lh} = g_{Rh} < \gamma$: We are going to concentrate in the $V = 0$ case. We assume $g_{Le} > g_{Re}$ and the symmetry of the system respect to the leads is broken. The light promotes carriers from hole to electron states whereas the leads inject carriers. However, the electrons flow from the QD to the left lead faster than the leads inject electrons to the hole level. This fact also modifies the optical rate. Thus, the currents incoming and outgoing are not equal creating a net current flux. This fact is shown in Fig. 5.2(b) where the different magnitudes of the currents are represented by arrows. In this case, the net current goes from the right lead to the left one. It is important to note that the system has lost charge respect the equilibrium state since the electron transmission coefficients are greater than the hole ones.
  A similar result is obtained for the $g_{Le} < g_{Re}$ case. In this scenario, the carriers are injected into the QD hole level faster than the electrons are removed from the electron level obtaining a net current in the opposite direction as the previous case, see Fig. 5.2(c), and the QD increases the charge.

- $g_{Lh} \neq g_{Rh} = g_{Le} = g_{Re} < \gamma$ We assume $g_{Lh} > g_{Rh}$. In a similar way as before, the leads inject carriers faster than electron energy level is empty. Thus, the QD gains charge and a net current is created.
  For the $g_{Lh} < g_{Rh}$ situation, the fluxes from the hole state can not compensate the fluxes from the electron state an a net current appears. Therefore, the QD looses charge.

- $g_{Le} = g_{Re} \neq g_{Lh} = g_{Rh} < \gamma$ For this configuration the net current is also zero as in the first case, Fig. 5.2(d). The main difference appears in the QD charge: for the $g_{Le} = g_{Re} > g_{Lh} = g_{Rh}$ case, the system loses charge since the extraction mechanism is faster than the injection one whereas for the $g_{Le} = g_{Re} < g_{Lh} = g_{Rh}$ case, the injection mechanism is faster. Thus, the charge increases.

Summarizing the obtained results, we have observed that the system is strongly dependent on the relation between the optical and the tunneling terms. In order to obtain a net photogenerated current in the $V = 0$ case, the system must be connected asymmetrically to the leads. Therefore, the geometry of the system under study appears as an important point that modifies and controls the electrical response of the system. In addition, the charge in the QD also depends on the tunneling couplings.

Concerning the $V \neq 0$ case, the occupation of the electron and hole energy levels are governed by the applied bias voltage. For the $V = 0$ case, we expect that the electron level is empty and the hole level is fill however, this scenario can be changed with the external applied bias potential. This fact affects to the optical transitions and the simple cases studied previously can not be used here since both process are strongly dependent on each other. Nevertheless, we can argue that for lower optical terms than current terms (small optical transitions rates or high applied voltage) the electrical response of

the system is similar to the dark case. Thus, for low voltages the optical term dominates but when the voltage increases, the electrical response of the system recovers the dark trend.

5.2 Complete energy level spectrum

Up to now, we have described the internal electronic structure of the QD in the simplest way: as a finite potential well in the Effective Mass Approximation (EMA) and only considering the $l = 0$ solutions. In the previous chapter, we have discussed the importance for the transport process of the correct description of the QD internal properties.

For light processes, in which photons of sufficient energy can excite electrons from filled states to empty ones, it seems very reasonable to think that the electronic properties of the system will also play an important role. Therefore, keeping as simple as possible the model to describe the electronic properties of the QD, we use the same approach presented before but unrestricted for the l quantum number. The Hamiltonian of the QD can be written as

$$H = -\frac{\hbar^2}{2m_e}\nabla_e^2 - \frac{\hbar^2}{2m_h}\nabla_h^2 + V_e + V_h + V_{h-e} + E_g, \tag{5.4}$$

where V_e and V_h are the finite confining potentials and V_{h-e} is the Coulomb interaction between electron and holes. As we will discuss latter, we assume that the interaction potential between the carriers is small in comparison with the kinetic part of the Hamiltonian. Therefore, the total Hamiltonian is separable in the electron and hole single particle contributions. We present here the derivation of the wave functions and the energy levels for the electron case. Concerning the hole wave function and the energy levels, the calculi are straightforward.

5.2.1 Single particle properties

The electron wave function for the QDs can be represented as the product of the periodic Bloch function $u_\kappa(\mathbf{r})$ and an envelope function [17]. The envelope function ϕ_{env} describes the motion of particles in the confinement potential. This "envelope function approximation" is valid when the QD diameter is much larger than the lattice constant of the crystal. The electron wave function can be written as

$$\psi_e = u_\kappa \cdot \phi_{env}. \tag{5.5}$$

The envelope function is the solution of the single particle Schrödinger equation. The radial part reads as

$$\left\{-\frac{\hbar^2}{2m_e}\left[\frac{\partial^2}{\partial^2 r}+\frac{2}{r}\frac{\partial}{\partial r}\right]+\frac{l(l+1)\hbar^2}{2m_e r^2}+V_e(r)\right\}R_l(r)=E_l R_l(r), \tag{5.6}$$

here, m_e is the electron effective mass which is different inside and outside the QD. l is the angular momentum quantum number. $V_e(r)$ is the finite confining potential

$$V_e(r)=\begin{cases} 0 \text{ for } r<R \\ V_0 \text{ for } R>r \end{cases}, \tag{5.7}$$

where R is the QD radius and V_0 is the value of the confining potential, i.e. the band offset between the QD and the surrounding material. E_l is the electron energy eigenvalue and $R_l(r)$ is the radial wave function. The angular dependence of the wave function, $Y_l^m(\theta,\phi)$, is given by the spherical harmonics.
The solution inside the QD is

$$R_l(r)=A\; j_l(k_0 r), \tag{5.8}$$

where $j_l(k_0r)=\sqrt{\frac{\pi}{2k_0 r}}J_{l+1/2}(k_0 r)$ is the spherical l^{th} order Bessel function and $k_0=\sqrt{\frac{2m_e}{\hbar^2}E_l}$.
The solution in the oxide is

$$R_l(r)=Bh_l^{(1)}(k'r), \tag{5.9}$$

where $h_l^1(k'r)$ is the spherical Hankel function and $k'=i\sqrt{\frac{2m_{Ox}}{\hbar^2}(V_0-E_l)}$. m_e and m_{Ox} are the electron effective masses in the QD and in the oxide, respectively. A and B are the normalization constants of the wave function. Therefore, the electron envelope function is written as

$$\phi_{env}=Aj_l(k_0r)Y_l^m(\theta,\phi)\Theta(R-r)+Bh_l^{(1)}(k'r)Y_l^m(\theta,\phi)\Theta(r-R). \tag{5.10}$$

Here, we have used the Heaviside step-function $\Theta(r)$ to separate the different space regions.

The continuity of the wave function and the probability flow conservation impose the condition

$$\frac{1}{m_{Ox}}\frac{j_l(k_0r)|_R}{\frac{\partial j_l(k_0r)}{\partial r}|_R}=\frac{1}{m_e}\frac{h_l^{(1)}(k'r)|_R}{\frac{\partial h_l^{(1)}(k'r)}{\partial r}|_R}. \tag{5.11}$$

From this condition, the binding states for each l are obtained. Regrettably, an analytical expression for the binding states does not exist. Thus, Eq. 5.11 has to be solved numerically. In Fig. 5.3(a), we show the numerical solutions of Eq. 5.11. The binding states are the circle points. Moreover, in Fig. 5.3(b) the radial probability distribution inside and outside of the QD for the $l=0$ case is also shown.

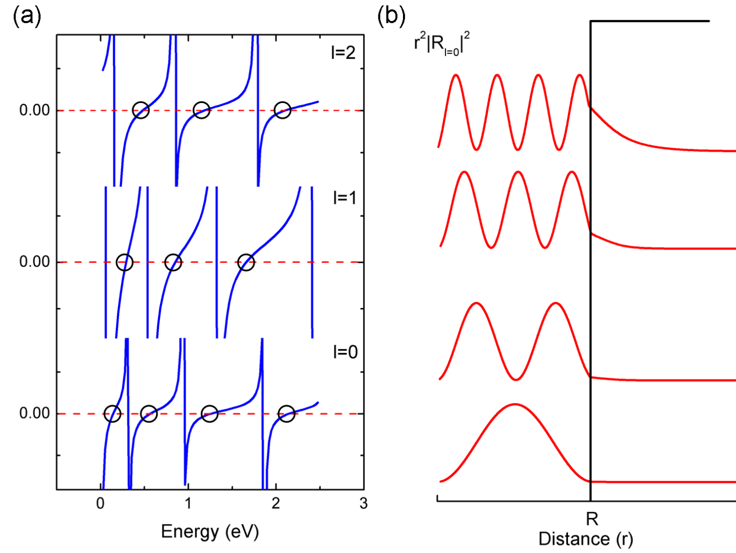

FIGURE 5.3: (a) Representation of Eq. 5.11 for the first angular quantum numbers. The binding states for each quantum number l are the points that cross $y = 0$. (b) Scheme of the radial distribution $r^2|R_l(r)|^2$ inside and outside the QD for the $l = 0$ case.

We remark that the degeneracy of each binding state is $(2l + 1)$, which implies that the number of binding states increases dramatically when the QD radius increases. Here, we have omitted the value of bulk energy gap of the material because it only adds a constant shift in the energy levels. Since the wave functions and the energy levels inside the QD are obtained, the DOS can be computed as in the previous chapters.

5.2.2 Pair states

The above description did not take into account the Coulomb attraction between the electron and the hole. In the following, we refer to the Coulomb interacting electron-hole pair as an exciton [18].

If the QD radius (R) is smaller than the bulk-exciton Bohr radius $R < a_B$, which is defined as $a_B = 0.529\varepsilon_r m_0(1/m_e + 1/m_h)$ [19] where ε_r is the dielectric permitivity of the QD, electron and hole are closer together than they would be in the corresponding bulk material. This leads to a dramatic increase of the pair energy with decreasing QD size. As a function of the QD radius, the kinetic part of the energy, that includes the confining potential, varies like

$$< H_e + H_h > \propto \frac{1}{R^2}, \tag{5.12}$$

whereas the interaction part behaves like

$$< V_{e-h} > \propto \frac{1}{R}. \tag{5.13}$$

To estimate the pair energy for small QD radius, $R << a_B$, it is a reasonable first-order approximation to consider the electrons and the holes essentially as non-interacting particles and ignore the Coulomb energy in comparison to the kinetic energy. This corresponds, in the frame of the EMA, to the strong confinement regime [20, 21, 22]: electrons and holes are considered as independent particles. This yields that the exciton energy E_{ex} is the sum of the electron and hole single particle energy states (obtained from Eq. 5.11)

$$E_{ex} = E_g + E_{e,lm} + E_{h,lm} \tag{5.14}$$

where we have written the different terms: E_g is the bulk band gap of the material; $E_{e,lm}$ and $E_{h,lm}$ are the single particle energy states of the electrons and holes, respectively. Therefore, the exciton is well described by the product of the single particle electron-hole wave functions $\psi_{eh}(r_e, r_h) = \psi_e(r_e)\psi_h(r_h)$ where we have omitted the spin terms for clarity.

Concerning the Coulomb interaction, it is not possible to solve analytically the electron-hole pair Schrödinger equation Eq. 5.4. However, in the strong confinement regime, the Coulomb interaction can be treated as a perturbation [23] adding a new energy contribution that reduces the optical effective gap [24] (i.e. the first excitonic level). An estimation of this energy shift can be obtained using the approximation presented in [25]

$$E_{e-h} \approx -\frac{2e^2}{4\pi\varepsilon_0\varepsilon_r}\int_0^R r_h R_l^2(r_h)dr_h \int_0^{r_h} r_e^2 R_l^2(r_e)dr_e. \tag{5.15}$$

In the Appendix section, we have included a comparison between the complete DOS obtained using EMA within the finite potential well and DFT calculations for Si/SiO_2 QDs.

5.3 Derivation of the optical properties

In this section, we introduce the calculation basis to simulate the dynamics of the electrons excited by external radiation. The system is subjected to electromagnetic field (laser/light source), which induces stimulated transitions: absorption and emission. The calculus starts from the previous obtained wave functions and binding energy levels, and evaluate inter- and intra- band transitions within the validity of Fermi's Golden rule. Here, we describe the approximations that we have assumed:

- Atomic levels: no band dispersion. This requirement includes the *discreteness of the energy levels*, as we have shown from the Schrödinger equation. Moreover, optical transitions from binding states to the continuum of states above the oxide conduction/valence band offsets are not considered.

- Energy levels are fixed also after the excitation. The *excitonic effects to the energy are not considered.*

- *Dipole approximation*, $exp(i\mathbf{k}\cdot\mathbf{x}) \approx 1$, valid for visible frequencies and lengths on the order of Å.

- Validity of the *Fermi's Golden-rule.*

- 2nd *order processes are neglected*: Raman, Rayleigh, Thomson, etc. These are generally much less probable with respect to 1st order processes.

We will show in a general trend the derivation of the optical transition probabilities. A detailed explanation can be easily found in many textbooks [15, 16, 17].

We start with the Hamiltonian that describes the electron-photon interaction. To describe the electromagnetic field, we introduce a vector potential $A(\mathbf{r},\mathbf{t})$ and a scalar potential $\phi(\mathbf{r},\mathbf{t})$. Because of gauge invariance, the choice of these potentials is not unique. For simplicity, we choose the Coulomb gauge [26], in which

$$\phi = 0 \text{ and } \nabla\cdot\mathbf{A} = \mathbf{0}. \tag{5.16}$$

Using the minimal coupling [27], that implies $\vec{p} \to \vec{p} - (e/c)\vec{A}$, the interaction Hamiltonian that describes the motion of a charge $-e$ due to the presence of the photon field can be written as

$$H' = -\frac{e}{mc}\vec{A}\cdot\vec{p} + \frac{e^2A^2}{2mc^2}. \tag{5.17}$$

For the purpose of calculating linear optical properties, we can neglect the term $e^2A^2/(2mc^2)$, which depends quadratically on the field. Thus, the interaction Hamiltonian can be written as

$$H' \approx -\frac{e}{mc}\vec{A}\cdot\vec{p}. \tag{5.18}$$

With regard to the spatial dependence of the vector potential we can write

$$\vec{A} = \vec{A_0}\cdot exp\left[i(\vec{k}\vec{x} \pm \omega t)\right] \tag{5.19}$$

where, for a loss-less medium, $k = nw/c = 2\pi n/\lambda$ is a slowly varying function of $\vec{x}$ since $2\pi n/\lambda$ is much smaller than typical wave vectors in solids. Here n, w, and λ are the real part of the refraction index, the optical frequency and the wavelength of light, respectively. The electric dipole approximation corresponds to expanding the $exp(i\vec{k}\cdot\vec{x})$ factor in a Taylor series and neglecting the k-dependent terms.
In a general form, using the Fermi Golden Rule the transition probability from initial state l to final state l' per unit volume and time is written as

$$R_{ll'} = \frac{2\pi}{\hbar}|M_{l'l}|^2\delta(E_{l'} - E_l \pm h\nu). \tag{5.20}$$

The + sign corresponds to photon emission and the − to photon absorption. Using the dipole approximation $\vec{A} = A_0\hat{e}$ where $\hat{e}$ is the polarization vector of the light, the matrix element reads as

$$M_{l'l} \approx < \psi_{i,l}(\mathbf{r})|\hat{e}\cdot\vec{p}|\psi_{j,l'}(\mathbf{r}) > . \tag{5.21}$$

The subscript i and j refer to electron and hole states. The matrix element is composed by three different terms

$$M_{l'l} \approx < u_{\kappa e}|u_{\kappa e} >< \phi^{l}_{env,e}|\hat{e}\cdot\vec{p}|\phi^{l'}_{env,e} >$$
$$+ < u_{\kappa h}|u_{\kappa h} >< \phi^{l}_{env,h}|\hat{e}\cdot\vec{p}|{\phi^{l}}'_{env,h} > + < \phi^{l}_{env,e}|{\phi^{l}}'_{env,h} >< u_{\kappa e}|\hat{e}\cdot\vec{p}|u_{\kappa h} >, \tag{5.22}$$

where we have used the orthogonality property of the Bloch function ($< u_{\kappa i}|u_{\kappa j} >= \delta_{i,j}$). The three contributions corresponds to: (1) intraband transition between electron states, (2) intraband transition between hole states and (3) interband transitions between electron and hole states.

The total transition rate between the initial l and final l' state under the influence of the interaction Hamiltonian described in Eq. 5.18 can be written as

$$R_{ll'} = \frac{16\pi^2\alpha}{\sqrt{\varepsilon_r}\Omega} I(h\nu)|M_{l'l}|^2\delta(E_{l'} - E_l \pm h\nu), \tag{5.23}$$

where α is the fine structure constant ($\approx 1/137$), ϵ_r the QD dielectric permitivity, Ω is the QD volume, $I(h\nu)$ is the flux of the incident light and ν is the photon frequency. $E_{l'}$ and E_l are the energy levels of the final and initial states, respectively.

5.3.1 Intraband transitions

The intraband transitions reflect the excitation of an electron inside the same band. For our case, since our DOS are not continuous, it implies that the electron moves only in the electron or hole states.
$M_{l'l}$ is the dipole matrix element averaged over all polarizations of the incident light

$$|M_{l'l}|^2 = \frac{1}{3}\left\{|x_{l'l}|^2 + |y_{l'l}|^2 + |z_{l'l}|^2\right\}, \tag{5.24}$$

where the polarization in the z-direction is

$$z_{l'l} = \int_0^\infty R^*_{l'}(r)R_l(r)r^3dr \int Y^*_{l'm'}Y_{lm}cos\theta d\Omega \tag{5.25}$$

and we have used $z = rcos\theta$. $R_l(r)$ is the radial part of the wave function. It is straightforward to calculate the matrix elements in the other two directions. Here, we have used the relation $< \phi_f|\vec{p}|\phi_i >= im\omega_{fi} < \phi_f|\vec{x}|\phi_i >$ where $\omega = (E_l - E'_l)/\hbar$. The selection rules for such transitions are determined by the angular part of Eq. 5.25. It

can be readily shown that the allowed transitions must fulfill the condition $|l - l'| = \pm 1$ and $|m' - m| = 0, \pm 1$.

5.3.2 Interband transitions

The interband transitions involve the electron and the hole states. They represent the promotion of an electron from a hole state to an electron state. Whereas in the previous case the transition corresponds to only one electron/hole, in this case, the transition involves two particles (electron-hole pair generation).
In order to compute the optical response, the dipole matrix element is written as [17]

$$|M_{ll'}|^2 = |\int dr^3 \phi_e^{l\,*}(r) \phi_{\ h}^{l'}(r)|^2, \tag{5.26}$$

where ϕ_e and ϕ_h are the single particle functions. The transition matrix element is only non-zero for electron and hole with identical quantum number and we derive the optical selection rules for interband transitions: $|l_e - l_h| = 0$ and $|m_e - m_h| = 0$. Since we only consider the single exciton creation, the electron-hole pair is created from the vacuum state to an state in which the electron an the hole have the same quantum numbers.

5.3.3 Absorption coefficient

The absorption coefficient is one of the most important experimental parameters, which is defined as the power removed from the incident beam, per unit volume, per unit incident flux of electromagnetic energy,

$$\alpha(h\nu) = \frac{(h\nu) \times \text{number of transitions/unit volume/unit time}}{\text{incident electromagnetic flux}}. \tag{5.27}$$

Since we have computed the transitions probabilities in the previous section, the absorption coefficient is easily obtained as

$$\alpha(h\nu) = \sum_i \frac{16\pi^2 \alpha}{\sqrt{\varepsilon_r}\Omega} h\nu |M_i|^2 \delta(\triangle E_i - h\nu), \tag{5.28}$$

where the subscript i refers to all the possible processes and $\triangle E_i$ is the energy level difference of the initial and final state. If we wish to calculate the absorption spectra at finite temperature, we also need to include the Fermi functions that represent the occupation of the initial and final states.

Summarizing the optical properties, the obtained selection rules are

- Intraband transition: allowed transitions only for $\triangle l = \pm 1$ and $\triangle m = 0, \pm 1$.
- Interband transition: allowed transitions only for $\triangle l = 0$ and $\triangle m = 0$.

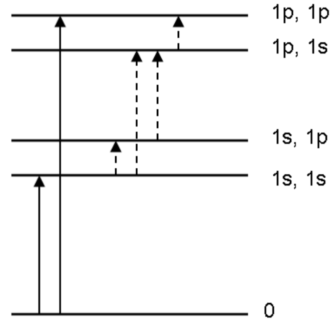

FIGURE 5.4: Energy level scheme of the states with zero or one electron-hole pair. We describe the states as a function of the electron and the hole angular momentum. The interband transitions are the continuous arrows whereas the intraband transitions are the dashed ones.

In Fig. 5.4, we plot schematically the energy spectrum of the energetically lowest one-electron-hole-pair states with angular momentum $l = 0, l = 1$. The solid lines indicate the most important dipole-allowed interband transitions. The dashed lines show the intraband transitions involving a change of the state of the electron or the hole.

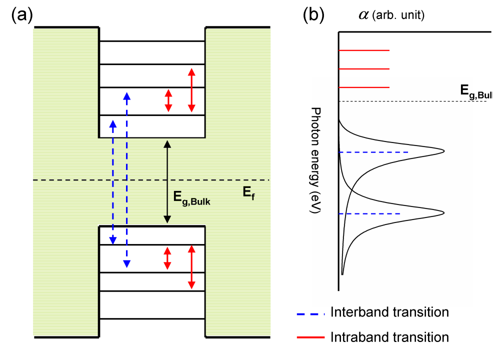

FIGURE 5.5: (a) Scheme of the binding states in the QD. Several optical transitions are shown, interband (blue lines) and intraband transitions (red lines), respectively. The equilibrium Fermi level (E_f) is also shown. (b) Representation of the absorption spectra for the previous system. The optical element matrix are shown as a vertical lines placed at the photon energy of the transitions (red lines for intraband and blue ones for interband). The absorption coefficient is the sum of individual absorption peaks related to each transition.

In Fig. 5.5(a) we show and scheme of the optical interband and intraband transitions. It is important to note that the intraband transitions are not obtained when the absorption spectra is measured since this measure is usually done without external polarization bias voltage. Thus, the probability of optical transitions between states of the same type is practically zero. In contrast, optical transitions that involve electron and hole states are more favorable. Fig. 5.5(b) shows the difference in the absorption coefficient for intraband and interband transitions. However, we are going to study the optical response of different systems under external bias voltage polarization making possible intraband transitions. Therefore, we include them as a “possible” transitions.

5.4 Optical device simulations

Since the theory of the light interaction has been studied and the optical transition rates are obtained, these new terms can be included in the rate equations to simulate the electrical response of the system under external light illumination.

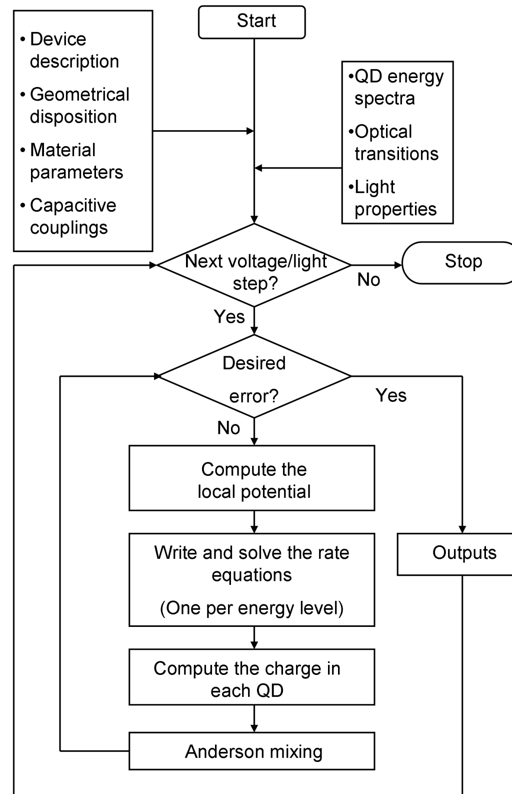

FIGURE 5.6: Scheme flowchart of the code that implements the methodology described in this chapter. The code is based on the previous presented one (SCF core) but several changes have been done in order to include the light.

The modifications in the rate equations in order to include the light processes have been included in the code in order to simulate different arrangements of QDs. The scheme flowchart of the code is presented in Fig. 5.6. It uses several parts of the previous developed code, such as the capacitive calculations and the transmissions coefficients. Basically, it is organized as follows:

1. Define the device's geometry: distance between the different elements of the system (QDs and leads, QDs-QDs), capacitive couplings.
2. For each QD of given radius, calculate: energy level spectra and optical transition elements. Solving the Schrödinger equation and obtaining the optical matrix elements.
3. Initialize the self-consistent field (SCF) for a given bias voltage and/or incident light conditions and solve the rate equations and the Poisson equation until a

desired convergence has been achieved. In this case, we write a rate equation per energy level. To solve them, since they form a set of non-lineal equations, the Newton-Raphson method has been implemented.

4. Calculate the final outputs.

5.4.1 Si/SiO_2 QDs: simulations

Here, we are going to simulate different kinds of systems based on Si QDs embedded in a SiO_2 matrix to demonstrate the feasibility of the previous developed model. First of all, the internal properties of the Si QDs are presented: the E_{gap} and the absorption spectra. Finally, a systematic study of the electrical and optical response of the basic system, an array of QDs placed between two electrodes, has been done.

5.4.1.1 Si QDs: optical properties

m^*_{ECB} (m_0)	0.40	$\phi_{1,ECB}$ (eV)	3.1
m^*_{EVB} (m_0)	0.30	$\phi_{1,HVB}$ (eV)	-4.5
m^*_{HVB} (m_0)	0.32	E_{gap} (eV)	1.12
$m^*_{Qd,CB}$ (m_0)	0.33	ε_{rSiO_2} (ε_0)	3.9
$m^*_{Qd,VB}$ (m_0)	0.28	ε_{rSi}	11.7

TABLE 5.1: Parameters used in the simulation in order to describe Si QDs embedded in SiO_2 insulator matrix. In all the simulations we assume T=300K.

The study of the energy states of the QD has been done assuming the finite spherical potential well model developed previously using the Si and SiO_2 effective masses and the confinement potentials assuming bulk values. In Table 5.1 we show the list of parameters used to describe the material: the oxide (m^*_{ECB} and m^*_{HVB}) and QD ($m^*_{Qd,CB}$ and $m^*_{Qd,VB}$) effective masses as well as the confinement potentials for electrons ($\phi_{1,ECB}$) and holes ($\phi_{1,HVB}$), respectively.

The wave functions and the binding states appear from the solution of the Schrödinger equation Eq. 5.6 and Eq. 5.11, respectively. Using the effective masses and the bulk Si permittivity described in Table 5.1, the bulk exciton Bohr radius is estimated as $a_B = 40.86$ Å[33]. Thus, for QD radius $R < a_B$ the strong confinement regime is valid. Before continuing, we study the obtained E_{gap}, the energy difference between the first electron and hole binding states. In Fig. 5.7, we show the obtained dependence of the E_{gap} as a function of the QD radius, and it is compared to experimental data obtained from photoluminescence measurements [28, 29, 30, 31, 32]. As it is seen, the EMA, using the values of Table 5.1, can reproduce the measured experimental E_{gap}.
An estimation of the energy shift due to the electron-hole Coulomb interaction for Si QD

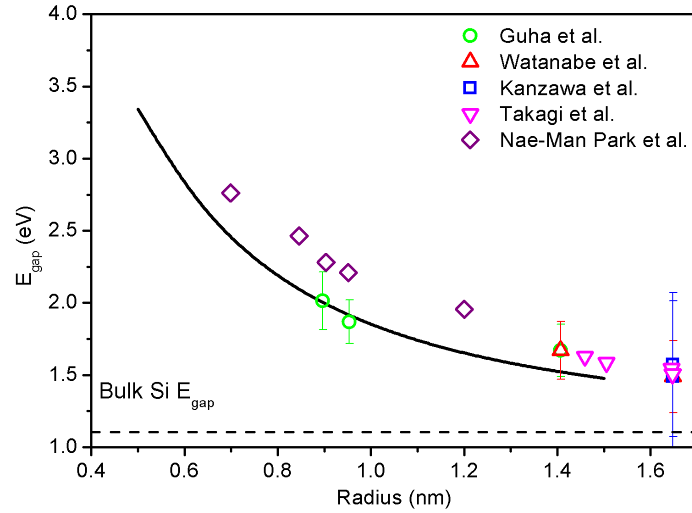

FIGURE 5.7: Dependence of the obtained E_{gap} as a function of the radius of the Si QD without taking into account the exciton shift. For comparison, experimental data obtained from photoluminescence measurements are presented [28, 29, 30, 31, 32].

of $R = 1$ nm can be obtained using Eq. 5.15. The interaction energy is $E_{e-h} \approx -0.138$ eV for the first allowed transitions, from vacuum state to the generation of electron and hole in the first s-state ($l = 0$). This effect decreases the optical band gap but, as can be seen from Fig. 5.7, the effective masses used to describe the QD agree with experimental measurements for small radius, reflecting that this effect is included in the effective mass value.

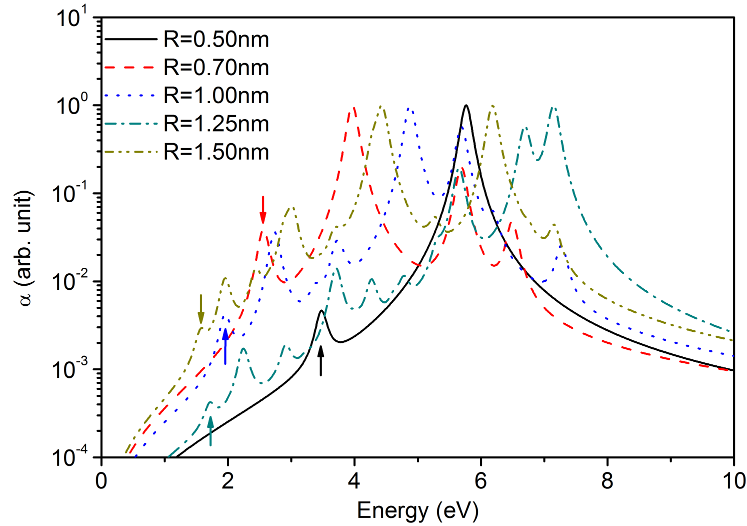

FIGURE 5.8: Simulated absorption spectra in the equilibrium state for different QD radii. The summation of all the contributions to the spectra has been done according to the Fermi Dirac distribution function, where for simplicity, the Fermi level has been placed in the energy origin, $\mu = 0$. The arrows represent the value of the E_{gap} for each QD radius.

The evolution of the simulated spectra as a function of the QD radius is presented in

Fig. 5.8. When the QD becomes larger, the number of energy states in the QD increases obtaining more possible optical transitions. Moreover, the value of E_{gap} decreases [34] thus, a redshift of the spectra is observed. For high photon energies, the absorption spectrum decreases since we only consider the transitions between the discrete energy states of the QD. Therefore, we neglect the continuum conduction and valence band states, and all the possible transitions from/to these bands.

For simplicity, we assume an incident monochromatic light with irradiance $I(h\nu) = 1Wm^{-2}$ for all the following simulations.

5.4.1.2 Single QD: the symmetry role

The first system under study is a single Si QD under illumination connected to two electrodes with a constant external bias voltage applied. From Eq. 5.1, many scenarios appear as a function of the value of the optical and transport terms. We study the particular case for $V = 0$. If the transport terms are greater than the optical ones, the non-equilibrium distribution function of the energy levels will follow the Fermi Dirac distribution function since the optical terms are a small perturbation. When the optical term increases, equal generation of electron and holes appears. Both carriers tend to diffuse to the electrodes creating currents and, depending on the probability of these transitions, the QD could be charged as we have explained before.
When an external bias voltage is applied the distribution functions of the two leads differ and a net current appears. Overlapped to this, the optical processes appear filling/emptying levels and adding new conductive channels to the transport enhancing the total current.

The results of the single QD are shown in Fig. 5.9. We present two scenarios: (a) the QD symmetrically connected to the leads and (b) in asymmetric configuration. An interesting result appears for $V = 0$. In the symmetrically coupled system (a), the current is zero since the incoming hole currents for each side equals the outgoing electron currents. Therefore, the net current is zero because the electron and hole currents compensate each other. This result derives intuitively from the rate equation, as we showed previously. Therefore, in order to generate a net photocurrent the symmetry of the QD respect to the leads must be broken, hence, different coupling to the leads are needed as is shown in the asymmetric case (b).

When an external bias voltage is applied, the transmission coefficients between the QD and the two leads change. Thus, the system becomes asymmetric and a net current appears. The current peaks are related to the maximum transition probabilities for an incident photon reflecting the absorption spectra. When the voltage increases, the current tends to be independent of the incident photon energy $h\nu$. This effect is the result of competition between two processes, the pure light current term and the external bias

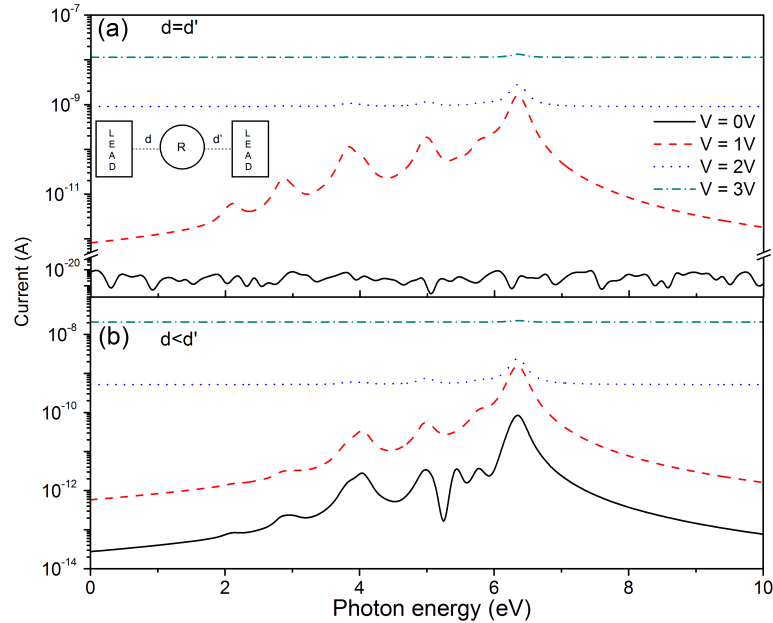

FIGURE 5.9: Photocurrent as a function of the energy of the incident light with an external applied bias voltage. In the inset a scheme of the system is presented, a QD of $R = 1.06nm$ is placed between the two electrodes. (a) Symmetric system $d = d' = 1.78nm$. For $V = 0$ case the current is zero while for $V \neq 0$ the symmetry of the system is broken and net current appears. (b) Asymmetric system $d = 1.47$ nm and $d' = 2.09$ nm. A net current is obtained even at $V = 0$. The current peaks refers the position of the maximum optical transition probabilities.

voltage term. For small voltages, the optical terms dominate and the optical transition peaks are observed, but when the voltage increases the tunneling currents become the most important terms and the current appears as a photon energy independent.

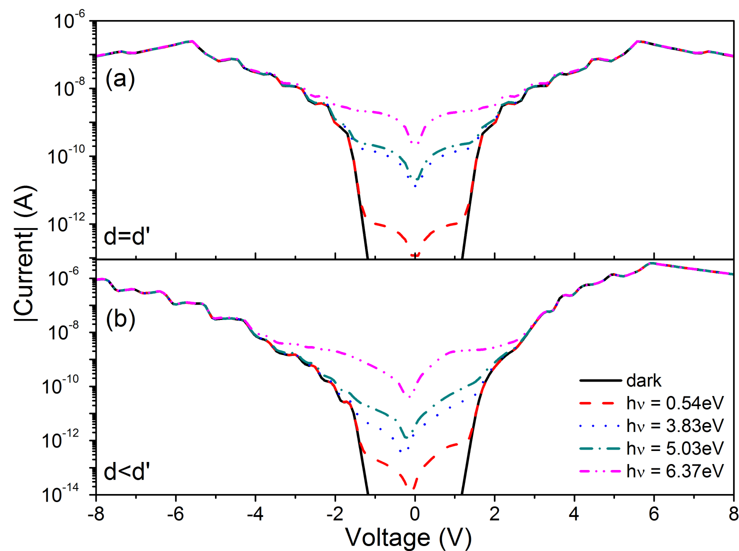

FIGURE 5.10: (a) The total I(V) curve (in absolute value) for the symmetric system in dark case and under different illumination conditions (incident photon energies). (b) The total I(V) curve (in absolute value) for the asymmetric system in dark case and under different illumination conditions (incident photon energies).

In the same way, in Fig. 5.10 we show the obtained current voltage curve I(V) under external illumination for the same previous system as a function of the energy of the incident photon. In Fig. 5.10(a-b) we show the current for the symmetric and asymmetric structure respectively. As it was demonstrated, the symmetry of the dark I(V) curves depends on the symmetry of the coupling to the leads, and current plateaus appear when conduction channels are opened. For the illuminated case, the main differences appear for small voltages. The I(V) curve looses the step like behavior since the occupancy of the energy levels are not sequential with the applied bias voltage due to optical transitions. Moreover, the optical transitions tend to fill the electron states while hole states become emptied increasing the electron/hole currents. As a consequence, more conducting channels are opened and the total current is bigger than in the dark case.

5.4.1.3 Parallel case

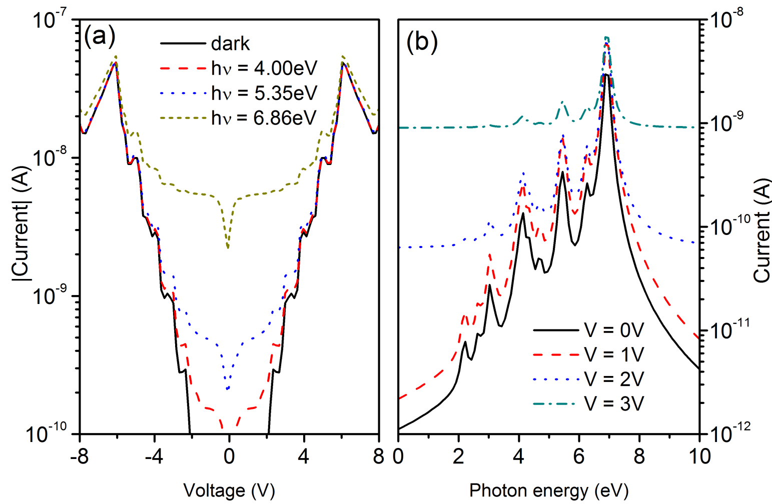

FIGURE 5.11: The QDs radii are $R_1 = 1.0$ nm and $R_2 = 0.8$ nm respectively. The distances between the first QD (QD_1) and the leads are $d_{L1} = 2.5$ nm and for the second one (QD_2) $d_{L2} = 2.5$ nm. The distance between the QDs is $d_{12} = 3$ nm. All the distances are measured from the center of the QDs. (a) The total I(V) curve (in absolute value) for the parallel system in dark case and under different illumination conditions (incident photon energies). (b) Photocurrent as a function of the photon incident energy for different applied bias voltage.

Now, we study the system composed by two QD in a parallel configuration. We use two QD of different radius in order to obtain different optical transitions.

The rate equations for each energy level of the QDs have three contributions: the leads, the neighbor QD and the optical contributions. In Fig. 5.11(a), we show the I(V) curve under different incident photon energies. These photon energies are related to the maximum absorption peaks, for $R = 0.8$ nm and $R = 1.0$ nm QDs. In a previous chapter, we have demonstrated that in parallel configuration the total dark current trough the system is the sum of the individual QD terms. At low voltages, the optical

terms dominate in the rate equation and the obtained I(V) curve differs from the dark curve. As shown before (in the single QD case), this trend is a competition between the optical transition probabilities and the transmission probabilities. For low voltages, the barriers are not transparent enough. Therefore, electron/holes are photogenerated in the QD changing the distribution function of the QD creating net fluxes incoming/outgoing from the QD to the leads. The electrons tend to move from the QD to leads and the holes follow the opposite direction, obtaining a net current when both currents do not compensate each other. When the voltage increases, the barriers are bended and the tunneling probability increases as well. Then, the optical term becomes smaller than the electrical terms and the dark trend is recovered. When the energy of the incident photon increases, the optical transitions involve the higher energy levels, which have the maximum transmission probabilities increasing the current.
Moreover, in this case, the electrons can also move to the other QD. Thus, a current between QDs appears and breaks the symmetry respect to the leads obtaining a net current for the $V = 0V$ case (Fig. 5.11(b)). As in the previous case, when the polarization voltage increases the photocurrent peaks tend to disappear. Since the two QDs have different radii, the optical transitions occur at different photon energy and the obtained photocurrent reflects both absorption spectra.

5.4.1.4 Serial configuration

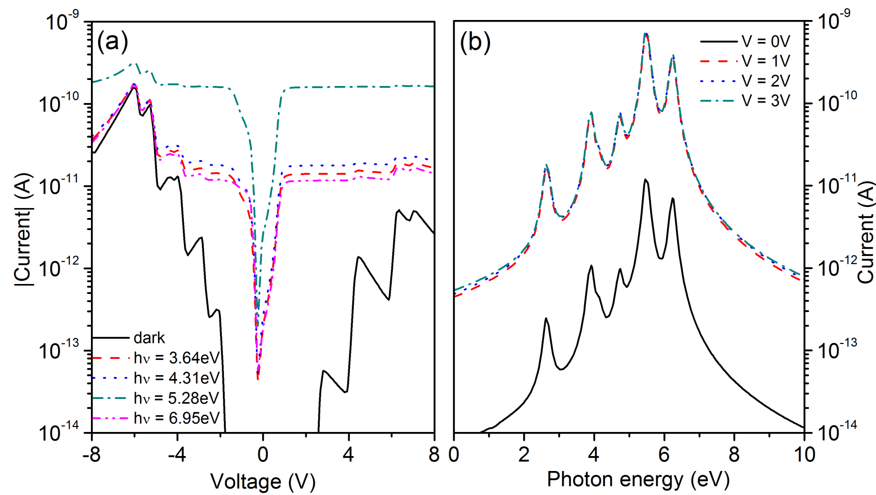

FIGURE 5.12: The QDs radii are $R_1 = 0.3$ nm and $R_2 = 0.8$ nm. The first QD is placed at $d_{L1} = 2.5$ nm and $d_{R1} = 5.1$ nm and the second QD is placed at $d_{L2} = 4.8$ nm and $d_{R2} = 2.8$ nm from the left and right leads respectively. The distance between both QDs is $d_{12} = 2.3$ nm. All the distances are measured from the center of the QDs. (a) The total I(V) curve (in absolute value) for the serial system in dark case and under different illumination conditions (incident photon energies). (b) Photocurrent as a function of the photon incident energy for different applied bias voltage.

The third type of arrangement is two QD in a serial configuration. This kind of arrangement has demonstrated the possibility of filtering the current trough the position

of the energy levels. Since overlapping between the energy levels of the QDs is necessary, only a few conduction channels are opened and the current is strongly dependent on the electrostatic coupling of the QDs obtaining NDR in the I(V) curve. We proceed in a similar way as in the previous case, the electrical response under an external bias voltage and under illumination with different photon energy. In this configuration, each QD is connected to one electrode (left or right) and the neighbor QD.

First of all, we present the obtained dark and illuminated I(V) curves in Fig. 5.12(a). In the dark case, the NDR and current resonant peaks are obtained. When light is applied, current increases, since the occupation of the higher energy levels increase, making favorable the tunneling processes. For certain photon energies, the current saturates in a voltage region as the transitions involve the higher/lowest energy states of the electron/hole states. Overlapped to these optical transitions, we have the electronic transport due to the applied voltage. In order to obtain electronic transport between the QDs, the condition of the overlapping of the energy levels has to be fulfilled. Therefore the NDR and the current peaks still remain in the I(V) curve.

In addition, we present the photocurrent generated as a function of the energy of the incident photon in Fig. 5.12(b). The values of the photon energy have been chosen in order to maximize the transitions probabilities in each QD obtaining different photo generation rates in each QD. The cases under external bias voltages are also presented. We obtained a similar trend as in the previous cases, the current reflects the absorption spectra of the systems obtaining current peaks when the transitions probabilities are maximal in the cases when the photon energy equals the difference between the energy levels involved in the transition. Different to the previous cases, the current saturates when the voltage is increased as a consequence of the no overlapping between the energy levels of the QDs. For this reason, we studied this kind of system: a small QD (with few energy levels) connected in series with a bigger one (with large number of energy levels). Therefore, the small QD dominates the behavior of the photocurrent since it controls the number of conduction channels. In this configuration, the photocurrent retains the current peaks when the external voltage increases since the small QD acts as a current filter.

5.4.2 Comparison with experiments: PbSe QDs

To complete this chapter, we present the comparison between the presented theoretical model and a real system. The experimental results have been taken from Prins *et al.* [35]. They fabricated a system based on two electrodes separated by 5 nm. A single layer of PbSe QD of 2 nm in radius was deposited on top of the electrodes. An scheme of the system is shown in Fig. 5.13. Therefore, they obtained a system of QDs placed in parallel configuration. This kind of structure is the same as we have studied before.

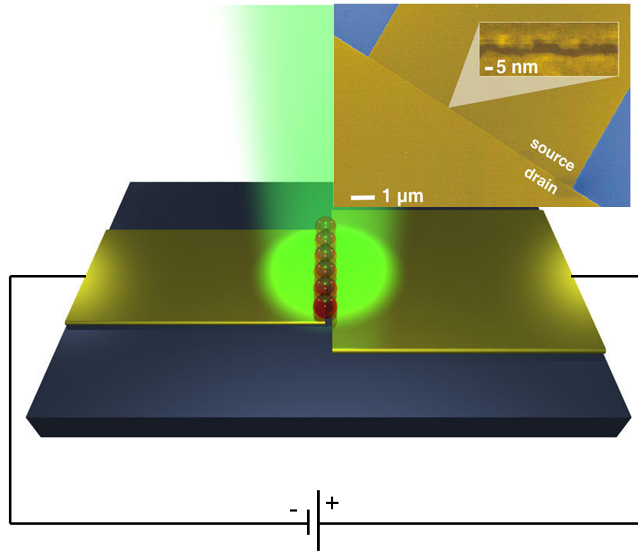

FIGURE 5.13: Scheme of the device fabricated by Prins *et al.* [35]. Two Au contacts are separated by a trench of ≈ 5 nm in which the PbSe QDs are placed. In the inset, a SEM image of the electrodes is showed. Both figures have been extracted from Ref. [35]. Reprinted with permission from ACS.

5.4.2.1 PbSe QDs: optical properties

In order to simulate this new system, we have changed the material parameters to describe the PbSe QDs. First of all, we describe the E_{gap} and the optical properties of the material. The PbSe QD is treated as a finite spherical potential well under the EMA neglecting the Coulomb interaction. PbSe QDs have been widely studied under several models within EMA [21], **K**· **p** Hamiltonian [36], finite barrier version of the EMA [37] and some variations as proposed in Ref. [37] and Ref. [36]. PbSe is narrow band gap semiconductor ($E_{gap} = 0.26$ eV) with large Bohr radius ($a_B = 46$ nm [38]) and small effective masses. The value of the effective masses and confinement potentials were taken from Pellegrini *et al.* [39]. We used $m^*_{Qd,CB} = 0.07m_0$ and $m^*_{Qd,VB} = 0.06m_0$ for electron and hole effective masses respectively. The confinement potentials are $\phi_{1,ECB} = 1.61$ eV and $\phi_{1,HVB} = 1.61$ eV. The obtained $E_{gap}(R)$ is presented in Fig. 5.14. The dielectric constant value is $\varepsilon_r = 23\varepsilon_0$ [36].

As shown in Fig. 5.14, the proposed model (finite EMA) is close to the results obtained experimentally and using other approaches, reflecting that the parameters used to describe the PbSe QD (effective masses and barriers) are correct. We can also estimate the binding energy of the ground-state exciton for a PbSe QD of $R = 2$ nm. The energy shift due to the electron-hole Coulomb interaction is $E_{e-h} = -0.03$ eV, where we have used Eq. 5.15 that agrees with results presented previously in other works[37].

We present in Fig. 5.15 a comparison between measured and simulated absorptions coefficients for PbSe QDs as a function of the QD radius. Experimental data has been

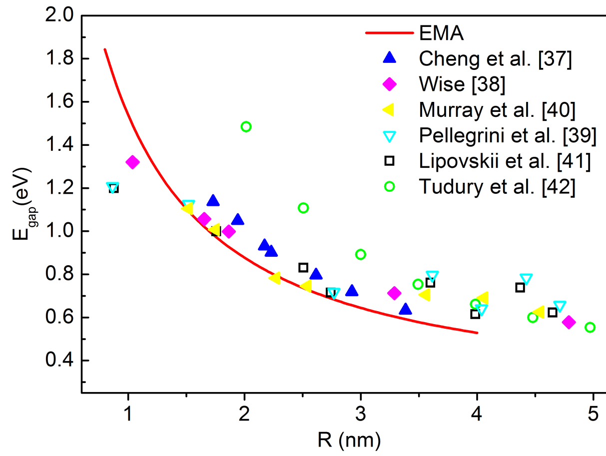

FIGURE 5.14: Dependence of the obtained E_{gap} as a function of the radius of the PbSe QD without taking into account the exciton shift (solid line). For comparison, experimental data (filled symbols) [37, 38, 40] and results from different theoretical approaches (hollow symbols) are also presented [39, 41, 42].

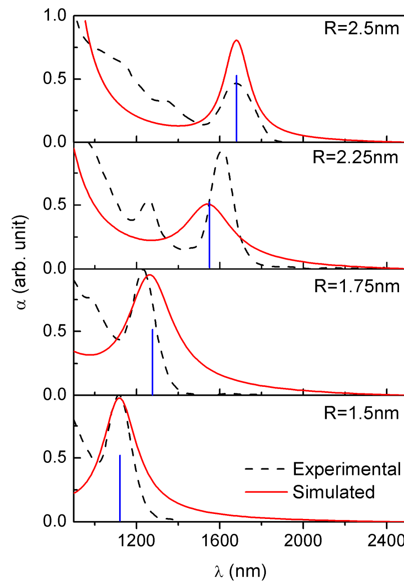

FIGURE 5.15: Simulated absorption spectra (continuous line) and experimental one (dashed line) for different PbSe QDs radii. Experimental data has been taken from Ref. [43].

taken from Ref. [43]. The EMA model can reproduce well the value of E_{gap}, the first electron and hole energy level, as the position of the first optical transition. However, the rest of the binding states are not well reproduced. This fact is visible since all the optical transitions can not be reproduced.

5.4.2.2 Simulation vs. Experiments

In order to compare our calculations with the experimental device, we created a system composed by ten QDs placed in parallel configuration. The QDs radii were generated randomly using a normal distribution with mean radius $\langle R \rangle = 2$ nm and $\sigma = 0.1$ nm. The QDs were placed in parallel configuration but the distance between them and the leads was chosen as a free parameter breaking the symmetry of the system. The leads separation was 5 nm and direct current among the leads was not considered.

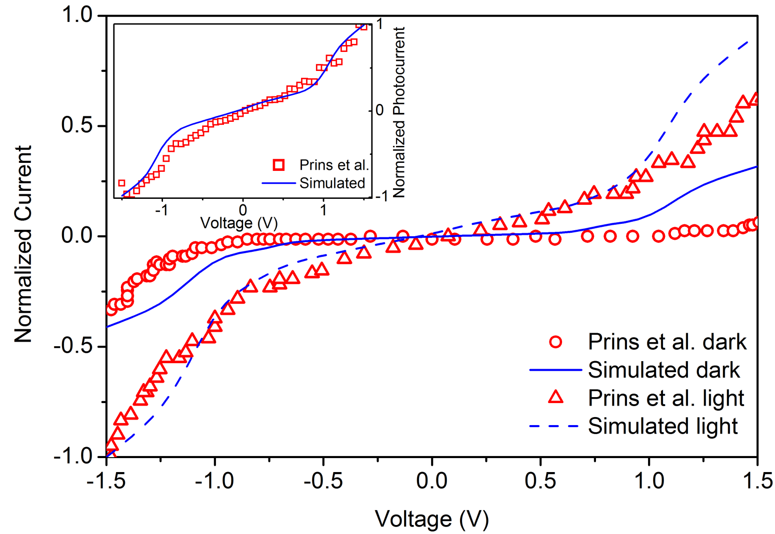

FIGURE 5.16: Simulated I(V) curve in dark (continuous blue line) and light (dash blue line) conditions respectively (normalized to the maximum current). In the inset we show the experimental (square red points) and simulated (continuous blue line) normalized photocurrent. Both figures are normalized to the maximum current. Measured I(V) points have been extracted from Prins *et al.* [35].

Fig. 5.16 shows the current voltage curve in dark and light conditions. The inset also shows the normalized net photocurrent as a function of the applied bias voltage for light illumination conditions equivalent to the experiment ($\lambda = 532$ nm and irradiation of $I(h\nu) = 0.16 W cm^{-2}$). Concerning the current curve in dark conditions, the electron/hole only crosses from one lead to the other trough the states in the QD. As a consequence of the discrete nature of the QD energy levels, the current increases step-by-step as the conductive channels open. The asymmetry reflected in the experimental measurements is related to the different capacitive coupling between the QD and the leads since the capacities are strongly dependent on the distance.

For the illuminated case, the behavior of the curve can be explained in an intuitive form directly from the rate equation type model. Eq. 5.1 shows that the distribution function in the QD is a combination of pure transport effects (tunnelling processes) and optical contributions. The optical terms mix the electron and hole states involving electron and hole pair creation. The response of the system under external perturbations (light and voltage) depends on the rate between the pure transport effects and the light terms. One

the one hand, the transport terms are described by tunneling junctions that are function of the tunneling distances and the energy barriers. Moreover, the rates depend on the occupancy of the energy levels. On the other hand, the optical terms are described by the transition probability, but they also take into account the occupancy of the energy levels. Thus, for low voltages we expect that the optical terms dominate creating a net photocurrent. When the voltage increases, the tunneling probabilities increase the transport terms making them larger than the optical terms and the photocurrent tends to zero [44].

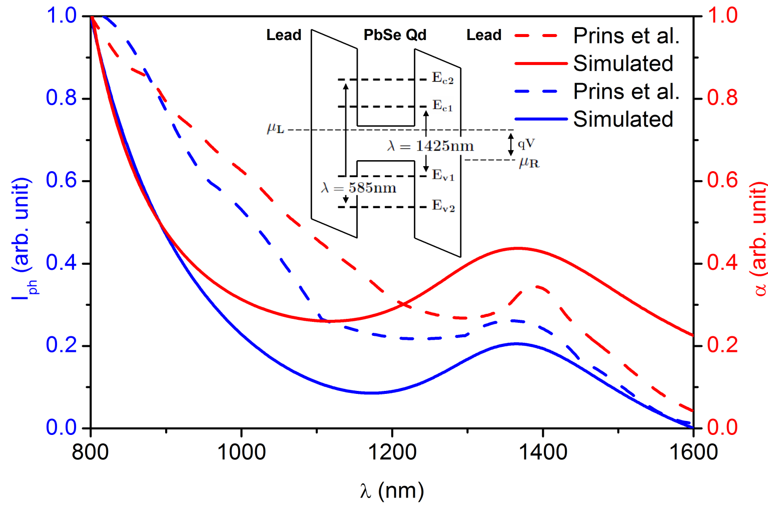

FIGURE 5.17: Simulated normalized photocurrent curve (continuous blue line) and experimental curve taken from Prins *et al.* [35] (dash blue line) as a function of the wave length of the incident light. Simulated normalized absorption coefficient (continuous red line) of the QD system and experimental absorption (red dashed line). In the inset, we show an scheme of the system under external polarization; the band diagram of the QD, the optical transitions and the band bending of the barriers due to the external bias voltage $V = 750mV$. Besides, the electrochemical potentials of the leads are also presented

We also computed the photo-conductive response as a function of the wavelength of the incident light as the current at a fixed bias voltage at $V = 750$ mV and constant irradiation for varying wavelengths between 800 nm and 1600 nm , Fig. 5.17, and the corresponding absorption spectra. Clearly, the photocurrent reflects the total absorption spectra of the system composed by the summation of the individual spectra of each QD. Due to the nature of the QD, the photon absorption only occurs for selected photon energies, as we discussed in the absorption coefficient. The photocurrent peak at $\lambda \approx$ 1400 nm is related to the first optical excitation, i.e. the first exciton creation (see the inset). Since we have an electron-hole pair, these carriers tend to transit to the electrodes. In order to obtain a net photogenerated current the tunnel transmission of electrons or holes have to be grater than the recombination time. Moreover, the electrons tend to go out from the QD to the leads but simultaneously electrons tend to go in from the leads to the empty energy levels (hole movement). So, a net photo-generation current only

appears if the electron and hole currents are different. Therefore, the tunneling junctions become a crucial point that determine the photoresponse of the device. Thereby, in order to enhance the device efficiency not only effective optical processes are needed, but also a good charge extraction mechanism is also desirable [44, 45, 46].

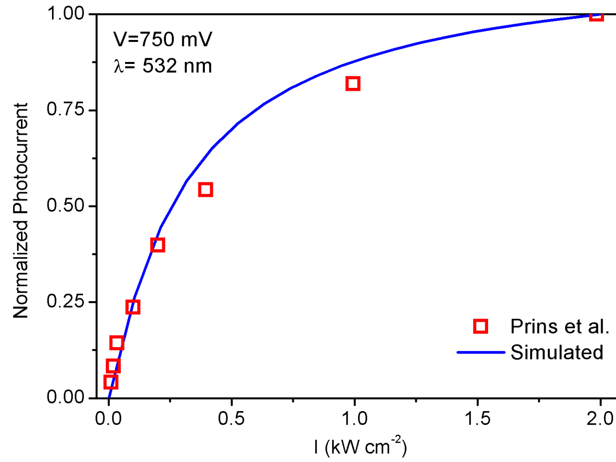

FIGURE 5.18: Experimental net photocurrent as a function of irradiance (square red points) and simulated (continuous blue line). Experimental points taken from Prins *et al.* [35].

Finally, the dependence of the photoresponse with irradiation was also properly explained. Fig. 5.18 shows the photocurrent for different irradiances at $\lambda = 532$ nm and bias voltage $V = 750$ mV. The photocurrent scales linearly with irradiance at low values. In contrast, it tends to saturate for higher powers densities since the energy levels that contribute to the current are filled, decreasing the efficiency of the optical processes [47].

5.5 Conclusions

In this chapter, we have included the optical transitions into the rate-equation-type model to simulate the optoelectronic response of devices based on QD arrays. Using the EMA, the optical properties of the QD have been studied as a needed input parameters for the transport model.

First of all, the complete DOS of the QD has been calculated, since in the case of the optical processes take place between states with different l quantum number. Thus, following the Qd description as a finite spherical well within the EMA, we have obtained the binding states unrestricted for the l quantum number.

The optical properties have been computed assuming the intraband and interband transitions considering excitonic effects in the strong confinement regime. To conclude, the absorption spectra has been also simulated. The selection rules for the optical transitions can be summarized as: $\triangle l = \pm 1$ and $\triangle m = 0, \pm 1$ for intraband transitions and

$\triangle l = 0$ and $\triangle m = 0$ for interband transitions. We must note that for the interband transitions, the selection rule imposes that the photogenerated electron-hole pair (the exciton) has the same quantum numbers.

The processes that govern the response of the device have been studied and analyzed. The electrical response is explained as a function of the ratio between the optical and the pure electrical rates. Moreover, interesting features appear as the different QD couplings to the leads impose geometrical restrictions.

The particular case of Si/SiO_2 QDs was studied in three systems: a single QD and two QDs in serial and parallel arrangements. The single case was used to validate that the symmetry of the couplings respect to the leads plays an important role in the final photoresponse. The photocurrent as a function of the energy of the incident light tends to recover the shape of the absorption spectra. Moreover, the I(V) curves in dark and light conditions were also presented and the obtained results were explained by the ratio between the pure electrical and optical terms. The same study was done for the two QDs systems. In the parallel arrangement, the coupling between the QDs breaks the symmetry respect to the lead coupling being possible to obtain a net photocurrent at zero bias voltage. Concerning the serial case, it was used as a energy filtering device: the small QD controls the final response of the system since the overlapping between the energy levels are needed.

To conclude, a device based on parallel arrangement of PbSe QDs has been simulated and compared with experimental measurements. The electrical response of the system has been evaluated in dark and light conditions, as a function of the wavelength of the incident light and also as function of the irradiance of the light. The simulations agree with the experimental results showing that: (i) we have recovered the I(V) asymmetry associated to the different capacitive coupling to the leads; (ii) the I(V) trends in dark and light conditions are well reproduced; (iii) the photocurrent follows the absorption spectra of the Qds and (iv) the photoresponse of the systems tends to saturate for high irradiances.

As a final comment, we must note that the photo-electrical response of the QDs is strongly dominated by the electrical and optical properties of the QDs (DOS and absorption spectra). Again, we deal with the problem that EMA oversimplifies the energy levels and therefore, the absorption spectra. Thus, the here presented simulations for the Si/SiO_2 basically show the capabilities of the model to design optoelectronic devices

5.6 Appendix

5.6.1 DFT vs. EMA in Si/SiO_2 QDs

Here, we are going to show the differences between the EMA used in this chapter and the *ab inito* approach. In this chapter, we have shown that binding states dominates the electrical response of the system and the optical properties of the QD. Therefore, a correct description of the internal QD structure is desirable. However, atomistic calculations are time consuming and some approximations are needed in order to simulate devices that contain hundreds of QDs. This fact is the main motivation to use the simplest EMA model to describe the optical and electrical properties of the QDs. At the end, there is a compromise between the accuracy of the description of a single QD and the number of QDs that form our device.

The DFT DOS results have been obtained from Ref. [48]. Several Si/SiO_2 QDs have been studied as a function of the radius and the amorphization level of the embedding matrix. We restricted our comparison to the crystalline SiO_2 phase since there are more QDs radii to compare. The comparisons between the DFT results and the EMA approximation are shown in Fig. 5.19 for $d = 1.27, 1.39, 1.5, 1.6$ nm QDs diameter.

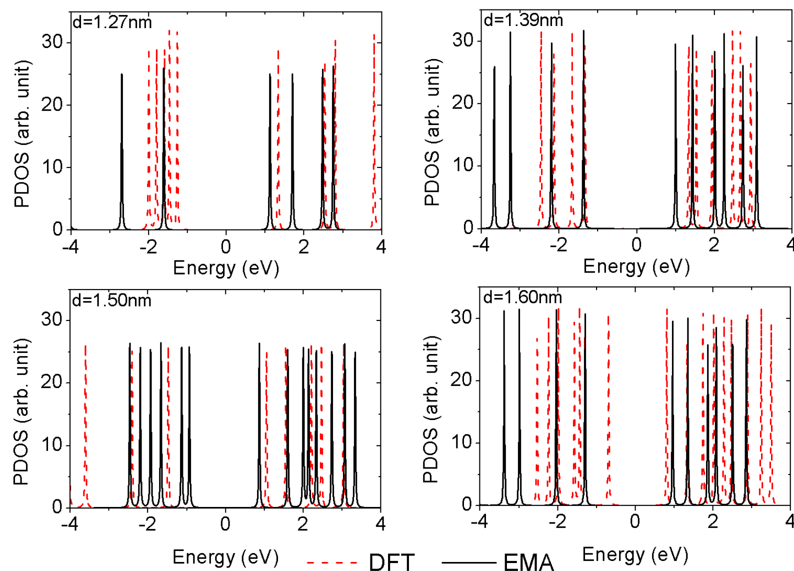

FIGURE 5.19: Comparison between the DFT results and the EMA approximation for the obtained DOS for different QDs diameters. DFT data has been taken from Ref. [48].

The differences between the two approaches appear clearly in the DOS spectra. Whereas the EMA approximation can describe exactly the value of the E_{gap} (see Fig. 5.7) the rest of the states are far of being well described. Furthermore, the EMA approach does not reproduce all the energy states obtained by the DFT.

Obviously, these discrepancies in the electronic structure of the QD are also shown in the optical properties. Optical properties of the DFT system and their comparison to the dipole transition elements obtained by the methodology used in this chapter are shown in Fig. 5.20. The absorption spectra has been taken from Ref. [49] for different Si QDs radii embedded in a amorphous SiO_2 matrix.

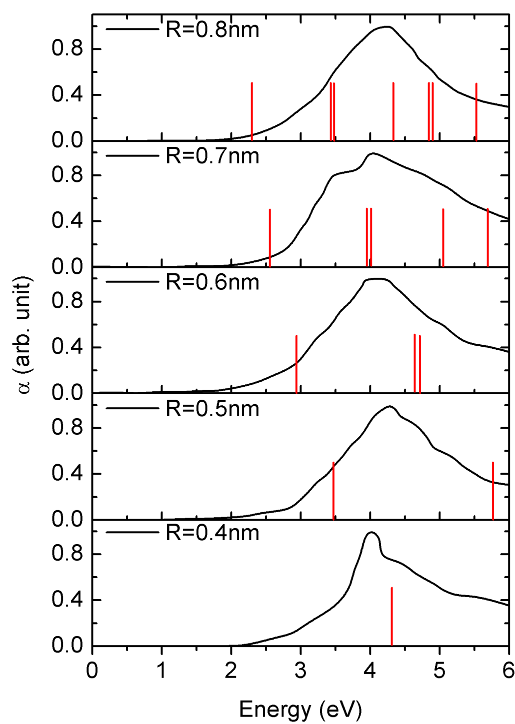

FIGURE 5.20: DFT absorption spectra for different QDs radii. Data has been taken from Ref. [49]. The matrix transitions elements calculated using the EMA approach are also shown.

Bibliography

[1] A E Zhukov and A R Kovsh. Quantum dot diode lasers for optical communication systems. *Quantum Electronics*, 38(5):409, 2008.

[2] Robert J. Walters, George I. Bourianoff, and Harry A. Atwater. Field-effect electroluminescence in silicon nanocrystals. *Nat Mater*, 2(4):143-146, 2005.

[3] L. Pavesi, L. Dal Negro, C. Mazzoleni, G. Franzo, and F. Priolo. Optical gain in silicon nanocrystals. *Nature*, 408:440–444, 2000.

[4] Gavin Conibeer, Martin Green, Eun-Chel Cho, Dirk König, Young-Hyun Cho, Thipwan Fangsuwannarak, Giuseppe Scardera, Edwin Pink, Yidan Huang, Tom Puzzer, Shujuan Huang, Dengyuan Song, Chris Flynn, Sangwook Park, Xiaojing Hao, and Daniel Mansfield. Silicon quantum dot nanostructures for tandem photovoltaic cells. *Thin Solid Films*, 516(20):6748 – 6756, 2008. Proceedings on Advanced Materials and Concepts for Photovoltaics {EMRS} 2007 Conference, Strasbourg, France.

[5] Gavin Conibeer, Martin Green, Richard Corkish, Young Cho, Eun-Chel Cho, Chu-Wei Jiang, Thipwan Fangsuwannarak, Edwin Pink, Yidan Huang, Tom Puzzer, Thorsten Trupke, Bryce Richards, Avi Shalav, and Kuo lung Lin. Silicon nanostructures for third generation photovoltaic solar cells. *Thin Solid Films*, 511–512(0):654 – 662, 2006. {EMSR} 2005 - Proceedings of Symposium F on Thin Film and Nanostructured Materials for Photovoltaics {EMRS} 2005- Symposium F {EMSR} 2005 - Proceedings of Symposium F on Thin Film and Nanostructured Materials for Photovoltaics.

[6] M. Zacharias, J. Heitmann, R. Scholz, U. Kahler, M. Schmidt, and J. Bläsing. Size-controlled highly luminescent silicon nanocrystals: A SiO/SiO_2 superlattice approach. *Applied Physics Letters*, 80(4):661–663, 2002.

[7] Tae-Wook Kim, Chang-Hee Cho, Baek-Hyun Kim, and Seong-Ju Park. Quantum confinement effect in crystalline silicon quantum dots in silicon nitride grown using SiH_4 and NH_3. *Applied Physics Letters*, 88(12):–, 2006.

[8] Yasuyoshi Kurokawa, Shinsuke Miyajima, Akira Yamada, and Makoto Konagai. Preparation of nanocrystalline silicon in amorphous silicon carbide matrix. *Japanese Journal of Applied Physics*, 45(10L):L1064, 2006.

[9] R. D. Schaller and V. I. Klimov. High efficiency carrier multiplication in PbSe nanocrystals: Implications for solar energy conversion. *Phys. Rev. Lett.*, 92:186601, May 2004.

[10] Randy J. Ellingson, Matthew C. Beard, Justin C. Johnson, Pingrong Yu, Olga I. Micic, Arthur J. Nozik, Andrew Shabaev, and Alexander L. Efros. Highly efficient

multiple exciton generation in colloidal PbSe and PbS quantum dots. *Nano Letters*, 5(5):865–871, 2005.

[11] Marco Govoni, Ivan Marri, and Stefano Ossicini. Auger recombination in Si and GaAs semiconductors: Ab initio results. *Phys. Rev. B*, 84:075215, Aug 2011.

[12] M. Gioannini, G.A.P. The, and I. Montrosset. Multi-population rate equation simulation of quantum dot semiconductor lasers with feedback. In *Numerical Simulation of Optoelectronic Devices, 2008. NUSOD '08. International Conference on*, pages 101–102, 2008.

[13] V. M. Apalkov. Generation of photocurrent in quantum dot infrared photodetectors: Role of pauli correlations. *Phys. Rev. B*, 75:035339, Jan 2007.

[14] John P. McKelvey. *Solid State and Semiconductor Physics*. Robert E. Krieger Publishing company, 1966.

[15] C. F. Klingshirn. *Semiconductor Optics*. Springer, 2007.

[16] Peter Y. Yu and Manuel Cardona. *Fundamentals of Semiconductors*. Springer, 2005.

[17] Stephan W. Koch Hartmut Haug. *Quantum Theory of the Optical and Electronic Properties of Semiconductors*. World Scientific, 2004.

[18] C. F. Klingshirn. *Semiconductor Optics*. Springer, 2007.

[19] G. T. Einevoll. Confinement of excitons in quantum dots. *Phys. Rev. B*, 45:3410–3417, Feb 1992.

[20] Yosuke Kayanuma. Quantum-size effects of interacting electrons and holes in semiconductor microcrystals with spherical shape. *Phys. Rev. B*, 38:9797–9805, Nov 1988.

[21] L. E. Brus. Electron–electron and electron hole interactions in small semiconductor crystallites: The size dependence of the lowest excited electronic state. *The Journal of Chemical Physics*, 80(9):4403–4409, 1984.

[22] S. Schmitt-Rink, D. A. B. Miller, and D. S. Chemla. Theory of the linear and nonlinear optical properties of semiconductor microcrystallites. *Phys. Rev. B*, 35:8113–8125, May 1987.

[23] U. E. H. Laheld and G. T. Einevoll. Excitons in CdSe quantum dots. *Phys. Rev. B*, 55:5184–5204, Feb 1997.

[24] A. I. Ekimov, F. Hache, M. C. Schanne-Klein, D. Ricard, C. Flytzanis, I. A. Kudryavtsev, T. V. Yazeva, A. V. Rodina, and Al. L. Efros. Absorption and

intensity-dependent photoluminescence measurements on CdSe quantum dots: assignment of the first electronic transitions. *J. Opt. Soc. Am. B*, 10(1):100–107, Jan 1993.

[25] Karuna K. Nanda, F. Einar Kruis, and Heinz Fissan. Energy levels in embedded semiconductor nanoparticles and nanowires. *Nano Letters*, 1(11):605–611, 2001.

[26] J. D. Jackson. *Classical Electrodynamics.* John Wiley Sons, 1999.

[27] J. J. Sakurai. *Modern Quantum Mechanics Revised Edition.* Addison-Wesley Publishing Company, 1994.

[28] S. Guha, S. B. Qadri, R. G. Musket, M. A. Wall, and Tsutomu Shimizu-Iwayama. Characterization of Si nanocrystals grown by annealing SiO_2 films with uniform concentrations of implanted Si. *Journal of Applied Physics*, 88(7):3954–3961, 2000.

[29] Kei Watanabe, Minoru Fujii, and Shinji Hayashi. Resonant excitation of Er^{3+} by the energy transfer from Si nanocrystals. *Journal of Applied Physics*, 90(9):4761–4767, 2001.

[30] Y. Kanzawa, T. Kageyama, S. Takeoka, M. Fujii, S. Hayashi, and K. Yamamoto. Size-dependent near-infrared photoluminescence spectra of Si nanocrystals embedded in SiO_2 matrices. *Solid State Communications*, 102(7):533 – 537, 1997.

[31] H. Takagi, H. Ogawa, Y. Yamazaki, A. Ishizaki, and T. Nakagiri. Quantum size effects on photoluminescence in ultrafine Si particles. *Applied Physics Letters*, 56(24):2379–2380, 1990.

[32] Nae-Man Park, Tae-Soo Kim, and Seong-Ju Park. Band gap engineering of amorphous silicon quantum dots for light-emitting diodes. *Applied Physics Letters*, 78(17):2575–2577, 2001.

[33] E. G. Barbagiovanni, D. J. Lockwood, P. J. Simpson, and L. V. Goncharova. Quantum confinement in Si and Ge nanostructures. *Journal of Applied Physics*, 111(3):–, 2012.

[34] J. P. Proot, C. Delerue, and G. Allan. Electronic structure and optical properties of silicon crystallites: Application to porous silicon. *Applied Physics Letters*, 61(16):1948–1950, 1992.

[35] Ferry Prins, Michele Buscema, Johannes S. Seldenthuis, Samir Etaki, Gilles Buchs, Maria Barkelid, Val Zwiller, Yunan Gao, Arjan J. Houtepen, Laurens D. A. Siebbeles, and Herre S. J. van der Zant. Fast and efficient photodetection in nanoscale quantum-dot junctions. *Nano Letters*, 12(11):5740–5743, 2012.

[36] Inuk Kang and Frank W. Wise. Electronic structure and optical properties of PbS and PbSe quantum dots. *J. Opt. Soc. Am. B*, 14(7):1632–1646, Jul 1997.

[37] Wen chao Cheng, Tie qiang Zhang, and Yu Zhang. Dielectric confinement effect on calculating the band gap of PbSe quantum dots. *Chinese Journal of Chemical Physics*, 24(2):162, 2011.

[38] Frank W. Wise. Lead salt quantum dots: the limit of strong quantum confinement. *Accounts of Chemical Research*, 33(11):773–780, 2000. PMID: 11087314.

[39] Pellegrini, Giovanni and Mattei, Giovanni and Mazzoldi, Paol. Finite depth square well model: Applicability and limitations. *Journal of Applied Physics*, 97(7):073706, 2005.

[40] Christopher B. Murray, Shouheng Sun, Wolfgang Gaschler, Hugh Doyle, Theodore A. Betley, and Cherie R. Kagan. Colloidal synthesis of nanocrystals and nanocrystal superlattices. *IBM Journal of Research and Development*, 45(1):47–56, 2001.

[41] A. Lipovskii, E. Kolobkova, V. Petrikov, I. Kang, A. Olkhovets, T. Krauss, M. Thomas, J. Silcox, F. Wise, Q. Shen, and S. Kycia. Synthesis and characterization of PbSe quantum dots in phosphate glass. *Applied Physics Letters*, 71(23):3406–3408, 1997.

[42] G. E. Tudury, M. V. Marquezini, L. G. Ferreira, L. C. Barbosa, and C. L. Cesar. Effect of band anisotropy on electronic structure of PbS, PbSe, and PbTe quantum dots. *Phys. Rev. B*, 62:7357–7364, Sep 2000.

[43] C. B. Murray, Shouheng Sun, W. Gaschler, H. Doyle, T. A. Betley, and C. R. Kagan. Colloidal synthesis of nanocrystals and nanocrystal superlattices. *IBM Journal of Research and Develpment, Organic electronics*, 45(1):47, 2001.

[44] Luxia Wang and Volkhard May. Charge transmission through single molecules: Effects of nonequilibrium molecular vibrations and photoinduced transitions. *Chemical Physics*, 375(2–3):252 – 264, 2010. Stochastic processes in Physics and Chemistry (in honor of Peter Hänggi).

[45] Michael Galperin and Abraham Nitzan. Molecular optoelectronics: the interaction of molecular conduction junctions with light. *Phys. Chem. Chem. Phys.*, 14:9421–9438, 2012.

[46] U. Aeberhard. Theory and simulation of quantum photovoltaic devices based on the non-equilibrium green's function formalism. *Journal of Computational Electronics*, 10(4):394–413, 2011.

[47] Evelin Beham, Artur Zrenner, Frank Findeis, Max Bichler, and Gerhard Abstreiter. Nonlinear ground-state absorption observed in a single quantum dot. *Applied Physics Letters*, 79(17):2808–2810, 2001.

[48] Nuria Garcia-Castello, Sergio Illera, Roberto Guerra, Joan Daniel Prades, Stefano Ossicini, and Albert Cirera. Silicon quantum dots embedded in a SiO_2 matrix: From structural study to carrier transport properties. *Phys. Rev. B*, 88:075322, Aug 2013.

[49] K Seino, F Bechstedt, and P Kroll. Influence of SiO_2 matrix on electronic and optical properties of si nanocrystals. *Nanotechnology*, 20(13):135702, 2009.

Chapter 6

Conclusions

Theoretical approach

In this work, we have developed a theoretical methodology for the electronic transport in the ballistic regime to reproduce the experimental trends of optoelectronic devices based on quantum dots (QDs) embedded in a insulator matrix. Within this approach, a compact device simulator (SimQD) has been created that can be used to aid in the design of these novel devices.

The scope of this PhD Thesis is fill the gap between the experimental measurements and the theoretical approaches. Although the theoretical fundamentals of the electronic transport are well known and there exist several approaches, they can not be used to simulate the large amounts of QDs that conform the usual devices. This fact is much clear in the case of *ab initio* or atomistic models, which are limited by their huge computational requirements. Thus, in order to overcome these constrains, several approximations and the relaxation of the accuracy of the expected results have to be done in favor of the possibility to simulate larger systems.

The basic building block that forms the devices based on QD is an insulator material in which the QDs are embedded. This system is placed between two electrodes, or leads, that inject current. The electronic transport takes place by tunneling processes through the QDs. The here proposed transport methodology is based on the assumption that the QDs are weakly coupled between them and to the leads; considering two consecutive tunneling events as independent processes, being possible to separate the whole system in different parts.

From this system decomposition and using the Transfer Hamiltonian approach to describe the tunneling currents, a set of non-coherent rate equations can be written to obtain the non-equilibrium distribution function of each QD. Within the Transfer Hamiltonian framework, the current is strongly dependent on the transmission coefficient

through the potential barrier and the density of states (DOS) in each side of the barrier. On the other hand, the electrostatic influence between the different elements of the system as well as the effects of the accumulated charge in the QDs are included in the model via the solution of the Poisson equation. The local potential in the QDs has a first term that strongly depends on the different capacitive couplings, the Laplace solution; and a second one that includes the charge variation in the QD. This second term imposes a simultaneous solution of the rate equations and the local potential within the self-consistent field regime. All of these assumptions conform the basis of the ballistic transport model presented in the first part of Chapter 2.

On the electronic transport model generalities

From some basic examples, the necessary transport conditions to obtain net current trough the device can be written as:

- The transport occurs in the conduction window created by the different electrochemical potentials of the leads.
- The energy levels of the intermediate QDs have to lie in the conduction window.
- Overlapping of the energy levels of the QDs is needed reflecting the ballistic nature of the model.

From these examples, the current voltage I(V) curves are obtained reflecting negative differential resistance (NDR) and current rectifying effect. Moreover, the main parameters that govern the final response of the system are highlighted, being strongly dependent on:

- The QD energy levels.
- The capacitive couplings.
- The transmission coefficients.

In the second part of Chapter 1, a direct comparison between the here presented transport model and the Non Equilibrium Green's Function Formalism (NEGFF) is shown. Both approaches give similar results but some effects related to the coherent treatment of the transport by NEGFF can not be well reproduced.

Modeling large scale arrays

After presenting and validating the transport model, we focus on the realistic description of the main parameters that govern the final electrical response (Chapter 3).

- Regarding the QD energy levels, we have assumed a finite spherical quantum well in the effective mass approximation in order to reproduce the discrete energy spectra of the QDs. The confinement potentials are the difference between the band edges of the material that forms the QD and the surrounding insulator media. The QD DOS is obtained as a sum of Lorentzian functions, and assumed as a constant for energies above the confinement potentials.
- The Wentzel Kramers Brillouin (WKB) approximation was used to calculate the transmission coefficients. Direct and Fowler-Nordheim tunneling are considered for trapezoidal and triangular oxide barriers, respectively.
- Concerning the capacitive couplings, an analytical expression for plane-sphere conductors has been used for the lead-QD capacitive coupling. For the QD-QD capacities, the numerical image charge method was used.

The inclusion of the holes in the transport model can be viewed as electrons restricted to move in the valence energy levels. Moreover, its inclusion adds extra terms in the rate equations in order to represent all the possible transitions.
To conclude this Chapter, the implementation of the transport model in the SimQD code is presented. This simulation tool, which only depends on several material parameters and the device geometry, was used to study the electronic transport in realistic devices.

Code implementation and realistic inputs

Due to the impossibility to obtain accurate QD DOS, the consideration of a constant DOS in the leads and the lack of information about the QD density in the experimental devices restrict our simulations to qualitative results instead of quantitative ones.

The possibility to use atomistic methodologies like Density Functional Theory (DFT) in order to obtain realistic QD electronic properties, basically the QD DOS, as inputs for the SimQD is presented for Si QD embedded in a SiO_2 matrix. Here, the importance of the exact position of the Fermi energy level in the equilibrium is discussed since its location governs the current and charge trends.

From theory to realistic devices

A complete study of the electronic transport, electrons and holes, for a single Si QD embedded in SiO_2 matrix was done as a function of its position respect to the leads. The total current, I(V) curve, is decomposed on hole and electron currents being the hole term smaller than the electron one because they view a lower potential barrier. The obtained effects in the I(V) curves can be summarized as:

- The current increases in step-like form each time that a conductive channel is opened. The tendency is clearly visible either for electrons or holes. However, for higher voltages, the continuous part of the DOS enters in the conduction window and the current increases in a continuous form.
- NDR is also obtained but, its nature is completely different from the previous case. Here, it is obtained because the ratio between the left/right transmission coefficients are voltage dependent.

The accumulated charge trends in the QD were also presented and show a strong dependence to the ratio among the incoming/outgoing current fluxes.
For sake of completeness, multilayer structures of 20 QDs were also simulated. Since the total I(V) curve is the sum of the current crossing through the different pathways, the previous explained effects are masked. However, the electron term is still the dominant current an the behavior of the I(V) curves show a strong dependence on the geometrical arrangement of the QDs.

To conclude the capabilities of the SimQD code, some transistor structures were simulated. An small modification was included in the Laplace solution in order to reflect the third electrode, the gate, which includes an extra term in the local potential. The obtained current maps reproduce the diamond-shape behavior due to the discrete nature of the QD DOS. Moreover, a double gate transistor was simulated reproducing the experimental trends.

The usually used transport mechanisms for samples including QDs are presented in the last part of Chapter 4. Experimentally, different current behaviors are obtained in different ranges of the applied electric field. Poole-Frenkel, Schottky emission, Tunneling and Trap assisted tunneling processes are usually fitted from the current density electric field curves J(E).

Within the rate-equation type model, the transport through defects or impurities can also be obtained as a function of the energy levels of the trap and its position respect to the leads. This new transport mechanism in combination to the previous QD transport and introducing tunneling between the leads allowed us to reproduce experimental measurements for three different Si/SiO_2 structures.

- SiO_2 layers of different thicknesses were used to validate the developed impurity transport model. The trap concentration as well as the average value of the trap energy level was obtained in agreement with other transport formalisms.
  Basically, for SiO_2 layers at low and moderate fields the predominant transport mechanism is mediated by inherent oxide traps whereas, for high fields, the direct tunneling through the oxide dominates.

- The silicon rich oxide (SRO) is a SiO_2 layer that contains several non-ordered QDs. For low fields, the QD contribution to the current is clearly visible and well reproduced by our model whereas for moderate and high fields the trap contribution dominates.

- A supperlattice of Si/SiO_2 QDs was also simulated. At low fields, NDR is well reproduced by the QD transport model and the trap contribution only appears for high fields.

On the inclusion of illumination effects

After doing the necessary test in the transport methodology, writing a compact transport tool and use it to simulate and reproduce experimental measurements, we have include the light interaction in the last Chapter of this Thesis (Chapter 5).

In the spirit of the previous rate equations, the carrier generation/recombination assisted by photons can be included in the transport model by two extra terms reflecting these processes. These terms are proportional to a optical transition rates and the distribution functions.

Concerning the optical transitions rates, they are calculated assuming: strong confinement regime, dipole approximation and the validity of the Fermi's Golden-Rule neglecting second order optical processes. Within these approaches, the intra- and inter-band transitions are obtained. Besides, the optical absorption coefficient of the QDs can be calculated.

From the simplicity of the rate equations and studying a toy examples, the electrical response of the system under illumination was inferred. The response of the QD is governed by the ratio among optical and electrical terms being necessary a geometrical asymmetry in order to obtain a net photo-current. These assumptions were validated simulating Si/SiO_2 QDs in three basic configurations: a single QD, two QDs in parallel and serial arrangements. The main trends are:

- The I(V) curves differ from the illuminated and dark cases at low-medium voltages in this range, since the optical terms in the rate equations are greater or comparable

to the electrical ones. For higher voltages, the dark trend is recovered since the electrical terms dominate.

- Current curves as a function of the energy of the incident photon are also obtained. The photo-current reflects directly the absorption spectra of the QD.

To conclude, an optoelectronic device based on PbSe QDs was simulated and compared to experimental measurements. This device corresponds to a parallel arrangement of QDs. The I(V) curves in dark and illumination conditions, the photo-current as a function of the energy of the incident photon and, also, the photo-current as a function of the irradiance (the power of the incident light) are well reproduced by the here present approach.

Future work

Overall, we have studied in detail the electronic transport in devices based on large arrays of QDs. On the other hand, this compact transport model was implemented in a code allowing to simulate realistic devices. This approach was successfully compared to other transport approaches and experimental results. Thus, this work covers the gap between the fundamental electronic transport theory and its applicability to experimental devices.

Looking backwards the building process of the here presented electronic transport methodology, its implementation in the SimQD simulator tool and the obtained results we consider that there are several points that could be extended and studied in future works. The list could be infinite, but we try here to sort them from the easiest to the most difficult ones:

1. Up to now, in order to show all the transport problems related to the intrinsic properties of the QDs and their arrangement in the insulator matrix, we have assumed constant DOS in the leads corresponding to metallic ones. However, the injection of one preferred type of carrier assuming semiconductor leads can modify the electrical response (and the accumulated charge in the QDs) of the device. Under illumination conditions, the different concentration of carriers will influence the generation/recombination fluxes changing the expected behavior.

2. A complete study of the best geometry of the QD array (number of QDs, QD arrangement, number of QD layers in multilayer systems, distance among the layers...) to optimize the electrical response of the device in order to adequate it to specific uses.

3. Concerning the use of DFT results to describe realistic QDs, at the beginning of this Thesis, the idea was to create a library of DFT DOS for different QD sizes

and materials to use it as inputs for the SimQD code. However, as we saw latter in the Thesis of Dr. Núria García-Castelló, the computational obtained QDs are still too small (around $1.2 - 1.6nm$ of diameter). Moreover, the properties of these small QDs are strongly dependent on the surface atoms, and on the morphology of the surrounding matrix, limiting the studied cases.
On the other hand, these small QDs systems were doped with P and B atoms and the study of the electronic properties and the new electronic transport features are going to be published shortly by Dr. Núria García-Castelló taking advantage of the here developed transport methodology.
Although we have restricted to Si QDs embedded in SiO_2 matrix, the Si QDs have been created inside other insulator matrices such as silicon nitride Si_xN_x or silicon carbide SiC. However, first attempts to study these systems by atomistic calculations revealed several structural problems, and the appearance of lot of defects in the nitride and carbide matrices, respectively.
We have used only DOS results from DFT calculations, however, we could also use the absorption spectra for the optoelectronic device. As we have seen, the DOS and the absorption are strongly related.
Anyway, the possibility to use DFT and the SimQD in combination to study equilibrium and transport properties has opened the possibility to simulate realistically new systems.

4. Another possibility to explore is the electroluminescent devices. Instead of using light in order to create current, these devices use current to emit light. Thus, a light emission spectra could be obtained. These kind of devices will be very interesting since the QDs have a sharp emission peaks and the possibility to use the QD array in order to filter the current and increase the light emission of determined lines can be used e.g. for laser sources.

5. To conclude, one of the basis of the here presented transport methodology is the assumption of ballistic transport. Thus, we have neglected scattering processes with phonons (the most important scattering process). Although it is well known that there exist a phonon-bottleneck, there are not enough energetic phonons (or the probability is too small) that can mediate in transitions between the energy levels of the QDs. However, for small tunneling rates both scattering rates will be comparable. Basically, we are underestimating the electronic transport since we are imposing the most restrictive transport conditions, i.e. the energy level overlapping condition would be relaxed if one assumes some possible energy mismatch due to the phonon. This new sophistication in the transport methodology would force us to rewrite from the beginning the rate-equations and the expressions for the tunneling currents. However, we have to note that with the inclusion of the light, we have mixed different conducive channels and the transport has become non-ballistic.

Appendix A

Scientific Curriculum

A.1 List of Publications

A.1.1 Journal Articles

- S. Illera, J. D. Prades, A. Cirera and A. Cornet. Transport in quantum dot stacks using the transfer Hamiltonian method in self-consistent field regime. *Europhysics Letters (EPL)* 98:17003, (2012).
- S. Illera, N. Garcia-Castello, J. D. Prades and A. Cirera. A transfer Hamiltonian approach for an arbitrary quantum dot array in the self-consistent field regime. *Journal of Applied Physics* 112(9), 093701-093708 (2012).
- Nuria Garcia-Castello, Sergio Illera, Roberto Guerra, Joan Daniel Prades, Stefano Ossicini, and Albert Cirera. Silicon quantum dots embedded in a SiO2 matrix: From structural study to carrier transport properties. *Physical Review B* 88, 075322 (2013).
- S. Illera, J. D. Prades, A. Cirera and A. Cornet. A Transfer Hamiltonian model for devices based on quantum dot arrays. *The Scientific World Journal* 2015, 426541 (2015).
- S. Illera, J. D. Prades and A. Cirera. Elastic tunneling charge transport mechanisms in silicon quantum dots/SiO_2 thin films and superlattices. Minor revisions in *Journal of Applied Physics*.
- Nuia Garcia-Castello, Sergio Illera, Joan Daniel Prades, Stefano Ossicini, Albert Cirera and Roberto Guerra. Energetics and carrier transport in doped Si/SiO_2 quantum dots. Submitted to *Journal of the American Chemical Society*.
- Y. Berencén, S. Illera, L. Rebohle, J. M. Ramírez, R. Wutzler, A. Cirera, D. Hiller, J. A. Rodríguez, W. Skorupa and B. Garrido. On the electroluminescent

mechanism of trivalent erbium ions into silicon-rich nitride host under electrical pumping. In preparation.

A.1.2 Oral Presentations

- *European Materials Research Society (E-MRS). Spring Meeting.* LOCATION: Nice (France). DATE: 2011. TITLE: First-principles study of the dependence of electronic transport properties on the growth direction of Si nanowires. AUTHORS: N. Garcia-Castello, S. Illera, J. D. Prades and A. Cirera.
- *European Materials Research Society (E-MRS). Spring Meeting.* LOCATION: Nice (France). DATE: 2011. TITLE: Non-coherent transport in serial/parallel quantum dots in self-consistent field regime. AUTHORS: S. Illera, N. Garcia-Castello, J. D. Prades and A. Cirera.
- *International Doctoral Forum of Electronic Science and Technology.* LOCATION: Beijing (China). DATE: 12th July 2013. TITLE: A compact transport model for devices based on quantum dot arrays: photovoltaic applications. AUTHORS: S. Illera, J. D. Prades and A. Cirera
- *Theory, Modeling and Computational Methods for Semiconductors (Euro-TMCS I).* LOCATION: Granada (Spain). DATE: 30th January 2015. TITLE: Electronic Transport in QD Based Structures: from Basic Parameters to Opto-Electronic Device Simulations. AUTHORS: S. Illera, J. D. Prades, A. Cirera and A. Cornet.

A.1.3 Poster Presentations

- *III Jornada del Instituto de Nanociencia y Nanotecnología de la UB (IN^{2}UB).* LOCATION: Barcelona (Spain). DATE: 13th October 2010. TITLE: First-principles study of the dependence of silicon electronic transport on the crystallographic growth. AUTHORS: N. Garcia-Castello, S. Illera, J. D. Prades and A. Cirera.
- *IV Jornada del Instituto de Nanociencia y Nanotecnología de la UB (IN^{2}UB).* LOCATION: Barcelona (Spain). DATE: 14th November 2011. TITLE: Non-coherent transport in serial/parallel quantum dots in self-consistent field regime. AUTHORS: S. Illera, N. Garcia-Castello, J. D. Prades and A. Cirera.
- *European Materials Research Society (E-MRS). Spring Meeting.* LOCATION: Strasbourg (France). DATE: 2013. TITLE: A compact transport model for devices based on quantum dot arrays: photovoltaic applications. AUTHORS: S. Illera, N. Garcia-Castello, J. D. Prades, A. Cirera and A. Cornet.

A.1.4 Stays in Foreign Centers

- DATES: October - November 2014 (2 months). INSTITUTION: Department of Physics, Technical University of Denmark (DTU). TOPIC: Study of bidimensional material heterojunctions by DFT using GPAW software. SUPERVISOR: Professor Kristian Thygesen. FINANCING: Fundació Montcelimar i la Universitat de Barcelona.

A.1.5 Participation in Projects

- TITLE OF THE PROJECT: "Silicon Nanodots for Solar Cell Tandem (NASCEnT)". PROJECT NUMBER: FP7-NMP-245977. FUNDED: European Project. PERIOD: July 2009 - August 2013.

A.1.6 Specialization Courses

- Fundamentals of Nanoelectronics: Basic Concepts. ORGANIZED BY: Nanohub, Purdue University (EUA). Online Course. DATE: 23/01/2012 - 09/03/2012.
- Fundamentals of Nanoelectronics: Quantum Models. ORGANIZED BY: Nanohub, Purdue University (EUA). Online Course. DATE: 19/03/2012 - 05/05/2012.
- Learning teaching. ORGANIZED BY: Institut de Ciences de l'Educacio (ICE). SUPERVISOR: Dr. Juan Daniel Prades Garcia. PERIOD: course 2012 - 2013.
- Introduction to Python for Science and Engineering. ORGANIZED BY: Dr. Sanriago Marco, Electronics department, University of Barcelona. DATE: 28/1/2013 - 8/2/2013.
- Curs Avançat de Química Computacional. ORGANIZED BY: Facultat de Química, Universitat de Barcelona. DATE: 2/7/2014 - 7/7/2014.

Appendix B

Resumen en Castellano

Objetivos de la Tesis Doctoral

En este trabajo, hemos desarrollado una metodología teórica del transporte electrónico en el régimen balístico para reproducir las tendencias experimentales de dispositivos optoelectrónicos basados en quantum dots (QDs) crecidos dentro de una matriz aislante. Teniendo en cuenta los posibles usos de estos sistemas, la metodología de transporte se implementó en un código que se puede utilizar para ayudar en el diseño de estos nuevos dispositivos.

Esta tesis doctoral trata de llenar el vacío existente entre las medidas experimentales y los diferentes modelos teóricos. Aunque los fundamentos teóricos del transporte eléctrico son bien conocidos y existen varias metodologías, estas no pueden ser utilizadas para simular las grandes cantidades de QDs que conforman los dispositivos creados experimentalmente. Este hecho está muy claro en el caso de modelos *ab initio* o atómicos, los cuales están limitados por su enorme demanda de requisitos computacionales. Por lo tanto, con el fin de superar estas limitaciones, muchas veces se ha de relajar la precisión de la descripción a favor del tamaño del sistema.

Bases del modelo teórico desarrollado

Para desarrollar las bases del modelo de transporte balístico de esta tesis, se han estudiado sistemas formados por QDs creados dentro de una matriz aislante. Los electrones están confinados en los QDs debido a la diferencia de band gaps entre el material de la matriz y el material que conforma los QDs. Por otro lado, para estudiar las propiedades eléctricas de este tipo de sistema, se usan dos electrodos externos que inyectan corriente al sistema.
Debido al confinamiento de los electrones se crean niveles discretos en los QDs. Estos

nuevos estados aparecen dentro band gap del óxido y están localizados en el espacio, por lo tanto no forman un continuo de estados o banda como en los materiales de bulk. Si consideramos el régimen de transporte eléctrico balístico, es decir, que las colisiones que sufren los electrones no implican pérdida de energía, los portadores inyectados por los electrodos conservan la misma energía en la entrada y la salida de la matriz aislante. El proceso de transporte ocurre de la siguiente forma: (i) un electrón es inyectado desde un electrodo y mediante un proceso túnel llega a un QD; (ii) desde este QD, el electrón vuelve a circular hasta otro QD o hasta el otro electrodo; (iii) en caso que llegue a otro QD, el proceso túnel se repite hasta que el electrón consigue llegar hasta el otro electrodo; (iv) el proceso se inicia para el siguiente electrón. De esta forma, podemos hablar de un transporte eléctrico secuencial a través de uniones túnel que comunican los QDs entre ellos y entre estos y los electrodos que inyectan portadores.

Mientras el sistema se mantiene en equilibrio, la ocupación de los estados de los QDs y de los electrodos viene descrita por la función de distribución de Fermi Dirac con un mismo potencial electroquímico para todo el sistema. El proceso de inyección de portadores de los electrodos a la matriz de QDs, ocurre cuando se aplica una diferencia de potencial externo entre los electrodos. De esta forma, se lleva el sistema a un nuevo estado de no-equilibrio en el cual la función de distribución de los QDs es desconocida. Si obtenemos esta nueva función de distribución de no-equilibrio, la ocupación de los QDs se puede obtener, así como las diferentes corrientes que circulan por el sistema.

El modelo de transporte desarrollado en esta tesis considera que la matriz total de QDs se puede describir como QDs aislados y conectados entre ellos mediante uniones túnel. Estas uniones, se pueden visualizar como una capacidad y un camino de corriente entre los diferentes elementos que forman el sistema. Mientras que la capacidad tiene en cuenta la influencia de los potenciales aplicados en cada elemento del sistema, el camino de corriente representa las corrientes túnel que circulan por el sistema. Estas corrientes túnel se han descrito mediante el formalismo de Transfer Hamiltonian que considera la ocupación y la densidad de estados en ambos lados de la barrera de potencial. También incluye la probabilidad de transmisión a través de la barrera de potencial. Considerando la suma de corrientes que entran y salen de cada QD en el estado estacionario, la función de distribución de no-equilibrio de cada QD se puede obtener.

Por otro lado, falta incluir los efectos del potencial aplicado que desplaza los niveles energéticos de los QDs. El potencial local en cada QD se obtuvo resolviendo la ecuación de Poisson que tiene en cuenta los efectos de carga de los QDs. La solución general de esta ecuación tiene en cuenta la variación de la carga en los QDs, así como la influencia de todos los elementos vecinos mediante capacidades eléctricas. Una vez se obtiene el potencial local en cada QD, los niveles energéticos de los QDs son desplazados. Esto afecta a las corrientes túnel y se ha de obtener la nueva función de distribución y por lo tanto, la nueva carga. El potencial se modifica y el proceso se repite, obligando a una

resolución autoconsistente de la ecuación de carga de cada QD y la solución de Poisson. Este régimen se denomina self-consistent field regime (SCF).

El modelo de transporte explicado previamente fue aplicado para estudiar la respuesta eléctrica de diferentes sistemas formados por uno y dos QDs en diferentes configuraciones: serie y paralelo. Partiendo de la descripción más simple de los QDs (único nivel energético por QD y probabilidades de transmisión constantes), nos permite estudiar a fondo y resaltar los parámetros que dominan la respuesta eléctrica del sistema. Las condiciones necesarias para obtener transporte eléctrico en este tipo de sistemas se pueden resumir en:

- El transporte eléctrico ocurre solo en el rango de energías (la ventana de conducción) creada por los diferentes potenciales electroquímicos de los contactos, que bajo la influencia de un potencial externo se pueden escribir como $\mu_L - \mu_R = qV$.
- Solo hay transporte eléctrico a través de los niveles energéticos de un QD intermedio que están dentro de la ventana de conducción.
- Debido a que solo consideramos transporte balístico, el transporte entre QDs implica que haya niveles energéticos disponibles en el QD final a la misma energía que en el QD inicial. De esta forma, el solapamiento entre las densidades de estados de los QDs juega un importante papel abriendo y cerrando posibles caminos de transporte.

Por otro lado, también se estudió la influencia de los diversos parámetros en la respuesta eléctrica del sistema viendo que esta depende de: los niveles energéticos de los QDs, el acoplamiento capacitivo entre los diversos elementos del sistema y los coeficientes de transmisión.

El modelo de transporte propuesto en esta tesis se comparó con otro formalismo de origen puramente quántico como son las funciones de Green de no-equilibrio. Se estudiaron varios sistemas y configuraciones obteniendo los similares resultados con ambos formalismos. De esta comparación se observo que el modelo de transporte aquí presentado no incluye los efectos de coherencia.

De la teoría a la implementación en código

Una vez que el modelo se validó y se remarcaron los parámetros más importantes que dominan la respuesta del sistema, estos fueron descritos de forma realista.

- Para la descripción de los niveles energéticos de los QDs, se uso un potencial del tipo pozo finito haciendo uso de la aproximación de la masa efectiva. De esta

forma, aparecen estados discretos directamente de la resolución de la ecuación de Schrödinger.

- Los coeficientes de transmisión se describieron mediante la aproximación WKB que permite introducir la dependencia energética, la longitud y la altura de la barrera túnel.
- Finalmente, expresiones analíticas y la aproximación numérica de las cargas imágenes se usaron para la descripción de las capacidades entre los QDs y los electrodos y entre QDs, respectivamente.

Por otro lado, también se introdujeron estados discretos por debajo del nivel de Fermi en el equilibrio correspondiente a estados de huecos. Estos estados, bajo un potencial externo, se pueden vaciar permitiendo que también haya transporte de electrones por ellos. Por lo tanto, es necesario introducir estos movimientos correspondientes a corrientes de huecos. El formalismo de transporte desarrollado junto con una descripción realista de los diversos parámetros (capacidades y transmisiones), así como de los niveles energéticos de los QDs forman el núcleo del código desarrollado en MATLAB© denominado SimQD. De esta forma, tenemos una herramienta computacional que permite simular la respuesta eléctrica de este tipo de sistemas basada solo en la geometría del dispositivo y en varios parámetros fundamentales del material.

Transporte en quantum dots de silicio

El código desarrollado se utilizo para simular QDs de silicio crecidos dentro de una matriz de dióxido de silicio, Si/SiO_2 QD. Se llevo a cabo un estudio de las corrientes (electrones y huecos) y de la carga acumulada en función de la geometría del sistema. Debido a que la barrera de potencial para electrones es más pequeña que la barrera para huecos, la corriente de electrones es el término dominante en la corriente total. La corriente aumenta de forma escalonada debido a la naturaleza de niveles energéticos discretos del QD. Además, al haber introducido la dependencia energética en el coeficiente de transmisión hace que aparezca un efecto de Negative differential resistance (NDR). La dependencia en la corriente y en la carga acumulada con la posición del QD respecto a los electrodos también se muestra. De forma similar, se utiliza el código para simular dispositivos basados en bicapas de QDs. El análisis de estos sistemas es mas complicado ya que existen muchos caminos posibles para la corriente y la respuesta final del sistema acaba dependiendo fuertemente de la geometría de este.

Aplicando una pequeña modificación en la solución de la ecuación de Poisson, incluyendo el efecto de un tercer electrodo, podemos simular la respuesta eléctrica de estructuras tipo transistor. Debido a los niveles discretos de los QDs, cuando se muestra un mapa de corriente en función de la diferencia de potencial aplicada y del potencial del tercer

electrodo la corriente obtenida forma estructuras de diamante. De forma análoga, se simuló un doble gate transistor reproduciendo la estructura en forma de hexágono para la corriente obtenida.

Finalmente, usando la misma metodología de transporte se describió el transporte a través de trampas o defectos propios de la matriz que contiene los QDs. Estos defectos se describieron como QDs puntuales con un solo nivel energético y el potencial en ellos se obtuvo considerando una caída lineal del voltaje en la matriz. Mediante el formalismo de Transfer Hamiltonian, la corriente túnel directa entre los electrodos (sin necesidad de procesos túnel intermedios en los que intervengan QDs o trampas) se puede explicar fácilmente. De esta forma, tenemos un modelo que tiene en cuenta tres mecanismos de transporte independientes. El modelo de transporte mediante trampas fue validado con resultados experimentales de medidas eléctricas de capas de SiO_2 de diversos grosores obteniendo la concentración y la posición energética media de la distribución de trampas. Para voltajes aplicados (campos) bajos y moderados es el proceso de conducción dominante mientras que para altos voltajes, el proceso de túnel directo entre electrodos domina. Combinando el modelo de transporte de trampas junto con el de QDs, se simuló una matriz aleatoria de Si/SiO_2 QDs. Para este caso, a bajos voltajes la tendencia experimental se reproduce con el modelo de transporte a través de QDs mientras que para voltajes medios y altos, el transporte por trampas es el mecanismo dominante. Por último, se simuló una superlattice de Si/SiO_2 QDs y se comparó con resultados experimentales. El modelo de transporte por QDs reprodujo las NDR de los datos experimentales a bajos voltajes mientras que a altos voltajes, el transporte por trampas el mecanismo dominante.

Interacción con la luz

Una vez que el modelo de transporte eléctrico fue testeado y usado para reproducir resultados experimentales, se modifico para tener en cuenta los procesos de generación/ recombinación de portadores asistidos por fotones. Con la introducción de dos nuevos términos en la ecuación de balance de cada QDs, estos nuevos procesos se pudieron considerar. Haciendo uso de la regla de oro de Fermi, las transiciones ópticas dependen de una probabilidad de transición entre estados y la ocupación del estado inicial y del estado final.

Las probabilidades de transición entre niveles asistidos por fotones se obtuvieron asumiendo régimen de fuerte confinamiento, la aproximación dipolar eléctrica y despreciando procesos ópticos de segundo orden. De esta forma, se describieron las transiciones intra- e inter- banda. Los resultados obtenidos se pueden resumir en:

- La respuesta eléctrica del QD viene dada por el ratio entre los términos eléctricos y ópticos siendo necesaria una asimetría en los coeficientes de transmisión a los electrodos para generar corriente solo con iluminación.

- Respecto a las curvas de corriente en función del voltaje externo aplicado con y sin iluminación, solo se obtienen diferencias a bajos voltajes, cuando los términos de luz son los dominantes. A altos voltajes, la respuesta eléctrica es prácticamente la misma que en el caso sin iluminación.

- La corriente fotogenerada en función de la energía del fotón incidente describe básicamente el coeficiente de absorción del QD.

- El modelo de transporte en combinación con la implementación de la luz fue usado para reproducir los resultados experimentales de un dispositivo basado en QDs en una configuración en paralelo. Las corrientes fotogeneradas con y sin iluminación externa, en función de la energía del fotón incidente así como en función de la irradiancia de la luz incidente fueron reproducidas.

List of Figures

1.1 (a) Scanning electron microscopy (SEM) picture of a lateral quantum dot structure. Six metallic gates that create the confinement potentials are deposited on top of a GaAs/AlGaAs heterostructure. The picture has been extracted from Ref. [1]. (b) Scheme of a vertical QD structure [2]. (c) Transmission electron microscopy (TEM) image of large array of Si Qds in a SiO_2 matrix with low magnification, extracted from Ref. [3]. . . 2
1.2 (a) Scheme of the Si-based tandem solar cell. (b) Bulk energy band alignments between crystalline silicon and its carbide, nitride and oxide. . 7

2.1 (a) 1D Energy band scheme of the structure of the system. The QDs are described as wells in the band structure of the oxide matrix. Since we are only considering ballistic transport, the electron crosses through the potential barriers by tunneling events. (b) Equivalent electrical scheme of a QD array embedded in an insulator matrix. The QDs (circles) are connected between them and the leads (color blocks) by tunneling junctions. The tunneling junctions can be described as a capacitor in parallel with a current path. 19
2.2 (a) Band energy scheme of the tunnel junction. The electron tunnels from an eigenstate E_L on the left side of the barrier to the eigenstate E_R on the right side. (b-c) The decomposition of the total Hamitonian H into two subsystems: H_L and H_R. The wave function ψ_L and ψ_R are also presented showing the exponential decay in the barrier region. 23
2.3 (a) I(V) curves of a single metallic QD in the Coulomb blockade regime for different temperature ranges. The current step-like behavior is recovered when the external bias voltage increases in multiples values of V_T. (b) Electron number in the QD as a function of the applied bias voltage. The accumulated charge also increases in discrete steps. In the inset, the energy band scheme, the Fermi levels of the leads (μ_L and μ_R) as well as the QD states with N and $N+1$ electrons are shown. The energy separation among the $N+1$ and N states is E_c. 29
2.4 Obtained I(V) curves for single semiconductor QD with a spin degenerated energy level for the two studied regimes: the self-consistent field (SCF) and the Coulomb blockade (CB). 32
2.5 Equivalent electrical scheme of the three basic systems under study: (a) single QD, (b) two QDs in serial configuration and (c) two QDs in a parallel arrangement. We also show the notation used to describe the tunneling junctions, the capacities and the transmission probabilities. . . 33

2.6 (a) Band scheme for the cases: $V = 0$ upper, $V > 0$ left and $V < 0$ right figures, respectively. (b) I(V) curves as a function of the QD energy level. (c) I(V) curves as a function of the charging energy and (d) varying the transmission coefficients of the leads. In the insets, the accumulated electrons in the QD (N) for each case is also shown. The used parameters were: $k_B T = 0.025eV$, $T_1 = T_2 = 0.005$, $U_0 = 0.25eV$, $C_d = C_s$, $\varepsilon_r \varepsilon_0 = 1$ and $\epsilon_0 = 0.2eV$. The varied parameters are shown in the legend of their respective figures. 34

2.7 (a-b) I(V) curves and (c-d) conductance characteristics obtained for the serial arrangement depicted on Fig. 2.5(b) for different capacitive coupling. (a-c) As a function of the left lead QD capacity C_s, showing a rectifying effect when the system is weakly coupled with the left lead. (b-d) As a function of the inter-dot capacity C_c. In both cases, NDR is obtained since when the voltage increases the overlapping between the energy levels decreases and the current also decreases. The simulation parameters were: $\mu_L = qV$, $\mu_R = 0$, $T_1 = T_2 = T_3 = 0.005$, $k_\beta T = 0.025eV$, $U_0 = 0.25eV$, $\epsilon = 0.2eV$ and $\varepsilon_r \varepsilon_0 = 1$. C_d is fixed at the initial C_s value. 37

2.8 I(V) curves for two QDs in the parallel arrangement for different capacitive couplings: (a) as a function of the left lead QD capacity C_s and (b), as a function of the inter-dot capacity C_c. In the inset the band scheme of the two QDs are also shown. The simulation parameters were: $\mu_L = qV$, $\mu_R = 0$, $T_1 = T_2 = T_3 = 0.005$, $k_\beta T = 0.025eV$, $U_0 = 0.25eV$, $\epsilon = 0.2eV$ and $\varepsilon_r \varepsilon_0 = 1$. C_d is fixed at the initial C_s value. 40

2.9 (a) The I(V) curve for one single QD obtained using the NCRE. We also show the NEGFF results for the same system. The NEGFF data have been taken from Sun *et al.* [63] (b) The electron number in the QD as a function of the applied bias voltage. The inset shows the connection geometry. The rectangles represent the two leads and the circle represents the QD. 47

2.10 (a) The normalized I(V) curve for two QDs in a serial configuration obtained using NCRE. We also show the NEGFF results for the same system, the NEGFF data are taken from Sun *et al.* [63]. The inset also shows the connection geometry. (b) The electron number in the QDs as a function of the applied bias V. 48

2.11 (a) The total and partial I(V) curves obtained using NCRE for a parallel configuration. The NEGFF results are taken from Sun *et al.* [63]. (b) The electron number in the QDs as a function of the applied bias V. . . . 49

2.12 (a) The I(V) curve, for the configuration plotted in the inset, obtained using NCRE. We also show the NEGFF results for the same system, the NEGFF data are taken from Sun *et al.* [63]. (b) The electron number in the QDs as a function of the applied bias V. 50

2.13 (a) The total and partial I(V) curves obtained using NCRE for the configuration showed in the inset. The NEGFF results are taken from Sun *et al.* [63]. (b) The electron number in the QDs as a function of the applied bias V. 51

2.14 (a-c-e) I(V) curves and (b-d-f) accumulated electron number for three different QDs arrangement. The insets show the connection geometry. The NEGFF results are taken from Sun *et al.* [63]. 52

2.15 The I(V) curves for the largest systems: (a) 100 QDs in parallel configuration, (b) 100 QDs in serial configuration and (c) 100 QDs in an array disposition 10×10. 53

3.1 (a) Electron (f_0) and hole ($1-f_0$) distribution functions, Fermi level (E_f), DOS (ρ_{CB} and ρ_{VB}) and electron ($f_0\rho_{CB}$) and hole populations ($(1-f_0)\rho_{VB}$) for an intrinsic bulk semiconductor. (b) Scheme of the tunneling junction and the tunneling transitions under external polarization. (c) Schematics of the different tunneling processes in bulk materials. Electron from conduction band to conduction band (ECB), electron from valence band to conduction band (EVB) and tunneling from valence band to valence band (HVB) processes. 70
3.2 (a) Scheme of arbitrary spatial varying potential $\phi(x)$ barrier and the input (A and D) and output (B an C) amplitudes. (b) Scheme of the spatial discretization of the previous presented potential barrier. 72
3.3 Scheme of the band diagram for the: (a) direct tunnel and, (b) the Fowler-Nordheim processes. 76
3.4 (a) Transmission coefficient as a function of the energy of the incident carrier for different polarization voltages. An scheme of the band bending is also shown in the inset. The value of the potential barrier is $\phi_0 = 3.1$ eV, $m_{ox} = 0.3m_o$ and barrier width $d = 3$ nm. The vertical dashed lines represent the transition from DT to FN tunneling processes. (b) Representation of the different tunneling process as a function of the voltage and the incident carrier energy for the previous barrier. We must note that the transport only occurs when the carrier is inside the transport window created by μ_L and μ_R. We fix $\mu_L = 0$ and $\mu_R = -qV$. 77
3.5 (a-b) Transmission coefficients for a rectangular and triangular potential barrier of $1nm$ width, respectively. The exact solution and the WKB approximation are shown for the rectangular barrier. The solution for the triangular case using the transfer matrix with different space discretization and the WKB approximation are also shown. In the inset, an scheme of the system is presented. (c-d) Transmissions coefficient for a rectangular and triangular potential barrier of 3 nm width, respectively. . 78
3.6 (a) Lead-QD capacity for different QDs radii as a function of the distance. (b) QD-QD capacity for different R_2 radii, the radius of one QD is hold at $R_1 = 1$ nm. In both cases, we have used $\varepsilon_r = 3.9$. 81
3.7 Scheme flowchart of the SimQD that implements the methodology described in this chapter. 84
3.8 List of the input parameters that describe the device. 85
3.9 (a) Band diagram scheme of a single QD and the energy grid. All the energy dependent parameters are evaluated at these grid energy points. Moreover, the “interesting” transport region is highlighted by the red square. As we saw previously, the transport only occurs in the energy window created by μ_L and μ_R. Since we are doing the transport calculus at room temperature, we also include an energy region above and below the electrochemical potentials. (b) Computing strategy to obtain the distribution function at each energy grid point. The set of rate equations are solved for each energy being P and A the transport matrices. 88
3.10 Computational time vs. number of simulated QDs. The time is referred for a single voltage point. Simulations were done in a dual core 2.60 GHz. 89

4.1 Obtained DOS for a QD of R=1nm. The broadened binding electron and hole states are shown. The position of the Fermi level E_F (zero energy point), the confinement potentials $\phi_{1,ECB}$ and $\phi_{1,HVB}$ and the Si bulk band gap E_{gap} are also shown. For energies above the confinement potentials, continuous DOSs are assumed. 98
4.2 (a) Relaxed structure of the QD of 32 Si atoms in crystalline (left panel) and amorphous (right panel) SiO_2 matrix. Red spheres are O atoms, green spheres are Si atoms and the yellow thick sticks represents the Si atoms that form the Qd. (b) Simulated DOS using DFT for different Si QD sizes embedded in amorphous a- or crystalline c- SiO_2 matrix. The subscript is the number of Si atoms that form the QD. For comparison, the amorphous silica (a-SiO_2) is shown in all the plots. From this comparison, the band offsets for each QD radius can be obtained. The figures have been taken from Ref. [8]. The position of the Fermi level is the vertical dashed line and it is located in the middle of the QD E_{gap}. 100
4.3 A single Si/SiO_2 QD of $R = 1.5$ nm placed in different positions between the two leads. x is the distance from the left lead to the center of the QD. The separation among the leads is 5 nm. (a-b) I(V) curve and accumulated charge for a centered QD. The hole and electron currents are also shown. (c-e) I(V) curves for different QD positions and (e-f) accumulated charge in the same cases. 102
4.4 Band diagram scheme of the single Si QD in different positions (x) and bias polarizations ($V < 0$ and $V > 0$). The thinnest arrows represent a lower transmission probabilities whereas the widest ones are the most probable transmissions. The conduction window, $\mu_L - \mu_R$, and the several electron (blue lines) and hole (green lines) energy levels are also shown. (a) and (d) reflect an electron accumulation regime whereas in (b) and (c) the QD losses part of its initial charge (hole accumulation). 104
4.5 (a-c) Obtained I(V) curves for two layers of Si/SiO_2 QDs (the systems details are described in the text). The total current as well as the electron and hole partials currents are also shown. In the inset, the QD radius distributions are shown. (b-d) Total accumulated charge ($\sum_i \triangle N_i$, where $i = 1..20$) of the structures as a function of the external bias voltage. In the inset, a top view of the systems are presented where the left and right leads are L and R, respectively. 106
4.6 (a) Structure of the system under consideration. The scheme shows the three electrodes (source, drain and gate) and the QD is placed in the middle. The QD is connected with the source and drain by 1nm and 2nm tunnel junctions respectively. The QD radius is 1nm. The gate electrode is placed at 7.5nm distance from the center of the QD. This tunneling distance justifies the assumption that the current between the QD and the gate is negligible. (b) Band diagram of the structure without applied voltage, under negative gate polarization (c) and under a positive gate polarization (d). The oxide barriers, the equilibrium Fermi level and the electron and hole energy levels are also shown. 109

4.7 (a) Current map as a function of the applied V_{ds} and V_{gate}. Current suppression is obtained until the energy levels are placed between the electrochemical potentials of the drain and source (μ_d and μ_s). Once a conducting energy level is open the current increases dramatically. Important voltage points are also highlighted. (b) Accumulated charge ($q\triangle N$) in the QD map as a function of the applied voltages. 109
4.8 Obtained current map as a function of V_{ds} and V_{gate}. The single current diamonds corresponding to each QD are overlapped but they are still recognizable. In the inset, an scheme of the transistor device is presented. The system is formed by 3 Si QDs randomly generated inside the SiO_2 insulator matrix. 111
4.9 Obtained current map as a function of V_{ds} and V_{gate}. Current suppression is obtained until the energy levels lie between the electrochemical potentials of the drain and source. Once a conducting energy level is open, the current increases dramatically. In the inset, an scheme of the transistor device is presented. The system is formed by 4 Si QDs randomly generated inside the SiO_2 insulator matrix. 112
4.10 (a) STM image of the device showing the two QDs $D_{1(2)}$, tunnel-coupled to the source and drain (S/D) leads and capacitively coupled to the gates $G_{1(2)}$. (b) Close-up of the two QDs. Both figures have been extracted from Ref. [54]. Reprinted with permission from ACS. 112
4.11 Scheme of the double gate transistor under simulation. The tunnel junctions and the capacity couplings are also shown. Due to the QD configuration, we assume that each QD is only coupled to one gate and one lead. Thus, the electronic transport occurs as in the serial QDs cases studied before. The QDs radii are 2 nm and $V_{ds} = 0.25$ V. 113
4.12 Simulated current map for the previous presented structure as a function of the applied gate voltages, V_{G1} and V_{G2}, for $V_{ds} = 0.25$ V. Moreover, in the insets an intuitive explanation of the obtained current trend are also presented as a function of the DOS of each QD. The conduction window is also shown (dotted line). 114
4.13 Energy band diagram of the system under external electric field. The different elastic tunneling transport processes are also shown: (I and II) tunneling through the oxide from the left to right leads, (III) elastic trap assisted tunneling and (IV) tunneling through the discrete energy levels of the embedded QD. The Fermi levels of each lead (μ_L and μ_R) and the Fermi functions (f_L and f_R) are also shown. μ_L is fixed as a energy reference. 118
4.14 Experimental and simulated tunnel current density for different SiO_2 active layer thicknesses. The direct current among the leads is not considered. Experimental data has been extracted from Ref. [77]. 121
4.15 Current map for a single trap as a function of the distance to the left lead and the energy trap level for different electric fields: (a) $F = 2.5$ MV/cm, (b) $F = 5$ MV/cm, (c) $F = 7.5$ MV/cm and (d) $F = 10$ MV/cm. 123
4.16 Experimental normalized current density and simulated current for the SiO_2 structure. Trap (I_{Traps}) and direct tunnel (I_{FN}) currents are also shown. Experimental data has been extracted from Ref. [6]. 124

4.17 Trapped charge studies for the $50nm$ SiO_2 layer. (a) Trapped charge distribution in the oxide layer for different electric fields and (b) trapped charge as a function of the applied electric field. 124
4.18 Experimental normalized current density and simulated current for the Si QD/SiO_2 structure. Current through the QDs (I_{QD}) and the traps (I_{Traps}) are shown. Experimental data has been extracted from Ref. [6]. . 125
4.19 Experimental normalized current density and simulated current for the SL Si QD/SiO_2 structure. Different current contributions, through the QDs (I_{QD}) and traps (I_{Traps}), are also shown. In the inset, the cross section of the structure is presented. Experimental data has been extracted from Ref. [6]. 126

5.1 Scheme of the simplest system under study composed by a single QD with two energy levels. The QD is connected by tunnel junctions to the leads. The sense of the different currents terms are also shown for illumination conditions and no external bias voltage applied. 140
5.2 Scheme of a single QD under external illumination conditions and no external polarization. The QD is composed by two discrete energy levels. The magnitudes of the current components (the arrow size) and their direction are represented for different values of the tunneling transmissions: (a) $g_{Le} = g_{Re} = g_{Lh} = g_{Rh}$, (b) $g_{Le} > g_{Re} = g_{Lh} = g_{Rh}$, (c) $g_{Le} < g_{Re} = g_{Lh} = g_{Rh}$ and (d) $g_{Le} = g_{Re} > g_{Lh} = g_{Rh}$. 141
5.3 (a) Representation of Eq. 5.11 for the first angular quantum numbers. The binding states for each quantum number l are the points that cross $y = 0$. (b) Scheme of the radial distribution $r^2|R_l(r)|^2$ inside and outside the QD for the $l = 0$ case. 145
5.4 Energy level scheme of the states with zero or one electron-hole pair. We describe the states as a function of the electron and the hole angular momentum. The interband transitions are the continuous arrows whereas the intraband transitions are the dashed ones. 150
5.5 (a) Scheme of the binding states in the QD. Several optical transitions are shown, interband (blue lines) and intraband transitions (red lines), respectively. The equilibrium Fermi level (E_f) is also shown. (b) Representation of the absorption spectra for the previous system. The optical element matrix are shown as a vertical lines placed at the photon energy of the transitions (red lines for intraband and blue ones for interband). The absorption coefficient is the sum of individual absorption peaks related to each transition. 150
5.6 Scheme flowchart of the code that implements the methodology described in this chapter. The code is based on the previous presented one (SCF core) but several changes have been done in order to include the light. . . 151
5.7 Dependence of the obtained E_{gap} as a function of the radius of the Si QD without taking into account the exciton shift. For comparison, experimental data obtained from photoluminescence measurements are presented [28, 29, 30, 31, 32]. 153
5.8 Simulated absorption spectra in the equilibrium state for different QD radii. The summation of all the contributions to the spectra has been done according to the Fermi Dirac distribution function, where for simplicity, the Fermi level has been placed in the energy origin, $\mu = 0$. The arrows represent the value of the E_{gap} for each QD radius. 153

5.9 Photocurrent as a function of the energy of the incident light with an external applied bias voltage. In the inset a scheme of the system is presented, a QD of $R = 1.06nm$ is placed between the two electrodes. (a) Symmetric system $d = d' = 1.78nm$. For $V = 0$ case the current is zero while for $V \neq 0$ the symmetry of the system is broken and net current appears. (b) Asymmetric system $d = 1.47$ nm and $d' = 2.09$ nm. A net current is obtained even at $V = 0$. The current peaks refers the position of the maximum optical transition probabilities. 155
5.10 (a) The total I(V) curve (in absolute value) for the symmetric system in dark case and under different illumination conditions (incident photon energies). (b) The total I(V) curve (in absolute value) for the asymmetric system in dark case and under different illumination conditions (incident photon energies). 155
5.11 The QDs radii are $R_1 = 1.0$ nm and $R_2 = 0.8$ nm respectively. The distances between the first QD (QD_1) and the leads are $d_{L1} = 2.5$ nm and for the second one (QD_2) $d_{L2} = 2.5$ nm. The distance between the QDs is $d_{12} = 3$ nm. All the distances are measured from the center of the QDs. (a) The total I(V) curve (in absolute value) for the parallel system in dark case and under different illumination conditions (incident photon energies). (b) Photocurrent as a function of the photon incident energy for different applied bias voltage. 156
5.12 The QDs radii are $R_1 = 0.3$ nm and $R_2 = 0.8$ nm. The first QD is placed at $d_{L1} = 2.5$ nm and $d_{R1} = 5.1$ nm and the second QD is placed at $d_{L2} = 4.8$ nm and $d_{R2} = 2.8$ nm from the left and right leads respectively. The distance between both QDs is $d_{12} = 2.3$ nm. All the distances are measured from the center of the QDs. (a) The total I(V) curve (in absolute value) for the serial system in dark case and under different illumination conditions (incident photon energies). (b) Photocurrent as a function of the photon incident energy for different applied bias voltage. . 157
5.13 Scheme of the device fabricated by Prins *et al.* [35]. Two Au contacts are separated by a trench of ≈ 5 nm in which the PbSe QDs are placed. In the inset, a SEM image of the electrodes is showed. Both figures have been extracted from Ref. [35]. Reprinted with permission from ACS. . . . 159
5.14 Dependence of the obtained E_{gap} as a function of the radius of the PbSe QD without taking into account the exciton shift (solid line). For comparison, experimental data (filled symbols) [37, 38, 40] and results from different theoretical approaches (hollow symbols) are also presented [39, 41, 42]. 160
5.15 Simulated absorption spectra (continuous line) and experimental one (dashed line) for different PbSe QDs radii. Experimental data has been taken from Ref. [43]. 160
5.16 Simulated I(V) curve in dark (continuous blue line) and light (dash blue line) conditions respectively (normalized to the maximum current). In the inset we show the experimental (square red points) and simulated (continuous blue line) normalized photocurrent. Both figures are normalized to the maximum current. Measured I(V) points have been extracted from Prins *et al.* [35]. 161

5.17 Simulated normalized photocurrent curve (continuous blue line) and experimental curve taken from Prins *et al.* [35] (dash blue line) as a function of the wave length of the incident light. Simulated normalized absorption coefficient (continuous red line) of the QD system and experimental absorption (red dashed line). In the inset, we show an scheme of the system under external polarization; the band diagram of the QD, the optical transitions and the band bending of the barriers due to the external bias voltage $V = 750mV$. Besides, the electrochemical potentials of the leads are also presented . . . 162
5.18 Experimental net photocurrent as a function of irradiance (square red points) and simulated (continuous blue line). Experimental points taken from Prins *et al.* [35]. . . . 163
5.19 Comparison between the DFT results and the EMA approximation for the obtained DOS for different QDs diameters. DFT data has been taken from Ref. [48]. . . . 165
5.20 DFT absorption spectra for different QDs radii. Data has been taken from Ref. [49]. The matrix transitions elements calculated using the EMA approach are also shown. . . . 166